A Contribution to the Online Monitoring of Partial Discharges in High-Voltage Grid Components

Von der Fakultät für Maschinenbau, Elektro- und Energiesysteme
der Brandenburgischen Technischen Universität Cottbus-Senftenberg
zur Erlangung des akademischen Grades eines
Doktors der Ingenieurwissenschaften

genehmigte Dissertation

vorgelegt von

M.Sc.
Iaroslav Shevchenko

geboren am 17.07.1994 in Sankt Petersburg, Russische Föderation

Vorsitzender: Prof. Dr.-Ing. Kathrin Lehmann
Gutachter: Prof. Dr.-Ing. Prof. h.c. mult. Harald Schwarz
Gutachter: Prof. Dr.-Ing. Peter Birkholz (TU Dresden)

Tag der mündlichen Prüfung: 20.10.2023

https://doi.org/10.26127/BTUOpen-6629

Abstract

Increasing utilization of HV power cable lines, and particularly the advent of long HVDC underground links, results in the need to sensitively monitor their condition, such as by tracking the emergence and development of partial discharges. This study demonstrates that existing solutions are poorly suited to the case of HVDC lines, and that a new, more sophisticated monitoring system needs to address a wide array of diverse problems.

First of all, the overview of the task and main functional blocks of the monitoring system is given. Following this, selected blocks are subject to detailed examination in subsequent chapters.

The first of these blocks, a high-frequency current transformer (HFCT), is responsible for capturing the signal in the power line and transferring it to the electronics. This component receives in-depth coverage: general design considerations, computation of leakage inductance, operation in presence of a power current, resonant behavior, balanced design. Particular attention is given to the application of Finite Element Analysis (FEA) in relation to the HFCT, however, the demonstrated techniques can also be applied to other magnetic devices. Last section of the chapter presents various stages of development, experimental setups, prototypes, and the final device which has been put into series production.

The next block addresses extraction of signals from noise. A literature analysis is conducted concerning noise suppression in partial discharge recordings, and the application of the signal separation approach based on Linear Predictive Coding is shown.

In the section on localization, examples illustrating problems encountered during the development of a partial discharge localization algorithm are presented.

In the chapter devoted to laboratory tests, various auxiliary experiments conducted during the system's development are compiled, where some of them are: Time Domain Reflectometry (TDR) TDR-based line characterization, estimation of monitoring sensitivity, measurement of the cable attenuation and reflection coefficients of the accessories.

In the final chapter – field tests – the installation of the system on a 110 kV line and the measured transfer function are demonstrated.

Kurzfassung

Mit der zunehmenden Nutzung von Hochspannungs-Stromkabeln, insbesondere durch das Aufkommen langer HVDC(HGÜ)-Leitungen, entsteht die Notwendigkeit, ihren Zustand sensibel zu überwachen, etwa durch die Verfolgung der Entstehung und Entwicklung von Teilentladungen. Diese Studie zeigt, dass bestehende Lösungen schlecht auf den Fall von HVDC-Leitungen zugeschnitten sind und dass ein neues, ausgeklügelteres Überwachungssystem eine Vielzahl von unterschiedlichen Problemen angehen muss. Zunächst wird ein Überblick über die Aufgabe und die Hauptfunktionsblöcke des Überwachungssystems gegeben. Anschließend werden ausgewählte Blöcke in den folgenden Kapiteln detailliert untersucht.

Der erste dieser Blöcke, ein Hochfrequenz-Stromtransformator, ist dafür verantwortlich, das Signal in der Stromleitung zu erfassen und an die Elektronik weiterzuleiten. Diese Komponente erhält eine ausführliche Behandlung: allgemeine Designüberlegungen, Berechnung der Streuinduktivität, Betrieb in Anwesenheit eines Leistungsstroms, Resonanzverhalten, ausgewogenes Design. Besonderes Augenmerk wird auf die Anwendung der Finite-Elemente-Analyse (FEA) in Bezug auf den Hochfrequenz-Stromtransformator (HFCT) gelegt. Die vorgestellten Techniken können jedoch auch auf andere magnetische Geräte angewendet werden. Der letzte Abschnitt des Kapitels präsentiert verschiedene Entwicklungsstufen, experimentelle Aufbauten, Prototypmodelle und das endgültige Gerät, das in Serienproduktion gegangen ist.

Der nächste Block befasst sich mit dem Problem der Signalextraktion aus dem Rauschen. Es wird eine Literaturanalyse durchgeführt, die sich auf die Rauschunterdrückung in Teilentladungsdaten bezieht, und die Anwendung des Signalabtrennungsansatzes basierend auf der linearen prädiktiven Codierung wird gezeigt.

Im Abschnitt über die Lokalisierung werden Beispiele für Probleme vorgestellt, die bei der Entwicklung eines Algorithmus zur Lokalisierung von Teilentladungen aufgetreten sind.

In dem Kapitel, das den Labortests gewidmet ist, werden verschiedene Hilfsexperimente zusammengefasst, die während der Entwicklung des Systems durchgeführt wurden. Einige davon sind: TDR-basierte Leitungscharakterisierung, Schätzung der Überwachungsempfindlichkeit, Messung der Kabeldämpfung und der Reflexionskoeffizienten der Zubehörteile.

Im abschließenden Kapitel - den Feldtests - wird die Installation des Systems auf einer 110-kV-Leitung und die gemessene Übertragungsfunktion vorgestellt.

Acknowledgment

This work was partially composed within the walls of BTU Cottbus-Senftenberg and partially at the HighVolt Prüftechnik Dresden. It is my honor to express my profound gratitude to all with whom I have had the opportunity to work over these past four years, spanning two different cities.

I would like to express my heartfelt gratitude to my supervisors: Prof. Dr.-Ing. Prof. h.c. mult. Harald Schwarz and Prof. Dr.-Ing. Peter Birkholz.

I would also like to individually acknowledge Mr. Erik Winkelmann, Mr. Christoph Steiner, Dr. Uwe Kaltenborn, Mr. Thomas Steiner, Dr. Ralf Pietsch, Dr. Vadym Bilous, Mr. Holger Häusler, and Mr. Gottfried Schuster for their interest and support, as well as the entire Prüffeld Team of HighVolt. Moreover, I express my deep gratitude to my former university supervisor in SPbPU, Dr. Yuriy E. Adamyan and, last but not least, Mr. Egor Volkov for shearing his experience.

Finally, my deepest thanks go to my wife, family and friends for their consistent patience and unwavering support during this journey. Their understanding and encouragement were invaluable and are greatly appreciated.

Contents

List of Figures

List of Tables

List of Abbreviations

AC - Alternating Current

ACER - Agency for the Cooperation of Energy Regulators

ADC - Analog to Digital Converter

CAD - Computer-Aided Design

CEEMD - Complete Ensemble Empirical Mode Decomposition

DAC - Damped AC

DC - Direct Current

DFT - Discrete Fourier Transform

DT-CWT - Dual-Tree Complex Wavelet Transform

DTS - Distributed Temperature Sensing

DWT - Discrete Wavelet Transform

EHV - Extra High Voltage

EM - Electromagnetic

EMC - Electromagnetic Compatibility

EMD - Empirical Mode Decomposition

EMF - Electromagnetic Field

ENTSO-E - European Network of Transmission System Operators

EU - European Union

FDR - Frequency Domain Reflectometry

FEA - Finite Element Analysis

FIR - Finite Impulse Response

FPGA - Field-Programmable Gate Array

GIS - Gas Insulated Switchgear

GUI - Graphical User Interface

HFCT - High Frequency Current Transformer

H-FSVD - Hankel matrix based fast singular value decomposition

HV - High Voltage

HVAC - High Voltage Alternating Current

HVDC - High Voltage Direct Current

IEC - International Electrotechnical Commission

IEEE - Institute of Electrical and Electronics Engineers

IIR - Infinite Impulse Response

IMF - Intrinsic Mode Function

IPC - Industrial Personal Computer

LAN - Local Area Network

LMS - Least Mean Squares

LPC - Linear Predictive Coding

LPCC - Linear Prediction Cepstrum Coefficients

LSB - Least Significant Bit

MDL - Minimum Description Length

MF - Magnetic Field

MSPS - Mega Samples Per Second

MV - Medium Voltage

NPF - Near Power Frequency

NWP - Netzentwicklungsplan

OVP - Over Voltage Protection

PC - Personal Computer

PCA - Principal Component Analysis

PD - Partial Discharge

PRPD - Phase Resolved Partial Discharge

PSD - Power Spectral Density

PSS - Power Spectral Subtraction

RE - Renewable Energy

RF - Radio Frequency

RLS - Recursive Least Squares

SAT - Site Acceptance Test

SCPI - Standard Commands for Programmable Instruments

SIDWT - Shift Invariant Discrete Wavelet Transform

SNR - Signal-to-Noise Ratio

SPICE - Simulation Program with Integrated Circuit Emphasis

STFT - Short-Time Fourier Transform

SVD - Singular Value Decomposition

SVL - Surge Voltage Limiter

TB - Technical Brochure

TDR - Time Domain Reflectometry

TRPD - Time-Resolved Partial Discharge

TYNDP - Ten-Year Network Development Plan

UDWT - Undecimated Discrete Wavelet Transform

UHF - Ultra High Frequency

UV - Ultraviolet

VLF - Very Low Frequency

VNA - Vector Network Analyzer

VPN - Virtual Private Network

XLPE - Cross-linked Polyethylene

1. Chapter:

Introduction

1.1 General Background

Since the beginning of electrical energy generation, fossil fuels have been the dominant energy source. However, this cheap and ubiquitously used resource has led to various problems that our society faces at present. Those are not limited to ecological issues, such as severe environmental impact: from local pollution disasters to global climate change - the consequences lie also in social and political spheres - for instance - the certain dependencies between resource-supplying and resource-demanding countries. These consequences are not only recognized by the public but already became common knowledge. The high public concern, which is especially pronounced in developed countries, acts as a basis for actual political decisions [1]. One of the most significant green movements of nowadays is the European Green Deal adopted by the European Commission on December 11, 2019, which is supposed to become a central component of the European Union's (EU) climate policy. The Green Deal is a set of policy initiatives to achieve zero net greenhouse gas emissions and zero total environmental pollution within the EU member states by 2050. The project is supposed to serve as the roadmap for the next three decades during the modernization of Europe: it contains proposals, defines targets, describes the legal framework, names investments needed and available funding tools, and overall, explains how to ensure a fair and inclusive transition to a green economy and sustainable future. The Green Deal concerns various policy areas: industry, building & renovation, transport, trade, agriculture, forestry, and most essential for this work, the energy sector. One of the main formulated objectives of the Green Deal is the reduction of CO2. As the production and use of energy account for more than 75% of the EU's greenhouse gas emissions, the energy sphere lies in full focus. The main mechanism of reducing emissions lies in the transition to generation from renewable resources (RE). Therefore, the energy sphere in the EU is undergoing rapid development, which accelerates over the years. To better convey the current situation and show the pressure which is changing the energy market we could mention a few most recent milestone events, which are either part of the Green Deal or were forerunners of it:

- In 2019 the "Clean Energy for All Europeans" package was introduced – a set of eight energy-related legislative acts. Within it, the National Energy and Climate Plans (NECPs) were defined for the first time by the Regulation on the Governance of the Energy Union and Climate. Also, the Renewable Energy (RE) Directive,

which in 2008 targeted 20% of renewables by 2020, was revised and established a new target of at least 32% for 2030.

- On March 4th, 2020, the European Climate Law was proposed and later adopted to transform plans, proposals, and political promises into a binding legal obligation. It ensures a predictable business environment for investments in RE and the whole RE industry.
- On 17 September 2020, a 2030 Climate Target Plan was presented, which aimed at stimulating investments in a resource-efficient economy, promoting innovations in clean technology, fostering competitiveness, and creating green jobs. Alongside for stimulating the joint work of the Member States on financing and deployment of RE projects, the European Commission adopts the rules for a new EU RE Financing Mechanism [2].
- On November 19, 2020, the European Commission presented the EU Offshore RE Strategy, which proposes an increase of European offshore wind capacity by 5 times its current level by 2030 and 25 times by 2050.
- On 14 July 2021, the European Commission sent to the European Parliament and the Council a proposal for the revision of the RE Directive: to raise the 2030 target for renewable energy as a share of the EU's final energy consumption from 32 to 40 %. This proposal is made as a part of the "Fit for 55" package named after the new desired level of emission reduction: 55% in contrast to the former value of 40%.
- In May 2022, the EU Commission unveiled a REPowerEU plan to respond to disruptions in global energy markets caused by Russia's invasion of Ukraine. The 2030 target for renewables is proposed to be increased from the current 40% to 45%.
- The EU Member States shall update their 10-year national energy and climate plans for 2021-2030 by June 2023 (drafts) and June 2024 (final versions) according to the new target values given.

This list mentions only a few EU-level accomplishments. Certainly, the RE initiatives are present not only on the EU level but they can also be found when going up or down in scale. Taking a step up to the United Nations one can find the "increase of RE" within the Sustainable Development Goal 7, which aims to "Ensure access to affordable, reliable, sustainable and modern energy for all." Going down in scale one can find the corresponding renewable-encouraging legal frameworks on the national levels. Those can be more independent, e.g., in Asian countries, or dictated by the union-level (e.g., EU) policy.

When conceding RE we can contrast ones that can be shown as a single point on a map, such as nuclear and big hydropower stations, to the ones that are spatially distributed, such as wind and solar plants and small-scale hydro sources. Eventually, distributed energy sources are about to take the leading part in the renewable's family. The total share of nuclear power, which was playing a major role among renewables, tends to decrease in Europe, mostly as the result of public safety concerns [3][4]. In recent years, due to a nuclear accident in 2011 at the Fukushima Daiichi Nuclear Power Plant the reputation of nuclear power got another blow despite all its outstanding benefits. At the same time, the expansion of hydropower in Europe has a few constrictions that are not likely to be overcome: the amount of possible locations for the new large-scale hydropower projects is very limited [5], while small plants, which delivered 91% of hydro-energy in 2021, became known to cause severe damage to the ecosystem and biodiversity [6].

Eventually, the focus of fulfilling the objectives of the 2030 Climate Target Plan lies in future extensions of solar and wind energies. As was already mentioned, an important particularity of these energy sources is their spatial distribution: relatively low-power sources are scattered over vast territories. Being dependant on weather conditions, solar and wind stations feature the self-evident disadvantage of non-constant and, moreover, rather unpredictable power output. The operation of the grid is a sophisticated process, as it must be constantly balanced in a way that the load matches the generation. With the rapid increase in RE, this balance is getting harder to maintain. The symptoms of this, such as frequency deviation or power quality issues, are not necessarily noticed by the end-costumer, which does not exclude the fact that the grid is brought closer and closer to its operational limit. Apart from alternating power output, the RE boost logistical issues, namely the increasing mismatch between the map of introduced RE sources and the map of the consumption hubs. Over the years, one of the core objectives in the development of a power grid was placing power plants closer to the points of consumption [7] This rule, however, is not valid for most of RE. Independently of which type is taken into consideration: hydro-, solar- or wind-power sources, their actual locations will depend on the land's availability and its appropriateness for the corresponding type of energy production – the distance to the consumer is not taken into consideration. Among other RE-related problems stand the non-compensated reactive power in the system, low densities of energy flows, and frequency stability issues resulting from the lack of rotating generators' inertia. These and a few other factors raise the demand for the so-called ancillary services.

"Ancillary services" is the term used to denote various operations other than generation and transmission, which are necessary to maintain network stability. Those include Redispatch, Feed-in Management, Frequency Containment/Restoration, Provision & Engagement of Reserve Power Plants, Loss Energy Procurement, Reactive Power Provision, and others. As a separate block can be noted means of energy accumulation, such as pumped-storage hydroelectricity and smart grids. During recent decades, the expenditures for these ancillary services keep increasing along with the introduction of RE.

Along with the use of ancillary services the adaption of the energy grid is taking place. The reshaping of the grid is a long-term strategy-based process as the latter had been evolving for over a century within a conservative means of generation. In the field of transmission networks in Europe, the goal is to noticeably increase their carrying capacity and to connect remote areas with each other. This should give a strong impetus to the development of renewable energy sources and storage capacities.

The transformation of the grid is planned via the Grid Development Plans – the national-level documents. At the European level, transmission system operators work together in the framework European Network of Transmission System Operators (ENTSO-E) [8] and every two years publish a joint development plan for the European network: a Ten Year Network Development Plan (TYNDP). The consistency between the TYNDP and national Grid Development Plans is proven by the EU Agency for the Cooperation of Energy Regulators (ACER).

Germany is one of the European leaders in implementing renewables, therefore the German Grid Development Plan is a good example showing the solutions in the adaptation of the national grid. There is a well-known example of the obstacle that should be solved in the future: The large and still increasing share of RE is being produced by the wind farms in the north and east regions of the country, while the large industrial consumers are in the southern and western states. The solution is though in developing several 2-4 GW transmission lines, which stretch from north to south and are known as the Corridor Projects. Initially, these links were planned as overhead lines. Despite widespread public approval of the transition to sustainable energy (in Germany this transition is known under the term "Energiewende"), the planning of the corridor projects led to the protests, even though these links are essential to fulfil the objectives of the "green" course. The solution was found in taking advantage of the HVDC (High Voltage Direct Current) underground cables.

Over the past decades, breakthroughs in material science and improvements in production technology led to the development and evolution of long HVDC cable lines, which are highly advantageous in bridging large distances. In 2015, the German federal government decided to use cables instead of overhead lines for performing corridor projects.

The proposals for the development of the grid are scoped in the document named the Grid Development Plan (In original naming: "Netzentwicklungsplan" (NWP) [9]), which is submitted by the four main German TSOs. Among others the current NWP 2021-2035 denotes four big onshore DC projects:

- A-North (approx. 300km)
- Ultranet (approx. 340 km)
- Suedlink (2 lines, eastern: approx. 750 km, western: approx. 500 km,)
- Südostlink (approx. 540 km)

The projects mentioned in NWP are included in the legal framework when they are added to the Federal Requirements Plan ("Bundesbedarfsplan"), which is an annex to the Federal Requirements Plan Act ("Bundesbedarfsplangesetz" (BBPlG)). In its current version (the year 2022) it notes 94 valid projects, among which 20 connections are using DC.

It is worth emphasizing that long-distance bridging due to the increase in RE is not the only booster of HVDC technology spread. Firstly, it is used as a standard solution for energy exchange between two systems working on different frequencies. Secondly, in some cases even though two big systems are running on the same frequency, it still can be beneficial to use DC in order to avoid the need in synchronization of them. A good example of this use case is the DC link between Russia and Finland [10]. It also may help to increase operational reliability by preventing cascading failures due to phase mismatch between the individual parts of a large power system. Furthermore, the connection of the regions or countries separated by large waterbodies can be performed only with an HVDC link, and the subsea cables are spreading over the last decades, binding together, for example, the Synchronous grid of Continental Europe with the British grid, the network of Ireland and grid of the Nordic regional group (Norway, Sweden, Finland and the eastern part of Denmark).

The links that interconnect regions and countries are tremendously relevant for the reliable functioning of the power grid. Due to such an important role, the possible outages – especially unpredicted ones – result in tremendous costs of dispatching and downtime. Unfortunately, a row of factors, such as the lack of operational experience, manually created

accessories, high operational stress, and overall size of the lines, make them prone to such failures. Therefore, the ratio between time-in-operation and the total lifetime, known as the "availability", of the cable lines is limited. A sophisticated quality assessment could remedy this problem and make HVDC projects even more economically beneficial than they are now.

Quality assurance of the HVDC cables is mostly addressed via factory- and site-acceptance tests. In contradiction to the common concept of testing stress representing the stress in operation, not only the DC voltage is applied through these procedures. AC testing is used as well, solely because it can be supplemented with the efficient measurement of partial discharge level (PD). The latter is one of the most frequently used techniques of quality assurance in high-voltage technology. The use of the AC stress on an HVDC cable during the site-acceptance test can serve as a workaround for performing a PD measurement with the state-of-the-art approach. During the operation of the HVDC cable line, this approach is naturally inapplicable, and, looking ahead, it should be said that in general the continuous monitoring of PD on DC cable lines is still a "Research and Development" topic.

Regardless of the subject, quality assessment with the use of PD measurement under AC stress is a very mature technology, extensively used worldwide for almost a century. Apart from the fundamental research of the PD phenomena, the real-world implementation of PD testing under AC stresses has been broadly represented in literature: for instance, as case studies for a variety of realizations on various equipment. The market in its turn offers a wide row of well-established products for its use. By contrast, for DC conditions PD measurement again remains a popular topic of ongoing research. The peculiarities of applying the DC PDs measurements to an HVDC cable line narrow the topic even more.

1.2 Motivation and Goal

As was shown the HVDC cable is a fast-spreading technology. The author considers continuous online monitoring to be an essential part of future HVDC cable projects. The successful pass of the factory- and site-acceptance test does not exclude failures in the long run. The HVDC lines are planned as capital projects with an expected long lifespan (e.g., 40 years). In its duration, the cable is subjected to numerous stresses: the varying voltage and load, heating & cooling cycles, switching impulses, standing waves from harmonics, and movement of the soil. Each component of the line is critical for its operation, therefore, without continuous health control, such a system is a "black box" that may fail at any

moment. If we would make an analogy to any other sophisticated system – anything from a car to a nuclear power plant – we would see that the operator always has access to readings from various meters, sensors, and data loggers, and in this way can judge the "health" of the system. For the HVDC lines, such health-status indicators are still under development.

Distributed Temperature Sensing (DTS) is a good instance of a health indicator that is already put in use [16]. It is a temperature control system that uses fiber optic sensor cables, and de facto it became a compulsory element in big cable projects. This system became widely spread for its relatively convenient practical implementation: the dielectric light fiber was easy to incorporate into the design of the power cable. This situation is different for the continuous PD measurements on the HVDC cable. As mentioned above, the PD measurements on DC were not used in industrial applications due to obstacles that will be further explained. The peculiarities of applying the PDs measurements to a HVDC cable line with respect to its topology, possible access points, and the sensitivity that should be achieved, put a lot of constraints on the possible solution. Up till now due to the hard practical realization, there were no off-the-shelf products that are sophisticated enough to solve all the issues relevant to PD measurements on HVDC cables.

A Partial Discharge (PD) monitoring system for continuous monitoring of HVDC power cables has been proposed and outlined in previously published works [Pub. 1] and [Pub. 2], while its individual modules were discussed in greater detail in [Pub. 3], [Pub. 4], [Pub. 5], [Pub. 6]. The purpose of this work is to restate and outline the goals and tasks of the monitoring system, then delve into several of its modules, namely, Sensor, Signal Separation, and Localization, and present a series of experiments and details that have not been included into the aforementioned articles, but nevertheless were important in the system's development process. In addition to this, the installation of the system on one of the cable lines is demonstrated, thus presenting some field-squared results.

1.3 Thesis organization

Chapter One outlines the change in the EU energy sphere and highlights the importance of the HVDC cable projects in the ongoing grid development. It claims that such complex projects need the ancillary monitoring solution for continuous quality assessment of the line elements. The motivation for the thesis is also deducted within this chapter as well as the goals of the work.

Chapter Two considers the most relevant standards, outlines existing methods of cable quality assessment & monitoring, describes typical HV cable lines as subjects to PD monitoring, and defines the difficulties in PD monitoring on DC in contrast to AC.

Chapter Three gives an overview of the monitoring system and the core blocks (modules) it contains.

Chapter Four is the largest chapter of this work and is dedicated to the design of the sensor, which is a High-Frequency Current Transformer (HFCT). Initially, it describes the role of the sensor in the monitoring system, its parameters, and then in the sub-sections studies the issues related to its design and operation.

Chapter Five is devoted to extraction of PD signals from noise.

Chapter Six explores the theoretical basis for PD localization based on the analysis of frequency content of received signals and measured transfer function of the cable.

Chapter Seven is dedicated to a variety of laboratory tests, which, firstly, complement the development work of the monitoring system described in the articles [Pub. 1 – Pub. 6], and secondly, are inherently interesting from the perspective of experimental technique.

Chapter Eight describes the installation of measurement equipment on a 110kV AC cable line and presents its transfer function measurement.

Chapter Nine summarizes the results and formulates the outlook.

2. Chapter:

HV cables quality assessment & monitoring

Before we get to the state-of-the-art PD monitoring solutions it is worth giving short descriptions of a few subjects that will be used further. In this way, this chapter will be divided into two parts. In the first one we will outline the general structure of the line and the particularities of its accessories that are important to us, while in the second we will move on to High Voltage Alternating Current (HVAC) and HVDC cable line topologies, measurement and monitoring approaches, sensors and their placement.

2.1 Introduction to cable lines and their components

It is not worth starting further discussion without an outline of the subject of our study, namely the cable lines in which the discharge occurs, with the topology and the most important elements. This paragraph is meant to give a short description of the HV cable lines. Even though most information within this sub-section is of common knowledge to most of the readers, we will still give a short description for those who are not closely familiar with the field. This brings the additional benefit of having a chance to depict the most important things regarding our topic and avoid saying c-too much.

The cable lines that we are considering within the scope of this work mostly belong to the HV and Extra High Voltage (EHV) classes, this corresponds to the range 110kV-525kV. In practice, the EHV abbreviation is frequently omitted within various publications, and instead, all cables above 110kV are referred to as “HV cables” for simplification. The cables can also be distinguished by belonging to transmission or distribution networks. For example, in Germany cables up to 110kV are usually a part of the distribution grid, and the cables starting from 220kV are part of the transmission grid, however, this border can significantly differ from country to country. At present, the 525 kV is the highest industrially used power cable rating. Below the 110 kV border lies Medium Voltage (MV) cables. The PD monitoring for MV cables is less vital compared to the HV case. The solutions for the continuous PD monitoring of the MV cables do not differ from the HV-case, however, the overall majority of the lend MV cables run unsupervised. The exception to this can be the lines outcoming from generators, where the sensors monitor not only the lines, but the generator as well, and therefore are installed more often. Another point to note is that we will not thoroughly consider the long subsea cable lines. The big subsea cable projects feature the longest existing cables, and PD monitoring is highly desirable, however, it is

practically impossible to implement any monitoring solution on it. Of interest, however, could be the relatively short MV cables stretching from/between the offshore wind parks.

Any HV cable line consists of the cable itself, joints that connect pieces of cable, and terminations, which end the cable line from both sides. Let's shortly outline each of these elements.

Fig. 2–1 HV cable structure [13]

Power cables have two main structures: three-core and single-core cables. The first is common for MV grids, while HV cables are generally single core type. Every cable has several main components: one (or three for MV case) central conductor (that will also be addressed as cable core), main insulation, metallic screen, and outer jacket. The typical structure of the extruded power cable can be found in Fig. 2–1. The central conductor (1) can be produced from copper or aluminium and can be sectionized to reduce the screen effect and consequent losses for the AC case (so-called Milliken conductor). The outer conductor (2), known as the cable screen or cable sheath [12] is dimensioned to carry the short-circuit current of the cable. The design of the cable outside of the main insulation, especially regarding the screen, can differ considerably (for example additional waterproof shells). The exterior of the cable is insulated with the outer jacket (3). Fiber cables of DTS incorporated into the screen are also visible in the Fig. 2–1. For our topic, it is important to mention that the basic insulation adjoins inner and outer conductors through thin (several millimetres) semiconductive layers, which provide electrical field control. The word semiconductive here means not the semiconductive materials used in electronics, but simply that their resistance places them between the dielectric and conductive materials. Due to this feature, these layers effectively dissipate Electromagnetic (EM) waves as they travel through the cable. Later we will return to the question of wave attenuation in the cable. In some publications the core-adjacent and screen-adjacent semiconductive layers can be named "core screen" and "insulation screen" respectively. We will not use this naming convention to avoid misunderstanding and will use the terms inner- and outer-semicons instead.

In terms of main insulation cables can be divided into oil-containing and extruded cables. In oil-filled cables, as the name implies, the basic insulator is a liquid mineral oil that impregnates layers of solid isolation, most commonly, paper. One of the main advantages of such cables is that oil insulation is regenerative and thus able to recover after local discharges. It is a very old technology that dates back to the 19th century, yet it has enabled the use of voltages up to 500 kV. Nowadays oil-filled cables are becoming obsolete. There are a few major disadvantages of this type, usually oil related: the complicated laying procedure, the necessity to maintain a defined oil pressure level, the maintenance of pumping stations, and the risk of oil leakage. Those result in high maintenance costs and high failure risks. Despite that, many such cables are still in operation, including DC ones: for example, the "Kontek" oil-filled DC cable which links Germany and the Danish islands. Notably, at least its land section will be soon replaced by a polymer cable.

For any extruded cables, the key factor in the manufacturing is the cleanroom environment within the process of extrusion. The polymer must have no air pockets, particles, or dirt of any kind. There are a few polymer materials that can be used as main insulation. At present Cross-linked Polyethylene (XLPE) is dominating the market for the HV and EHV ratings. A typical maximum rating of the XLPE cable lines is 525 kV, however, the 640 kV cable has already been produced in the past [15]. As the name implies, XLPE differs from polyethylene in having additional internal bonds, which makes it difficult to recycle. Therefore, alternative recyclable material is highly desired and is a matter of extensive research [17]. In addition to recyclability and good electrical and mechanical properties, the maximum operating temperature is an important optimization objective in the search for a substitute material, as this value is directly proportional to the maximum current load of the cable. In this regard, propylene-based materials are beneficial in comparison with ethylene-based by having a higher melting point [18]. Various propylene-based materials or ethylene-propylene-based copolymers could be future successors to the XLPE cables.

Regarding the topic of condition assessment, a big difference between extruded and oil-filled cables lies in the duration of the failure development. As was already mentioned, the regenerative properties of the oil can to some extent oppose the development of the defect, on the contrary, the evolvement of failures in extruded cables is much shorter: from several months to several days. As a result, periodic quality assessments of cable lines carried out at long time intervals (from a year and more), which was a common practice for oil-filled

cables, lose their sense for extruded cables. One-time measurements are justified only as a commissioning test after laying or after repair.

The production length of one piece of underground cable is limited by the maximal weight and dimensions that can be carried by land. Typically, this value does not exceed 1 km. The cable pieces are connected with the use of the joints (to a lesser extent the term splice is also used).

The design of a cable joint may significantly differ depending on the types of connected cables, dimensions, used materials, building procedure, complementary features, etc. A thorough study of existing designs can be found in [38].

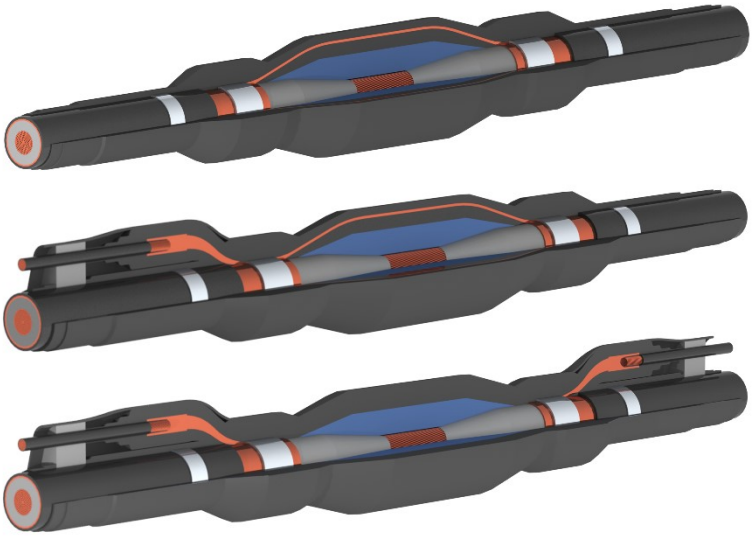

Fig. 2–2 Types of HV joints [Pub. 1]

From the perspective of PD monitoring, it is important to distinguish between the joints by the way how the screens of the incoming cables are handled, because this leads to different possibilities for sensor installation. Regarding this, three main types of joints may be highlighted. They are presented in Fig. 2–2 as to some extent generalized examples and can be described as follows:

- Straight joint (Fig. 2–2, top): Screens of the incoming cables are connected directly and covered with insulation. This type is commonly used when to earthing of the screen is needed and the task is just to prolong the existing cable section.
- Straight joint with a grounding lead (Fig. 2–2, middle): Directly connected screens are linked with the conductor that comes out of insulation and is used for earthing of the screens.

- Joint with screen separation (Fig. 2–2, bottom): Screens are not connected and have separate grounding leads. This type is used for the grounding or the cross-bonding of the screen.

Joints of underground cables are created on-site by the construction crews, therefore the quality of the joint mostly depends on the skill of the workers, their workmanship, accuracy, neatness, etc. The most detailed published description of the mounting of the joints can be found in the according Cigre Technical Brochure (TB) [19]. As the joints for extruded cables have polymer isolation, they are in the same way demanding the cleanness of the assembling process. As the conditions in the field are never as good as in the factory, the EHV cable joints are considered to be the "weakest" points of the line [21].

A termination is the connection interphase between a cable and some other electrical equipment. The possible designs can significantly differ as well as designs of joints. They depend on the type of incoming cable (oil-filled or extruded), type of connected equipment (busbar of the substation, Gas Insulated Switchgear (GIS), transformer, etc.), voltage rating, indoor or outdoor installation, etc. In common they have the necessity to provide the appropriate handling of electric field (commonly with the use of the stress cone), appropriate length of the creeping current path, mechanical support to the cable, thermal stability during operation, etc. Two high-current connections should be ensured: from the cable central conductor to the busbar, to transmit the main power current, and from the cable shield to the "earth", to bring the screen of the cable to the earth potential and forward the short circuit current to ground. Due to the separation of the screen and power conductor, termination is a well-suited place for the sensor installation. The particularities of sensor installation on the accessories will be further discussed in the next chapters.

Fig. 2–3 shows typical HV cable terminations: outdoor (72,5 to 550 kV), synthetic outdoor (72,5 to 123 kV), GIS (72,5 to 550 kV), and transformer compatible (72,5 to 245 kV).

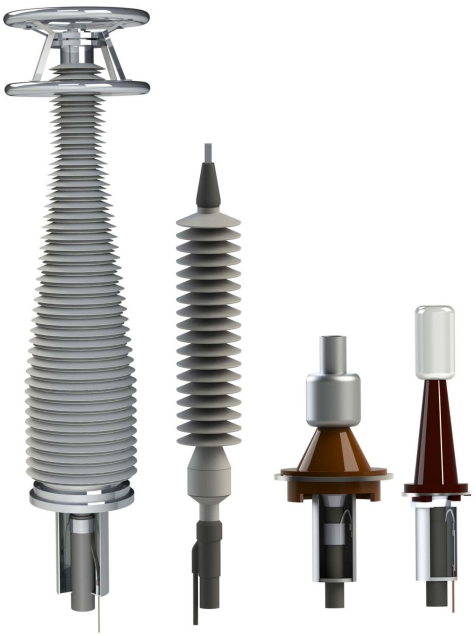

Fig. 2–3 HV Terminations according to [13]

So far, we have outlined the cable and its accessories. The important aspect that was not mentioned yet is the way the line is constructed on-site, or in other words, how it runs across the land. In fact, there are a few types of cable laying, some representatives are shown in Fig. 2–4. Accordingly, the accessibility to the cable and its accessories after commissioning differs. The Berlin Diagonal, an extra-HV line that runs through the urban area of Berlin, is laid in a large gallery and, therefore, offers multiple coupling options to PDs. At the same time, long lines outside cities are preferably subjected to direct burial, so both the line itself and most of the joints are inaccessible after laying. A good overview of the field experience in cable projects construction can be found in Cigre TB 338 [16].

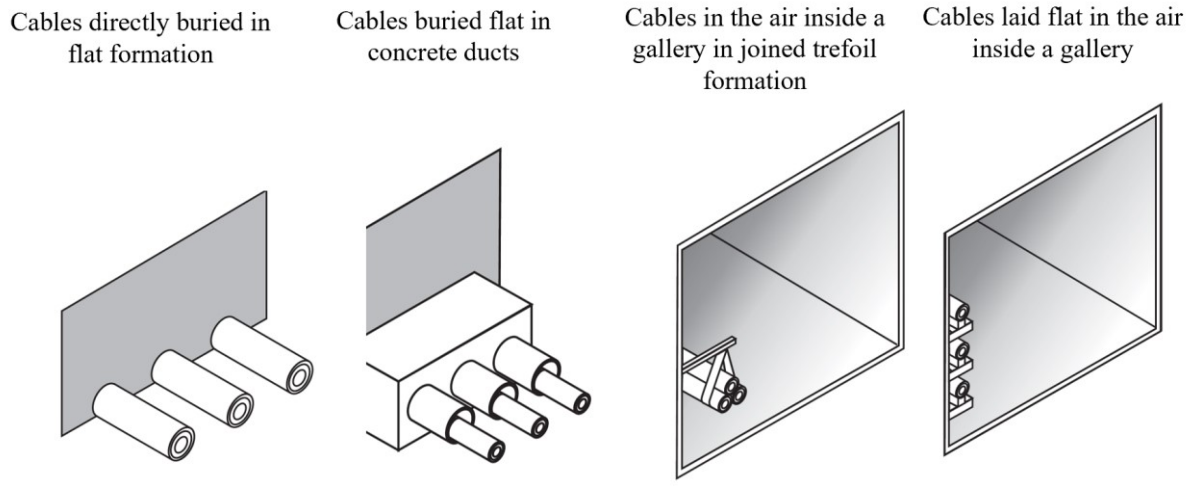

Fig. 2–4 Types of laying the cable line from [14]

2.2 Partial Discharge measurements on laid cables: standards and solutions.

After cable drums are shipped on-site, laid in the duck, and connected with joints, after the terminations are placed and the handling of the screen is performed, and the newly established line is ready to be put into operation it usually undergoes the commissioning tests (also known as on-site test, Site Acceptance Test (SAT), after laying test, etc.). A few types of tests can be performed during commissioning, e.g. testing of the outer jacket of the cable, the full list of tests may be found in International Electrotechnical Commission (IEC) 60060-3 [25]. For our topic, the most important is the withstand test (also referred to as HVAC test), which can be performed with a few types of ac voltages, known as: Near Power Frequency (NPF), Very Low Frequency (VLF) and Damped AC (DAC) – the whole

description of them can be found in the Cigre TB 841 [20]. The main intention of these tests is to proof the insulation quality of the established line. Since defects most often develop gradually, at present this test is often supplemented by the PD measurements measurement to check the accessories for incipient defects. This sub-section is intended to give an impression of the normative documents and state-of-the-art solutions of such PD measurements. It is important to add, that we are starting with the AC-case and the DC is left away. The standards commonly do not concern the dc, and we will use the AC as the starting point and also it is important for the description of the state-of-the-art solution. Because the measurements during commissioning make a base for continuous PD monitoring.

In high-voltage technology, a measurement of Partial Discharges is one of the most frequently used methods of quality assurance performed at different stages of the HV equipment lifecycle:

- Insulation parts of the future device can be tested during the first design stages for dimensioning and assessment of the overall design.
- Overall field-managing and insulation design of the HV facility can be assessed via the type-tests.
- Finished components of the future system, e.g., reactors, transformers, terminations, undergo routine PD tests at the factory before they are shipped.
- When the components are introduced to the system onsite, the component undergoes the acceptance test that can be also followed by continuous monitoring of the PD level of most valuable elements as it is done for the power transformers.

The differences between the test objects and test types lead to a great variety of possible measurement techniques. However, the conventional way of PD measurements is described only in the standard IEC60270 [23], which is ubiquitously recognized by the industry. For more than 50 years this standard unifies the PD measurements throughout the world and is known to every worker in the HV industry. The IEC standards for tests on HV equipment, including cables and accessories, all invariably refer to the IEC 60270. For instance, if we begin with the IEC 62067 [24] – which pertains to the testing of extruded HV cables — we would ultimately arrive at the IEC 60270 by following this sequence of references:

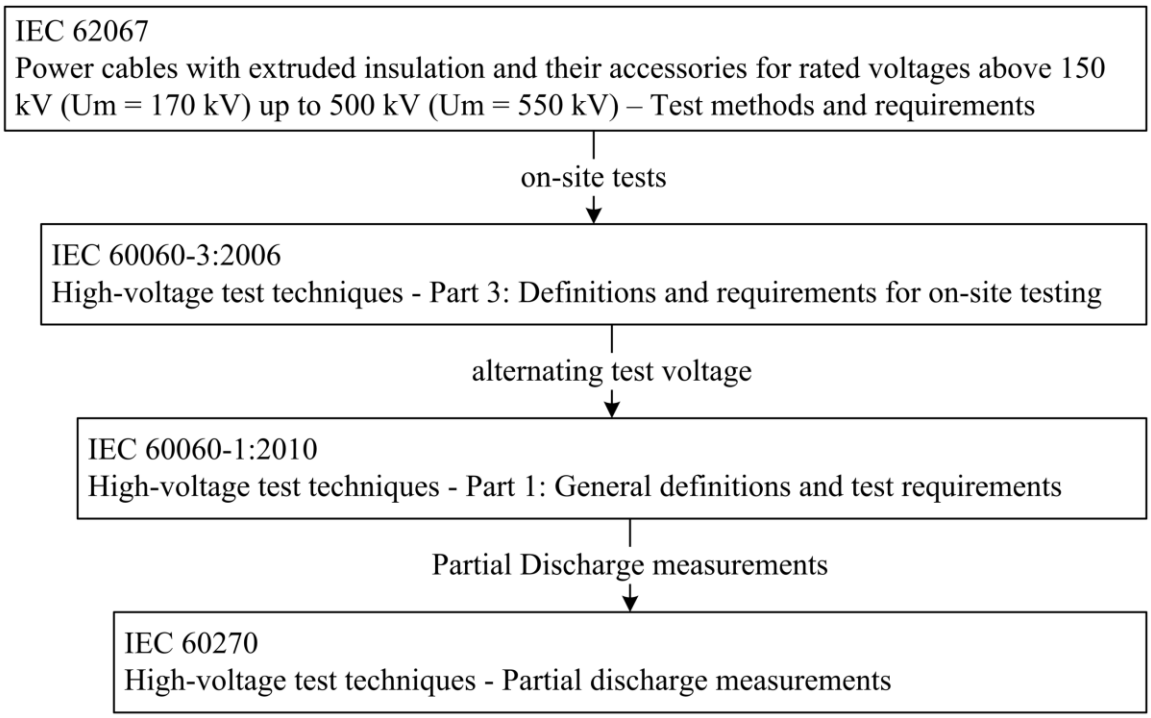

Fig. 2–5 Cross-references between standards [24], [25], [26], [23].

Being first developed in 1968 and despite two major revisions in 1981 and 2000 the IEC 60270 still has leftovers from limitations of the measuring hardware available at the time. Moreover, for certain types of equipment, the methodology of the standard cannot be applied effectively. Significant limitations are arising because the standard rather treats the tested equipment as a lumped-element model – below is the quote from the standard:

> "A detailed treatment of partial discharge measurements on objects with distributed elements, in which traveling wave and complex capacitive and inductive coupling phenomena take place, is beyond the scope of this standard."

Even though the inner structure of many HV components (e.g. winding products - transformers, reactors, etc.) acts as a system with "distributed elements" for internal PD activity, in most applications it is acceptable to not take this into account - so that the standard will be applicable. From a formal point of view, the inconsistency is avoided because the standard uses not the true charge value but the apparent charge value instead. The apparent charge is a very important methodological concept – apparent charge is a charge that must be injected into the insulation of the controlled equipment to restore the internal EM equilibrium in the insulation disturbed by the occurrence of a discharge at the point of origin. The methods of the standard allow measuring from "outside" the response of the system to a PD occurring "inside" the insulation. Therefore, the term "apparent

charge" is used - as the true value of charge remains unknown. The recorded pulse depends on the parameters of the internal discharge but, to a great extent, is shaped by the propagation path inside the tested object, which can be rather sophisticated. Nevertheless, since direct measurements are usually not possible and a certain correlation between apparent and real charges exists, the measurement of apparent charge continues to serve the purpose of assessing the quality of HV equipment, conducting acceptance tests, etc.

As was mentioned for some HV components assessment of apparent charge is sufficient, however, if, for example, we would execute the measurement according to the standard on a long cable, the PD originating in the middle of the cable would either reach the coupling capacitor highly attenuated or may not reach it at all.

The standard IEC 60885-3 (Electrical test methods for electric cables – Part 3: Test methods for partial discharge measurements on lengths of extruded power cables) [27] still mostly refers to the IEC 60270 but makes important adjustments and can be used, for example, for routine tests performed in the laboratory. It introduces additional calibration procedures to cope with attenuation in power cables and methods to overcome the problem of multiple reflections of PD pulses traveling back and forth along the cable. However, this standard does not concern measurements made on installed cable systems and implies the use of a coupling capacitor and thus leaves other sensors (e.g., inductive sensors) out.

In comparison to the IEC standards, the Institute of Electrical and Electronics Engineers (IEEE) 400.3 standard (Guide for Partial Discharge Testing of Shielded Power Cable Systems in a Field Environment) [28] directly addresses the PD measurements of laid cables. It also mentions IEC 60270 giving comments on its content. In contrast to the IEC, it allows the use of inductive sensors apart from "conventional" capacitive ones. It also proposes the use of the distributed measurement system, namely the installation of the sensors on the accessories of the cable line, providing the figures where the placement of the sensor is defined. Within this standard, the calibration and localization topics are also covered. The localization of a PD pulse – a process of determination of the location of the spatial origin of the PD pulse – according to the standard can be done by the common time-domain approach (TDR, or Time of arrival), but also via the frequency-domain methods. The question of calibration discussed within the standard is rather sophisticated – one could say that the standard extends and adapts the calibration procedure known from IEC to the case of distributed objects with non-conventional sensors.

By contrast to the outlined standards, much more detailed recommendations and analyses can be found in the Cigre Brochures. At least two of them should be mentioned: the TB 841 (After Laying Tests on AC and DC Cable Systems with New Technologies), which summarizes measurement principles, and indicates the TB 728 (On-Site Partial Discharge Assessment of HV and EHV Cable Systems) [28] a more thorough version in regard of PD. The latter document contains an extensive analysis of the IEC standards and the reasons for their inapplicability to field tests. This document is not intended to be used solely as a normative document, but it describes in a more informal way the principles of measurement from the theory side and provides statistics on how measurements are commonly performed. Thus, this document can be used as a reference for the further outline of the state-of-the-art on-site PD testing.

At present, two methods of measuring partial discharges are used commonly: the Terminal PD test and the Distributed PD test.

The Terminal test is close to the IEC standard methodology and therefore to the type-tests carried out in the laboratory. It can be used for testing short cable lines, normally with no, or at most two, joints. In this method, the PD pulses are acquired with the use of the conventional coupling capacitors positioned at the terminations.

The Distributed test in which the PD measurements are performed at the locations of the cable accessories, often with the use of unconventional ways of coupling - most often inductive sensors. This multiterminal measurement is aimed to cope with the attention of the PD signals in the cable: Occurring pulses do not have to travel all the way to the termination to be registered, instead, they are measured immediately near the point of origin. Therefore, this method is used on long cable lines. In practice, the measurement can be realized either with the permanent installation of sensors on each location or with the mobile crews moving from assessor to accessory, the latter is known as “joint hopping”. The permanent installation of sensors arises serious challenges for the measuring system: a big number of channels, data transmission, required hardware, power supply, and security measures – therefore when the continuous monitoring during the operation is not planned the joint hopping can be the preferential solution.

Another important question that is addressed by the TB 728 [28] is a common intention, or rather a necessity to convert the voltage measured by the sensor to the charge value. In conventional measurements, this task is performed with the calibration procedure, and the

latter cannot be carried out during the on-site measurements. As state-of-the-art recording hardware can properly digitize the shape of the PD signals, and if the measured voltage can be converted to the current of the PD pulse (e.g., via the transfer impedance of the sensor), then the charge can be achieved via integration. However, the received value is physically different from the apparent charge known from IEC 60270. This note is important because the apparent charge known from IEC is the unifying value, which everyone would like to get in the end. This difference should not in general be taken out of consideration. It is worth citing TB 728 [28] standard to underline the difference between these two values:

> "Specifically, the apparent charge as evaluated on integrating the appropriate area of a measure partial discharge current relates to the time-dynamic response of the measuring circuit (including the cable or accessory under test) during the partial discharge event while the apparent charge as evaluated via a conventional PD measurement relates to the electro-static response of the measuring circuit (including the cable under test) following completion of the PD event".

The PD monitoring during line operation is not concerned by the IEC/IEEE standards, as it is not part of the test chain that accompanies the supply of the cable from the cable manufacturer to the grid operator, and is, on the contrary, is, strictly speaking, initiated by the will of the cable operator to control the condition of the cable.

It's important to define the meaning of the term "PD monitoring" which will be used within this paper. We will use it to address the continuous PD measurements performed over a long period of time during the operation of the cable line with the permanently installed monitoring system. Cigre brochures sometimes use the terms "PD monitoring" and "PD measurements" interchangeably meaning the short-term measurements executed during, for example, commissioning. Indeed, the commissioning can be performed with the system for continuous PD monitoring, however, to avoid misunderstanding, the author will use the term "PD monitoring" when the permanent measurement is implied.

In this paragraph, we have addressed the common PD measurements performed on the laid cables, and in the next sections will go in the direction of PD monitoring, which is standardized to a far less extent. Before we do so, we have to pause and give and describe sensors used for the detection of PDs on cable lines. We have already shortly mentioned the inductive sensors and now is the right time to disclose the topic. After this task is finished,

we will return to the cable lines and see how the sensors are placed on the cable lines of different topologies.

To avoid losing the thread of the narrative, we will divide the description into two parts. The next section will provide only a general description of the sensors, which is necessary for a better visualization of the overall picture, while a more detailed analysis will be allocated to a separate chapter.

2.3 Sensors for PD coupling

There is a great variety of sensors for measuring partial discharges, designed to work on different equipment, exploiting different physical laws and therefore working in different frequency bands. This exploited frequency range is very broad. It starts with acoustic sensors (app. 20Hz to app. 500 kHz), continues with inductive sensors – HFCTs, Rogowski coils, different capacitive methods of coupling (Coupling Capacitors, TEV-sensors [40], foil electrodes), goes into the Radio Frequency (RF) range (Ultra High Frequency (UHF) sensors [39][74], antennas of various designs [75], directional couplers), and ends with the optical methods (Ultraviolet (UV) cameras). Often, several types of sensors can be implemented simultaneously. For example, in testing transformers for internal PD both acoustic and ultrahigh-frequency sensors can be used; in search for coronating spots on HV electrodes – UV cameras and directional ultrasonic sensors. From a practical perspective, however, for measuring PD on cable lines inductive sensors with a magnetic core, namely high-frequency current transformers, are most beneficial, and therefore most common.

A high-frequency transformer is, in essence, a rather simplistic electrotechnical device. Its arrangement can be described in just a single sentence: A magnetic core braided with several turns of wire and housed in a suitable enclosure. An example is shown on Fig. 2–6, with the housing being omitted. HFCT couples to any current passing through its aperture, and the working principle is rather straightforward: propagating current creates the magnetic flux within the core and a consequent voltage drop on the winding. To be able to install it on an already existing conductor without disconnecting the latter, the “split-core” design is used. The magnetic core will thus be a closed magnetic conductor in one case or have an unavoidable non-magnetic gap once the split design is used.

Now we have described the simplest case, the situation becomes a little more demanding when it is necessary to ensure operation in the presence of a superimposed power-frequency current, for example, the main cable current. In this case, the air gap must be introduced

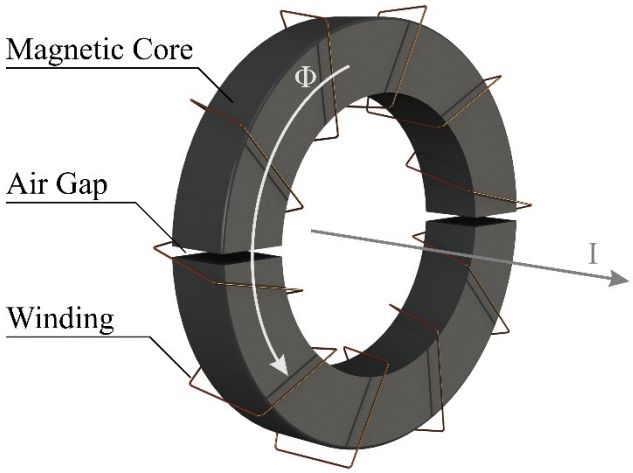

Fig. 2–6 Working principle of a High-Frequency Current Transformer

necessarily to prevent saturation. The dimensioning of the gap is the bargain between the performance and saturation properties. The choice of the core material and the selection of its geometry, the presence or absence of an air gap, number and distribution of turns allow adjustment of the bandwidth of the sensor within a wide range. For example, by decreasing the magnetic conductivity of the core it is possible to shift the bandwidth towards high frequencies until the HFCT turns into a Rogowski coil.

In practice, though the bandwidths of the sensors on the market differ, they do have some common features. For example, the low cut-off frequency is usually 100kHz, which coincides with the range given in IEC 60270 for wideband instruments: 30 kHz ≤ f1 ≤ 100 kHz. This selection of the lower bandwidth can be explained by practical reasons, rather than the intention to fit the standard, as we are dealing with unconventional measurement anyway. The advantage of the band-pass characteristic of HFCT is the possibility to attenuate the unwanted frequency components, such as various external distortions that are not PD related. Noise and harmonics from the HVDC converter stations **[30]** or introduced by non-linear properties of transformer cores are significant in the order of tens of kilohertz, therefore the start of the band-pass in the range 50kHz-100kHz is rather reasonable.

The upper cut-off frequency, on the other hand, has no relation to the standard. It is determined by the resonance characteristics of the device: core material, dimensions, winding design, etc. Unlike the lower boundary, it usually does not result from requirements or optimization but is rather an indirect result of the design itself. Typically, this value lies

in the range from 10 to 20 MHz. This limit goes even higher than what is needed for PD monitoring in cable, because, as it will be further shown, signals above a few MHz get drastically attenuated.

It should be also noted, that, apart from the aforementioned inductive sensors, exists a large number of other possible sensor designs, which are based on different physical ways of coupling, and can be used for PD measurements on the cable accessories. Those are internal capacitive and internal inductive sensors, sheath interruption sensors, directional couplers, sensors that take advantage of the axial magnetic field caused by the helical structure of the shield, etc. Most of the existing types are addressed in the Report № 182: "Partial Discharge Detection in Installed HV Extruded Cable Systems" of Cigre Working Group 21.16 [31]. This report analyses each type and presents case studies of their use in the on-site tests. Apart from this rather thoughtful document, brief literature research can bring out plenty of articles that propose modified or customized sensor designs, however, there is no doubt, that inductive sensors, namely HFCTs, became the predominant solution. We will leave out of scope the in-depth comparison between HFCTs and the sensors of other types and will thus limit the comment to only a few following remarks.

In contrast to the optical fiber of DTS systems, the introduction of any conductive or magnetic element in the cable or accessory design increases the risk of its failure. This marks internal sensors outlined in the standard as highly undesirable solutions, regardless of the achieved sensitivity. An HFCT on the contrary provides the most convenient way of coupling, as it does not require preinstallation, and the level of coupling is not dependent on the distance to the conductor, which is not so for external capacitive sensors, antennas, directional couplers, etc. Another consideration is the general comparison between the nature of coupling: electric or magnetic field. The physics of capacitive coupling makes it more beneficial the higher the frequency of the signal is. Contrarily, due to the low-pass effect of the cable, the high-frequency content of the PD pulses attenuates rapidly while low-frequency components propagate over large distances. Therefore, for a PD sensor, it is rather important to efficiently couple out the low-frequency content, and therefore the capacitive coupling might focus on the wrong part of the frequency spectrum. By contrast, an HFCT has a few tuning parameters, e.g. permeability of the magnetic core and amount of secondary turns, that can be selected properly to fit its band-pass characteristic to the desired part of the frequency spectrum. This consideration is valid for both Terminal PD tests and Distributed PD tests.

2.4 HVAC & HVDC Cable Line Topologies and State-of-the-Art monitoring solutions

Now, when the main building blocks of cable lines are explained, we should outline the typical topologies of AC and DC cable lines with extra attention to the points of screen separation. This topic should be considered because in this way we will determine the possible propagation paths of PDs, and consequently define the best points for coupling. Here we will have to distinguish between the AC and DC cases, also in terms of available references. For the AC case, our sources can be IEEE Guide for Bonding Shields [32] and Cigre TB [33] on the same topic. For the HVDC case, Cigre has not published the according brochure yet, as the creation of the working group concerning this question was just proposed in November 2021 [34]. Certain information, such as the distance between the eating points of the cable screen is sometimes mentioned in the articles studying steady-state sheath voltages and overvoltages of the HVDC cables [35], [36]. However, such studies are more "calculational" related than addressing practical cases, and therefore real topologies. On the other hand, the typical "basic" sources that present real cases and statistics, such as, for example, the Cigre Green Books on Overhead Lines [37] unfortunately do not exist for the HVDC cable lines at present. To some extent, the following structure of the DC line is based on the communication with the TSOs, and therefore cannot be directly referenced.

We will start the survey with the AC case. The Cigre TB lists and explains the following well-known types of screen grounding [33]:

- Solid or multi-point bonding,
- Single-point & sectionized single-point bonding,
- Mid-point bonding,
- Cross-bonding (& cross-bonding in tunnel installation),

and a few more sophisticated types:

- Impedance bonding,
- Siphon lines (Circuits connecting overhead lines and underground cables).

However, if we consider the Cigre service experience survey [21], we can denote that cross-bonding, more specifically the sectionized cross-bonding, is absolutely dominating in the transmission and HV end-of-distribution rates, as shown on Fig. 2–7.

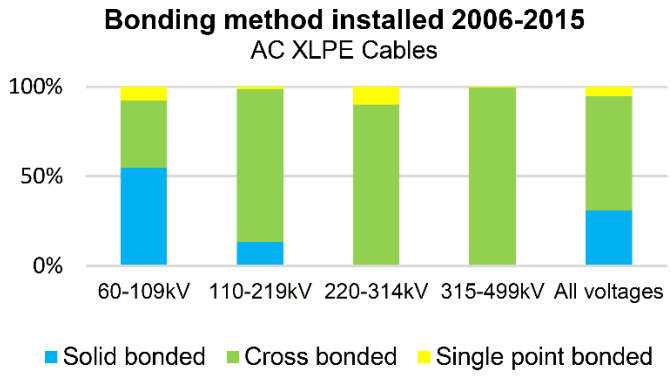

Fig. 2–7 Statistics on the use of screen bonding methods

Furthermore, single-point and solid bonding are used on short lines, and therefore such lines frequently contain no joints at all. In a case when the line is long enough to require some joints to be installed, but for some reason cross-bonding is not used, the intermediate grounding is usually performed.

The Fig. 2–8 shows some schemes of grounding the cable screen and the placements of the typical screen-coupled HFCTs. Notably, not always a proper screen-coupling is possible. For example, the intermediate joints of the solid bonding scheme (top of Fig. 2–8) can be performed as straight joints with a grounding lead (middle Fig. 2–2), therefore the grounding lead is the only possible place to clamp on the sensor. In this case, however, the sensor is not measuring the main discharge current flowing "inside" the cable (Fig. 2–9, red lines), but only the negligible high-frequency portion flowing to earth (Fig. 2–9, blue lines) and the damped Electromagnetic Compatibility (EMC), if the discharge happens in the close vicinity. At the same time, such a connection is also prone to various non-PD-related external distortions. All terminations at solid bonding can be equipped with sensors, which, however, should be capable to operate under the high power-frequency current induced on a cable shield. In the single-point bonding schemes, the installation of inductive sensors on terminations' screens grounded via voltage limiter is rather unreasonable. The same applies to the joints used in sectionized single-point bonding. For such joints one shield end is connected to ground directly and the other via Surge Voltage Limiter (SVL), therefore only the directly grounded side can be used for the sensor installation. Consequently, when a PD occurs on the SVL side of the joint, the sensor will pick up only the high-frequency component of the signal.

- Solid bonding:

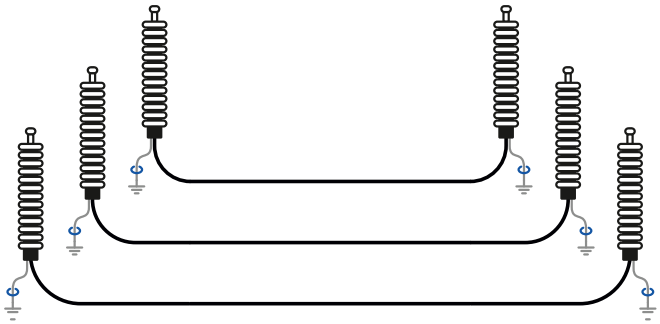

- Solid bonding with intermediate joints:

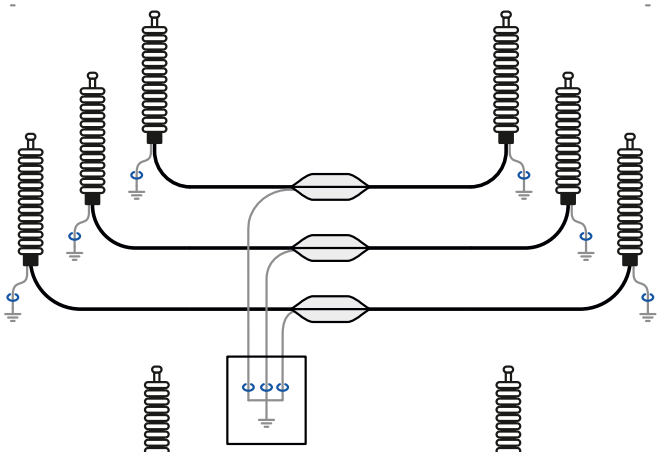

- Single-point bonding:

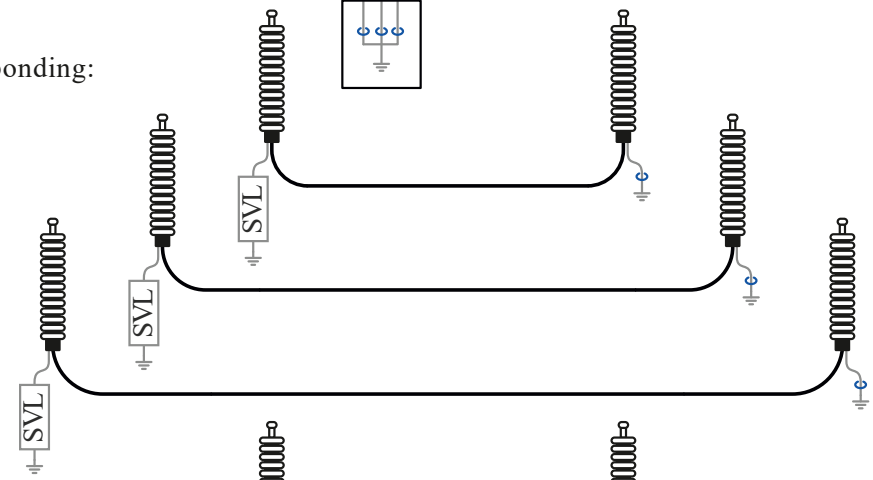

- Sectionized single-point bonding:

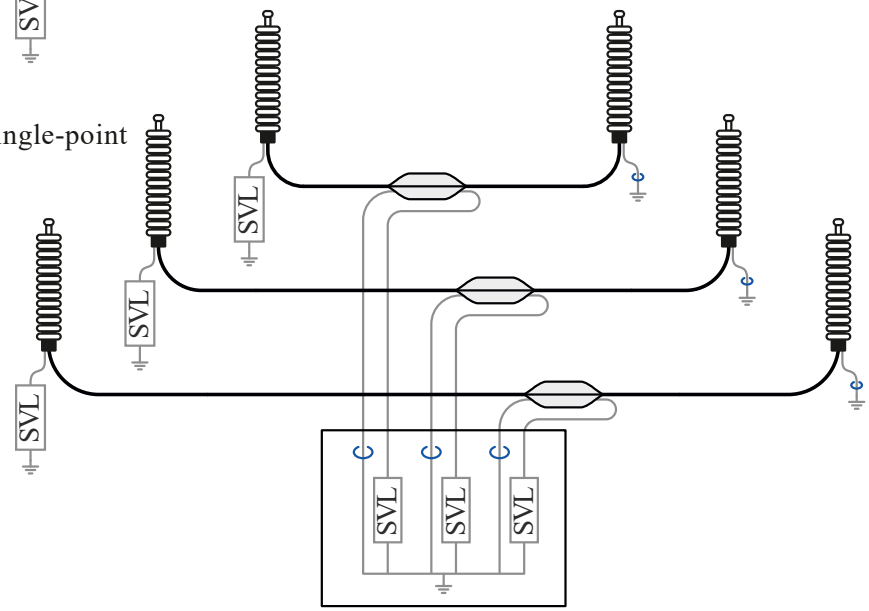

Fig. 2–8 Bonding cases and screen-coupled sensor placement.

Although we have outlined the monitoring for solid- and single-point-bonding schemes for the sake of completeness, it should be noted that monitoring such lines is rather rare. The less frequent use of such schemes, their relatively low voltage rating and therefore low liability, the small number of joins and therefore lower probability of failure, make the monitoring of them be used in more exceptional cases.

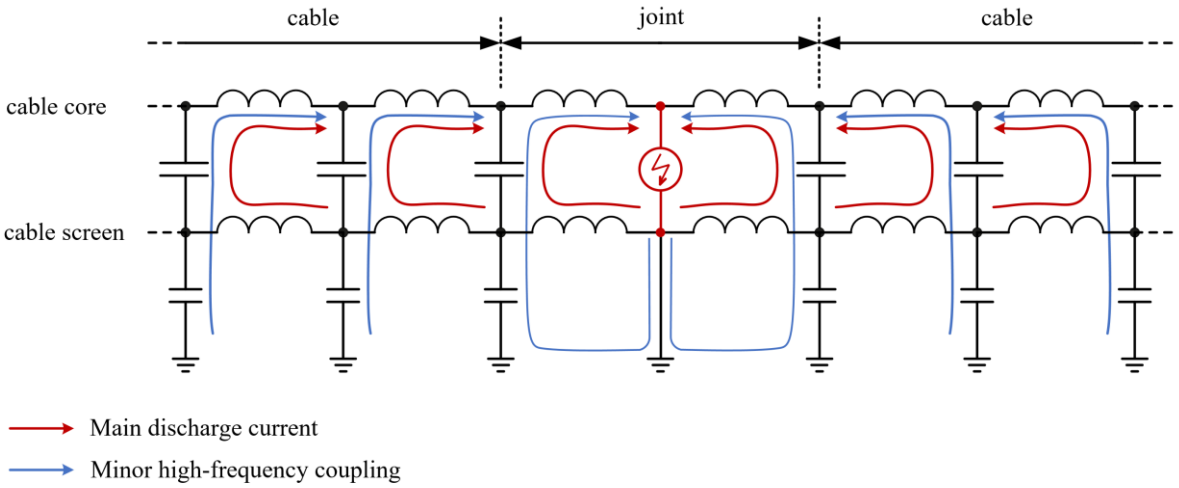

Fig. 2–9 PD currents at a straight joint with a grounding lead

In the absolute majority of cases, therefore, monitoring is carried out on lines with cross-bonding. Such systems are shown on Fig. 2–10. This solution can be used solely as a distributed PD measurement system for commissioning; however, it is more common for permanent installation and continuous PD monitoring. This example shows two instances of the HVAC line:

- Two major sections of a sectionalized cross-bonded system, where bonding is performed directly (top of Fig. 2–10)
- Two major sections of a sectionalized cross-bonded system with cable transposition, where the screens are connected in the cross-bonding boxes (bottom of Fig. 2–10).

Each cross-bonding group of three joints is monitored by a group of three inductive sensors (HFCTs) installed nearby: either directly on bonding links, or in the cross-bonding boxes. Terminations have the sensors installed at the grounding links. The bottom of the Fig. 2–10 additionally shows the acquisition and data-transferring equipment connected to the sensors. Each group of sensors is connected to the acquisition unit, which filters, amplifies, and digitizes the incoming analogue signal. The acquisition units are connected via the fiber cable or the wireless connection to the central control unit, which gathers the data from the

acquisition units and, for example, uploads it to the cloud framework or to the local Personal Computer (PC) of the operator.

The necessity to transpose the screens leads to the joints with screen interruptions making it possible to install inductive sensors on almost every each of them. This system has certain pros and cons. The clear advantages are:

- A PD detected by a sensor can be assigned directly to the supervised joint,
- A rather high sensitivity is achieved as the sensors are placed on all accessories, and therefore, close to the possible locations of discharge.
- Acquisition and processing hardware is not particularly demanding, as the signal-processing chain is rather straightforward and simple. Filtering with Field-Programmable Gate Array (FPGA), integration of the current to retrieve the charge and plotting of the Phase Resolved Partial Discharge (PRPD) pattern. Apart from the sensors, the hardware and the general approach is not too far from the IEC 60270.

and certain drawbacks:

- The big amount of needed hardware and axillary elements: sensors, acquisition units and communication connections between them, and power supply at every location. When the cable is laid in the concrete tunnel the recording hardware can be easily mounted at the location of every joint. However, a more frequent case is when the cable is buried directly and the only element that is accessible and above the ground level is the cross-bonding box. In this case, firstly, it is not clear where to get power from, and secondly, it would be necessary to install some kind of separate cubicle or vault for PD acquisition hardware.
- Second drawback is the scaling of this system: one additional joint adds another channel of measurement, therefore the 3-phase 10 km system with two chains would require 15 joints per phase, 15 points of installation with power supply and everything included, 45 sensors per chain, 90 measuring channels in total.

Let us now examine the topology of DC lines and as was done earlier for AC lines, consider the possible locations of the sensors. It is worth noting, of course, that if the description of the AC case has a basis from the systems available on the market, described in brochures and press releases, then in the case of DC monitoring the published material is very scarce.

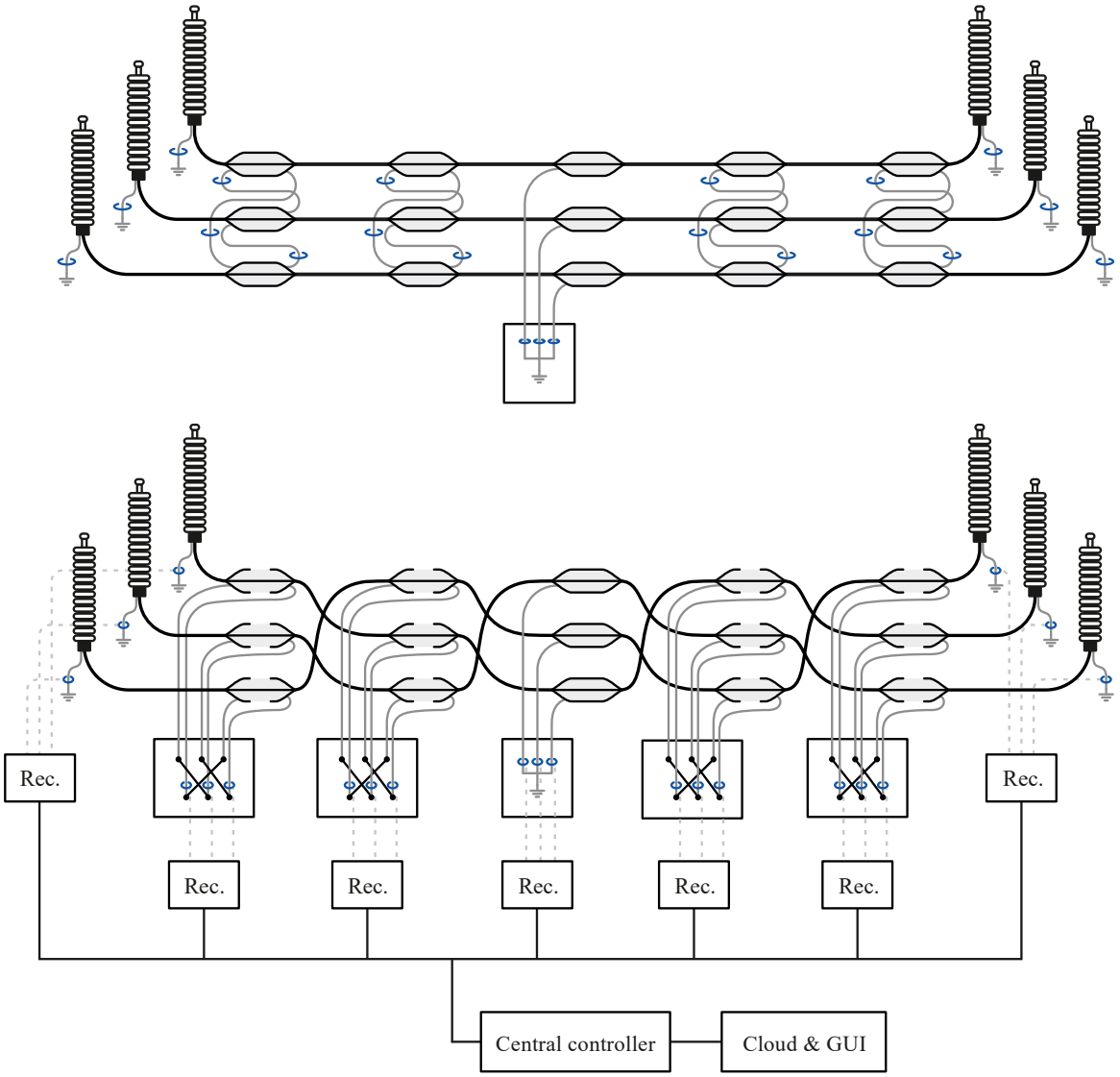

Fig. 2–10 Cases of cross-bonding and sensor placement

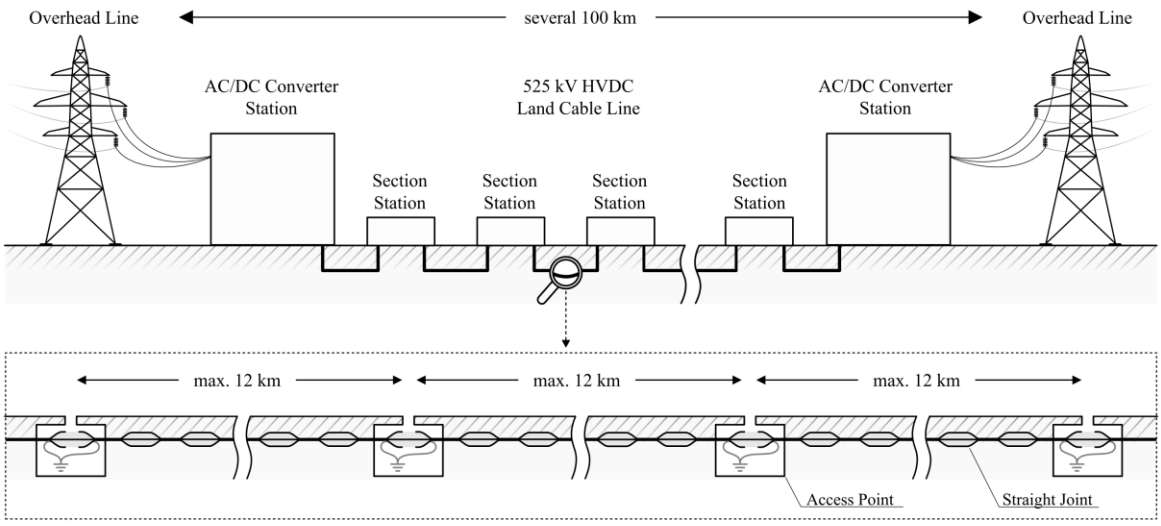

Fig. 2–11 Topology of the HVDC line, modification of figure from [Pub. 1]

Let's start with the example presented on Fig. 2–11. At the near and far ends of the HVDC transmission system, converter stations connect the line to the AC grid. After up to 160km, a section station is built to separate cable sections produced by different manufacturers and provide the possibility to connect a HV test system. During the SAT or commissioning test, every single section is tested according to the standards or as agreed between the manufacturer and operator. The longer the tested section is, the higher the power that a test system has to deliver. Especially for tests carried out at near power frequency the design of the required resonant test systems is challenging **[**7**]**.

The cable line between section stations (Fig. 2–11, lower left part) is divided into smaller segments by a number of access points, where joints with shield separation are installed and the screen grounding is performed. As the current is alternating, there is no voltage induced on the cable shield, and therefore how frequently the grounding is performed is determined by other factors.

The first of these is, of course, the intention to minimize the number of grounding points for economic reasons – after all, each grounding point requires certain auxiliary infrastructure and service. On the other hand, grounding is needed due to the overvoltage protection and the need to test the outer sheath (jacket) of the cable. The letter requirement is explicitly mentioned in the Cigre TB 852 which concerns the testing of DC extruded cables up to and including 800 kV. The proposed testing procedure, however, is the same one that is common for AC and is described in IEC60229 **[**23**]**. In this test, the screen of the cable should be disconnected from the ground and subjected to a few kV of DC voltage while the conductive outer surface of the cable jacket serves as a ground electrode. Due to this configuration, the possibility to disconnect the screens from the neighbouring sections also comes in handy. At least within the German cable corridors, grounding is planned to be performed at distances of about 6 – 10 km. The underground section between these spots is not supposed to provide grounding and thereby is constructed with straight joints which are not accessible after laying (Fig. 2–11, lower part). Due to the typical inland weight transportation limits, the maximum length of a cable on a drum usually does not exceed 1 km. Therefore, the distance between two joints can be assumed equal to approx. 1km. as well. As a result, there may be a significant number (approx. up to 12) of inaccessible straight joints between two access points.

Unlike AC where split screen joins prevail and therefore each of them can be equipped with an inductive sensor, at the HVDC cable line about 90% of all joins would be straight and

therefore not suitable for inductive coupling to PD signals. As follows, and again opposing to the AC case, at HVDC long sections of cable with numerous joins are not available for the installation of measuring equipment, nevertheless, they need to be subjected to a sensitive PD measurement during commissioning [20] and, rather preferably, during operation as well.

Thereby in the design of the measuring system, we are forced to move from local sensitivity (one sensor for one joint) to global sensitivity, there the whole inaccessible area of strait joints and cable pieces should be sensitively monitored by the sensors installed at its ends. In this respect, it is not only a question of sensitivity, in addition to this it is also necessary to solve the problem of locating the place where the partial discharge takes place, and to calculate its initial magnitude.

Additional difficulties come from the PD measurements under the DC stress, which, from a state-of-the-art perspective is the topic of ongoing research. During the commissioning tests the HVDC line may be tested with the AC voltage [20], which simplifies the PD measurements to a certain extent. During the operation, however, one would have to enter the field of PD under DC stress. The main difficulties here come from the lack of phase information and low repetition rates. During the AC measurements, the acquired apparent charge values are commonly plotted on the phase-resolved PD diagram (PRPD), and form "patterns" or "clusters". To estimate the type of discharge, and distinguish it from the non-PD disturbances, the shape of the cluster/s is usually analyzed, along with its constancy in time, intensity, position with respect to phase angle, etc. Individual points are thus almost never taken into account, at least because their non-repetitive behavior most often indicates that they are not originating from the device under test. In contrast, real PDs are usually relatively constant over time at AC voltages and form clusters quickly. For DC the situation is completely opposite. Firstly, there is no phase information, and therefore no PRPD diagram, and no clusters to judge. Secondly, the repetition rate is by orders lower than it would be for the same defect at AC. Thus, instead of clusters, at DC only rare points are present on the Time-Resolved PD pattern, as shown in Fig. 2–12. Therefore, we can no longer exclude these points from consideration, as we did in the case of AC – they are all that is left at our disposal. Thus, it is very important to capture each signal and interpret it accordingly. On the other hand, a low repetition rate also means a low speed of PD development, which means an increased pre-failure observation time and a longer time window for predictive maintenance.

Another problem is the presence of numerous sources of PD, which result in mixed points on PRPD and Time-Resolved Partial Discharge (TRPD) diagrams. While on AC the appearance of clusters can to a certain extent signalize the presence of different PD sources, at DC only a mixed sequence of points can be observed. The PD measurement is much more valuable if the signals from different sources can be separated, as shown in Fig. 2–13 with colour. Then not only different sources can be distinguished, but also non-PD disturbances can be excluded from observation.

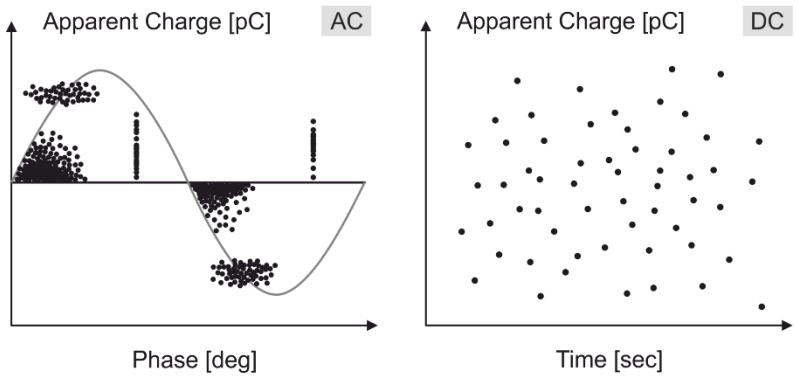

Fig. 2–12 PRPD and TRPD patterns with signals from multiple sources

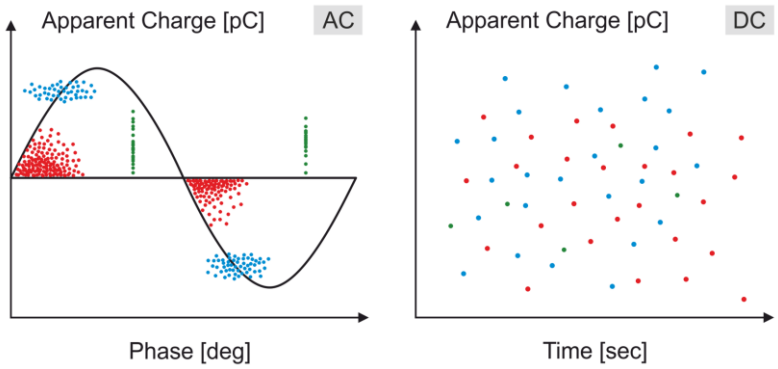

Fig. 2–13 Separation of the sources by clustering

The appropriate methodologies for differentiating between the sources were proposed over the last decades by numerous groups of authors [47] – [54]. The generic idea is usually the same, as shown in Fig. 2–14: First, each PD is described by the N-element vector (usually called the “feature vector”). Then the set of, in such way, encoded signals is used for clustering in the N-dimensional space by standard machine learning algorithms such as K-means, Gaussian Mixture Model, etc. The way of obtaining the feature vector differs, and therefore the vectors are explaining signals in a different way which results in differing effectiveness of clustering. Usually, the publications proposing ways of feature extraction

show the working example on some laboratory setup, however the on-site measurements are usually out of scope.

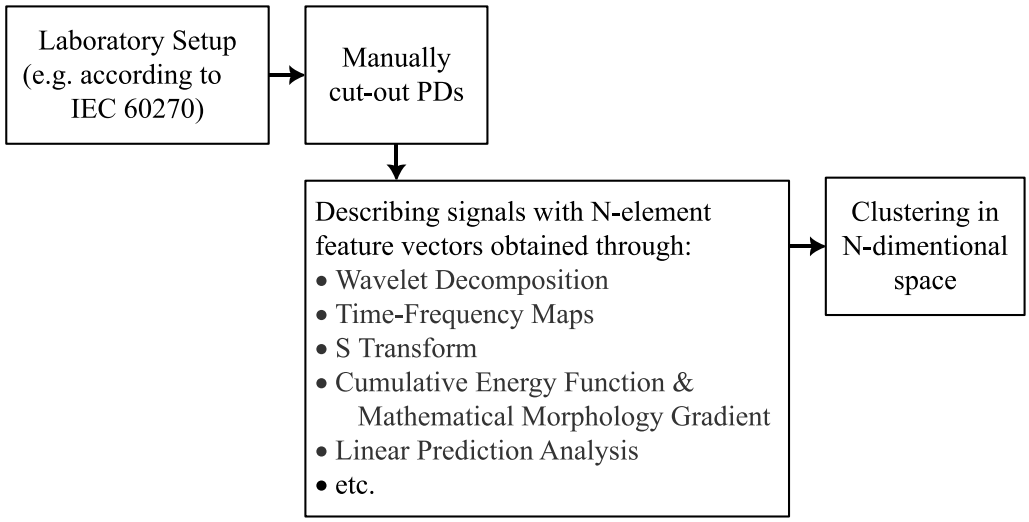

Fig. 2–14 Common pipeline in studying PD source separation.

At this point, we can preliminarily conclude the description of the general approach to the tasks of measuring PD and monitoring in high-voltage underground cables and move on to the next chapter, which directly describes the monitoring system and its components.

3. Chapter:

Blocks of Monitoring System

3.1 Goals and Functions

The aim of this chapter is to describe the proposed monitoring system in both general terms and specifics. We will start with a general outline of it using an example case of HVDC line, shown on Fig. 3–1. This does not mean that HVAC cables are excluded, as the proposed approach is also applicable to them, but the main focus is still on HVDC lines, so they will be the starting point as well.

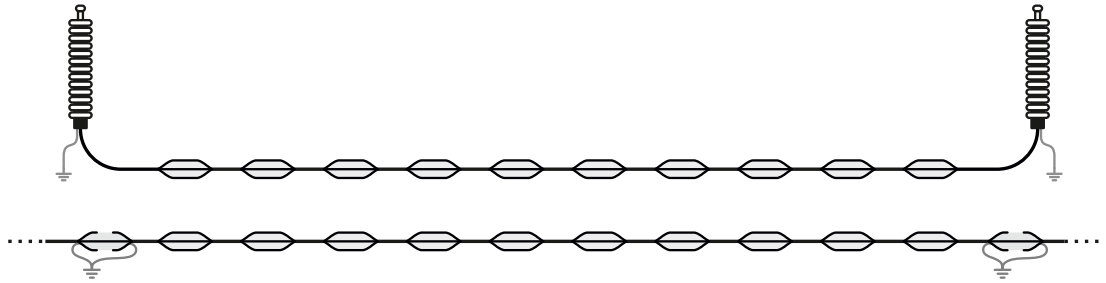

Fig. 3–1 Example of the short HVDC connection (top) and part of the long HVDC line (bottom)

On Fig. 3–1we see an instance of the HVDC cable lines. At the top of the picture is a short HVDC connection constructed with straight joints only. The bottom of the same picture shows the part of the long HVDC line between two grounding points that are performed with the joints having screen separation. It is clear that the topologies of the monitored segments are alike, and therefore the design of the monitoring system is more or less independent of the line length. Let's assume that a few faults are starting to develop along the cable line. These defects emit pulses propagating in both directions along the cable line. When the pulses propagate along the cable, they undergo severe attenuation. As already explained at the end of the previous chapter, installation of an inductive sensor is only possible at the locations where the cable shield is grounded, i.e., at the left and right ends of the displayed segments. The continuous signal stream coupled by the sensors at the ends of the line, is transmitted to the downstream acquisition hardware which filters and digitizes the signals. Digitization is the start of the signal processing pipeline, which, in the end, should lead to the monitoring results shown to the end user. Let's define what these results should be:

- Coordinates along the line of the origins of PDs:
  The system should be able to define the amount of PD sources and provide the coordinate along the line for each of them. At the same time, non-PD disturbances originating outside of the monitored segment should be marked and rejected.

- Charges of the PD pulses at the spots of their origin:
  As PD propagates along the cable line it undergoes severe attenuation, therefore the measured charges are considerably decreased in comparison with their values at the point of origin. Due to distance-to-fault dependency, it is hard to judge the severity of the defect: a small measured charge originating from the middle of the monitored segment can be an evidence of the severe damage.

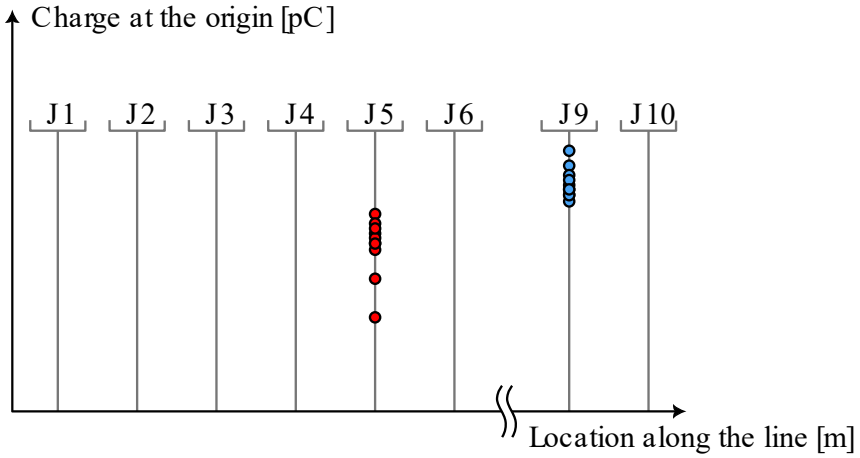

Fig. 3–2 Distance-to-defect resolved data with the measured PC charge being compensated for the attenuation in the cable and in this way recalculated to the point of origin.

This information can be represented in the form of a diagram shown in Fig. 3–2, where on the horizontal axes lies the location of the fault and on vertical axes the recalculated charge at the point of origin. This example plot would show that joints with numbers 5 and 9 are producing partial discharges with the displayed range of magnitudes accumulated along the vertical axis.

This data on its own can be used for predictive maintenance, and at the same time can be the starting point in gathering statistics for the Big Data approach of failure prediction.

Based on these requirements we can design a pipeline that would lead to such results. It would consist of blocks (or modules) of physical and algorithmic levels:

Content Omission Placeholder

Publication note: In order to protect intellectual property, the remainder of this chapter (pages 40 – 41) of the original document, which contains sensitive information related to the monitoring system's modules, has been excluded from the publication.

Omitted content summary: The pipeline chart of the monitoring system, showing modules and their interfaces, can be found in Fig. 3–3 placed below.

These modules are being developed by a project team, and a detailed analysis of all of them is beyond the scope of this thesis. Descriptions of some of these modules can be found in publications [Pub. 1] – [Pub. 6] and patents [Pat. 1 – Pat. 4], as well as in the following sections of this dissertation, where the author presents his contributions to the development of some of these modules.

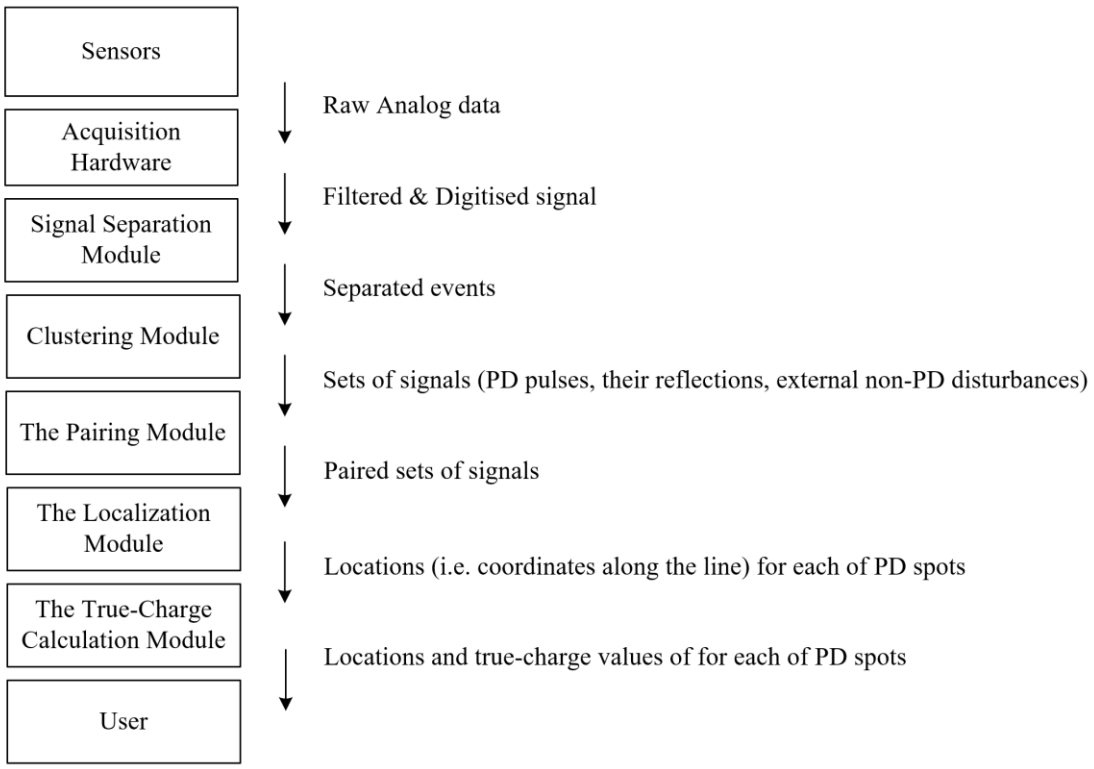

Fig. 3–3 Blocks of Monitoring System

This content was omitted from the publication.

This content was omitted from the publication.

End of the Content Omission Placeholder

4. Chapter:

Sensor

4.1 HFCT as a Part of Monitoring System

As mentioned in Chapter 2, HFCT is probably the most popular non-conventional method for signal coupling on HV cable lines. In the vast majority of cases, these sensors are only used to extract signals from the cable. However, anticipating ahead, the localization method used in our approach requires measuring the cable's transfer function (as described in the chapter 6: “Localization”), which necessitates injecting pulses into the cable. Thus, the HFCT serves as a bidirectional sensor – both for measuring small signals and for injecting calibration signals into the cable. Taking into account the peculiarities of the developed monitoring system, a custom current transformer shown in Fig. 4–1 was designed and put into series production.

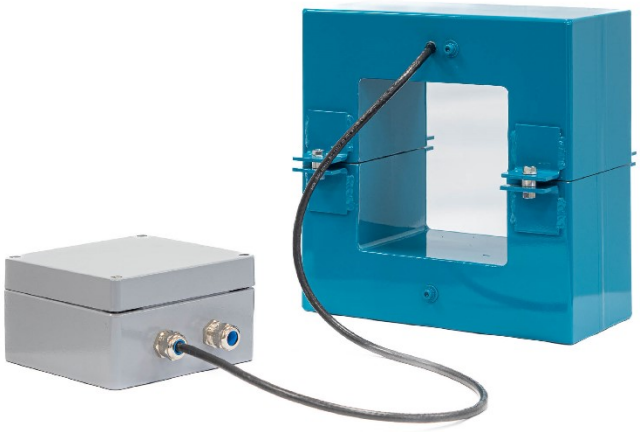

Fig. 4–1 Developed HFCT with the over-voltage protection (OVP) box. For the next models, the OVP is attached to the housing of HFCT.

In terms of the HFCT sensor positioning, for HVDC cable lines, this encompasses all joints with a screen separation, which are usually located at a distance of approximately 6 – 12 km, as well as terminations (the topology of the HVDC lines was explained in the end of chapter 2.4). In the case of HVAC lines, these could be joints for screen cross-bonding and again, terminations. In general, there are two optional ways of coupling: coupling to the cable shield and coupling to the central conductor of the cable. The first option is more common to the HV and EHV cable accessories and is usually performed on the links outgoing from the cable shield, e.g. the grounding or bonding links (e.g.[55], [56], [57]). In this case, the HFCT is decoupled from the power current and its dimensions are relatively small and independent of the cable rating. Within this approach usually locally sensitive monitoring is used – meaning that one sensor monitors only the joint on which it is installed. Establishing the coupling to the cable core is a common practice at medium voltage (MV) cable terminations. In this case the HFCT is installed around the whole cable with an extra

loop of the existing grounding strap going through the HFCT in the opposite direction of the cable as it is shown in Fig. 4–2. Here, the magnetic fields from the cable shield and grounding link cancel each other out. As a result, only the magnetic field of the cable central conductor remains. Some sources claim this coupling position to be more beneficial [58].

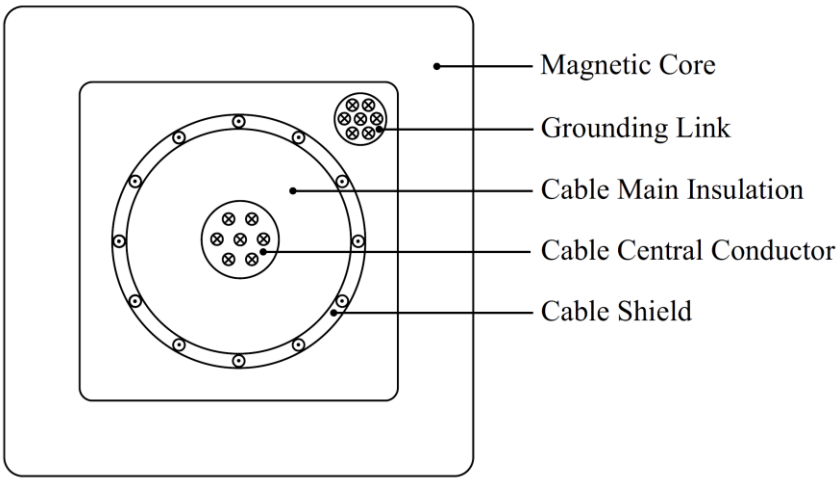

Fig. 4–2 Cross-section of a cable-core-coupled placement [Pub. 3].

Within the scope of our research, the connection to the cable core is used. Fig. 4–3 depicts a typical example of sensor installation on a joint with screen separation, such as those used on HVDC lines for screen grounding or on HVAC lines for cross-bonding. It can be clearly seen how the cable screen forms the mentioned double loop, excluding its current from the HFCT coupling. The peculiarities of the PD localization method employed in this study recommend the installation of one sensor on both sides of accessible joints.

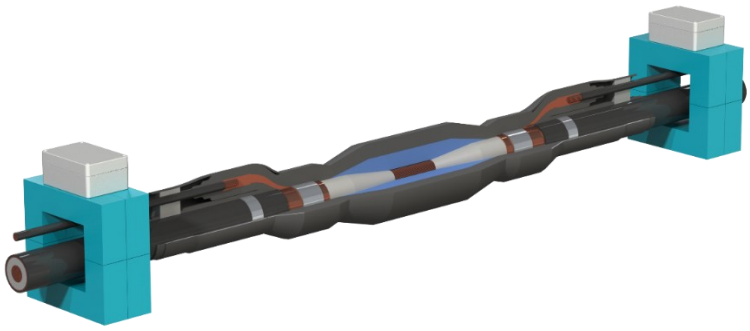

Fig. 4–3 HFCTs installed on the joint with the screen separation.

In Fig. 4–4, the installation of two HFCTs on a cable end termination is shown. It should be noted that the base of the termination always stands on insulators and thus isolated from ground potential. Its connection to ground is always performed with an additional wire,

which in our case passes through the apertures of the HFCTs, also providing a means of subtracting the ground signal.

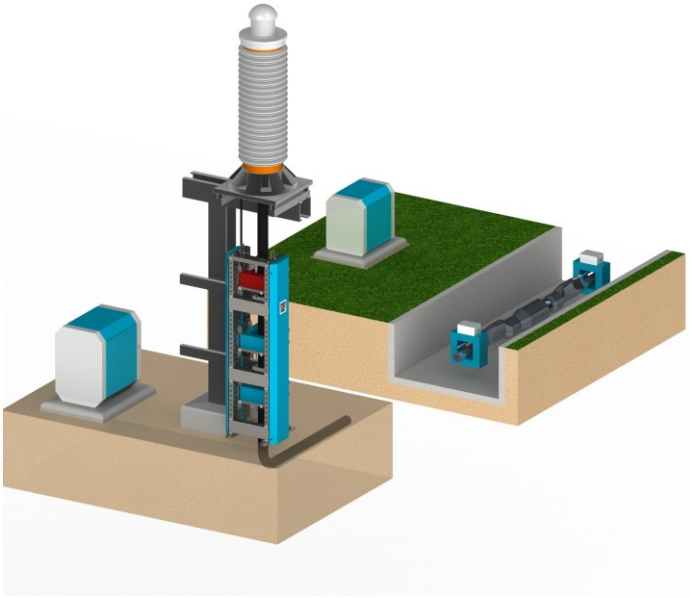

Fig. 4–4 On the front: installation of HFCTs on a cable end termination,
The acquisition hardware cubicle is visible on the left,
on the background: HFCTs installed on the joint.

Working with cable core coupling introduces several additional requirements. Foremost among these is the need to ensure the coupling of small signals in the presence of high-power cable current. From the perspective of signal separation, this is not problematic, PD waveform can be easily separated from the power frequency oscillations due to their completely different frequency ranges. However, it is crucial to ensure that the cable current does not lead to the saturation of the HFCT's magnetic core, while also maintaining an optimal transfer function. In addition, it is essential that the HFCT is able to withstand transient events that may occur in the cable system. This includes impulses from switching operations, as well as surge currents, which must not cause any harm to the HFCT itself or any downstream electronics.

The requirements for a cable-core-coupled HFCT can be summarized as follows:

- Ability to operate in the presence of a rated cable current,
- Ability to withstand possible surges,
- Negligible influence on the cable system,
- Thermal stability,
- Attenuation of unwanted frequencies.

The developed HFCT has the following specifications:

- Possible parameters of cables:
  - Type — HVAC and HVDC
  - Perm. load current — 3000
  - Cable diameter — max. 175 mm
  - Max. surge current — 150 kA (8/20µs)
- Main features:
  - HV core design — split core, differential
  - Cable-side inductance — < 2 µH
  - Bandwidth — 0.1 … 9 MHz
  - Design lifetime — 40 years
- Installation features:
  - Temporary or permanent,
  - Outdoor, protection degree IP 68, can be buried in the soil directly,
  - Installation on existing cable systems is possible due to split-core design.

This concludes the surface-level, but minimally necessary description of the transformer as a block in the monitoring system. To maintain the narrative flow, this description was presented from the perspective of the final product that has passed the industrialization phase. However, the design of the transformer can be compared to the design of antennas, where despite the apparent simplicity of the principle and small number of components, decision-making in the development process is not always straightforward, but deals with a plenty of comparable configurations. Design of an HFCT involves a large number of parameters to tune, from material selection to winding width. In literature the design optimization is addressed quite usually but also often rather superficially. To close this gap, which is relevant not only within the main line of this thesis but also for the HFCTs themselves, this work provides six additional sections that will examine the design features of the HFCT:

- Basic Design Calculations
- Leakage Inductance Estimation
- HFCT Operation under Biasing Current
- Balanced Design
- Resonant behavior of HFCT
- Prototyping & Performance Assessment

4.2 HFCT: Basic Design Calculations

An HFCT is increasingly used as a device for PD measurements, and in recent years there has been a significant increase in publications related to its design aspects [59]– [72], as well as comparisons of signal coupling via HFCTs with other types of sensors [73] – [76].

Quite often the influence of design parameters, such as the number of turns, size of the gap, material of the core, etc., on the resulting performance of HFCTs is studied empirically: these parameters are varied within the simulation [61] or on the sample prototypes [63].

Analytic approaches usually start with the common equivalent circuit of transformer, which is studied with varying degree of simplification. In addition, authors sometimes make a distinction between high-frequency and low-frequency models, as was done in one of the most thoughtful related studies – the Doctoral Thesis by Kütt [59], which addresses air-core sensors. On the other hand, when choosing the level of simplification, the practical aspect of the issue is often ignored, namely, how easy it will be to apply the derived formulas.

In [68], the transfer impedance equation is presented rather implicitly and includes the parasitic capacitance of the coil – a quantity that is often unknown and difficult to calculate. The authors do note this point, acknowledging that the universally accepted method for its calculation was not found. Thus, this unknown quantity makes the formula derived in a general form most often can be inapplicable in the form in which it is proposed. Certainly, this does not mean to diminish the value of formulas that include all parasitic parameters, but rather shows a general trend in publications towards deriving most general equations.

In this study, the description and design of HFCT is approached from a slightly different perspective than that presented by Kütt in for air-core transformers [59]. For example, the model of HFCT will not be tailored to three frequency ranges. In general, it makes sense to approach the analysis of the device design from two sides: firstly, without resorting to overly complex models and secondly, avoiding purely empirical approaches that have been noted for some previous studies. Our task is simplified by the fact that the design calculations of HFCT, at least within our purposes, do not require precision since its final characteristics do not require it. On the other hand, this device has a large number of parameters that may or may not affect its operation, such as the number of turns, shape and parameters of the magnetic core, the presence of an air gap, and the type of wire used for winding, among others. Therefore, the valuable task would be to analyze the combination of these factors, identify the important ones, and separate them from the ones that do not influence. Derived

formulas, e.g. transfer function, should be easily applicable and contain quantities that can be calculated or estimated.

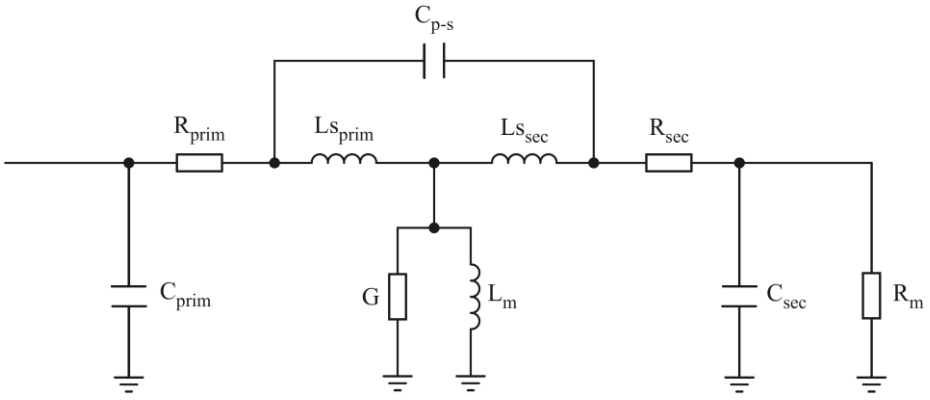

Fig. 4–5 Transformer Equivalent Circuit

We will start with the complete conventional equivalent circuit of the transformer with the additional measurement impedance R_m on the secondary side shown in Fig. 4–5. Here the elements are denoted as follows:

- C_{prim}, C_{sec} – primary and secondary side parasitic capacitance,
- Ls_{prim}, Ls_{sec} – primary and secondary side leakage (stray) inductance,
- G – admittance due to the active losses in the core
- L_m – magnetizing inductance
- R_m – measuring impedance
- R_{prim}, R_{sec} – primary and secondary side resistances of the winding
- C_{p-s} – parasitic capacitance between primary and secondary windings,

Instead of simplifying this circuit right away, I want to first provide some comments on the meaning of each of these parameters for the case of an HFCT and regarding the need to retain or exclude an element for the simplified circuit.

- **Measurement impedance R_m** usually cannot be selected voluntarily. At least for the case of PD measurements, which is probably most frequent case of use, HFCT is commonly designed as a passive device. It means that the active hardware (amplifier and digitizer) is not included in it, but is an external module usually placed at a more convenient place at a certain distance from the HFCT. The connection between them is performed with a signal cable, e.g., coaxial or twinaxial, whose characteristic impedance has to match the measurement impedance. In this way the selected cable defines the value of measurement impedance. At the same time the range of impedances of available cables is broad, but limited, as it is defined by the cross-section dimensions of

the cable itself. It is possible to find even 12 Ohm coaxial cables, but the dielectric is rather thin in order to lower the per-meter inductance and increase capacitance. On the other side of the scale one can find 75 Ohm, 93 Ohm, and 100 Ohm coaxial cables. Among higher impedances one still can find 150 Ohm twinaxial cables. The very limit of this scale are the twin-leads, that could go up to 600 Ohm, however practical use of such in our field would be unlikely. The most common values are 50 Ohm for coaxial and 100 Ohms for twinaxial cables. Clearly when the device is meant for mass-production these values are preferential. Therefore, most commonly within design procedure this value is set to 50 Ohms by default. However, it should be noted still, that in special applications when the amplifier can be placed directly at the output of the winding the enabled possibility to tune the measurement impedance value can give more room in compromise between the bandwidth, transfer impedance and number of turns. A study where this value is selected arbitrarily to achieve narrow-band coupling can be found in [84].

- **Resistance of the HFCT winding R_{sec}** often can and should be omitted of consideration. The HFCT usually has a rather small number of turns, because higher number of turns means low transfer impedance (this will be demonstrated later along with presented formulas). Typically, if the goal is to maximize the transfer impedance, then 3 or 4 winding turns may be used, whereas if the goal is to lower the cutoff frequency, there may be several tens of windings, but usually not more. Even with thin wire and several tens of turns, taking into account the skin effect, the winding resistance will be by several orders less than the measurement impedance, e.g., [68]. For instance, a winding with a wire diameter of 1 mm and a length of two meters (20 turns around a square core with a side of 2 cm plus extra for inter-turn distance) at a frequency of 10 MHz will have a resistance of about 500 mOhm, i.e., one percent of the measurement impedance value. Since the winding resistance forms a divider with the measuring impedance, the transfer function at this frequency will drop by this value. On the other hand, including the winding resistance in the formula for deriving the transfer function makes little sense, as this value, on the one hand, has a strictly negative impact, and on the other hand, can be easily minimized by simply choosing a wire with a slightly larger surface area – in our example it was only 1 mm in diameter. An empirical rule here could be: if for some reason working in the range of about ten megahertz is assumed and several tens of turns are wound with thin wire, and every percent of sensitivity is important, it makes sense to check the resulting resistance and if needed, take the thicker

or wider wire. On the other hand, this situation is not so likely for HFCT – here either the frequency range will be lower, or there will be fewer turns. In general, taking into account the active resistance of the winding is more relevant for Rogowski coils – since the frequencies there are higher and there are more turns. But for HFCT for simplicity the winding resistance can be excluded from further equations.

- **The primary parameters:** $Ls_{prim}, C_{prim}, R_{prim}$ here are referring to the power cable itself, and do not influence the transfer impedance and the current transfer functions before the start of the resonance behavior. Therefore, the parameters referring to the primary side are usually omitted. Although it should be noted that in reality, this simplification can backfire: no matter how wide the bandwidth is, the HFCT never works as stand-alone device, but is installed on a certain conductor, in a certain system, so the high-frequency end of the resulting transfer function will of course differ from the one measured in the lab with a test loop or calculated using only the secondary-side properties. This fact is usually overlooked or not mentioned in the publications, as HFCT is most often studied "separately", although there exist examples where this influence is taken into account. For example, [70] shows that the upper cutoff frequency when the sensor was installed on a joint dropped from 95 MHz to approximately 15 MHz and exhibited a pronounced resonance peak at a frequency of 10 MHz. Additionally, the flatness of the bandwidth was also disrupted, with the gain increase starting at several megahertz.

- **Inter-winding capacitance** C_{p-s} is usually excluded along with the primary parameters. In our case, this is the apparent capacitance between the cable and the screen or winding of the HFCT, and it will also participate in the overall resonance behavior of the system formed by the cable and HFCT.

- **The leakage inductance** Ls_{sec} of an HFCT's winding is a parameter that can be calculated using empirical formulas or numerical methods. The leakage inductance takes into account the geometry of the winding, as well as the material properties and geometry of the magnetic core. Therefore, empirical formulas provide only approximate results, and numerical methods should ideally be performed in 3D. However, we will show later that 2D can provide good predictions as well. On the other hand, cases can be identified in advance where this parasitic parameter can be ignored without the need for any calculations. First and foremost, this applies to cases where the magnetic core does not have an air gap and at least ~6 turns distributed over it more or less evenly,

and the effective relative permeability of the core $\mu_{r_{eff}} > \sim 50$ within the frequency range of interest. For closed magnetic cores, the last holds true for most magnetic materials. Clearly, the magnetic permeability decreases with frequency, but the winding evenly distributed over the perimeter of the core itself will provide good coupling even when the relative permeability drops. If these aspects are fulfilled, the leakage inductance will be by several orders smaller than the magnetizing inductance and will not influence on the HFCT performance. Therefore, the geometry of the turns and how dense the winding encloses the core will be of little importance.

The more complex case arises when a non-magnetic gap is present, which reduces the effective magnetic permeability of the magnetic core. Since such a gap is often introduced to perform a split-design of HFCT, a common practice is to place the winding on one half of the magnetic core only. In this case, the leakage inductance may raise to a double-digit percentage of the magnetizing inductance, especially with concentrated winding and large non-magnetic gaps needed to increase the saturation current. The calculation of leakage inductance via Finite Element Analysis (FEA) is presented in subchapter 4.3.

- **Admittance *G*** represents active losses in the core, which are usually neglected, and for most ferromagnetic materials, they are indeed negligible. However, for cores made of amorphous steel, for example, this condition is not always met.

- **Parasitic capacitance C_{sec}** of an HFCT is a parameter that is least amenable to calculation. In the circuit, this capacitance is needed, again within the framework of HFCT, to determine the upper cutoff frequency of the transfer function, in other words, to simulate its resonance behavior. Accordingly, it should be noted that in the case of an HFCT, unlike, for example, a power transformer, the capacitance shown in the circuit is not much related to electrostatic capacitance between the turns. The resonance of HFCT and single-layer coils in general is related to wave phenomena in the coil, and the capacitance shown on the circuit diagram can only represent the electric field of the EM wave. Therefore, the calculation of this capacitance cannot be reduced to a simple electrostatic problem. Certainly, it is possible to calculate the electrostatic capacitance by dividing the coil into virtual individual turns, as demonstrated, for instance, in [70] and [83]. However, using this capacitance value for the resonant model would be incorrect as the resulting capacitance value is firstly, likely to be much smaller than the apparent parasitic capacitance inferred from the resonance frequency, and secondly,

does not reflect the nature of the EM wave resonance which takes place in the core. Consequently, it makes no sense to optimize the winding based on the electrostatic capacitance and formulas for its calculation – for a common HFCT, the distance between the turns on the coil and the distance from the winding to the magnetic core essentially will not affect its resonant frequency, which is also shown in the subchapter 4.6. The resonant behavior of HFCT, as a case where the EM wavelength is comparable to the geometric dimensions, should be addressed using the theory of transmission lines. For the case of air-core solenoids, this topic is well developed due to its applicability in the field of radio engineering, and there exist formulas that allow approximate calculation of the apparent capacitance and resonant frequencies, which can be adapted to the case of a Rogowski coil. In the case of HFCT, the problem is not so much the complexity of the calculation itself, but that the parameters of the magnetic core material necessary for the calculation are not usually provided in standard datasheets of materials. Further information about the resonance behavior of an HFCT will be provided in a separate subchapter 4.6.

In the studies that concern HFCT design its transfer function is used as a performance quality indicator. In general, the transfer function is the relation between signal on the output and the input of the device. However, as a measure of the signal we have different quantities: voltage, current, and power. Therefore, we can speak of the various ratios: output voltage to input voltage, output voltage to input current, output power to input power, etc. Moreover, each of them can be referred either to the primary or to the secondary side. In articles most common is the ratio of the output voltage referred to the secondary side to the input current referred to the primary side: $\bar{V}_s''/\bar{I}_p'$. Here the superscript $'$ means that the value is referred to the primary side and $''$ – to the secondary. It is presented in this form $\bar{V}_s''/\bar{I}_p'$ in [63], [64], [66], [67], [68], [70], [84]. This ratio is called the transfer impedance. It appears to be handy for practical use: it is rather common that the approximate magnitude of the current to be measured is known, in this case, the transfer impedance can give an estimate for the voltage induced by HFCT on the input of the recording hardware, thus enabling comparison with its dynamic range.

The transfer impedance is measured in Ohms. The higher the transfer impedance, the larger is the voltage obtained on the measuring resistance. To anticipate, as stated by Eq. (4.6) to increase the transfer impedance, the number of turns should be reduced. Furthermore, it is easy to estimate typical values of transfer impedance for different sensors. For example, if

there is a measurement resistance of 50 Ohms and four turns of winding, the transfer impedance will be 12.5 Ohms.

We will not present the transfer function formula in the most general case – if all parasitic elements are taken into account, it becomes rather cumbersome and loses its clarity and practical significance. At the same time, if all parameters should be taken into account, it would be easier to conduct modeling in any Spice simulator. Often, in the literature, the transfer function formula is given for to some extent simplified circuit and, most often, in the Laplace domain. Good examples can be found in [65], [67], [68]. In this work, we will present the formulas in the frequency domain, again for practical reasons, for the equivalent circuit simplified as shown in Fig. 4–6.

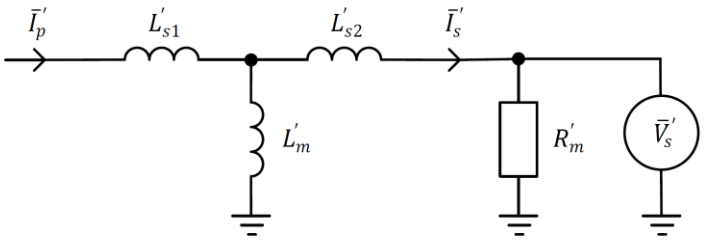

Fig. 4–6 Simplified equivalent circuit of HFCT

Let us define the transfer impedance the ratio of the output voltage referred to the secondary side to the input current referred to the primary side:

$$\bar{H}_{V/I} = \frac{\bar{V}_s''}{\bar{I}_p'} = \frac{\bar{V}_s''}{\bar{I}_p''} \cdot n = \frac{\bar{I}_s''}{\bar{I}_p''} \cdot n \cdot R_m'', \tag{4.1}$$

where $n = \frac{1}{N}$ is the turns ratio and N is the number of the HFCT turns.

From the equivalent circuit, we can derive the Eq. (4.5) for the transfer impedance.

$$\bar{H}_{V/I} = \frac{Z_m''}{Z_m'' + Z_2''} \cdot n \cdot R_m'', \quad \text{with } Z_2'' = R_m'' + j \cdot \omega \cdot L_{s2}'', \tag{4.2}$$

$$|H|_{V/I} = \frac{n \cdot R_m'' \cdot \omega L_m''}{\sqrt{R_m''^2 + \omega^2 (L_{s2}'' + L_m'')^2}}, \tag{4.3}$$

$$|H|_{V/I} = \frac{n \cdot \omega L_m''}{\sqrt{1 + \left(\frac{\omega (L_{s2}'' + L_m'')}{R_m''}\right)^2}}, \tag{4.4}$$

If the leakage inductance can be neglected, it can be further simplified to the following form:

$$|H|_{V/I} = \frac{n}{\sqrt{\frac{1}{(\omega \cdot L_m'')^2} + \frac{1}{R_m''^2}}} \tag{4.5}$$

Here, in both formulas (4.4) and (4.5), the values are already referred to the secondary side, which is the winding of an HFCT. Therefore, these are quantities that can be measured on the winding of HFCT. Using this formula, one can estimate the transfer impedance within the bandpass. In this case in Eq. (4.5) the term $\frac{1}{(\omega \cdot L_m'')^2} \rightarrow 0$, therefore in the bandpass:

$$|H|_{V/I} = R_m'' \cdot n = \frac{R_m''}{N} \tag{4.6}$$

This simple relationship shows that increased number of turns leads to a decrease in the transfer impedance. Therefore, most HFCTs have a small number of turns, e.g., 3, 4, 5.

On the other hand, representing the transfer function in the form of transfer impedance also has its drawbacks: it shifts along the y-axis depending on the number of turns, and it is unclear what value the curve is tending towards. In other words, if we consider the HFCT as a second-order bandpass filter, with this representation it is harder to visually estimate the cutoff frequency and the attenuation in the passband. As a result, the influence of parasitic elements, such as active losses in the core or leakage inductance, becomes less intuitive.

A more illustrative way to examine these effects is to consider the ratio of the secondary current to the primary current, with both currents referred to the same side of the transformer:

$$|H|_{I/I} = \frac{\overline{I_s''}}{\overline{I_p''}} \tag{4.7}$$

$$|H|_{I/I} = \frac{\omega \cdot L_m''}{\sqrt{R_m''^2 + \omega^2 (L_{s2}'' + L_m'')^2}}, \tag{4.8}$$

$$|H|_{I/I} = \frac{\omega \cdot L_m''}{\sqrt{R_m''^2 + (\omega \cdot L_m'')^2}}, \tag{4.9}$$

The graph plotted in this way on a decibel scale is "weighted" relative to zero. In the ideal case, where the influence of active losses, scattering, etc. is negligible, the graph will approach 0 dB within the passband. This means that it is convenient to use the 0 dB point as a reference for judging the performance characteristics:

- Cutoff frequencies,
- Ripple in the passband,
- Sensitivity, in terms of how close the transfer function is to 0 dB in its flat part.

From (4.9) can be derived that the ratio between R''_m measurement impedance and inductance L''_m defines the lower cutoff frequency (at the −3 dB value):

$$f_{\text{low}} \approx \frac{R''_m}{2 \cdot \pi \cdot L''_m}, \tag{4.10}$$

At the same time, as we have already mentioned, the measurement impedance R''_m is usually preselected, therefore low cutoff frequency can be tuned by change of the magnetizing inductance $L''_m = N^2 \cdot L'_m$. The common inductance formula which can be used for various forms of the core (rectangular, oval, etc.) gives an estimate that is accurate enough for our purposes:

$$L_m \approx N^2 \frac{\mu_0 \mu_{eff} S}{l_{mid}} \tag{4.11}$$

where l_{mid} is the middle line of the magnetic core, S – the core cross section, μ_{eff} effective relative permeability of the core.

With the Eq. (4.11) the low cut-off frequency can be expressed as:

$$f_{\text{low}} \approx \frac{l_{mid} R''_m}{2\pi \cdot \mu_0 \mu_{eff} S N^2} \tag{4.12}$$

In practical case several variables in the Eq. (4.12) have to be predefined: the desired aperture size of the HFCT defines the length of the magnetic core middle line l_{mid}, the value of measurement resistance R''_m should meet the wave impedance of the signal cable.

The right part of the Eq. (4.13) shows the values that can be tuned to influence the low cutoff frequency. At the same time the transfer impedance, as was shown above by Eq. (4.6), is inversely proportional to the number of HFCT turns. Therefore, if one needs to keep the transfer impedance and shift the cutoff frequency to the lower range, it would be necessary to increase one-turn inductance of the core, either by cross-section or by its effective permeability.

$$f_{\text{low}} \sim \frac{1}{\mu_{eff} S N^2}\ ; \qquad |H|_{V/I} \sim \frac{1}{N} \tag{4.13), (4.14}$$

At the same time, if the non-magnetic gap is introduced, it would lower the effective permeability and to keep the cutoff frequency and transfer impedance it would be necessary to increase the core cross-section.

For the HFCT design, equations presented above may come in handy as they do not contain values that require complex calculations; nevertheless, they convey the basic relationships

and represent the resulting transfer functions. In other words, this is the minimum baseline needed for HFCT design. Among the material parameters, these formulas only feature magnetic permeability, which is usually known for magnetic materials and can be easily recalculated in the case of a gapped magnetic circuit. Strictly speaking, relative magnetic permeability is a value that decreases with increasing frequency, and its specifications often include a graph that can be used when calculating the magnetizing inductance. Transferring data from the graph is not always convenient, so to obtain a quick result, one can use its value at the cutoff frequency of the future HFCT.

4.3 Leakage Inductance Estimation

4.3.1 Theoretical framework

The leakage inductance of a transformer is caused by the fact that the magnetic coupling between the two transformer windings is not ideal. The magnetic flux created by one winding is not fully coupled to the second. The part of the flux that is only coupled to the generating coil is the leakage flux, and the corresponding quantity of inductance is called the leakage inductance. The leakage inductance depends on the geometry of the core, the arrangement of the windings relative to the core and to each other, the geometry of the coil, the magnetic permeability of the core, and so on. The problem of calculating the leakage inductance can be solved analytically, while FEA software had limited capabilities in the past, formulas exist for performing such calculations in specific fields, such as, for instance, the development of power transformers.

On the other hand, leakage inductance estimation is the case where the numerical methods can be simpler, faster, and more accurate. This is primarily due to the fact that, despite that magnetic field is excited by an alternating current, the problem itself is static. This allows us to select steady-state modeling instead of the frequency domain one, and therefore, the electric field does not have to be calculated. These factors lead to stable convergence and short calculation time.

I will consider the case of two-winding transformer and describe how the leakage inductances are calculated for the primary and secondary windings. We will use an equivalent circuit diagram that reflects only the inductive part of the transformer, shown on Fig. 4–7.

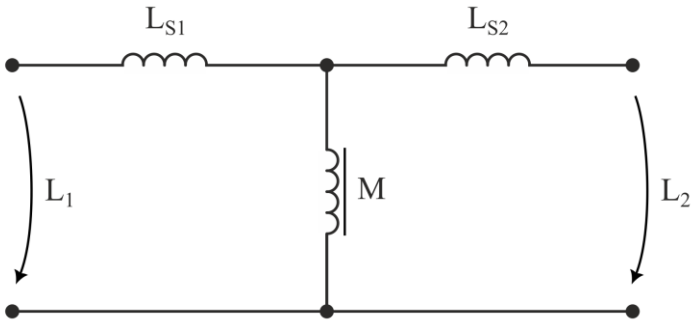

Fig. 4–7 Inductive Equivalent Circuit

Self-inductance of the primary winding if the secondary is open circuit is defined as:

$$L_1' = L_{s1}' + n \cdot M, \tag{4.15}$$

therefore leakage inductance of the primary winding is:

$$L_{s1}' = L_1' - n \cdot M, \tag{4.16}$$

Self-inductance of the secondary winding if the primary side is open circuit is defined as:

$$L_2'' = L_{s2}'' + \frac{1}{n} \cdot M, \tag{4.17}$$

therefore leakage inductance of the secondary winding is:

$$L_{s2}'' = L_2'' - \frac{1}{n} \cdot M, \tag{4.18}$$

where n – is the winding ratio:

$$n = \frac{w_1}{w_2} \tag{4.19}$$

We will express inductances through the total magnetic fluxes (concatenated flux) of the windings. We will assign two subscripts to the concatenated flux $\Psi_{n,m}$: the first will indicate to which coil the flux belongs to, and the second – which winding's current generated this flux.

If the secondary side is open circuit:

$$L_1' = \frac{\Psi_{11}}{I_1}, \tag{4.20}$$

$$M = \frac{\Psi_{21}}{I_1}, \tag{4.21}$$

using (4.15) and (4.16):

$$L_{s1}' = \frac{\Psi_{11}}{I_1} - n \cdot \frac{\Psi_{21}}{I_1}. \tag{4.22}$$

If the primary side is open circuit:

$$L_2'' = \frac{\Psi_{22}}{I_2}, \tag{4.23}$$

$$M = \frac{\Psi_{12}}{I_2}, \tag{4.24}$$

using (4.17) and (4.18):

$$L''_{s2} = \frac{\Psi_{22}}{I_2} - \frac{1}{n} \cdot \frac{\Psi_{12}}{I_2}. \tag{4.25}$$

Thus, we obtain a set of equations that allow us to obtain all the parameters of the equivalent circuit, drawn together in Table 1.

Table 1 Equivalent parameters defined with calculated concatenated fluxes.

Inductance	secondary side is open circuit	primary side is open circuit
Self-inductances of the windings	$\mathrm{L}_1 = \frac{\Psi_{11}}{\mathrm{I}_1}$	$\mathrm{L}_2 = \frac{\Psi_{22}}{\mathrm{I}_2}$
Leakage inductances	$L_{s1} = \frac{\Psi_{11}}{I_1} - n \cdot \frac{\Psi_{21}}{I_1}$	$L_{s2} = \frac{\Psi_{22}}{I_2} - \frac{1}{n} \cdot \frac{\Psi_{12}}{I_2}$
Mutual inductance	$M = \frac{\Psi_{21}}{I_1}$	$M = \frac{\Psi_{12}}{I_2}$

In COMSOL Multiphysics software [77] which I use for FEA-simulations the concatenated flux denoted as Ψ_i is a variable calculated by default for Coil objects. However, we can also verify the calculation by solving the problem via the magnetic vector potential **A**.

The line integral of **A** over a closed loop, **Γ**, is equal to the magnetic flux, $\Phi_{\mathbf{B}}$, through a surface, **S**, that it encloses:

$$\oint_{\Gamma} \mathbf{A} \cdot d\mathbf{\Gamma} = \iint_{S} \nabla \times \mathbf{A} \cdot d\mathbf{S} = \Phi_{\mathbf{B}}\,. \tag{4.26}$$

When modeling coils, it is more convenient when their geometry is closed – this way, the current does not need to "exit" the model at one port of the coil and enter at the other – closed lines of current can circulate over the closed domain. In this case, one of the generatrixes of the coil, l, can be taken as the closed contour. Then, by going from the magnetic flux to the total flux Ψ of the coil:

$$\Psi = \oint_{l} \boldsymbol{n}_l \cdot \mathbf{A}\, dl\,, \tag{4.27}$$

where $\boldsymbol{n}_l$ is the unit tangent vector of the coil.

Therefore, by initiating a current in one of the coils, one can calculate the magnetic fluxes belonging to each of the windings by taking the integral along their contours, l_1 и l_2:

$$\Psi_{11} = \oint_{l_1} \boldsymbol{n}_{l_1} \cdot \mathbf{A}\, dl_1\,, \tag{4.28}$$

$$\Psi_{21} = \oint_{l_2} \boldsymbol{n}_{l_2} \cdot \mathbf{A}\, dl_2\,. \tag{4.29}$$

Here, again, the first subscript indicates the winding for which the flux is calculated for, and the second indicates the winding that generated the flux.

Then by initiating the current in the other coil of the pair:

$$\Psi_{22} = \oint_{l_2} \boldsymbol{n}_{l_2} \cdot \mathbf{A}\, dl_2\,, \tag{4.30}$$

$$\Psi_{12} = \oint_{l_1} \boldsymbol{n}_{l_1} \cdot \mathbf{A}\, dl_1\,. \tag{4.31}$$

In COMSOL, as vector $\boldsymbol{n}_l$, the scalar components of the unit "coil direction" vector can be used: mf.coil1.eCoilx, mf.coil1.eCoily, mf.coil1.eCoilz. With its use the equivalent expressions for COMSOL can be constructed as follows:

$$\Psi = \oint_{l_1} (A_x \cdot mf.coil1.eCoilx + A_y \cdot mf.coil1.eCoily + A_z \cdot mf.coil1.eCoilz) dl_1 \tag{4.32}$$

With a sufficiently dense mesh, the leakage inductance values calculated via the magnetic vector potential match with those obtained using the "built-in" concatenated flux. For coarse meshes, the built-in flux value is more accurate.

As a final note, for the sake of completeness, I will present another method that allows for a rough estimation of the upper limit of leakage inductance. The inductance of a coil can be determined through the energy of the magnetic field W:

$$W = \frac{LI^2}{2}, \tag{4.33}$$

then the self-inductance L_i of the *i*-th winding is:

$$L_i = \frac{2 \cdot W}{{I_i}^2}, \tag{4.34}$$

where:

I_i – current in the *i*-th winding,

W – energy of the magnetic field in the model.

Let's assume that magnetic flux in the core is coupled to both windings. In general, this assumption is incorrect as the magnetic flux in the core consists of both the coupled flux and the leakage flux. However, for the purposes of the rough calculation, we will use this assumption:

$$L_M = \frac{2 \cdot W_{core}}{{I_i}^2}. \tag{4.35}$$

We will also assume that the leakage inductance is the difference between the inductance determined by the magnetic core and the total inductance of the winding, i.e., all the flux outside the magnetic core. This is also not strictly correct, as the windings are partially coupled through the air as well. However, using this assumption, we can roughly estimate the value of the leakage inductance as:

$$L_{s2} \approx L_i - L_M. \tag{4.36}$$

Although based on several inaccurate assumptions, this last calculation is still useful for double-checking the result acquired via fluxes. Moreover, it is helpful to estimate what portion of the flux, and therefore of inductance is determined by the magnetic core and by the air domain.

4.3.2 FEA and results validation

When addressing the leakage inductance estimation with FEA-simulations, there are several concerns in regard to the model construction. The first problem to be mentioned is numerical: the leakage inductance can be several orders of magnitude less than the magnetizing inductance, which imposes requirements on the simulation error, and we will return to this question later.

Considering the winding model – it is easy to adapt to the number of turns: if the number of turns is relatively small, it makes sense to draw the winding "as is", and as this number increases, at some point the winding can be reduced to a single domain. However, there are some difficulties. Firstly, the modeling should be performed in 3D, so the calculation time takes from minutes to hours, and when the model is being established, a number of features must be taken into account. The complexity of the simulation is, of course, determined by the number of nodes, i.e., the density of the grid. If the winding is performed with the thin wire, very small-sized polygons will be applied by default to draw its surface, and the meshing algorithm will have to combine them with a larger grid of the rest of the model. Therefore, the winding mesh has to be optimized manually, and although the programs for FEA modeling provide the tools for this task, this step still can be time-consuming. One helpful tip that can be used in a number of cases is to increase the cross-dimensions of the turn within the model. For example, we study a single-layer winding on a core, the largest dimension of the computational area is 500 mm, and the winding is made with a wire of 0.2 mm. In this case, it is easier to model the turns with a large diameter, for example, 1 mm, this will not greatly affect the result, but the model will converge better.

The same problem is created by the gap between the magnetic core and the winding, and the simple solution can be the same as before: if in reality the winding is would directly over the core, during the modeling it is better to create an additional margin between them.

As with any modelling, the question of its accuracy and overall correctness of the result arises upon completion. This issue is particularly acute in this case, as we are looking for a small part of the total magnetic flux. Therefore, in addition to describing the model, we will attempt to solve the problem of its validation, checking that the obtained result corresponds to reality.

Below, I will provide a description of 2D and 3D simulation models for calculating leakage inductance.

Instead of the HFCT itself, four hypothetical prototypes shown on Fig. 4–8 were used for the simulation. Those were differing in the way how the winding is configured. First of all, the winding was enclosing either one or tree sides of rectangular core – these configurations are consequently called U-type and I-type windings. Additionally, within these types, the winding was either distributed or concentrated. Thus, these various configurations allowed obtaining a range between small and large values of leakage inductance depending on how thoroughly the winding was enclosing the core. Similar prototypes were manufactured – shown on a Fig. 4–15 – and used to validate the model and calculation methodology.

The current transformer is installed on the cable and magnetically coupled to one of its conductors – either the shield or the core – and the return conductor is remote from the transformer. In both cases, this situation is approximated by a model in which a conductor passes through the aperture of the transformer, and the return current is closed outside, through the “distant” surface of the infinite domain. Therefore, in all models, the second winding is represented by a straight conductor passing through the center of the HFCT and closed in infinity. The air domains and the central conductor are modeled by cylindrical shapes (Fig. 4–9).

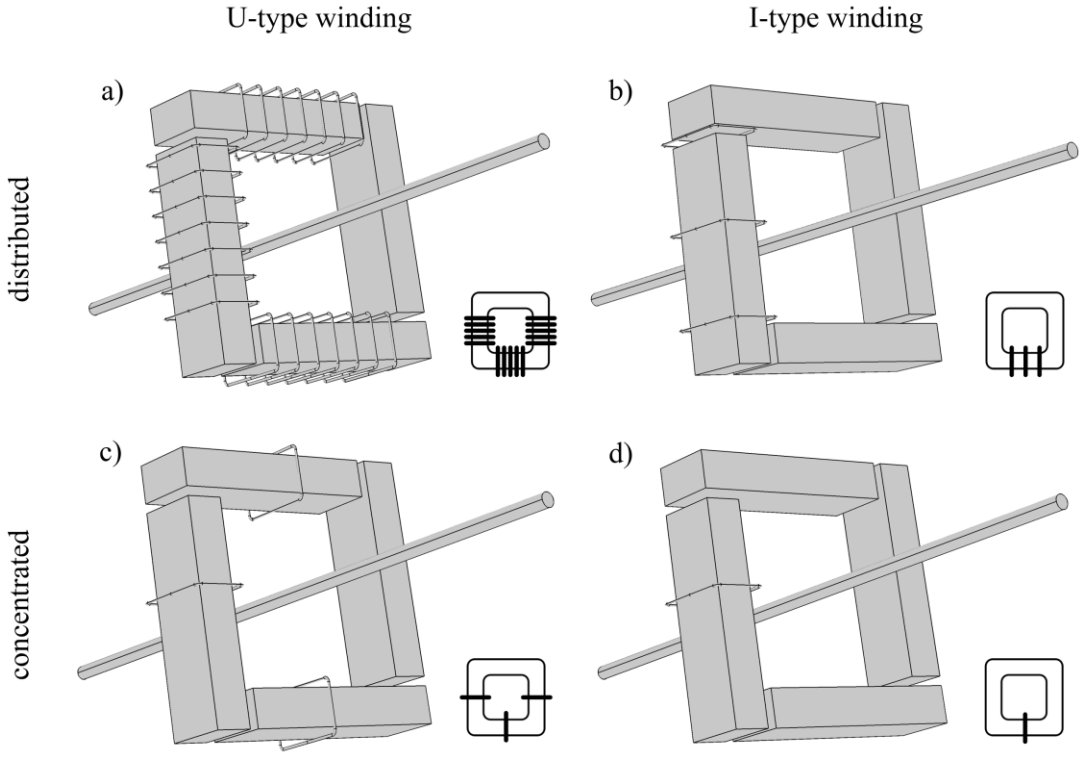

Fig. 4–8 3D models for leakage inductance calculation. a) configuration featuring lowest leakage inductance and d) featuring highest leakage inductance.

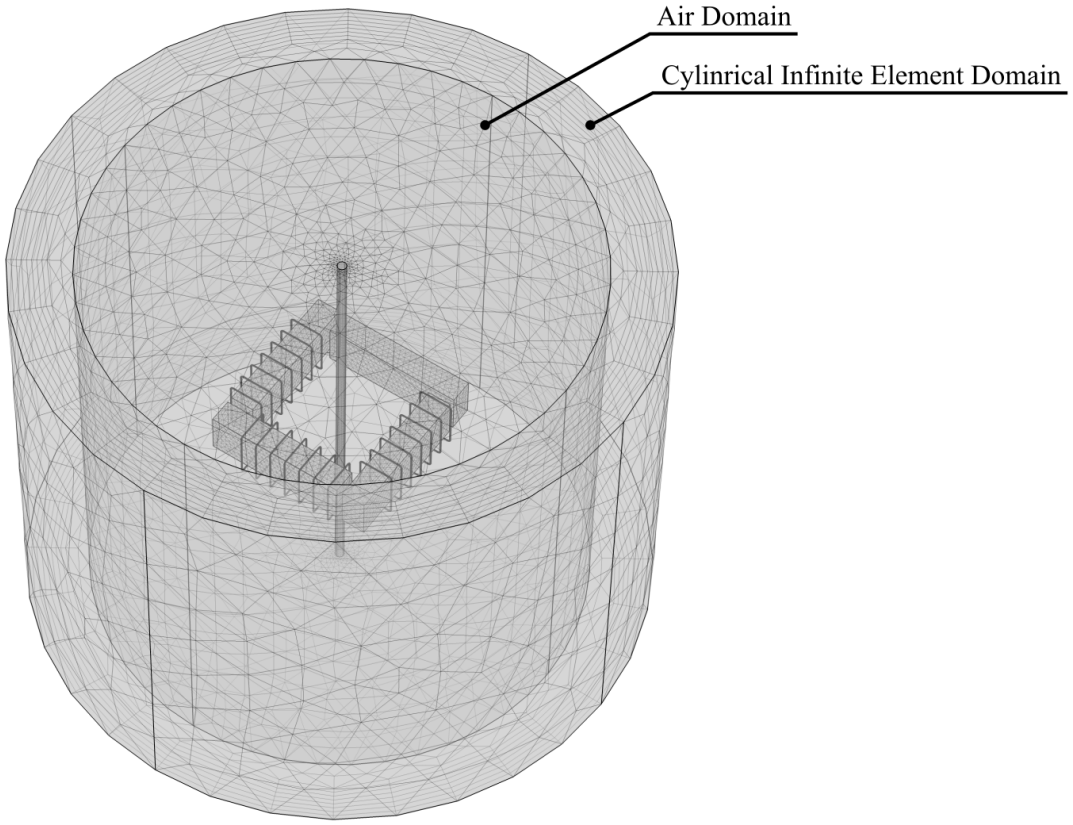

Fig. 4–9 Calculation domain

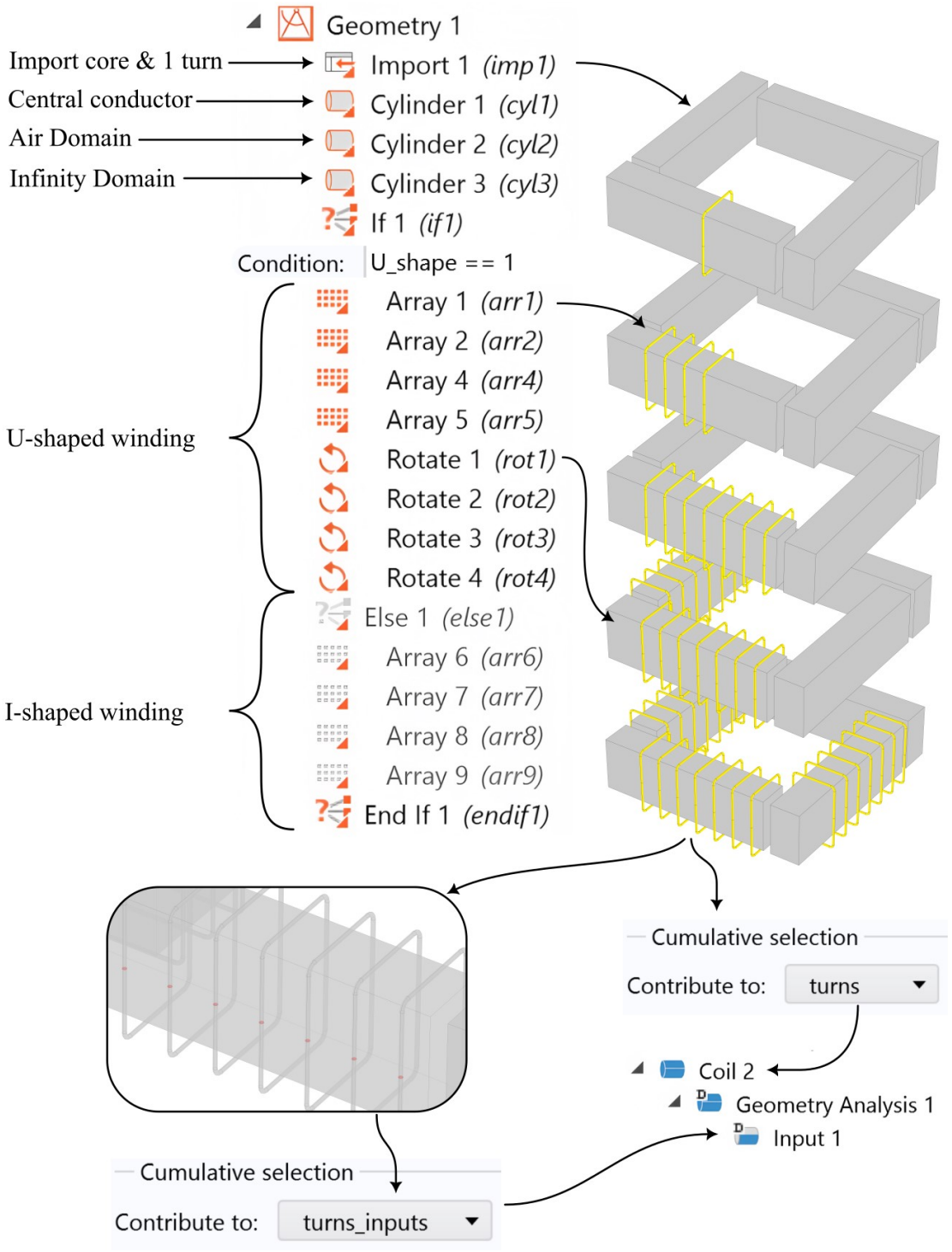

Fig. 4–10 Automated geometry generation for 3D model

Within the simulation model, the HFCT winding was not drawn realistically, but as separate coils. The main reason for this is the simplicity of drawing and redesigning. Since the calculation was performed for varying number of turns, it is convenient when the geometry is reconfigured within one parametric sweep. In terms of calculation error, such an approximation is quite acceptable. Since drawing geometry is still easier in specialized programs like SolidWorks, in the presented case, a magnetic circuit with a single turn was

imported into the model, which will then be transformed into an array. Fig. 4–10 shows the main elements of geometry construction. Thus, the U-shaped coil is obtained in four steps: two arrays drawn in opposite directions and two rotations of resulting geometry. At the same time, each turn should contain cross-sectional plane which is can be used as a current input. Since this plane is present in each turn, it is necessary to perform on it all the same operations as for the winding domain - that is why in the construction tree we see two more arrays and two more rotations. Certainly, this plane could have been included in the winding domain, but as can be seen in the lower part of the Fig. 4–10, the winding and plane domain are ultimately collected under different selections, which are then imported directly into the physical interface of the model. Of course, such geometry generation can be done in different ways, and here only one of the possible methods was presented.

The physics of the model is fairly simple: there are two coil domains, one for the cable and the other for the HFCT's winding (Fig. 4–11). The winding coil domain contains all the turns, while the input boundary condition contains cross-sections for all the turns. In this case, the coils are connected in parallel, or more precisely, it is one distributed coil. However, since it is defined as a Homogenized Multiturn Coil, it is possible to set the number of turns in the interface and obtain scaled values of inductance instead of values "per one turn".

The model calculation includes two stages: first, since we used the "coil" objects in the physics of the model, it is necessary to perform the coil geometry analysis step, and stationary field calculation is performed afterwards. These stages are carried out cyclically within the framework of parametric sweep. The sweep task involves, firstly, rebuilding the model geometry in accordance with the changing number of turns. Secondly, in more general case, when we are interested in the leakage inductances of both windings, it is necessary to perform an open circuit test on both sides alternately, that is, to initiate current in each of the windings one after another. Therefore, apart from the parameters related to geometry, there is one additional parameter in the sweep that changes the index of the current-carrying coil, which is checked in the interface of the coils in the physics model.

Upon completion of the calculation, equivalent parameters are calculated in accordance with Table 1. Furthermore, it is possible to visually assess the distribution of the field, shown in Fig. 4–12 and examine how the leakage fluxes flow.

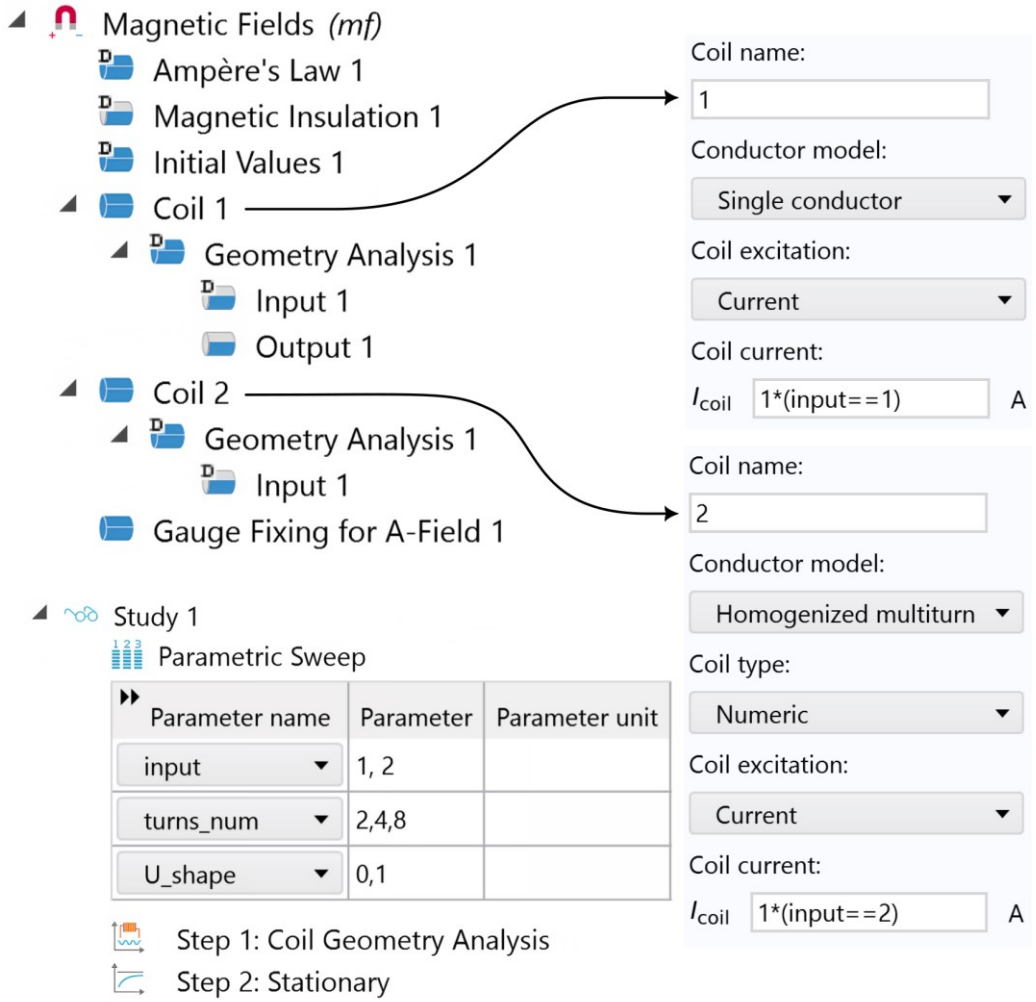

Fig. 4–11 Physics and Study setups for 3D model

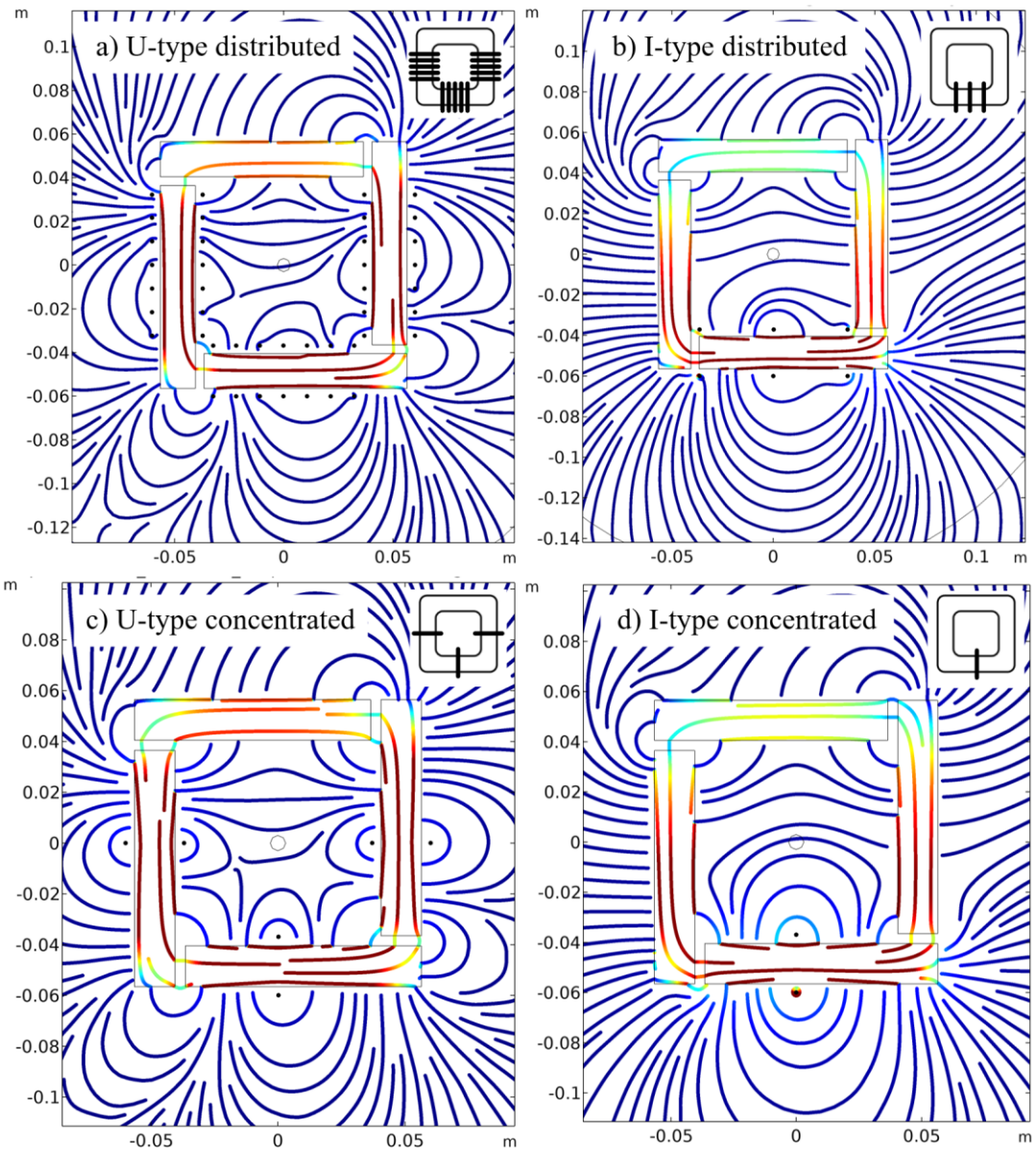

Fig. 4–12 Magnetic field in cutting plane of a 3D model.
It is clearly visible how some of the magnetic field lines surround both the winding and the central conductor (linked magnetic flux), while others are solely closed around the winding (leakage flux).

Another aspect that is investigated is the possibility of a 2D approximation of this and similar problems and the resulting error. Although the static calculation of magnetic fields is one of the simple cases for 3D simulation, the model design with the Computer-Aided Design (CAD) software, import, and calculation itself can still be rather time-consuming. It would be beneficial to approximate our problem to a problem with reduced dimensionality – axisymmetric or 2D problem – in this case the solution will take seconds, it will be much easier to draw the model, and meshing elements can be much smaller.

Unfortunately, the geometry we are investigating cannot be simplified within the topic of leakage inductance without losing accuracy. On the other hand, the 2D model still allows

us to obtain a meaningful result. In this case, we observe the model in cross-section, as shown in Fig. 4–13. Both the construction and physics of the 2D model are quite simple. The automatic generation of winding turns runs in the same way as in the 3D model. Just like in the 3D case, there are only two coil domains. However, since we are looking at a cross-section of the turns, those on the inner side of magnetic core carry a current opposite to that of the outer turns. Additionally, the model allows specifying its depth (thickness), that is the size of the model normal to the modelling plane. Consequently, all quantities are calculated with this size taken into account. In our case, it makes sense to set this depth equal to the thickness of the magnetic core.

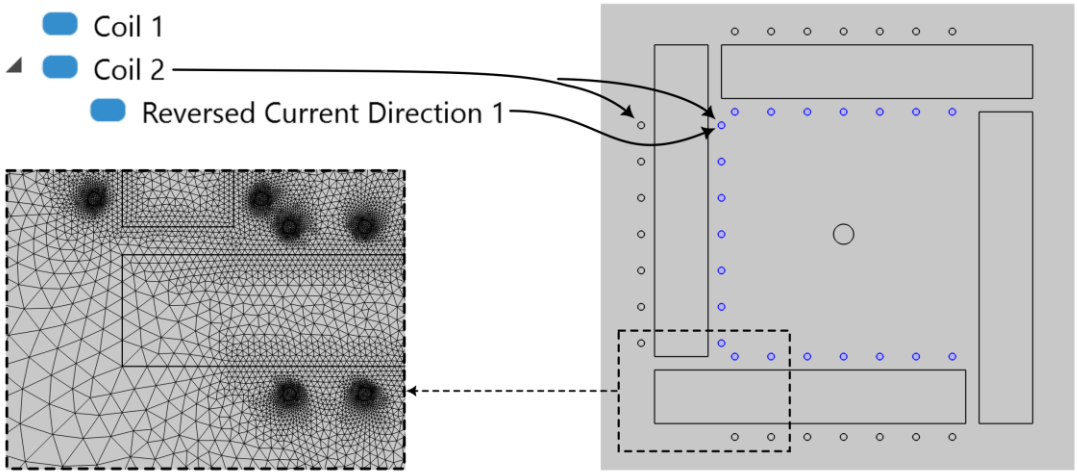

Fig. 4–13 2D model geometry and coil conditions assignment (air domain reduced)

The physics of an infinite domain is not used here; instead, an air domain is modelled to be large enough not to affect the modelling results. On the other hand, two-dimensional simulation allows for a very dense mesh, as also visible on Fig. 4–13.

Fig. 4–13 shows geometry of the 2D simulation, extruded within the plotting by the value of the model depth. By comparing it with the 3D model, it is easy to see which part of the magnetic field is simulated and which part is not covered. Since the model thickness is equal to the thickness of the magnetic core, the air domain is modelled as truncated, and as a result, the calculated value of leakage inductance will be underestimated. On the other hand, such a model still representative for the influence of the winding arrangement on the leakage inductance. Further on in this section, we will compare the results of 3D and 2D simulations, but first let's look at the measurements conducted to validate the results.

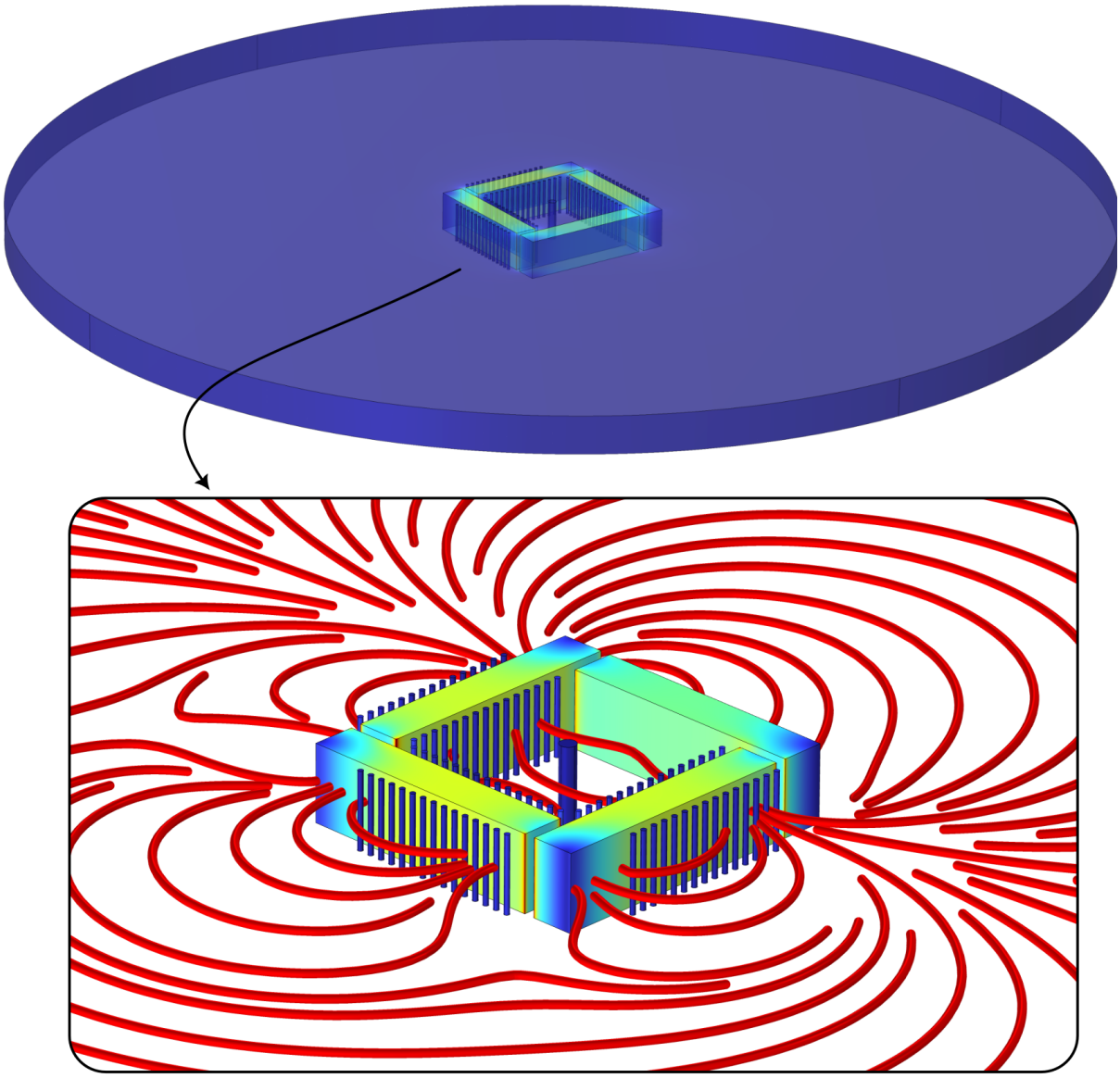

Fig. 4–14 Example of 2D simulation, showing the field distribution extruded to 3D.

As mentioned earlier, four prototypes were manufactured, which corresponded to the winding designs shown in Fig. 4–8. To reduce the influence of parasitic parameters and make the results of different samples more comparable, the number of turns remained constant for all prototypes – only their arrangement along the magnetic core was varied. For the second winding, a rectangular loop passing through the centre of the HFCT and returning at a sufficient distance was used, as shown on Fig. 4–16. For better signal quality, the rectangular coil had several turns. It should be noted that this setup was optimized for measuring the scattering inductance and comparing it with FEA results, and was not intended, for example, to measure the transfer function, although it has a similar structure.

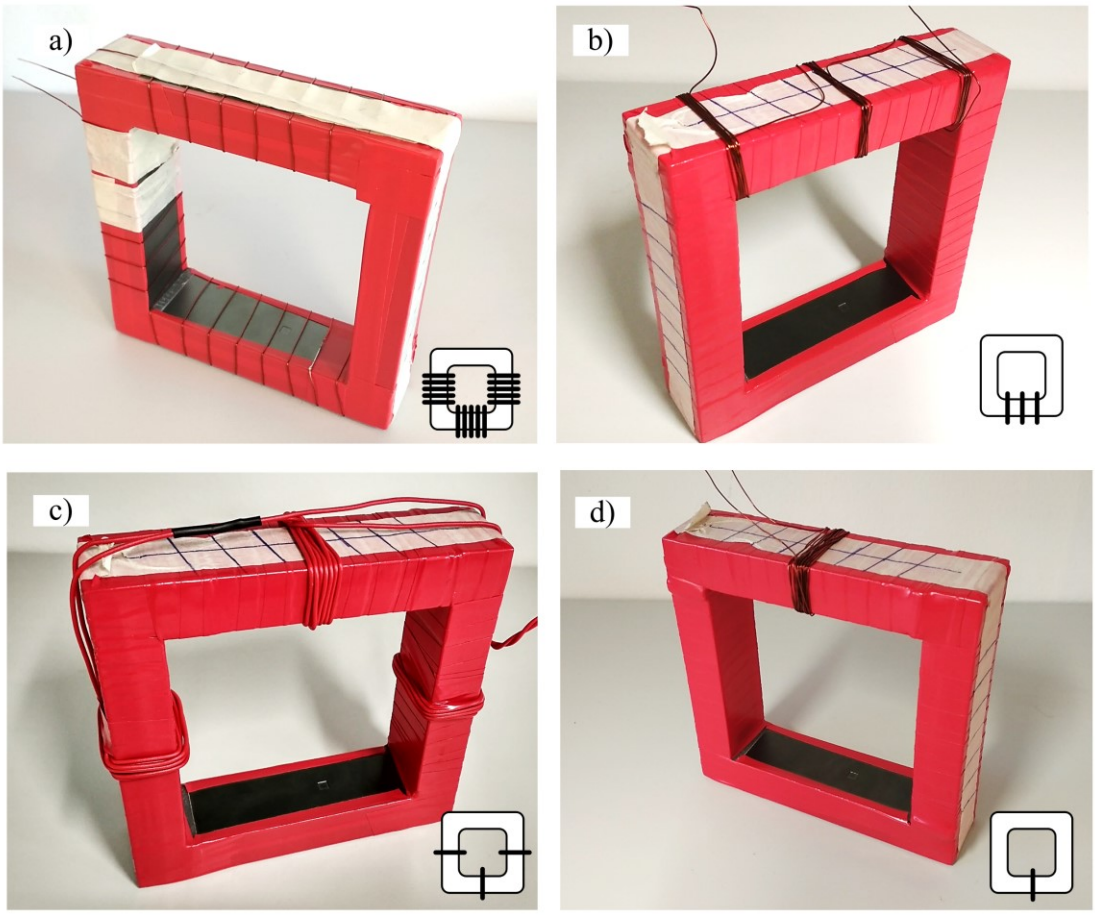

Fig. 4–15 Prototypes for validation of the FEA results.

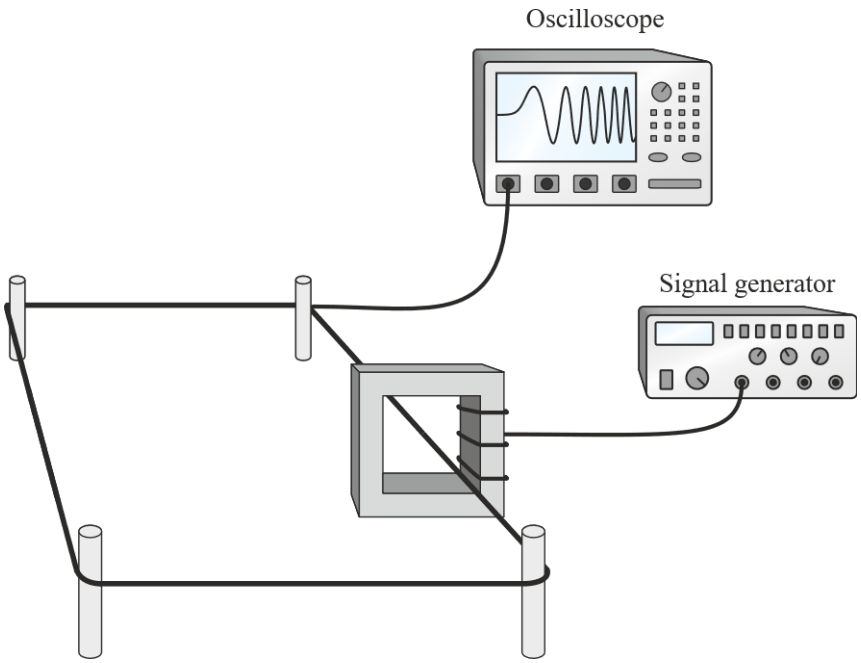

Fig. 4–16 Setup for leakage inductance measurement.

During the measurements, the cables coming to the oscilloscope and signal generator can be swapped to obtain the leakage inductance for the primary and secondary windings. Due to the used geometry, the resonance of the setup starts at relatively low frequencies, as shown in Fig. 4–17, so it is important to take several points and make sure that the measurement is performed at sufficiently low frequencies.

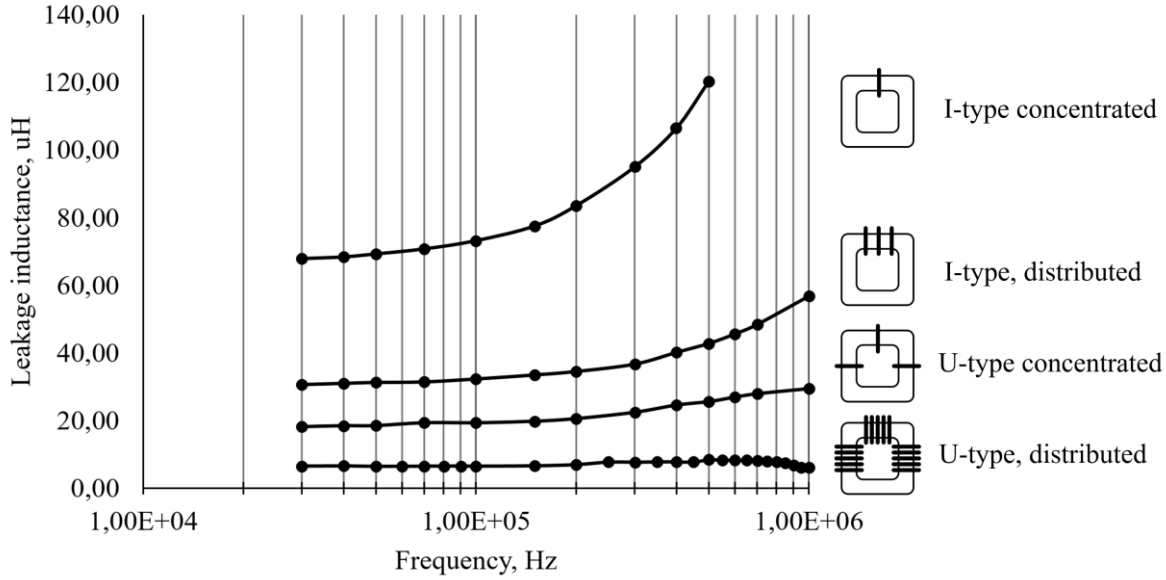

Fig. 4–17 The measured leakage inductance exhibits a frequency-dependent behavior due to the onset of resonance. Therefore, it is important to ensure that the measurement is performed on a significantly low frequency.

Fig. 4–18 compares the obtained values of magnetizing inductance and leakage inductance from the 2D and 3D simulations with the results obtained during the measurement. Let us first consider the 3D simulations and measured data – the first two columns in each column group. It can be seen that the value of magnetizing inductance does not change significantly for different prototypes, since it is mostly determined by the coupling through the magnetic core, which remains unchanged. As expected, the scattering inductance increases as the winding covers less of the magnetic core. Interestingly, variant c) has a lower scattering inductance than variant b), which is somewhat counterintuitive. However, this conclusion is supported by both measurements, and all performed simulations. Overall, comparing the measurements and 3D modelling, a good agreement can be observed. Moreover, it is particularly noteworthy that the modelling accurately reflects the changes in inductances when the winding configuration is altered. Regarding the 2D modelling, the value of the magnetizing inductance matches quite accurately, but the resulting value of the leakage inductance is underestimated. This result is expected and understandable since the field is modelled only for a disk-shaped domain with a thickness of a magnetic core. On the other

hand, for a rough approximation, a correction factor can be introduced. For example, for the samples considered and other samples with different windings that were not included in our description, multiplying the leakage inductance by three gives a result comparable to the experiment and 3D modelling, as shown in the third column in each group in the Fig. 4–18. At the same time, it is intuitively clear why such a coefficient gives the correct result – in addition to the air in the lateral surface of the prototype, the scattering inductance also corresponds to the air volume above and below the core. Of course, this coefficient depends on the ratio of the width and height of the core. In this case, it was equal to two: the height was twice the width, which is a fairly common ratio. Accordingly, if the core becomes higher, this coefficient should decrease. At the same time, it should be noted that most often the width of the core in magnetic devices does not exceed their height.

A similar result can be achieved by increasing the magnetic permeability of the air volume outside the magnetic core by the factor we used to multiply the leakage inductance, in this case by three. The results of this simulation are presented in the fourth column of each group in Fig. 4–18.

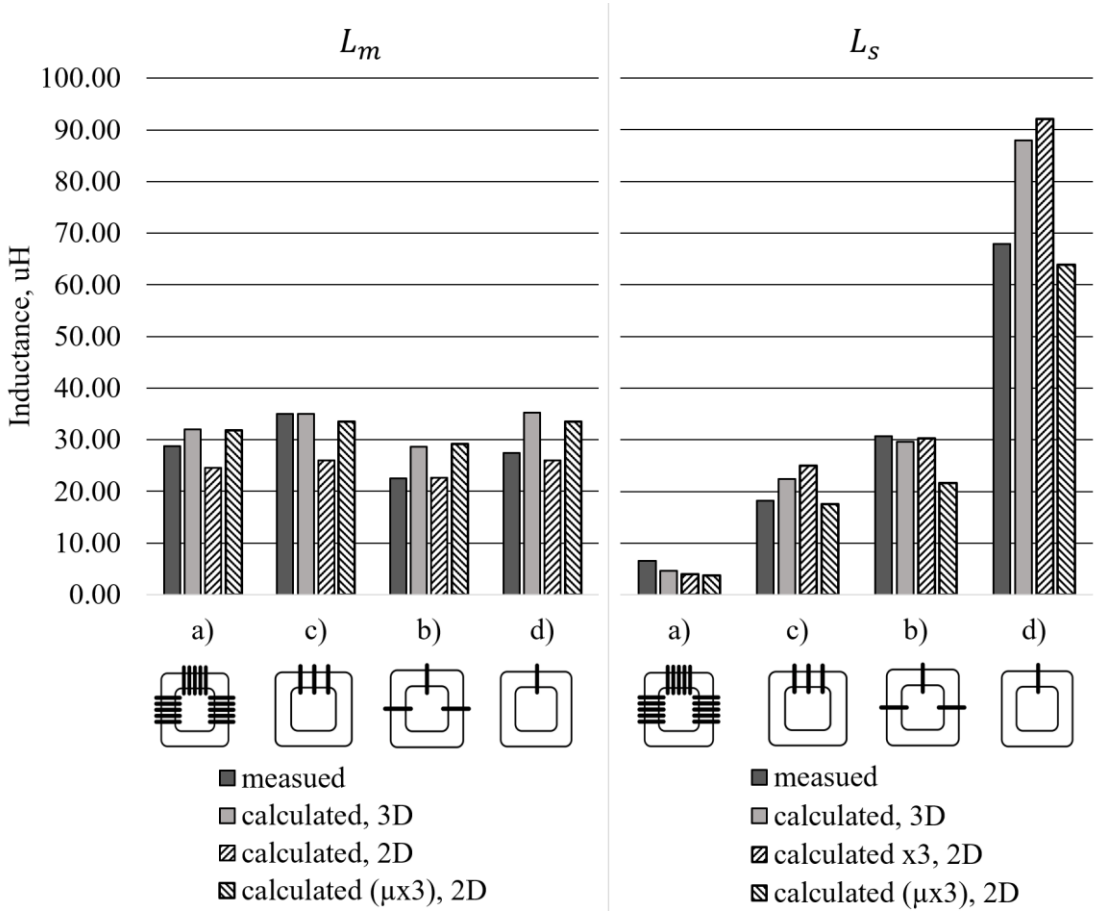

Fig. 4–18 Comparison of magnetizing and leakage inductances for measurements, 3D and 2D simulations.

4.4 HFCT Operation under Biasing Current

Part of the content presented in this subsection I had been published in the article [Pub. 3]. However, here, I would like to include this material for the sake of completeness of the narrative and, firstly, to further supplement it.

In the presence of high-power current magnetic flux in a ferromagnetic core change accordingly to the hysteresis curve. Derivative of the BH-loop defines the incremental permeability, that is determined both by reversible and irreversible magnetization processes. It changes in a wide range comparing to the initial value of about 80 units.

Contrarily, so-called "reversible permeability", resulted by reversible changes only, determines material behavior in a case of small-signal analyses, in other words relates to a change of magnetic flux due to a small change of a current. This topic of "Different inductances" of the same inductive component, is well described in [78].

For a high rated cable current the magnetic flux density $\vec{B}$ and magnetic field strength $\vec{H}$ vectors relate to each other via incremental permeability of the hysteresis curve. Contrarily, reversible permeability μ_{rev} (that determines core behavior for a small PD signal) is a function of induced by a rated current H-field, thus it forms some uneven pattern in the core. Computationally this pattern can be reduced to just one "equivalent" value $\mu_{eq,rev}$ that can be used for core inductance estimation. Small signal magnetization inductance $L_{m,s}$, that is proportional to the equivalent reversible permeability $\mu_{eq,rev}$, influences the lower cutoff frequency:

$$f_{\text{low}} \approx \frac{R_m}{2 \cdot \pi \cdot L_{m,s}}, \tag{4.37}$$

Consequently, as the rated current increases, the $L_{m,s}$ reduces, and the lower cut-off frequency shifts to higher values, thus shortening the bandwidth.

The current transfer function T_i in its flat part is also dependent on $L_{m,s}$:

$$\left|T_{i,flatpart}\right| = \frac{L'_{m,s}}{L'_{m,s} + L'_s}. \tag{4.38}$$

The magnetizing inductance of the core is more affected by saturation than the leakage inductance L'_s. Hence, when a high current leads to a notable decrease in core permeability, the sensitivity decreases. However, the extent of this impact varies based on the winding geometry.

For efficient functioning under superimposed power current, it's essential to incorporate an non-magnetic gap into the core (also referred as “air gap” independently if it is air or any other dialectic material). If the size of this gap is insufficient, the core could be pushed into the saturation zone. Conversely, a gap that is overly large will neutralize this effect, but it will also cause too drastic reduction in inductance. To put it differently, the function $L_m, s = f(\text{air gap})$ doesn't demonstrate monotonic behavior. Instead, it showcases a single global maximum, indicating the optimal gap value that would guarantee maximum small-signal inductance for the chosen primary current.

A quick approximation of the necessary gap size, which bypasses considerations of intricate geometries, employs Ampere's circuital law, it can be demonstrated that the magnetic flux density B_i in the middle of the core:

$$B_i = \frac{\mu_{eff} \cdot \mu_0 \cdot I'}{l_{mid}}, \tag{4.39}$$

In this equation, μ_{eff} represents the effective permeability of the core with a distributed gap, l_{mid} middle line length, and I' denotes the value of the rated cable current. As a result, to avoid core saturation, the effective permeability μ_{eff} must be at a minimum limited to the subsequent value:

$$\mu_{eff} \leq \frac{B_{sat} \cdot l_{mid}}{\mu_0 \cdot I'}, \tag{4.40}$$

The permeability can be approximately calculated with the well-established formula $\mu_{eff} = l_{mid}/\delta$, as long as the magnetic material’s permeability is at least by order larger than μ_0 [17]. Assuming that the operational magnetic flux density should be at least 20% lower than the saturation value, the overall gap δ needed to can therefore be estimated as:

$$\delta \geq \frac{\mu_0 \cdot I'}{0.8 \cdot B_{sat}}, \tag{4.41}$$

To get the first impression, lets calculate the gap for several core-materials if the primary current I' is equal to 3000 A:

- Ni-Zn ferrite, assuming $B_{\text{sat}} = 0.3$ T at least 16 mm gap would be required,
- Mg-Zn ferrite, assuming $B_{\text{sat}} = 0.45$ T $\rightarrow$ at least 10 mm,
- Amorphous steel, assuming $B_{\text{sat}} = 1.5$ T $\rightarrow$ at least 3.1 mm,
- Silicon steel, assuming $B_{\text{sat}} = 1.9$ T $\rightarrow$ at least 2.5 mm,

It should be noted that this calculation provides a lower bound for the clearance gap, and furthermore, it is important to consider that with such relatively large clearances, fringe flux

will play a significant role in shortening the effective gap distance. Therefore, the actual clearance gap should be further increased.

The optimal air gap can be iteratively adjusted during the prototyping process, which is convenient for small-scale devices like HFCTs. On the other hand, in more complex configurations, one can resort to solving such optimization problems through FEA simulations.

The case of superposition with a DC is known in the literature as “biasing” of a magnetic core. This widely implemented technical solution is described in numerous publications [78] – [82]. The physics of this process aligns with the scenario of sensor placement on an HVDC cable. Taking the HFCT as an example, we will demonstrate how FEA modeling can be conducted to address this issue, which may be relevant for other inductive devices as well.

The major goals of the simulation are:

- Finding the optimum air gap,
- Estimating the change of the transfer function under the influence of the rated cable current (sensitivity drop and shift of the low corner frequency).

The theoretical side of the procedure can be described in the following way: Initially, the core is “energized” to a certain operational point at the main magnetization curve. The resulting pattern of magnetic field strength in the core establishes the reversible permeability at each point of geometry, which in turn determines the small-signal inductance and the corresponding transfer function experienced by the coupled signal.

The first choice in the simulation model development is the number of dimensions and the type of the coordinate system.

As discussed earlier, it is possible to simulate HFCT geometries on a standard PC within EM tasks, though this method poses challenges. Preparing a 3D model typically requires an additional CAD program, which is a time-consuming process, especially when realistically depicting the winding or simplifying it. Furthermore, the 3D simulation itself, particularly with a parameter sweep, can be lengthy. In contrast, 2D modelling avoids these issues and its limited accuracy is satisfactory for this study, hence the choice of the 2D approach.

The study was conducted using the COMSOL Multiphysics [77]. The model's geometry is shown in Fig. 4–19. This simulation was performed for a prototype that had a distributed

gap – here, the magnetic core is comprised of multiple rectangular ferrite plates separated by small non-magnetic gaps. Some of the other model-building features are:

- The winding turns are uniformly distributed across the magnetic core,
- The "out-of-plane thickness" is set to match the respective thickness of the core,
- The same approach for modelling the winding, as described in the previous section, was employed: The wire cross-sections on the core's inner side carry current of equal magnitude but of opposite polarity compared to the outer cross-sections.
- Two data-sheet plots are imported as interpolated functions: namely, the initial magnetization B-H-curve and the dependency of reversible permeability on magnetic field strength $\mu_{\mathrm{rev}}(H)$.
- An important additional feature is the “material switch”, that applies appropriate constraint – B-H-curve or $\mu_{\mathrm{rev}}(H)$ – to the magnetic core material. Different material properties require appropriate nodes in the physics setup, and therefore divide the study into two simulations: the high-signal and small-signal cases, as it is shown in Fig. 4–20.

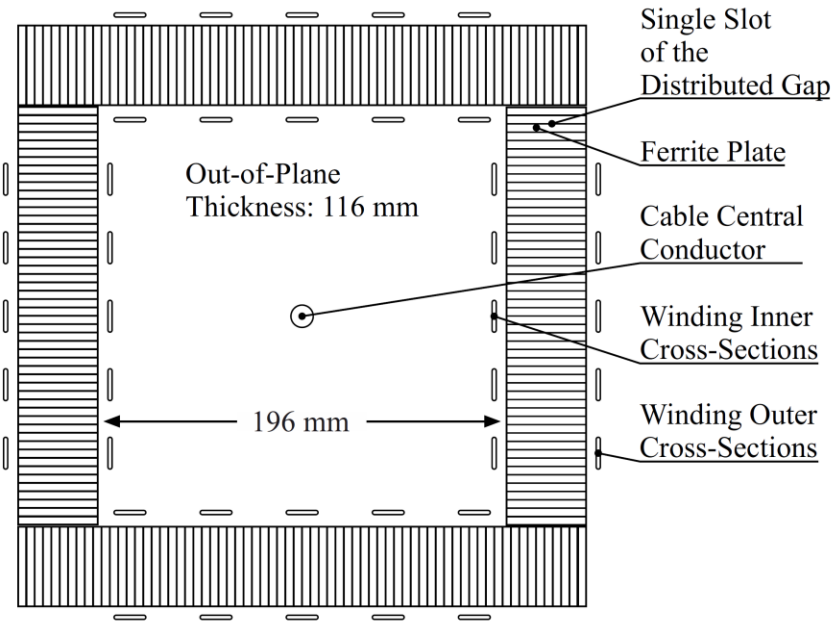

Fig. 4–19 Model geometry for the FEA simulation, reused from [Pub. 3]

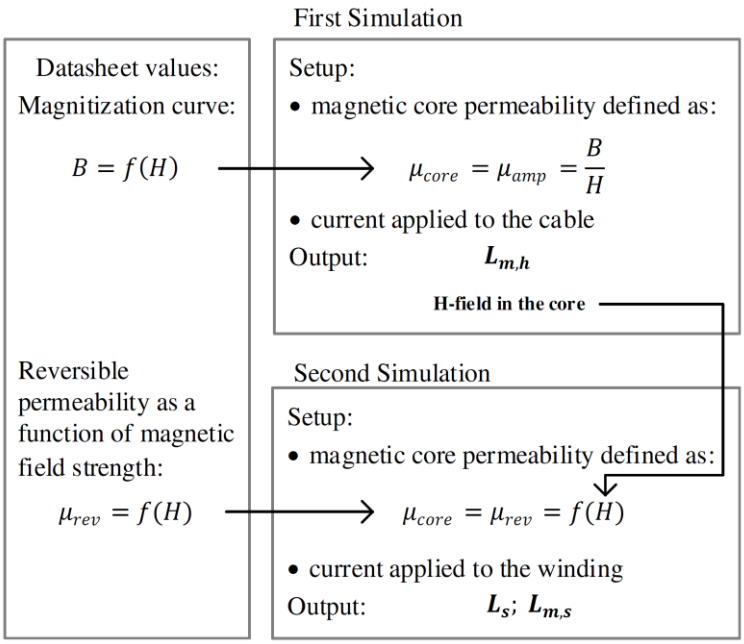

Fig. 4–20 FEA study description, reused from [Pub. 3]

Let's further elucidate the simulation pipeline shown in Fig. 4–20. In the first step of the simulation, the core is magnetized by the chosen rated cable current. The high-signal inductance of the core can be obtained at this stage as the by-product. The distribution of the H-field over the core is transferred to the subsequent simulation, which determines the mutual small-signal inductance between the winding and the cable. At this point the leakage inductance can be derived in the same way as was described in the section 4.3. This procedure is run within two parameter sweeps: for the superimposed current and for the size of the air gap. The key definitions of the physics setup are consolidated in Table I.

Table 2 Physics Setup in COMSOL for saturation modelling, reused from [Pub. 3]

Geometric Entity	**Physics 1: Magnetic Fields (mf)**	**Physics 2: Magnetic Fields (mf)**
Magnetic Core	Node "Ampere's Law" (Constructive Relation: "B-H-curve")	Node "Ampere's Law" (Constructive Relation: "Relative Permeability")
Cable Central Conductor	Node "Coil" ("Single Conductor", coil current: rated cable current)	Node "Coil" ("Single Conductor" coil current: 0 A)
Inner Winding Cross-sections	Node "Coil" ("Homogenized Multi-turn", coil current: 0 A)	Node "Coil" ("Homogenized Multi-turn", coil current: 1 A)
Outer Winding Cross-sections	Node "Coil" ("Homogenized Multi-turn", coil current: 0 A)	Node "Coil" ("Homogenized Multi-turn", coil current: -1 A)
Distributed Gap	Node "Thin Low Permeability Gap"	

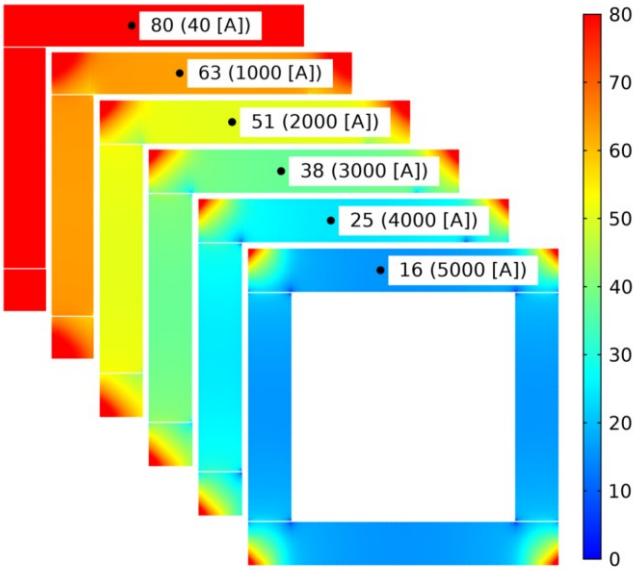

Fig. 4–21 Reversible permeability pattern in the magnetic core, reused from [Pub. 3]

The upper subplot of the Fig. 4–22 presents the relationship among the small-signal inductance, total distributed gap value, and DC biasing current. The lower subplot of the same figure showcases the optimal gap specifically chosen for a DC biasing current of 2500A.

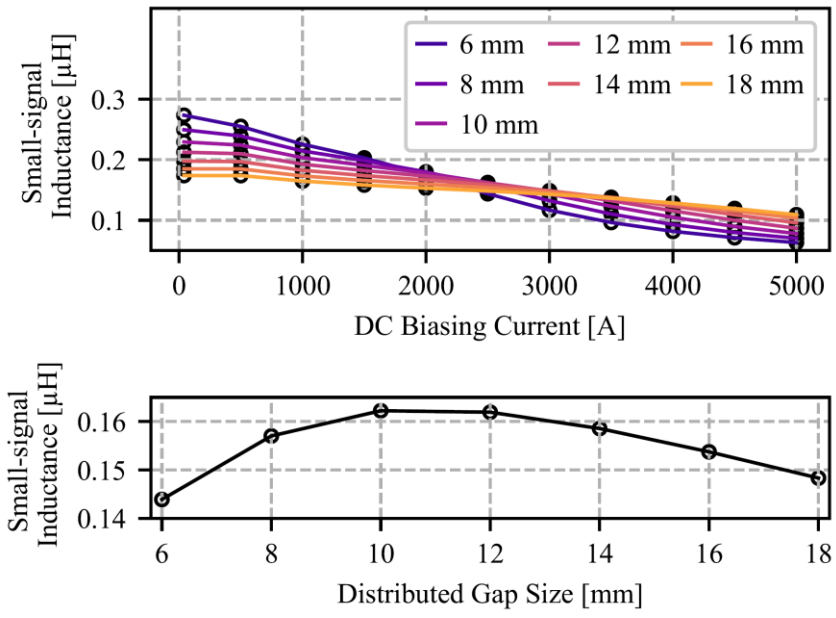

Fig. 4–22 Dependencies between small-signal inductance and the total distributed gap, reused from [Pub. 3]

The upper plot of Figure 8 illustrates the change in the transfer function magnitude as the cable current increases, calculated according to equation (2). The noticeable shift of the corner frequency, which can also be estimated using equation (4), is further displayed on

the lower subplot. This effect is also clearly shown in the experiments presented in chapter 4.7, which involved measuring the transfer function during the superposition of power current on cores of various materials.

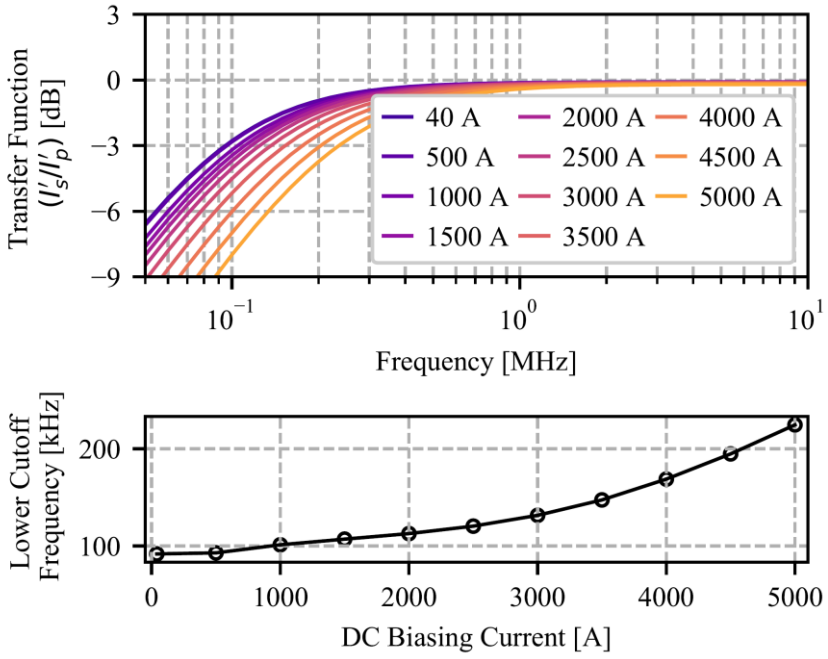

Fig. 4–23 Influence of the DC biasing current on the transfer function (top plot) and the lower cut-off frequency (bottom plot) for the selected distributed gap of 12mm, reused from [Pub. 3]

4.5 Balanced Design

Fig. 4–24 shows a common design and connections of HFCT feeding the amplifier. A metallic housing surrounds the winding and has a gap so that not to form a closed loop (in the plain of the draft, not shown) – it is a common solution implemented for two reasons: to provide mechanical solidity and to shield external noise. The screen is connected to one end of the winding and to the shield of outgoing coaxial cable.

The problem of such design is a poor noise damping. Here, we can distinguish two cases: when the HFCT housing is additionally grounded with a short line (when the switch in the Fig. 4–24 is closed), and when it is grounded only through the cable shield (switch open).

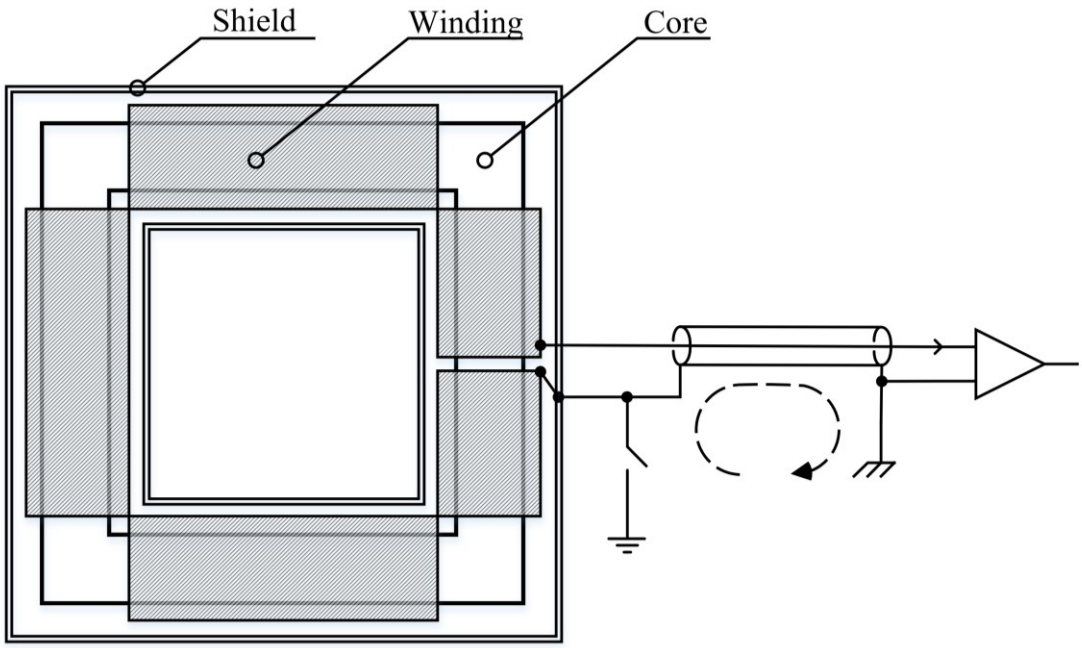

Fig. 4–24 A common connection between an HFCT and an amplifier.

In the first case, grounding the cable shield on both ends (amplifier and HFCT side) creates a current loop that couples with the magnetic component of EM noise, as shown on Fig. 4–25a. Induced current I_s causes a voltage drop on the shield resistance R_s – consequently, on the input of the amplifier occurs the noise with magnitude:

$$V_{in} = R_s I_s. \tag{4.42}$$

Additional noise can be introduced by the difference in the ground potentials on different ends of the cable [173].

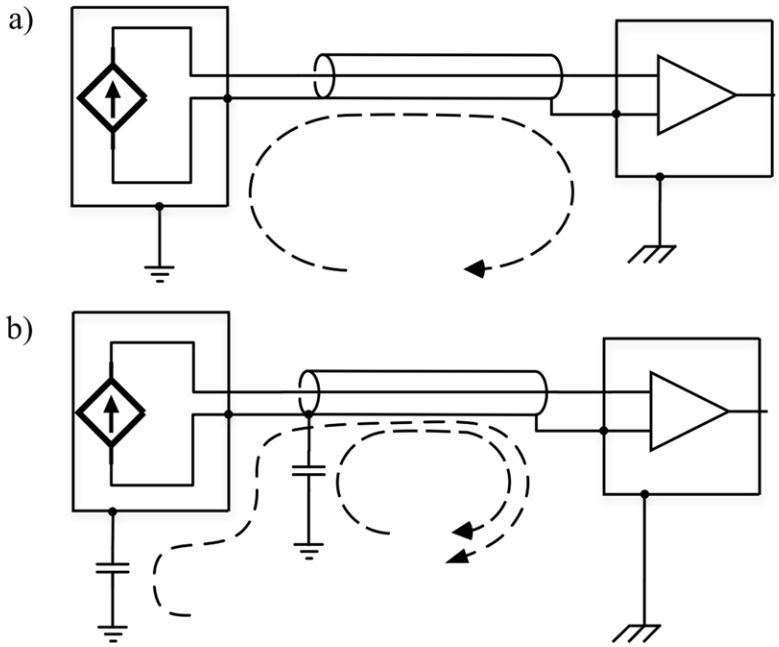

Fig. 4–25 Currents circulating through the cable screen.

The second case, single-point grounding, depicted in Fig. 4–25b, does not eliminate the problem. Here, I would quote a well-known book on the subject by H. Ott [173]:

> "Even if the shield is grounded at only one end, shield noise currents may still flow due to capacitive coupling to the shield. Therefore, for maximum noise protection at low frequencies, shield should not be one of the signal conductors, and one end of the circuit must be insulated from the ground."

Extremal length of the cables that should be used in our case (about 10 meters), additional HFCT screen and desired frequency bandwidth up to 10 (or 20) MHz insures high impact of such noise. State of the art PD measuring systems, however, negotiate this rule and use the single BNC connectors and coaxial cables.

Balancing – is a well-known method of noise reduction. The definition and main idea of balancing are concisely addressed in the aforementioned book [173]:

> "A balanced circuit is a two-point conductor circuit in which both conductors and all circuits connected to them have the same impedance with respect to ground and to all other connectors. The purpose of balancing is to make the noise pickup equal in both directions, in which case it will be a common mode signal, which can be made to cancel out in the load."

Based on the considerations described above, I have decided to apply the idea of balancing to the design of the HFCT. Principal draft is shown below in the Fig. 4–26. The main difference from the common design is that the middle point of the winding is connected to the shield and grounded – this way the output of HFCT becomes balanced.

Balanced HFCT should be connected to the signal-acquiring unit by a balanced transmission system, in the final design this role was fulfilled by the twinaxial cable.

The working principle can be explained as follows: The impedance of two winding sides sensed by the noise in the screen of HFCT and cable is equal, thus the noise current injected on both sides of the balanced system is the same. As the differential amplifier is used to pick up the signal, this common-mode noise will be rejected.

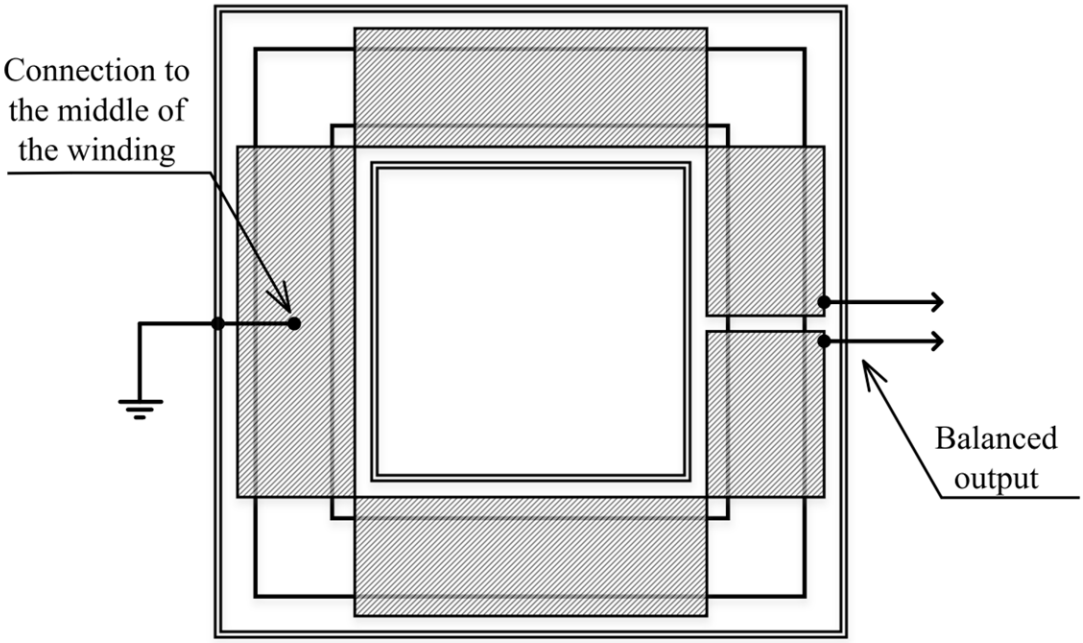

Fig. 4–26 HFCT balanced design

In this particular implementation of grounding connections, exists a certain volatility. For example, the additional grounding of the screen, depicted in gray on the Fig. 4–27, can have both positive and negative effects. On one hand, such grounding closes the earth loop, resulting in an increased induced current. However, it should be noted that this current will be common-mode. On the other hand, when there is no such grounding and the HFCT is grounded only through the cable screen, the high frequency noise collected by the HFCT screen senses the changing characteristic impedance of the cable screen, especially at resonance frequencies. This becomes particularly relevant considering the potential length of these cables.

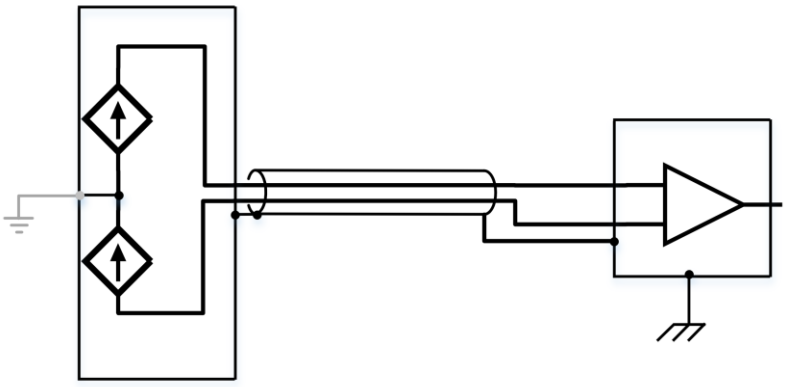

Fig. 4–27 Connection between the balanced HFCT and the differential amplifier.

4.6 Resonant behavior of HFCT

In general, the resonance behavior of HFCT is rarely studied and seldom presented in a clear manner. As mentioned earlier, many articles tend to avoid this topic. Therefore, it would be beneficial to illustrate the resonance behavior of HFCT, which we will do below.

4.6.1 Basic information

As mentioned earlier, the resonant behavior of HFCT is primarily an EM wave resonance, in the meaning that the wavelength of the EM wave is comparable to the size of the dimensions of the device, and wave propagation delay (or phase) cannot be ignored. Moreover, here we are talking not about the wavelength in a vacuum, but rather the wavelength in the magnetic core. Unlike the Rogowski coil, in HFCT a magnetic core is used, and the EM wave in it gets slower and shorter, as shown by Eqs. (4.43) and (4.45):

$$v_{medium} = \frac{1}{\sqrt{\bar{\mu}\bar{\varepsilon}}}, \tag{4.43}$$

$$\bar{k} = \frac{2\pi}{\lambda} = 2\pi f\sqrt{\bar{\mu}\bar{\varepsilon}}\,, \tag{4.44}$$

$$\lambda = \frac{1}{f\sqrt{\bar{\mu}\bar{\varepsilon}}} = \frac{c}{f\sqrt{(\mu_r{}' - j\mu_r{}'')(\varepsilon_r{}' - j\varepsilon_r{}'')}}, \tag{4.45}$$

where $\bar{\mu}$ and $\bar{\varepsilon}$ are the complex absolute permeability and permittivity of material, whose relative values are denoted as $\bar{\mu}_r = \mu_r{}' - j\mu_r{}''$ and $\bar{\varepsilon}_r = \varepsilon_r{}' - j\varepsilon_r{}''$.

Strictly speaking, the resonance of behavior of HFCT can be simulated by the means of FEA and the COMSOL provides corresponding modules for such calculations. Generally speaking, in COMSOL, the resonance of an inductive element can be calculated in several modules: “ Electromagnetic Fields” (EMF), "Magnetic Fields" (MF), and in the "Radiofrequency" (RF) module. The EMF module is usually used for low-frequency applications when the skin effect is not very pronounced, and the current flow is modelled within the conductive domains. In the MF module, on the contrary, is meant for the higher frequencies. There the current inside the flux-inducing conductor will no longer be modelled – its geometrical domain is drawn, but since the current flows only on the surface of electric conductors, the conductor domain itself is excluded from the calculation. It would be incorrect, however, to assume based on the module's name that only magnetic fields are modelled in the MF module. This is indeed the case for stationary calculations, but in the frequency domain, a varying magnetic field generates a varying electric field during simulation, and the same is valid for the EMF module. The difference between the EMF and

MF modules lies in the fact that the scalar electric potential V is not included in the formulation of the electric field intensity E in the MF module. Let's compare the definitions of the fields as they are formulated in the EMF module:

$$B = \nabla \times A, \tag{4.46}$$

$$E = -\nabla V - j\omega A, \tag{4.47}$$

and MF module:

$$\boldsymbol{B} = \nabla \times \boldsymbol{A}, \tag{4.48}$$

$$\boldsymbol{E} = -j\omega \boldsymbol{A}. \tag{4.49}$$

When solving an electrostatic problem, in the corresponding "Electrostatics" module, the field is defined as:

$$\boldsymbol{E} = -\nabla V \tag{4.50}$$

In the case of EMF, the electric field is generally a superposition of the electrostatic field from the "Electrostatics" module and the vortex field from the MF module.

Since both the electric and magnetic fields are modelled in the EMF and MF modules, the resonance can be calculated in both modules. Regarding the HFCT, simulation of resonant behavior is to some extent shown in the article [61]. Here, the choice of the appropriate module for simulation is also discussed: whether it should be MF or RF. The actual choice of the module within this article was based on EM wave wavelength. The RF module was preferred when:

$$L_c < \frac{\lambda}{100}, \tag{4.51}$$

where L_c is the characteristic length of the object. The article does not directly mention wavelength in what medium is meant, but from the context, one can assume that the overall size of the model was compared to the wavelength in free space. It can be easily calculated that at the given material parameters and a frequency of 1 MHz, the wavelength in the magnetic core will be about 1.2 meters. However, the MF module is still used, indicating that the choice of module was based on the wavelength in free space rather than the wavelength in the core material.

4.6.2 Stray capacitance of HFCT winding

In addition to this article, modelling, or calculation of the HFCT with a magnetic core self-resonance is usually mentioned briefly. There are publications that relate its resonance to the aforementioned static inter-turn capacitance, such as [60], [83], [86], and [85]. However, it can be shown how little influence the static inter-winding capacitance (and related coil geometry, distance between turns, progressive winding pitch, etc.) have on the HFCT

resonance. To demonstrate this, two prototypes shown in left side of Fig. 4–28 Setup and samples for evaluating the influence of winding-to-core distance. were used. Here, a square core was assembled from four N87 ferrite blocks from Epcos AG. The winding was placed on one side of this core only. Two samples of winding-on-a-core were made, which differed in the distance from the winding to the magnetic core (1.6 mm and 3.2 mm). The ferrite itself has a relatively low electrical resistance, so the total inter-winding capacitance is largely determined by coupling through magnetic core. The number of windings (68, 50, 20) was also varied for these samples, and the corresponding resonant frequency was measured for all configurations. It is important that the resonance occurred at relatively low frequencies (up to 1 MHz), where the effective magnetic permeability remained approximately constant. The measurement was performed using a low-capacitance (1.8 pF) active probe, a signal generator, and a common oscilloscope.

Fig. 4–28 Setup and samples for evaluating the influence of winding-to-core distance.

The solid lines on Fig. 4–29 show the apparent stray capacitance, calculated from inductance and resonant frequency also taking in account the capacitance of the measurement channel. The capacitance of the generator itself is not known, and therefore is not taken into account directly, but it should not change the presented results and conclusions made. When the number of turns is large, we indeed can see some dependence on the distance to the magnetic core and the resulting parasitic capacitance: the smaller spacer leads to the higher capacitance. However, this dependence disappears when the number of turns is small. In addition, the apparent parasitic capacitance significantly increases with a small number of turns. The dashed lines on the same graph represent the static parasitic capacitance calculated in COMSOL. Although the inter-turn capacitances are connected in series in the equivalent circuit, their overall coupling through the core increases the total capacitance with a larger number of turns. However, we can note that with a small number of turns, the

gap between the apparent parasitic capacitance and the calculated static capacitance increases, and the latter's contribution to the resonance is minimal.

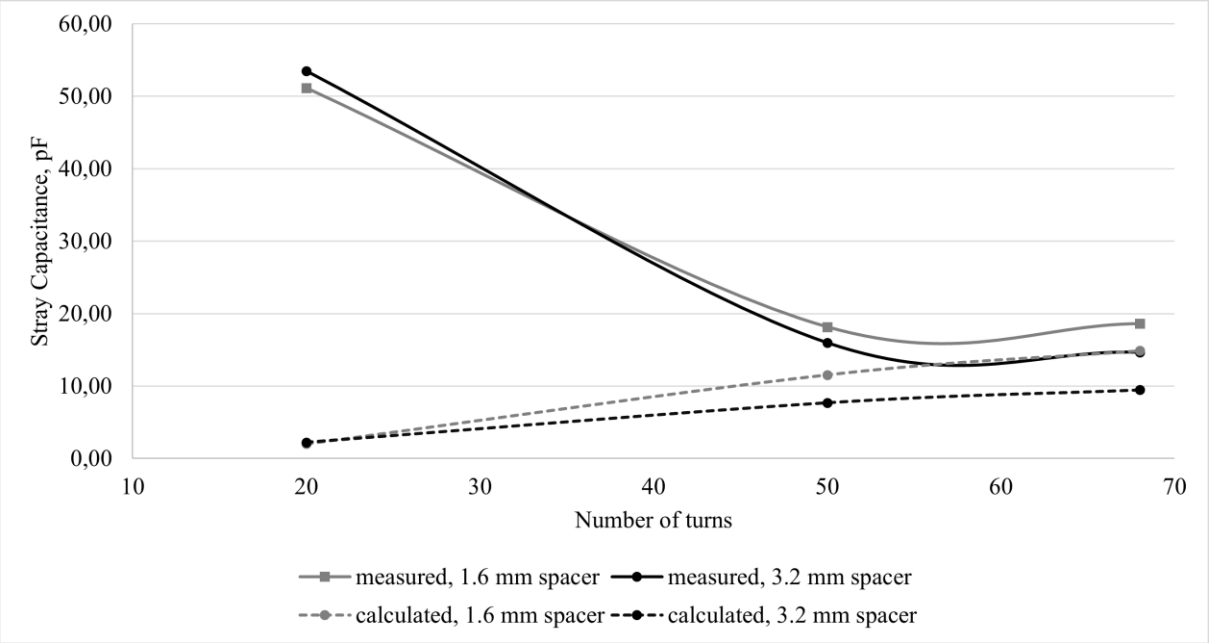

Fig. 4–29 Dependence of the apparent stray capacitance on the distance to the core.

Since we have touched upon the calculation of HFCT winding static capacitance in COMSOL, let us say a few words to wrap up the topic.

Calculating static capacitance can be done using 3D and 2D simulations. In 3D, such calculation practically takes no time as the Electric Currents module is used in stationary mode. Terminal and ground boundary conditions are assigned to winding terminals and a floating potential to the core in order to get the voltage distribution over the winding and subsequently evaluate the capacitance from the electric field energy.

In 2D, we see a section, or rather a projection, of the core in 2D space (Fig. 4–30): for capacitance calculation the depth of the simulated plane is equal to the perimeter of one turn. The result of such a calculation will be a matrix of inter-turn capacitances and reducing it to a single lumped capacitance would be incorrect. However, we to simulate resonance based purely on static parameters – and just to present the case the according procedure is shown below. Such simulation has to be split in two models. In the electrostatics interface (Fig. 4–30), a Maxwell capacitance matrix can be obtained. Via the MFs module (Fig. 4–31), we obtain a matrix of self and mutual inductances of turns in the same way as was explained in the section that concerned leakage inductance evaluation. With the use of an

axillary script these matrices can be converted into a netlist that is imported into any of the SPICE-based programs to calculate the resonance and resulting "apparent" capacitance.

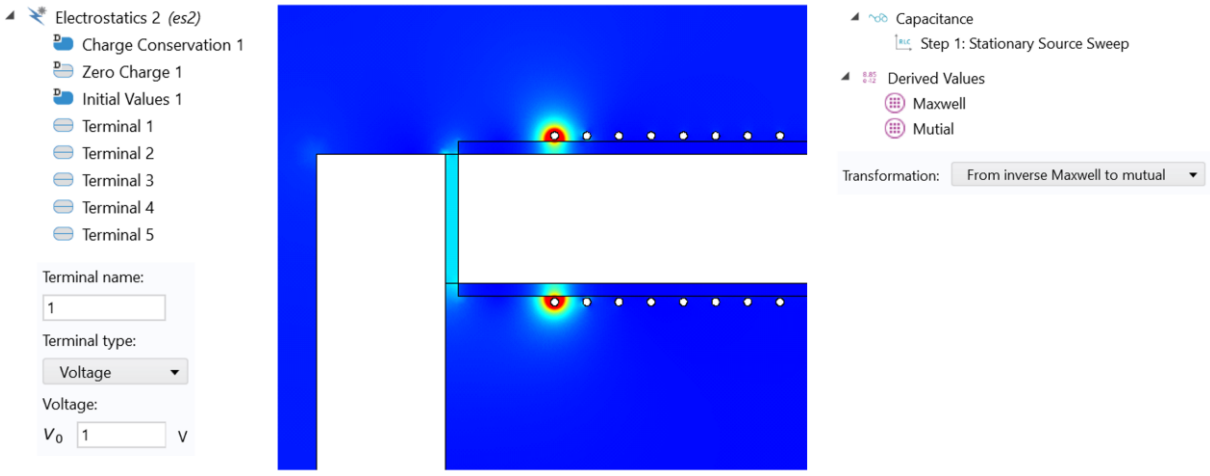

Fig. 4–30 Electrostatics simulation setup

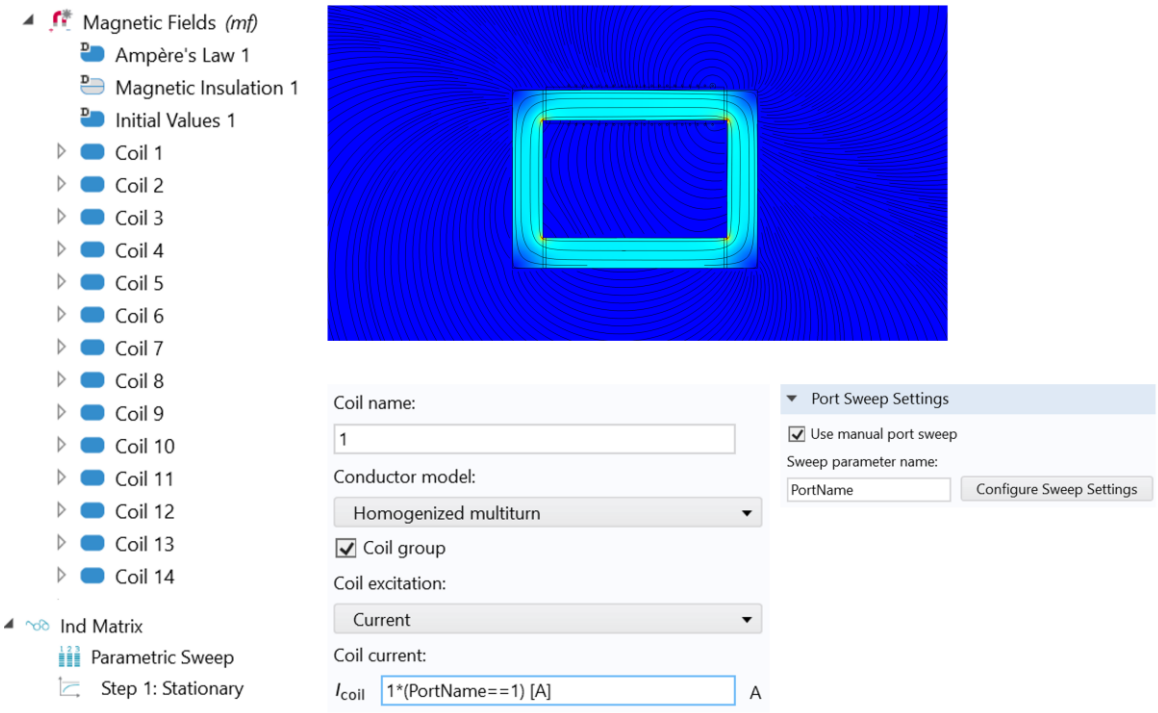

Fig. 4–31 Magnetic Fields simulation setup

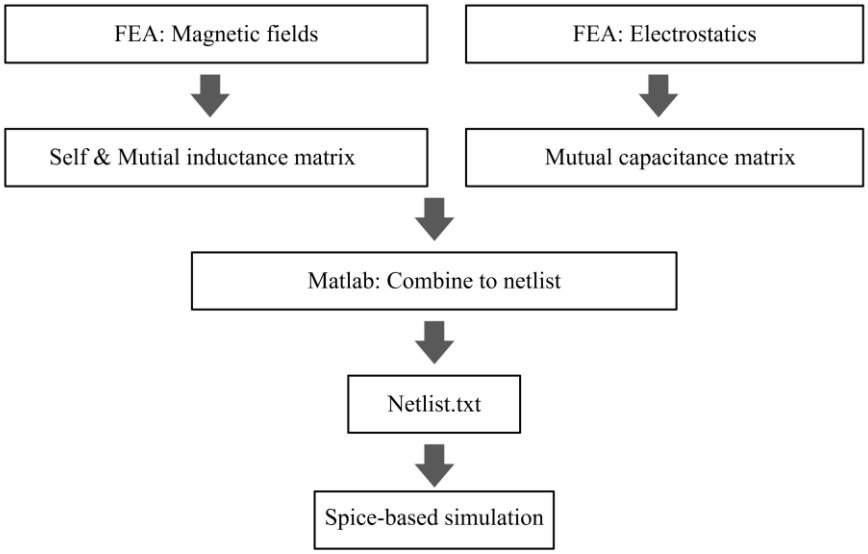

Fig. 4–32 Simulation Pipeline

4.6.3 Dimensional Effects in the Core of HFCT

For cases of coil without a core (helical antennas), there do exist formulas that allow approximate calculation of the resonant frequency based on the coil geometry: length, width, and winding pitch. This is best described, for example, in the works of [87] and [88]. The elementary idea is based on the fact that EM waves propagate along a metal wire with a speed close to the speed of light in a vacuum. Thus, it can be assumed that this property is also preserved for a wire coiled in a helix. Accordingly, along the axis of the spiral, the propagation of the wave is slower by a factor determined only by the geometry of the spiral and not dependent on frequency. A more accurate theory is based, for example, on replacing the spiral with a thin-walled cylinder, in which the conductivity in the direction of the spiral line is sufficiently high and is equal to zero in the direction perpendicular to it. This assumption is sufficient to obtain a solution in the form of a slowed-down wave [89]. The exact theoretical consideration can be found in [92], [91], but for now, we will use the simple representation described above. The calculation is usually carried out based on the condition of recalculating the phase velocity along the axis of the helical antenna. For example, in [90] and [88], the velocity factor of this wave can be calculated as follows:

$$v_{\mathrm{f}} = \frac{1}{\sqrt{1 + 20\left(\frac{D}{s}\right)^{2.5}\left(\frac{D}{\lambda_0}\right)^{0.5}}}. \tag{4.52}$$

where *s* is the space between adjacent turns, D is a helix diameter and λ_0 is a wavelength in a free space. The resonance takes place when the height of the helix matches the integer number of quarters of wavelength of in this way "slowed" wave. With a few substitutions and approximations, the self-resonance frequency is defined as:

$$f_0 = \frac{K}{nD}\left(\frac{H}{D}\right)^{0.2}, \tag{4.53}$$

where numeric value for K can be calculated as:

$$K = \frac{c}{\sqrt[5]{400}} \cdot R^{\frac{4}{5}} = 90.51 \cdot R^{\frac{4}{5}}, \tag{4.54}$$

where R is the resonance mode. For a halfwave resonator, R is 1/2, 1, 3/2, 2, etc, and for a quarter wave resonator, is 1/4, 3/4, 5/4, 7/4, etc.

Article [93] provides a good analogy for understanding the effect of external capacitances/inductances on the resonant frequency of a helical coil.

If we consider purely empirical formulas, the study in [94] was conducted on a series of samples. There the self-capacitance can be found using the formula:

$$C_{self} = H \cdot D, \tag{4.55}$$

where D is the diameter of the coil (in cm); H is a coefficient that characterizes the coil's form factor, which was presented as a table and varies from 0.47 to 5.80. In the case where the ratio between the length of the solenoid and its diameter is between 0.5 and 2, this formula can be reduced to a simple empirical rule: the self-capacitance of a single-layer coil in pF is approximately equal to the winding radius in cm.

As for coils with magnetic cores, the most comprehensive work is probably the one by Skutt [95]. Here, the distribution of the field in the magnetic circuit at high frequencies is associated with the cumulative effect of two phenomena: the reduction of the wavelength in the medium leading to spatial resonance and the skin effect of the magnetic field. This conditional division is related to the influence of two material characteristics: electrical conductivity for the skin effect and dielectric permittivity for spatial resonance.

Regarding the skin effect, the picture is quite simple: the magnetic field in the core generates eddy electric currents, which in turn generate a magnetic field that is opposite to the main field in the centre of the magnetic circuit. As a result, the field is pushed out of the centre of the magnetic circuit, which for some applications can be regarded as the decrease of effective cross-section. The conductivity of Mg-Zn ferrites is quite high leading to the high induced currents are large and the skin effect being pronounced already when approaching the megahertz range for cross-sections with widths greater than one centimetre. In this

regard, certain questions arise regarding the FEA simulation carried out in [61], where the ferrite is modelled with zero conductivity.

In the case of dimensional resonance, a standing wave is observed in the material. Although there may be several resonance modes in a three-dimensional core, in the work of Skutt [95] and in many others the main focus is on the wave that fits within the cross-section of the magnetic core. The object of study itself contributes to this: in the majority of works the dimensional resonance is studied in the context of Mg-Zn ferrites. It is not surprising, since these materials are widely used in power electronics, and therefore require careful research to optimize their parameters in the conditions of mass production of devices containing them. Mg-Zn ferrites have a certain set of basic parameters that determine their resonant behavior, namely high magnetic permeability, dielectric permeability, and electrical conductivity. This set leads to a pronounced skin effect even at approaching the megahertz range, and to spatial resonance in the cross section of the magnetic core - the main influence is played by the pronounced mode developing in the cross-section of the core: magnetic field at the edges of the magnetic core and in the middle of it start to be directed oppositely, so that the resulting magnetic flux approaches zero.

Dimensional resonance of cores is studied for toroidal samples [96], as well as for other geometries [97], [98], and infinite stubs in Skutt's [95]. However, it is most commonly studied for the material itself, without the influence of a winding. However, to study the HFCT resonant behavior, it is necessary to move away from the "core in a vacuum" approach.

We will conduct 3D modelling based on data for two magnetic core materials. The first material will have characteristics described in Skutt's work [95], primarily reflecting the properties of Mg-Zn ferrites, namely high conductivity, magnetic and dielectric permeability. For the second material, we will take the Ni-Zn ferrite used for more high-frequency applications. The resistance and real part of the dielectric permeability data for this material are taken from [99], and the complex permeability data is based on the specification of Ferroxcube's 4F1 ferrite [100]. The final parameters are reflected in Table 1 and Table 2.

Table 3 Properties of the “Ni-Zn” material used for FEA simulations.

Frequency	μ_r'	μ_r''	ϵ_r	σ_{eff}
10 kHz	80.0	0.0010	50.0	1.01E-05
100 kHz	80.0	0.0010	36.2	1.10E-05
200 kHz	80.0	0.0011	33.4	1.20E-05
500 kHz	80.1	0.0017	27.9	1.51E-05
1 MHz	80.3	0.0038	25.0	2.00E-05
2 MHz	81.0	0.0122	22.6	2.94E-05
5 MHz	82.9	0.0708	17.6	5.60E-05
10 MHz	87.6	0.2780	15.0	1.00E-04
20 MHz	95.3	1.1007	14.2	1.94E-04
30 MHz	105.9	5.7876	13.6	2.91E-04
40 MHz	119.6	19.392	13.1	3.90E-04
50 MHz	122.7	57.417	12.7	4.91E-04
60 MHz	110.3	85.093	12.5	5.93E-04
70 MHz	78.8	101.18	12.3	6.95E-04
80 MHz	49.5	107.52	12.1	7.97E-04
90 MHz	33.7	110.32	12.1	8.99E-04
100 MHz	21.7	109.69	12.0	1.00E-03
130 MHz	9.2	101.73	11.8	1.30E-03
200 MHz	3.0	74.240	11.5	2.00E-03
300 MHz	1.8	46.187	11.1	3.00E-03

Table 4 Properties of the “Mg-Zn” material used for FEA simulations.

Frequency (Hz)	μ_r'	μ_r''	ϵ_r	σ_{eff}
10 kHz	2000	10	202000	0.173
100 kHz	1833	126	130000	0.349
200 kHz	1802	146	116000	0.483
300 kHz	1822	196	109000	0.599
400 kHz	1845	270	105000	0.705
500 kHz	1863	362	101000	0.807
600 kHz	1864	475	99100	0.906
700 kHz	1842	596	97400	1.010

The relationship between the complex dielectric permittivity ϵ and conductivity σ is established through the following equation:

$$\tan \delta_e = \frac{\epsilon''}{\epsilon'} = \frac{\sigma}{\omega \epsilon'}, \tag{4.56}$$

$$\epsilon'' = \frac{\sigma}{\omega}. \tag{4.57}$$

In the simulation, the dielectric permittivity is set as a real value, while its imaginary part is represented by the conductivity.

We will start with a simplified case, that lies close to the aforementioned researches there the core was studied on its own. Due to the peculiarities of the boundary conditions imposed in COMSOL, the excitation of the core is easiest to implement by simplifying the winding to a cylindrical "turn" covering the core with a small gap between them – as is shown on Fig. 4–33. The calculation itself is interesting to carry out in the frequency domain to have a complete picture of the field distribution for different frequencies and phases. It should also be noted that for the unambiguous solution of the resonant pattern, the coil is displaced relative to the magnetic circuit for some small distance, which is not noticeable at first glance, but is important for confident convergence. The solution will be performed in the EMF module.

The final geometry is shown in Fig. 4–33, where we see two rings with rectangular cross-sections. The inner ring is the magnetic core. The outer surface of the larger ring, except for one side, is modelled as an ideal conductor. The resulting domain covering the inner ring models air – for calculation it is necessary to have some dielectric insulation between the conductive magnetic core and the current-carrying layer of the outer ring. Excitation is performed through a Lumped Port condition applied to one of the side surfaces of the outer ring. This boundary condition applies a uniform electric field between two perfectly conductive surfaces of the ring.

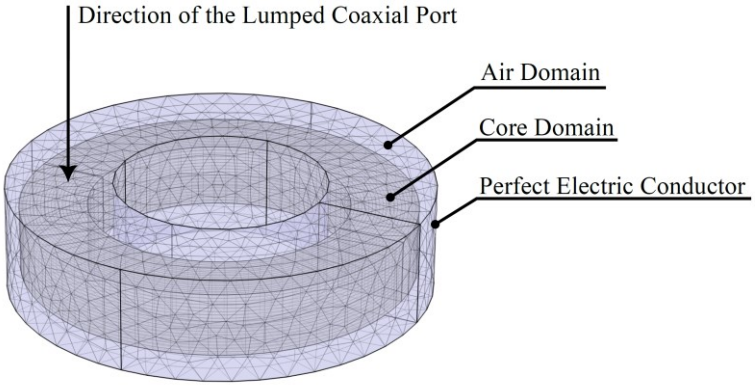

Fig. 4–33 Geometry and boundary conditions for single-turn simulations

Since the wave is significantly shorter in Mg-Zn material than in Ni-Zn, the resonance of these cores will occur at different frequencies. Therefore, the calculation for Mg-Zn material was carried out in the range 10 kHz – 1MHz, and for Ni-Zn material in the range 10 kHz – 180 MHz. The Fig. 4–34 shows the inductance graphs recalculated from the Lumped Port impedance for simulations performed for Mg-Zn (left) and Ni-Zn (right) material properties.

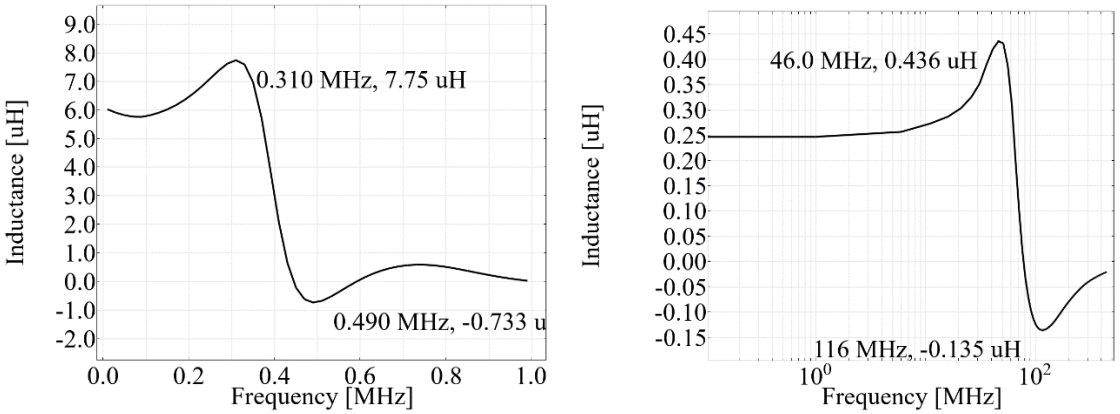

Fig. 4–34 Inductance of the single-turn winding for Mg-Zn (left) and Ni-Zn (right) simulations.

Let's consider the distribution of the magnetic field both at low, pre-resonant frequencies and during resonance. We will plot the distribution of the magnetic flux density perpendicular to the cross-section of the magnetic core, further denoted as B_n. For clarity, this cross-section is marked in red on the right part of the Fig. 4–35.

The distribution of the field in the cross section of the magnetic core is shown for Mg-Zn core in Fig. 4–36 and Ni-Zn core in Fig. 4–37 for a row of frequencies. Since this distribution also depends on the phase, the horizontal direction shows the change in the field during half a period, while the vertical direction shows the selected frequencies. At low frequencies, the field is approximately uniform, with noticeable enhancement closer to the centre of the ring, where the magnetic line length is shorter. As the frequency increases, a resonance peak starts to grow at the centre of the section, initially in the same direction as the initial magnetic flux and then turning against it. It can be seen that as the frequency increases, a larger and larger part of the wave is accommodated in the transverse section, and the resulting distribution acquires new peaks. In general, the distribution is similar to that presented by Skutt [95] for the case of low losses due to eddy currents, shown in Fig. 4–38 and Fig. 4–39. This distribution is generally similar for both materials.

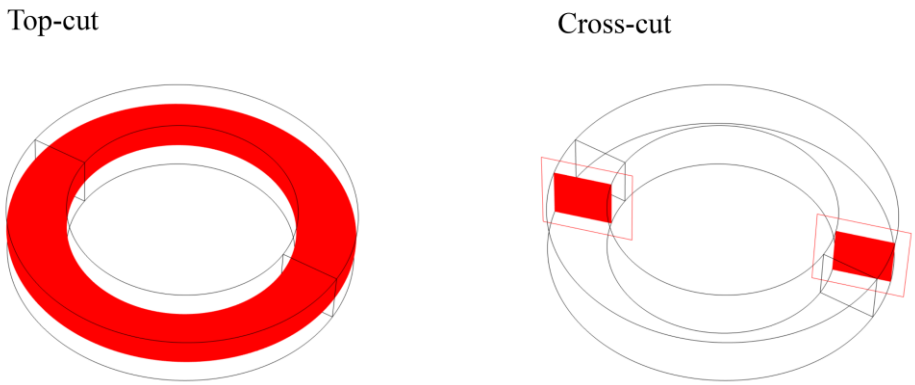

Fig. 4–35 Cutting surfaces used for plotting the magnetic flux density: top-cut on the left and cross-cut on the right.

The distribution of the field is axially symmetric for the main axis of the ring. This can be clearly shown by considering the cut-view from top: left part of Fig. 4–35. The top-cut should not be therefore mixed with the term "core cross-section". To avoid misunderstanding with the term cross-section further within this paper we will always mean the surface which is normal to the direction of the low-frequency magnetic flux, one instance of which is shown as a right part of the Fig. 4–35. However, even though the view angle changed, as before, we will plot the magnitude of the magnetic flux density normal to the cross-section of the core at each point along the magnetic circuit. In other words, we are interested in the part of the field that flows along the core, therefore we will plot projection of the magnetic flux vector onto the normal of the cross-sectional area of the magnetic circuit. In our case, the Y-axis coincides with the main axis of the ring. It can be derived that the required projection of the field onto the normal to the cross-sectional area is calculated as:

$$B_n = \frac{B_x \mathrm{z} - B_z x}{\sqrt{\mathrm{z}^2 + \mathrm{x}^2}}. \tag{4.58}$$

Fig. 4–40 describes the change in the field during one half-period for selected frequencies in the investigated materials. It can be seen that the field distribution across the cross-section, which was presented in the previous Fig. 4–36 and Fig. 4–37, is symmetrical with respect to the main axis of the ring, both for the Ni-Zn and Mg-Zn cores, as expected.

We can simplify the representation by only considering the amplitude of the standing wave, calculating the absolute value $|B_n|$ of the complex magnetic flux density at each point of geometry. Such simplification leads to the representation in Fig. 4–41 for Mg-Zn material, where the pattern of the standing wave is clearly visible. However, the direction of the magnetic flux vector obviously disappears.

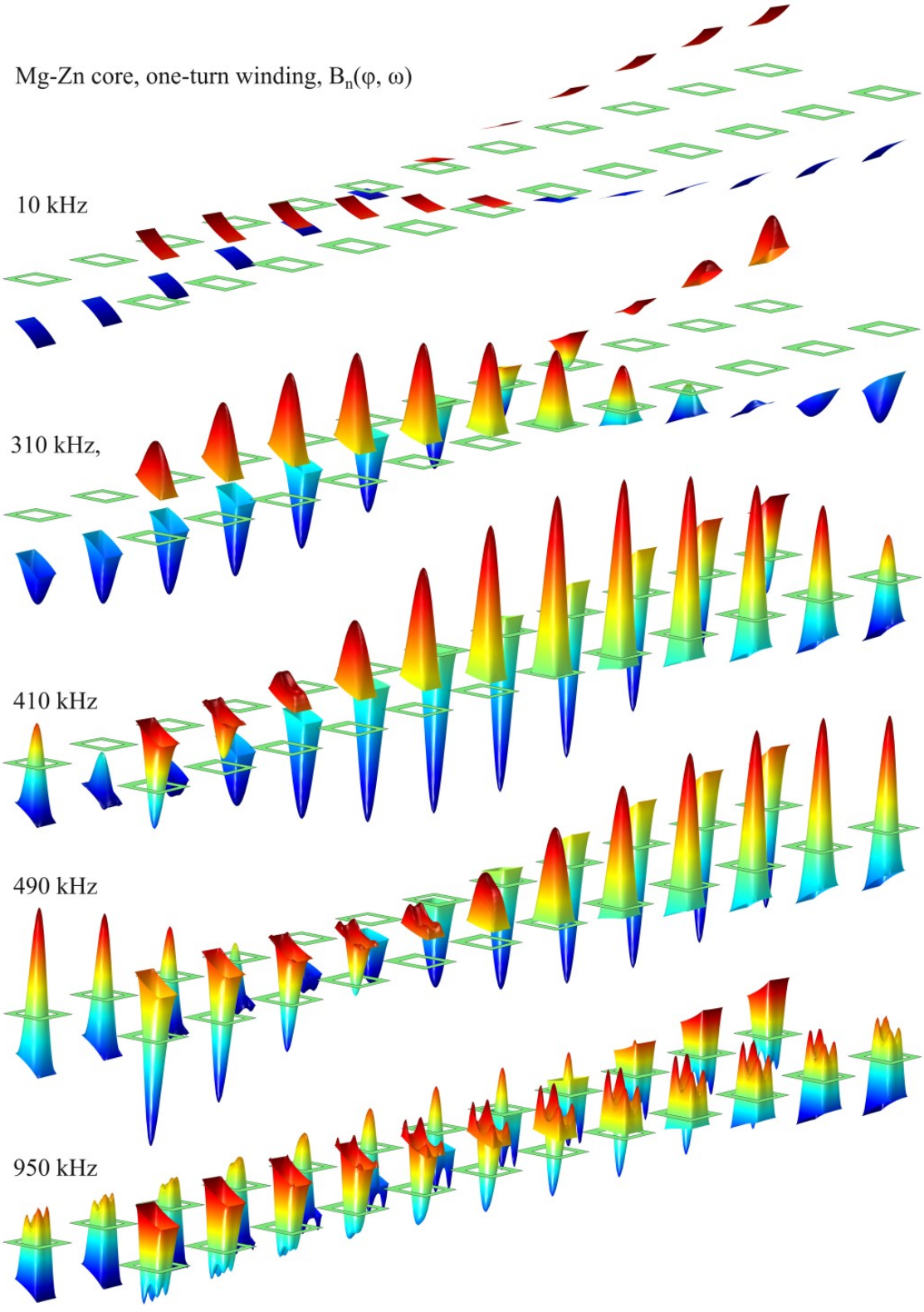

Fig. 4–36 Magnetic flux density in the cross-section of the core.
Single-turn winding simulation, Mg-Zn material.
In horizontal direction: alteration of the field during half-cycle,
In vertical direction: sweep over selected frequencies.

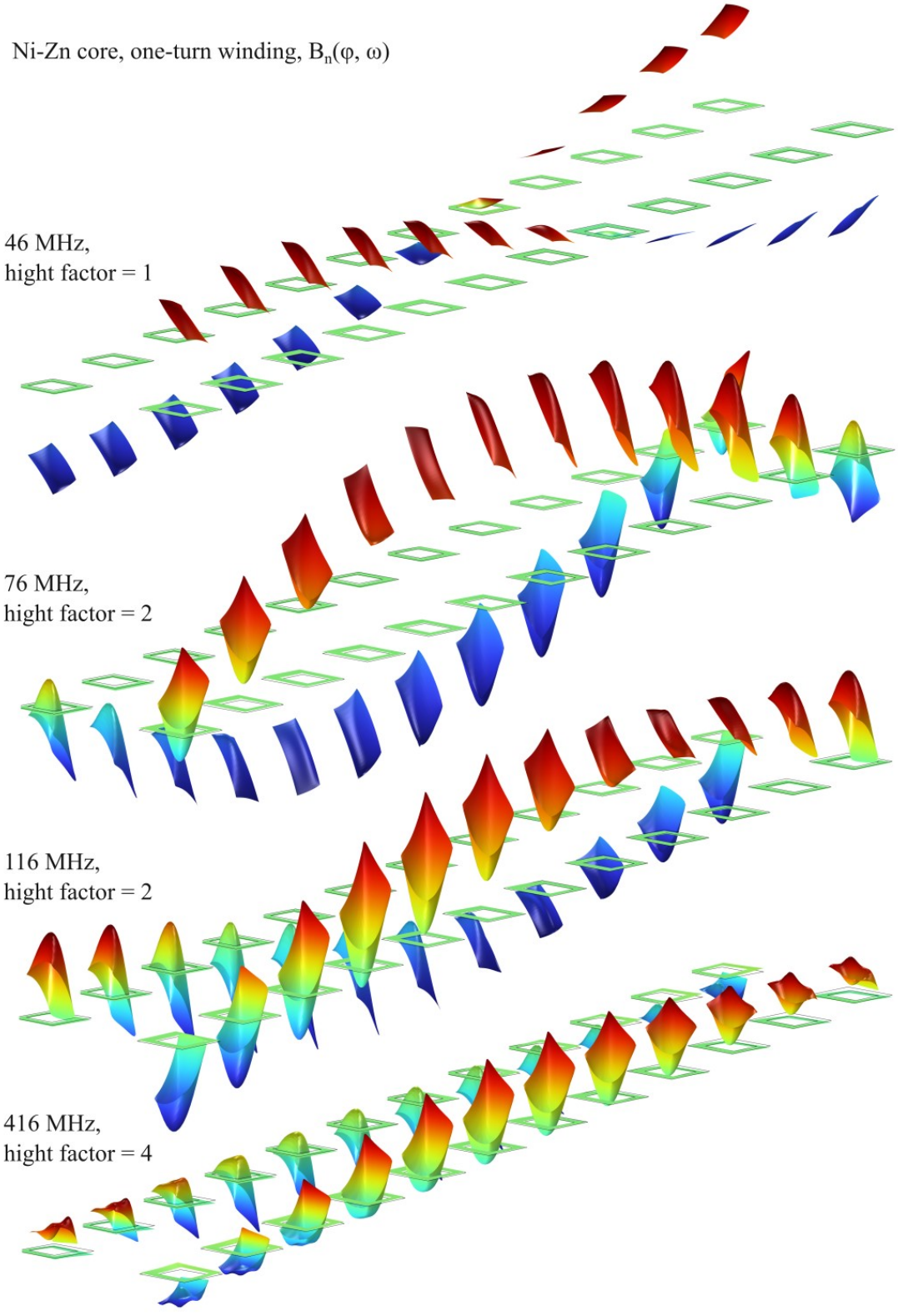

Fig. 4–37 Magnetic flux density in the cross-section of the core.
Single-turn winding simulation, Ni-Zn material.
In horizontal direction: alteration of the field during half-cycle,
In vertical direction: sweep over selected frequencies.

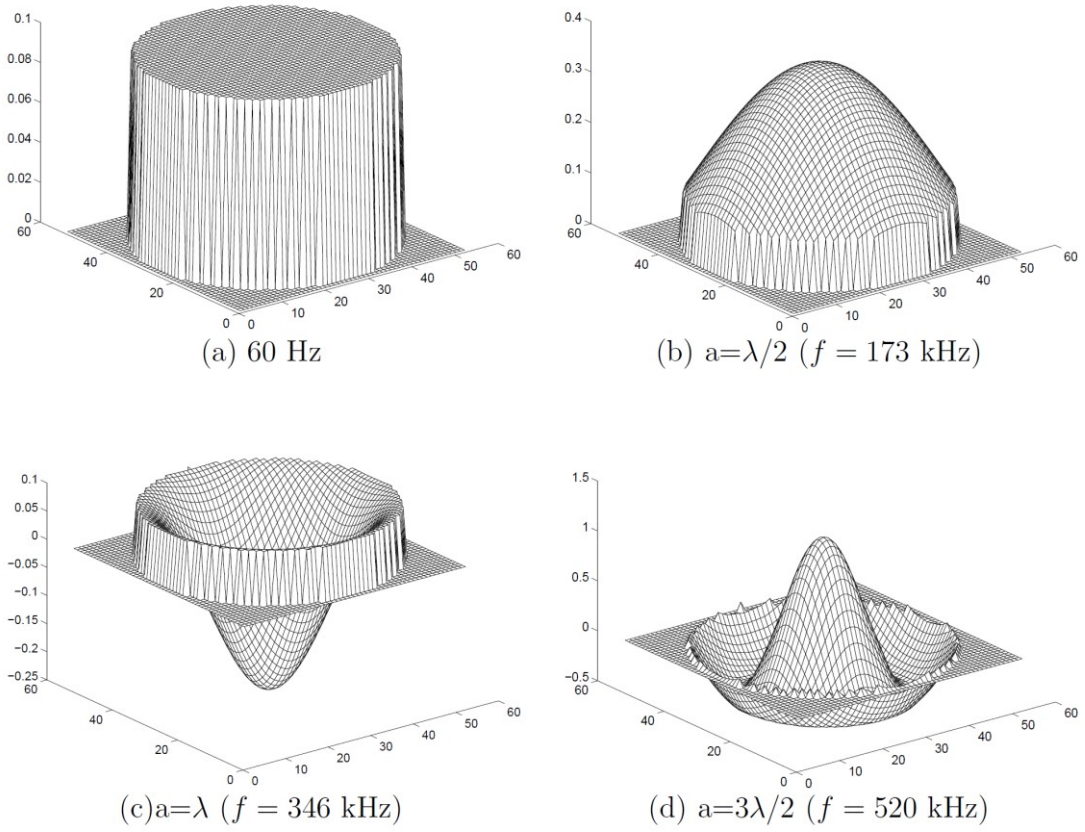

Fig. 4–38 Dimensional resonance in a lossless cylindrical ferrite core from [95]

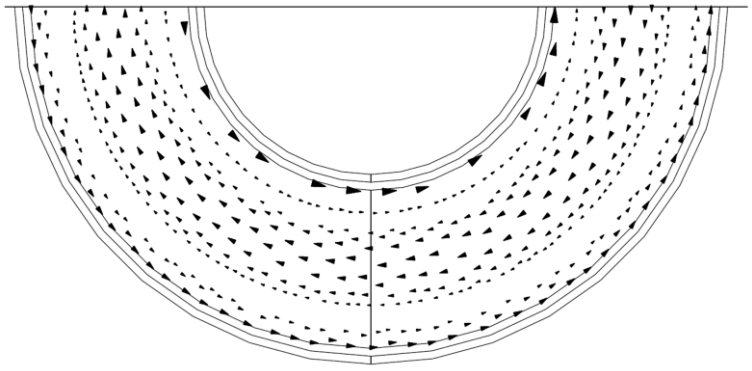

Fig. 4–39 FEA simulation of field distribution in the annular toroid model at 1MHz from [95]

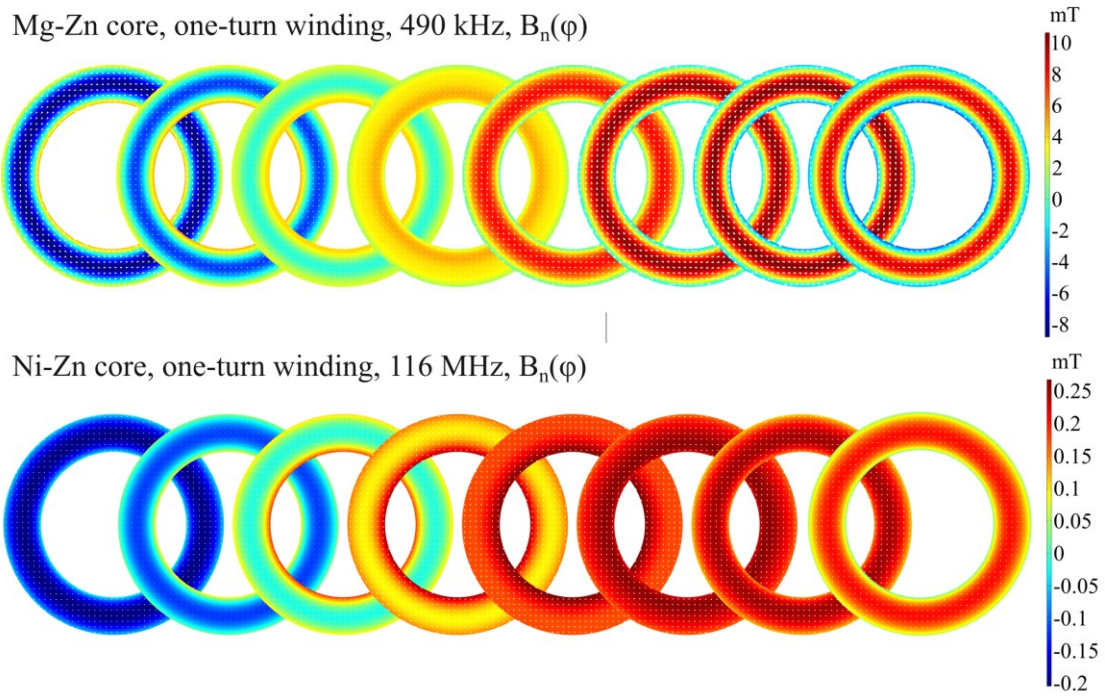

Fig. 4–40 Magnetic flux density normal to the core cross-section viewed from the top-cut.
Mg-Zn and Ni-Zn materials, single-turn simulation.
In horizontal direction: alteration of the field during half-cycle.

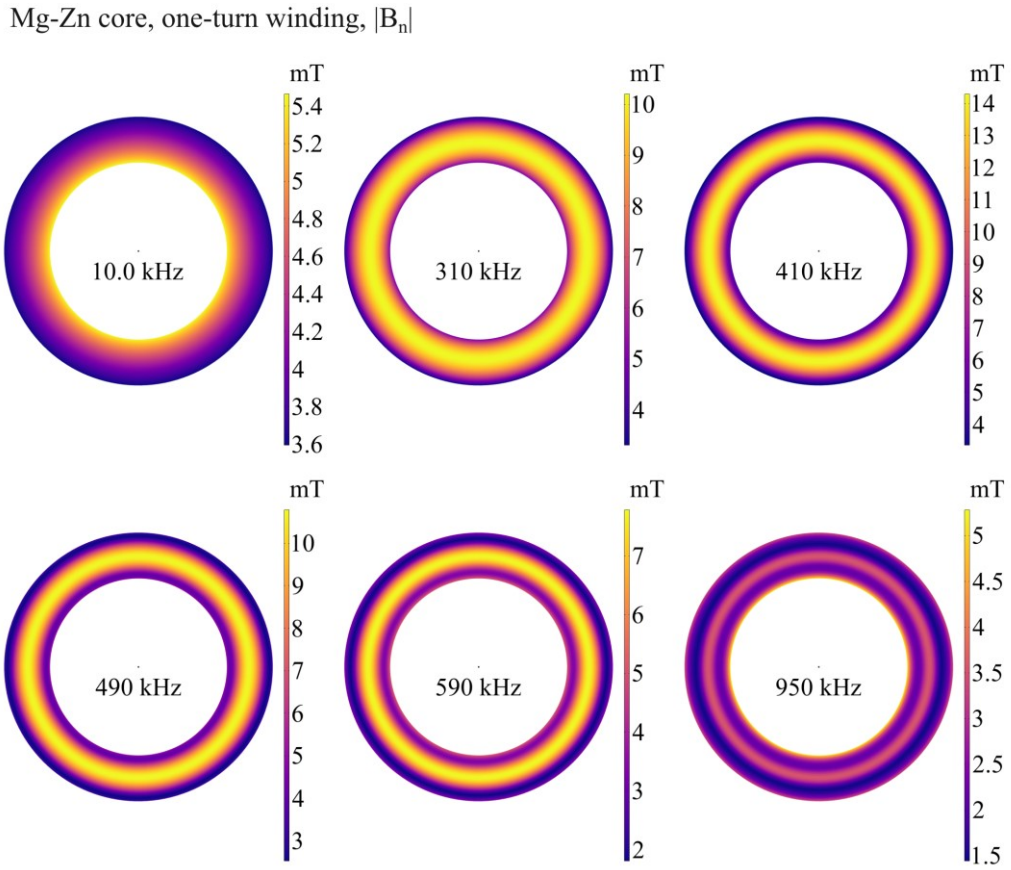

Fig. 4–41 Standing wave pattern:
Absolute value of magnetic flux density normal to the core cross-section viewed from the top-cut.
Mg-Zn material, single-turn simulation.

So far, the main role in the resonance was indeed played by the cross-sectional mode - a wave pattern that fits into the cross-section of the magnetic core and is symmetric with respect to the main axis of the ring. However, now we will move on from the artificial simplification to towards the simulating HFCT with the real-geometry winding. Fig. 4–42 shows the new calculation model.

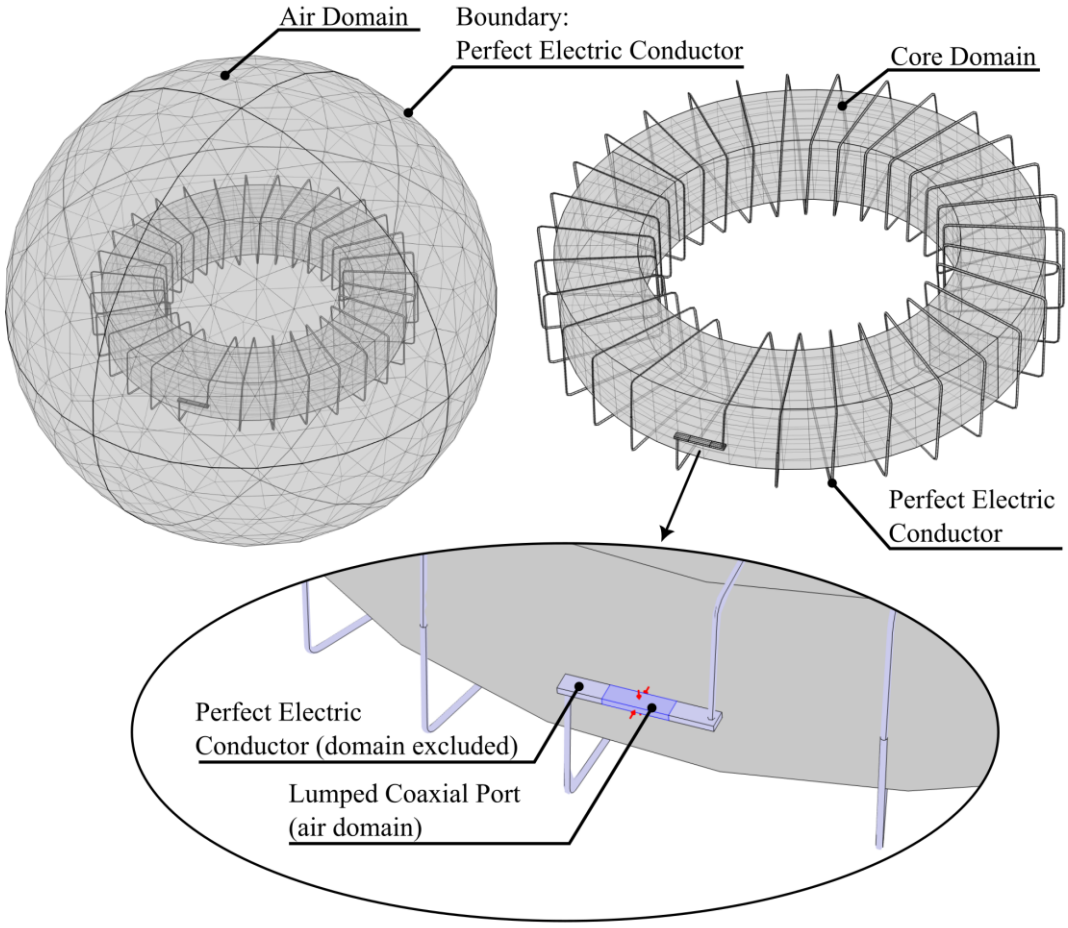

Fig. 4–42 Geometry and boundary conditions for multi-turn simulations.

This model consists of only three domains:

- The magnetic core,
- The air domain,
- A small rectangular air domain between the ends of the windings, which is needed to apply the Lumped Port condition.

The winding domain itself is excluded from the calculation and is modelled through the ideal electrical conductor condition. There is another alternative: the impedance boundary condition, but since the winding is not too long and the core material itself causes significant active losses needed for convergence, we will use the ideal conductor condition.

The outer shell of the sphere also has the electric conductor condition as well. There are also many alternatives here – the use of an infinite domain or scattering conditions, which can be used if the task is to model a transformer in a free-space. However, since the investigated core has a ring shape, the field is mainly enclosed, so modelling can be carried out without these more complex outer-boundary conditions.

It is important to note that due to the small size of the winding geometry compared to the overall dimensions of the model, it is crucial to optimize the mesh as much as possible, both for the winding and the magnetic core. In this regard, mapped mesh, distribution nodes, and quad meshes are extremely useful. As mentioned earlier, it is also important to have some margin between the winding and the core in the geometry of the model. The presence of rectangular (non-rounded) faces in the geometry do not affect the convergence. Regarding solvers – the direct solver shows good results compared to the iterative one, with a calculation time of about 15 minutes for a single frequency.

Let us examine the results in the same order as we did for the single-winding coil. First, we present the impedance graphs for both materials in Fig. 4–43.

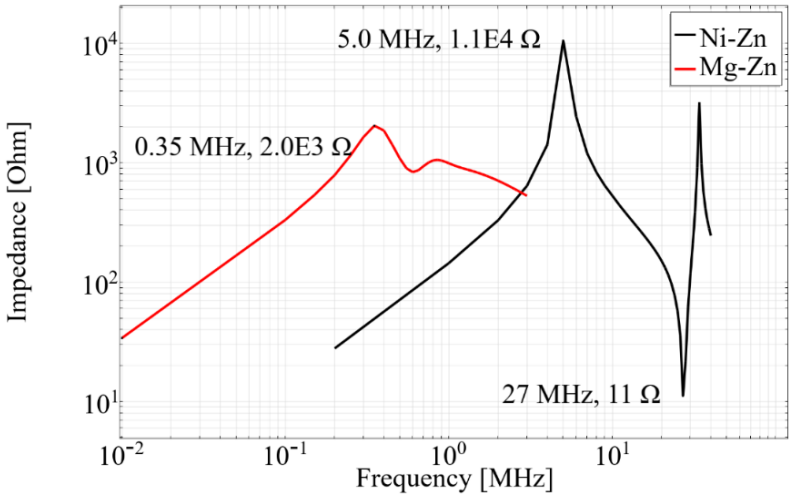

Fig. 4–43 Impedance of the multi-turn winding.

First of all, we will again examine the field distribution in the cross-section of the magnetic core presented in Fig. 4–44 and Fig. 4–45 for a range of frequencies and two selected materials. It can be clearly seen that in the case of the Mg-Zn material (Fig. 4–44), the field distribution at resonance in the magnetic core is similar to the modelling with the simplified single-turn winding – as the frequency increases, a standing wave pattern appears in the cross-section of the magnetic core, axisymmetric and developing with increasing frequency. If we refer to Fig. 4–45 it can be seen that the second material – Ni-Zn – resonates differently, the magnetic flux through two diametrically opposite sections is no longer

mirrored about the axis of the magnetic core, as in the case of the Mg-Zn core. On the contrary, at a frequency of about 15 MHz, the magnetic flux density is almost zero for the upper cross-section of the core, in other words, there is a minimum of the standing wave, while a maximum is observed on the opposite cross-section. At a frequency of 27 MHz two maxima can be observed – and the wave in both cross sections is directed in the same direction relative to the common cut-plane and in the opposite direction relative to the central line of the magnetic core. In other words: a standing wave pattern stretches along the central line of the magnetic core.

To show the standing wave pattern along the magnetic core, we will use the top-cut view we have previously used (Fig. 4–35, left part). As before, despite observing the core in the top-cut, for each point of the surface we will compute the value of the magnetic flux density aligned with the central line of the magnetic core, just as we did before. Fig. 4–46 shows the alternation of magnetic flux density over one full period. The maxima and minima of the standing wave distributed along the magnetic core are clearly visible.

Again, as was done before for single-turn simulation, we will take the absolute value and show the shape of the standing wave. In Fig. 4–48 it can be shown how a cross-sectional mode develops in Mg-Zn core and at the high end of the frequency range the field is pushed into a thin surface layer. In Fig. 4–49 it can be seen how with the increase of frequency a longitudinal mode develops in the Ni-Zn core, acquiring new minima and maxima along the magnetic path. Based on the above, it can be established that the resonant behavior of the HFCT, in general, can be determined by different modes, which in turn depend on the material of the magnetic core. The reason why the described longitudinal mode in magnetic cores has not been well-documented in the literature has several reasons. Firstly, Ni-Zn ferrite is a less common and higher frequency material than Mg-Zn ferrites, and dimensional resonance studies are usually closely linked to the desire to accurately model losses in the magnetic core, which are important in the operation of inductive devices in power electronics, and for this material, as already shown, the cross-sectional mode is more actual. Additionally, this is also related to the peculiarities of the calculation and/or modelling of such devices. In the case of resonance with the longitudinal mode, the solid magnetic core during resonance is divides into two parts, and the magnetic fields of the two halves are closed through an air domain included in our simulation model (Fig. 4–47). Thus, if the magnetic core is considered outside the air gap, this mode cannot occur, as was the case with the single-turn model described earlier.

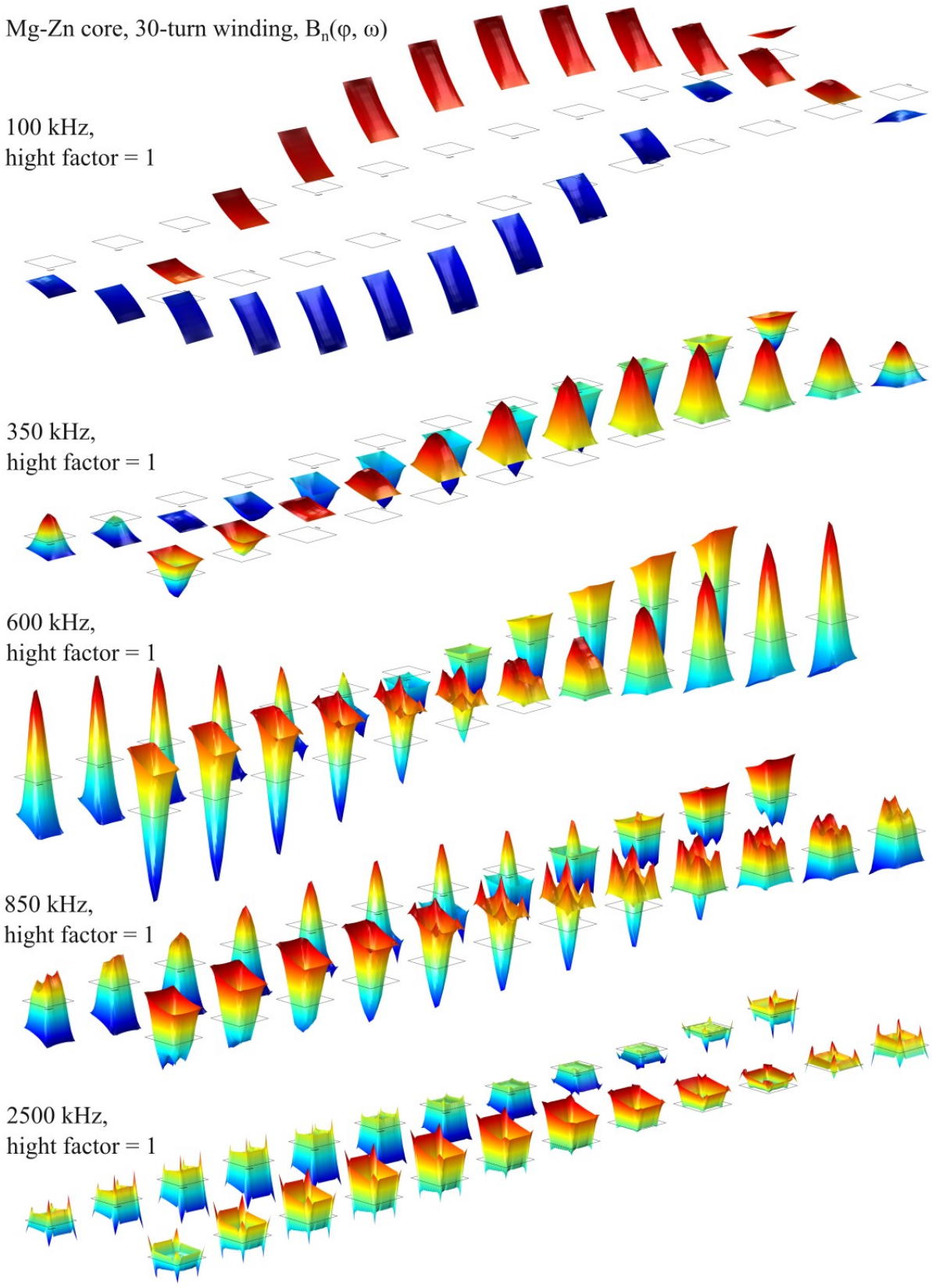

Fig. 4–44 Magnetic flux density in the cross-section of the core.
Multi-turn winding simulation, Mg-Zn material.
In horizontal direction: alteration of the field during half-cycle,
In vertical direction: sweep over selected frequencies.

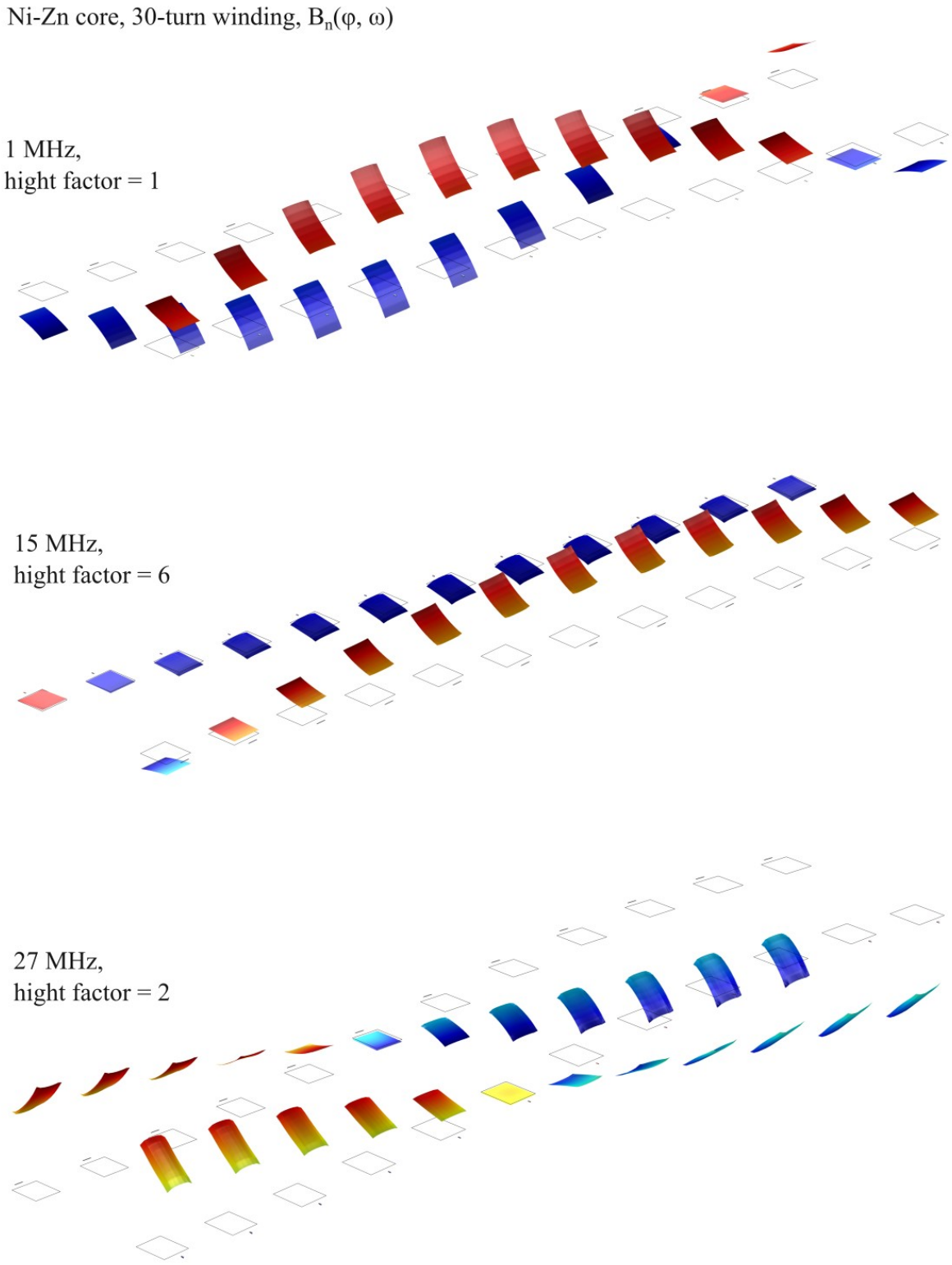

Fig. 4–45 Magnetic flux density in the cross-section of the core.
Multi-turn winding simulation, Ni-Zn material.
In horizontal direction: alteration of the field during half-cycle
In vertical direction: sweep over selected frequencies.

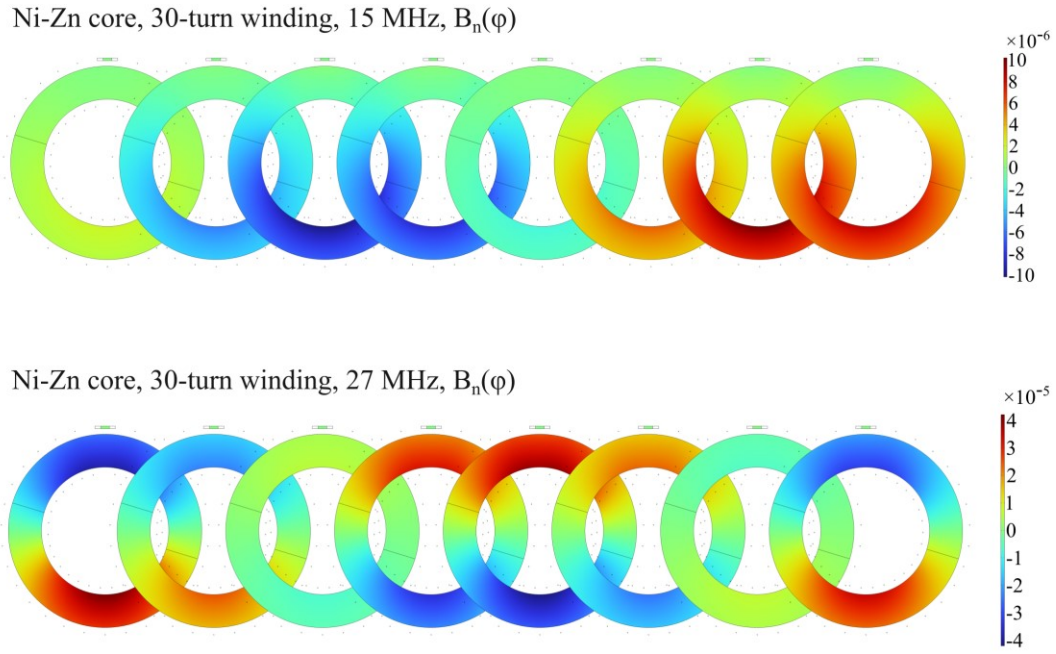

Fig. 4–46 Magnetic flux density normal to the core cross-section viewed from the top-cut.
Ni-Zn materials, multi-turn simulation, two selected frequencies,
In horizontal direction: alteration of the field during one full cycle.

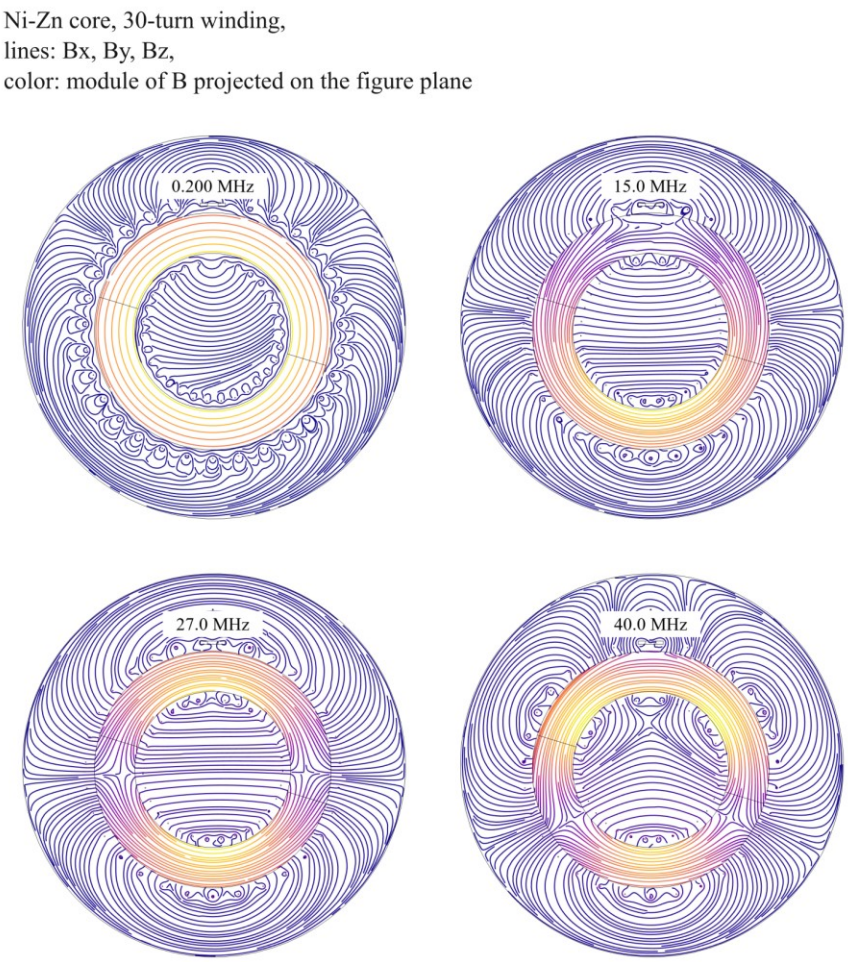

Fig. 4–47 Magnetic field viewed from the top-cut. Ni-Zn material, multi-turn simulation.

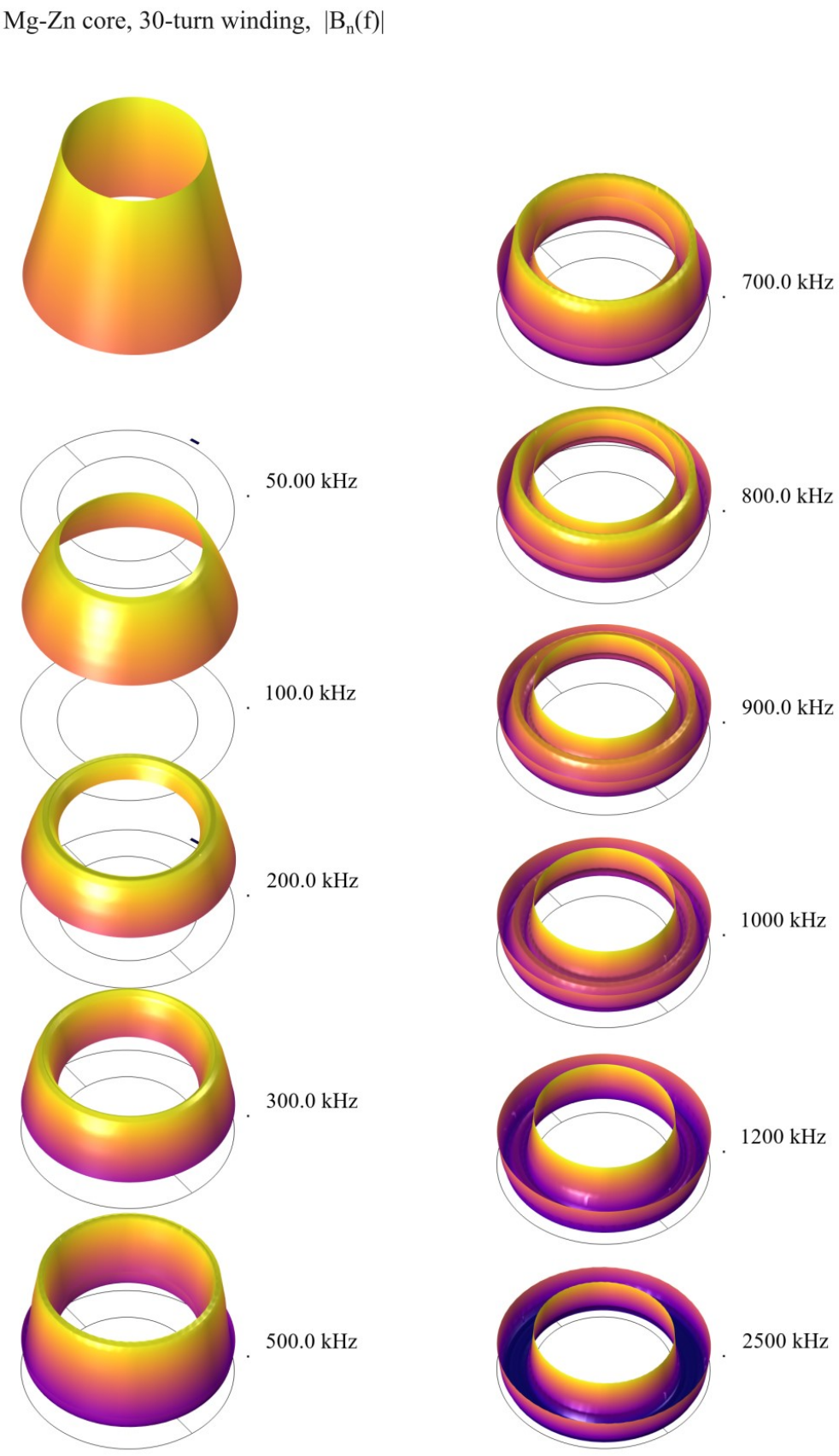

Fig. 4–48 Standing wave pattern:
Absolute value of B normal to the core cross-section viewed from the top-cut.
Mg-Zn material, multi-turn simulation.

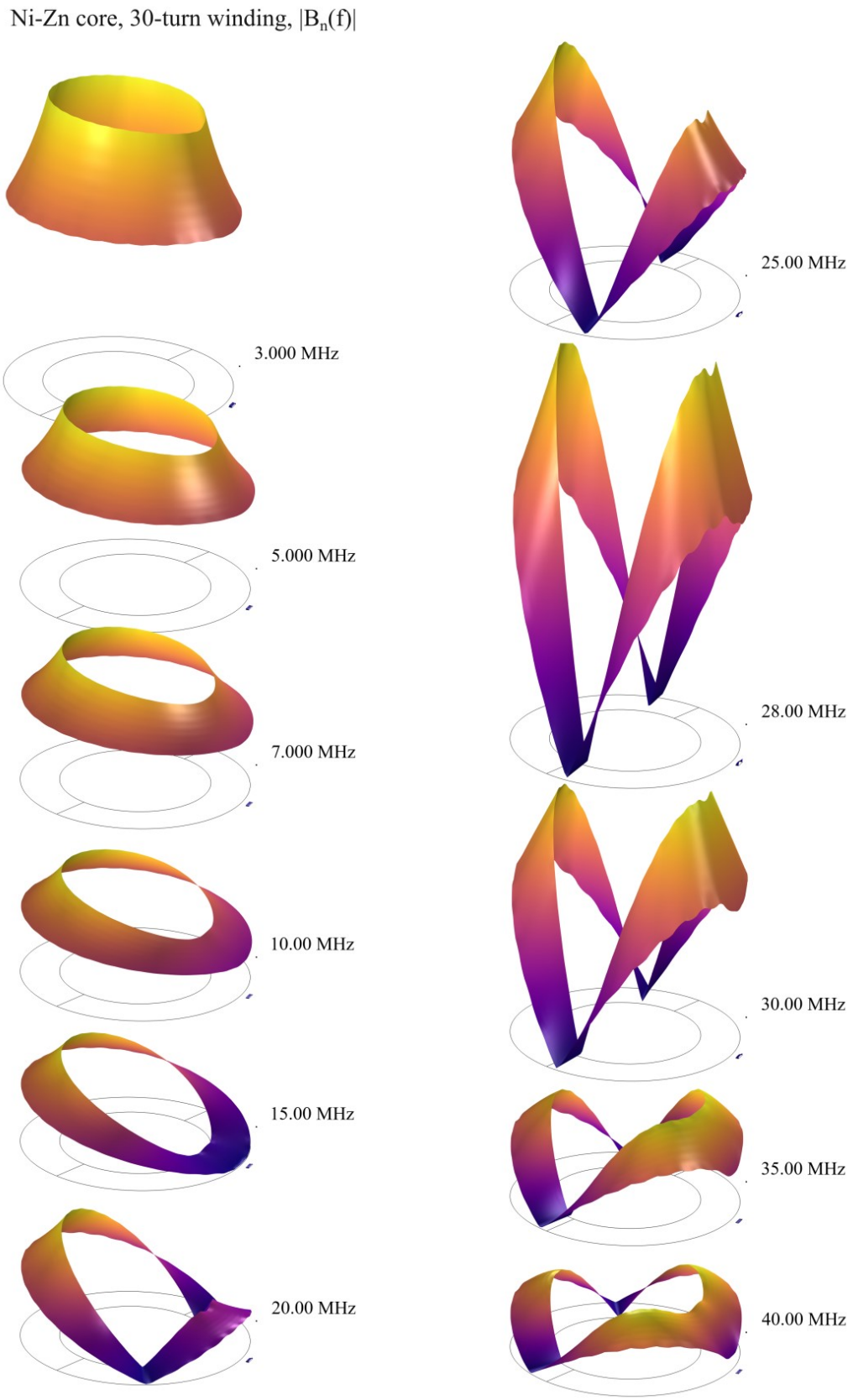

Fig. 4–49 Standing wave pattern:
absolute value of B normal to the core cross-section viewed from the top-cut. Ni-Zn material, multi-turn simulation.

4.7 Prototyping & Performance Assessment

The question of selecting optimal core material and a row of other design parameters can be addressed firstly on a theoretical basis, following the methods described in previous chapters. On the other hand, prototyping is an equally important phase. As was already mentioned, the transfer function reflects the HFCT's main purpose of signal coupling and is accordingly used to assess its performance. Therefore, before starting the prototyping section, it is necessary to say a few words about how the transfer function is measured.

4.7.1 HFCT Transfer Function Measurement

To measure the transfer function of HFCT, an additional test loop has to be used. This loop is magnetically linked to the sensor as a primary winding, effectively converting a single-port HFCT into a two-port filter. To obtain the transfer function, a broadband signal (typically a frequency sweep) is applied to the primary side, and the signals on the input and output are measured. At some point, the setup begins to resonate, and the resonance frequency is determined not only by the current transformer but also by the primary winding. Using a loop with multiple turns decreases the resonance frequency region, and even a single primary turn made from thin wire will lead to the same effect. As the box-shaped loop maximizes the setup's resonance frequency, it became a frequently used solution [13]-[15].

Accordingly, a measuring chamber, shown in Fig. 4–50, was prepared, large enough to accommodate the HFCT with some margin left. The measured resonance of the transformer is determined by the interaction between the chamber and the HFCT, so the high cut-off frequency is to some extent dependent on the size of the chamber, on the other hand, it is also affected when the HFCT is installed on the cable.

Injection and recording of the signals can be performed:

- based on VNA and S21 parameter, which is the most convenient way [68], [70].
- an oscilloscope and a step/pulse generator [64],
- an oscilloscope and an arbitrary function generator that produces a sweep [61], [67].

At the beginning, I typically used the "Keysight E5061B ENA" vector network analyzer. Like most similar devices, it combines a VNA and an impedance analyzer, making it possible to be used not only for measuring the transfer function through S-parameters but also for evaluating individual magnetic cores by measuring their inductance and active losses. Despite the technical merits of this device, its user interface has certain inconveniences: each curve has to be saved individually, only one curve per channel can be

added to memory, a curve saved in memory doesn't update when the frequency range boundaries are changed, etc.

Later, I largely moved away from using this device and primarily used the “Bode 100 VNA”, recently released by OMICRON electronics GmbH. This device has a lower bandwidth: 1 Hz to 50 MHz, which, however, suits our purpose perfectly. The use of this device is extremely convenient, and in my humble opinion, it's probably the most suitable device for evaluating HFCT performance.

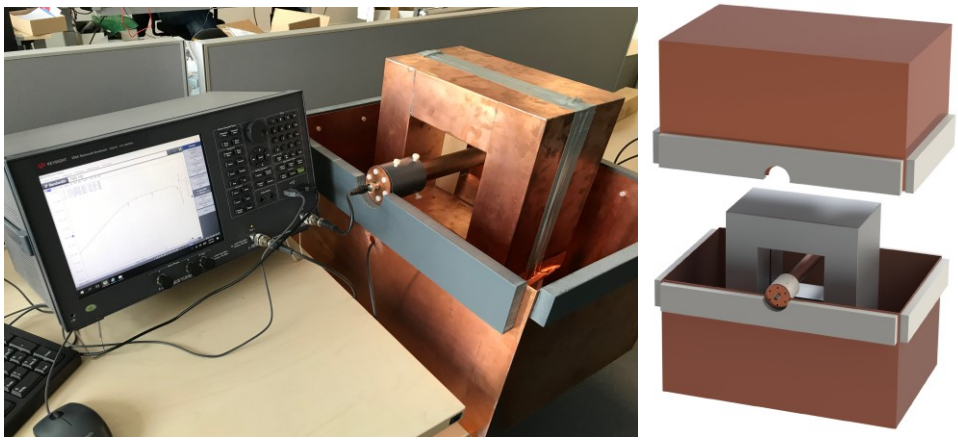

Fig. 4–50 HFCT in the measurement chamber connected with the VNA, right part of the picture was previously published in [Pub. 3]

4.7.2 HFCT Prototyping

The first prototypes, depicted in Fig. 4–51, were primarily fabricated to give an initial understanding of the gap between theoretical predictions and real-world performance, as well as to identify design features that don't substantially influence the operation. These sensors had a core with a relatively low magnetic permeability, in order to prevent the material from saturating and to avoid the emergence of resonance in the magnetic circuit. Here the lower the core's permeability was and the fewer the number of turns, the more attention had to be devoted to the stray inductance - hence the wide winding observable on sample in the Fig. 4–51a.

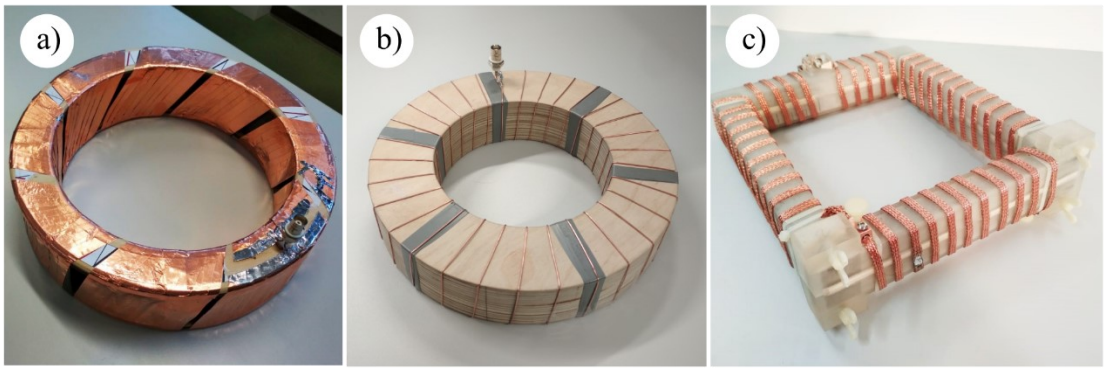

Fig. 4–51 First HFCT prototypes

The transformer equivalent circuit features a row of parasitic elements, that represent the stray inductance, losses in winding resistance, losses in the magnetic circuit, etc. First the author aimed to determine how closely the transformer could resemble an "ideal transformer" in which these losses are neglected, and therefore primary and secondary currents relate through the the turns ratio - i.e., the secondary current equals the primary one, referred to the secondary side. In practice, this task turned out to be relatively simple - the losses in ferrites are indeed small, and the use of a wide winding encompassing the entire magnetic circuit can minimize leakage inductance to the value negligible in comparison with the mutual one. Therefore, all three HFCTs depicted in Fig. 4–51, despite their rather low relative magnetic permeability (several tens), behave almost like ideal transformers (-0.5 to -1 dB) within their bandwidth.

However, a low transfer impedance is not particularly convenient in practice. From one point of view, if there are currents of useful signals and interference currents in the line, then their ratio on the secondary side of the transformer should not depend on the transfer impedance, therefore the Signal-to-Noise Ratio (SNR) should remain constant. However, in practice, in addition to the DC noise in the line, one must consider the dynamic range of the Analog to Digital Converter (ADC), the thermal noise of the amplifier, etc., and as a result, for measuring small signals, it is still more convenient to have a higher transfer impedance of the passive sensor.

Subsequent optimization was mainly directed towards maximizing the transfer impedance, while keeping the losses low through ensuring that the relation between primary and secondary currents in the bandpass is close to the turns ratio, while providing a specified bandwidth and being capable of operation under specified superimposed power-frequency current. Preventing the saturation from power current requires a non-magnetic gap in the core, which implies a constraint on achievable inductance of magnetization brunch and

defines the amount of turns that is needed for the specified low cut-off frequency, automatically resulting in the certain value of transfer impedance.

Initially, preference was given to ferrite materials, and the first prototype used in PD localization studies described in publications [Pub. 1], [Pub. 2] and [Pub. 4] was built using Ni-Zn ferrite, chosen primarily for its high-frequency properties, low losses, isotropic properties in all directions, and the absence of dimensional resonance. This type of ferrite was available in the form of rectangular plates, which made it easy to assemble a core of any size. Another advantage was the ability to create a distributed non-magnetic gap along the length of the core. As before, this prototype was created with the aim of minimizing parasitic parameters such as stray inductance, core losses, etc. (Fig 4–52).

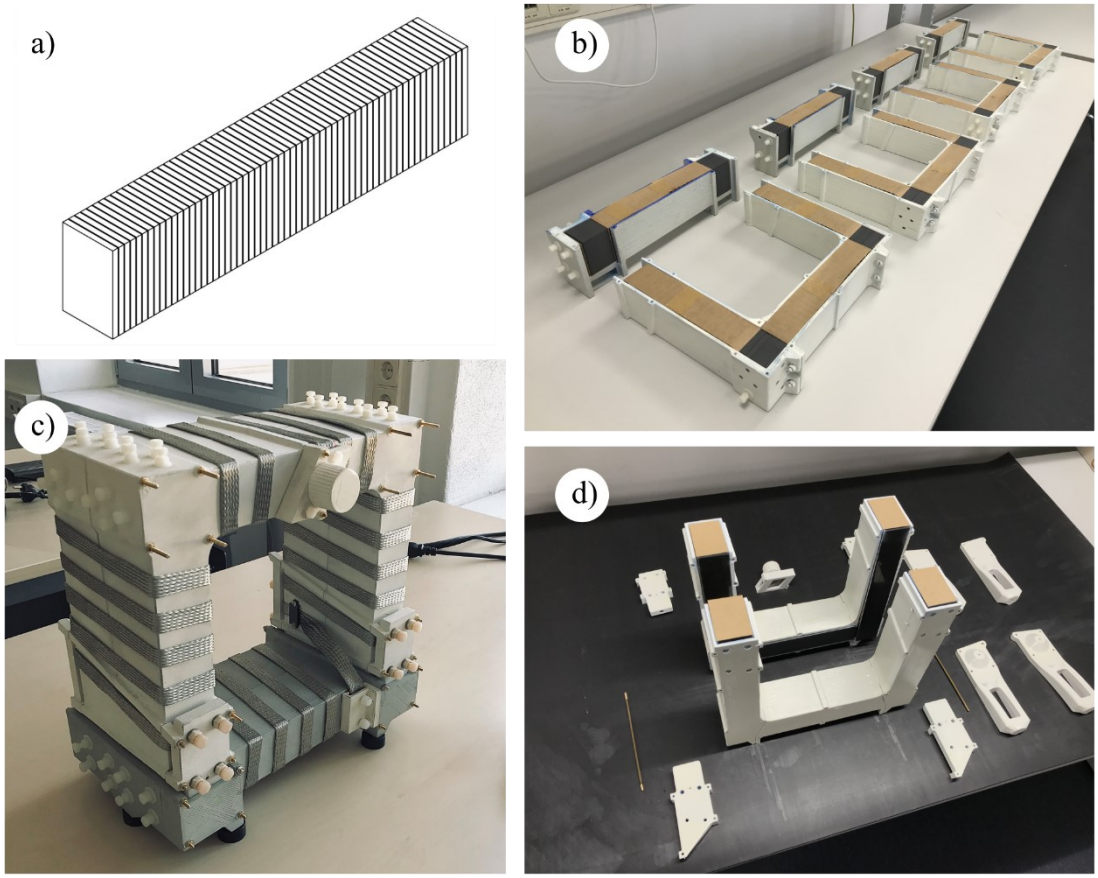

Fig. 4–52 Ferrite-based prototype used for first PD localization studies

The cross-sectional size was chosen such that, with the introduced non-magnetic gap, it provided a sensitivity of 20 pC at a distance of more than 10 km – this experiment is detailed in the chapter 7. Furthermore, the first prototype had additional requirements: first, a split-design was needed; second, since the creation of this prototype coincided with the first

localization experiments of partial discharges (PDs), to initially simplify the localization task, it was required that the first four HFCT prototypes have identical transfer functions.

For this prototype the housing for the magnetic core was 3D printed. Ferrite plates were lined out with a paper tape providing the required distributed gap, and assembled into blocks, which were then placed into the housing. The coil was wound on top of the housing, and the resulting prototype did not have shielding enclosure. The identical transfer functions were achieved by not gluing the magnetic core: the blocks filling it could be tightened by bolts located at the ends of the prototype. The transfer function of this prototype is presented in Fig. 4–53.

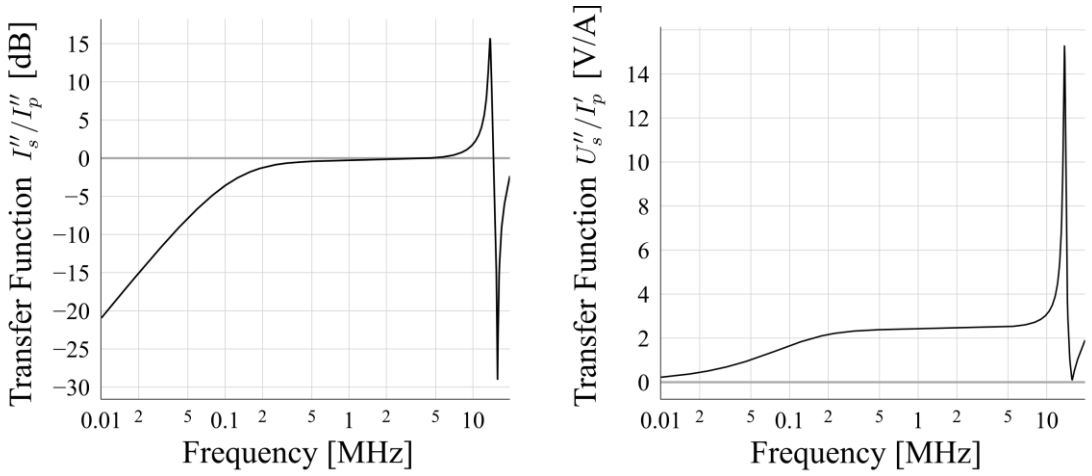

Fig. 4–53 Transfer Function of the ferrite-based prototype

Two things are clearly visible in these graphs. Firstly, the proximity of the right graph to zero indicates that indeed both the leakage inductance and the losses in the material are minimal. The graph of transfer impedance also shows that it approaches the lossless value of 2.5 Ohms: $|H|_{V/I} = \frac{R''_m}{N} = 50\ \text{Ohms}/20\ \text{turns} = 2.5\ \text{V/A}$.

On the other hand, it is interesting to note that use of such a high-frequency material with low losses leads to the emergence of a resonant peak with high quality factor. For the core-algorithms of the monitoring system, such a peak is not a problem, moreover, it lies in the area above 10 MHz. On the other hand, it is interesting to note that the gradual decline in the transfer function at high frequencies after the bandpass, which is common for many industrial sensors happens due to the utilization of core materials that exhibit a decrease in core permeability and an increase in active losses.

The disadvantage of the ferrites is the small saturation flux, which leads to an increased air gap, which in turn necessitated an increase in the number of turns to achieve the required

lower cut-off frequency and, accordingly, the decrease of the transfer impedance. At the same time, if the leakage inductance is kept low (if the winding tightly envelops the magnetic circuit), then despite the drop of the magnetic permeability of the core at high frequencies the impedance of the magnetization branch will still far exceed the active impedance of the measuring resistance, and thus the transfer function will not decrease significantly. Therefore, the high-frequency properties of Ni-Zn ferrites, such as non-decreasing permeability that completely covers with the desired bandwidth, are not necessary for the transfer function to remain constant.

Based on this considerations, attention was shifted to other materials that have higher saturation flux values, namely, amorphous steel and conventional electrical steel. Usually these materials are used in devices operating at lower frequencies, and it was difficult to preliminarily assess whether their application would be justified. First of all, U-shaped cores made of two materials were tested: Fe-based amorphous steel and 3% Silicon Electrical Steel with 0.05 mm layer thickness. The thickness of the electrical steel lamination was chosen to be the smallest possible to manufacture.

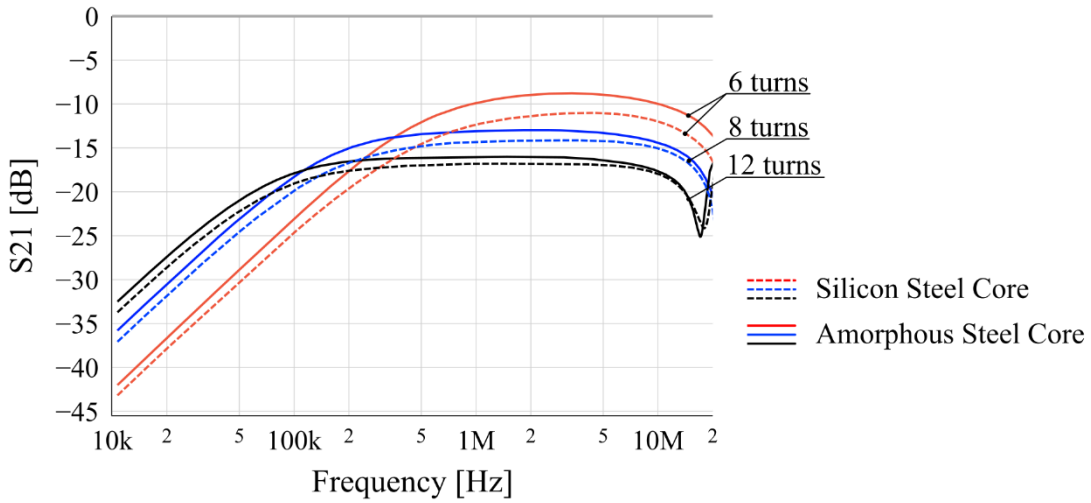

Fig. 4–54 Transfer functions of amorphous steel and silicon steel based prototypes

First of all, the transfer function of both materials was measured with the common procedure in a measuring chamber, and the results are shown in Fig. 4–54. The number of winding turns was also varied. This graph presents curves for the S21 parameter uncompensated, in the way they are displayed on the VNA screen, to also show how the curves shift downwards as the number of turns increases, as the introduced impedance jump between the input and output of the VNA gets higher. Here it is already clear that the transfer functions of both materials exceed the value at 10 MHz, thus demonstrating their suitability as the HFCT core

material. On the other hand, it can be seen that the steel curves lie below the amorphous material curves, which may be related to skin effect losses due to the layer thickness being still too high for the purpose. On the other hand, first of all, the quality of the production of cores from silicon steel is higher than that of amorphous ones. Secondly, these two steels have different hysteresis curves and the saturation magnetic flux density of silicon steel should have been slightly higher. Therefore, there was a chance that silicon steel would perform better than amorphous when operating under superimposed power current.

In the following experiments, the transfer function was measured in the presence of a superimposed power current, both constant and variable. The scheme of the test is shown below, in Fig. 4–55. In addition to the HFCT in the measuring chamber, there is also a power-supplying part, consisting of a current source (AC or DC) and additional power turns wound on the prototype. Fig. 4–56 shows the implementation of this scheme for a DC current, where the source has rather modest dimensions. Skipping ahead, the implementation for an AC current is shown in Fig. 4–61, where the source of the HV test field was used. Additionally, it is worth mentioning the blocking inductance shown in Fig. 4–55: it is needed to isolate the high-frequency circuit "VNA - Measurement Chamber - HFCT" from the power current loop. Naturally, this inductance's conductor should have cross section high enough to carry a power current up to 500 – 600 A – therefore it is a relatively big device also visible on Fig. 4–61c. In experiments conducted on a constant current, a smaller inductance was used, that was not sufficient to provide complete decoupling of the circuits. The consequent effect is also shown in Fig. 4–57 - here one transfer function is taken with the power circuit being opened, and the other – when it is closed. As lower frequencies leak into the power circuit the slope that appears on the curve measured when the circuit is closed. However, in the task of comparison between two core materials, this slope is not a problem, as it is common to all recorded curves, therefore the experiment continued, and this slope will be present in the graphs presented below. Later, for tests with AC current, a larger blocking inductance was manufactured (the one shown on Fig. 4–61c), so the curves corresponding to AC tests no longer have this slope.

Since the materials have different magnetization curves, there exists an optimal non-magnetic gap for each of them. Consequently, biasing current work was tested for various gap sizes.

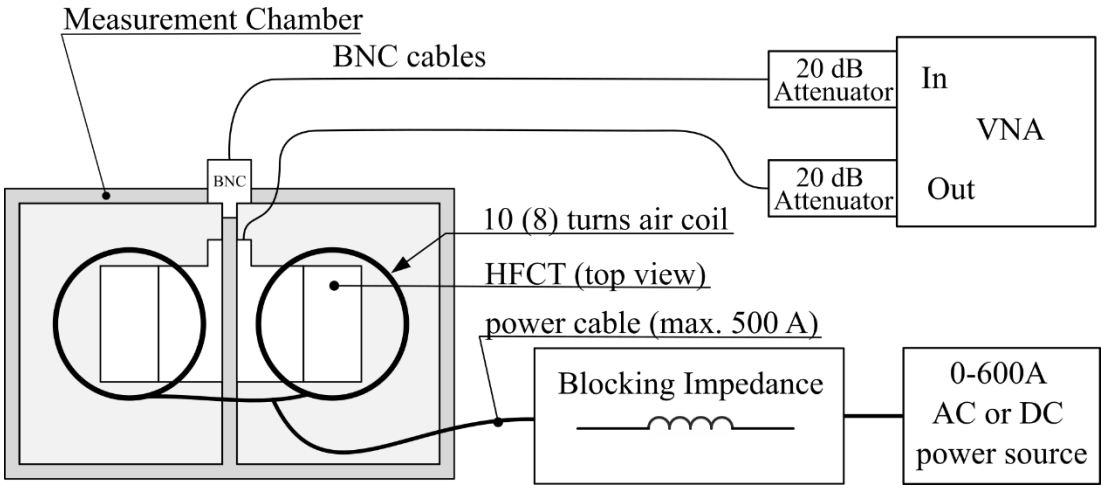

Fig. 4–55 Setup for measurement of HFCT transfer function in the presence of superimposed power current (AC or DC)

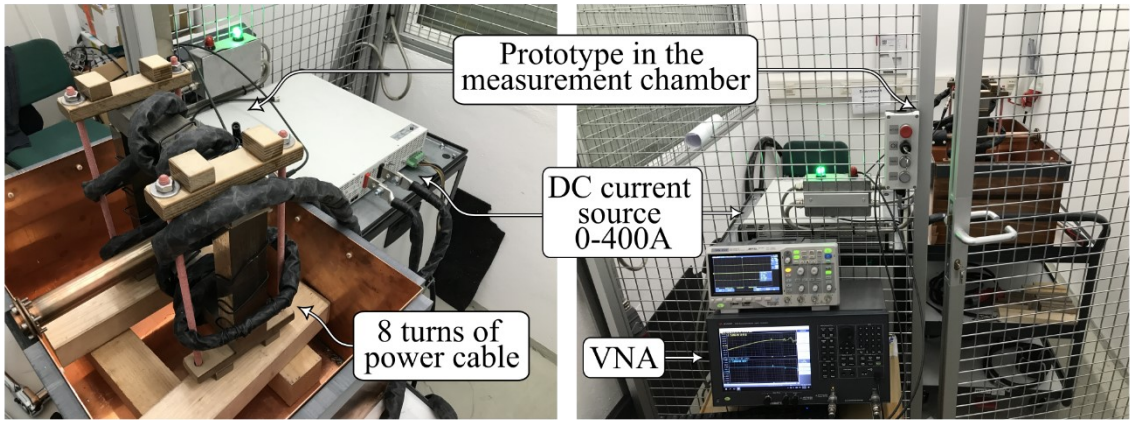

Fig. 4–56 Measurement of HFCT transfer function with superimposed DC power current

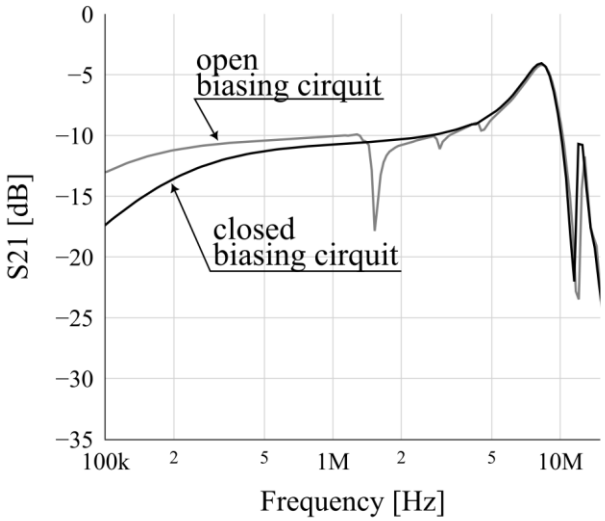

Fig. 4–57 Effect of insufficient decoupling of small-signal and high-signal loops.

Firstly, let us discuss the curves shown in Fig. 4–58. They were recorded for amorphous steel and two different gap sizes (1 mm and 5 mm) as the constant current was increased from zero to three kiloamperes. A resonance, provoked by the presence of a power winding, can be observed on the right side of the graph, though this is not the primary point of interest. Instead, we are particularly interested in the relative position of the curve on the Y-axis and the shift in the curve as the current increases. It is evident that with a small gap (Fig. 4–58a), the curve significantly drops as the current increases, while with larger gaps, the curve barely shifts (Fig. 4–58b) but lies rather low. The optimal gap value is somewhere between these two states.

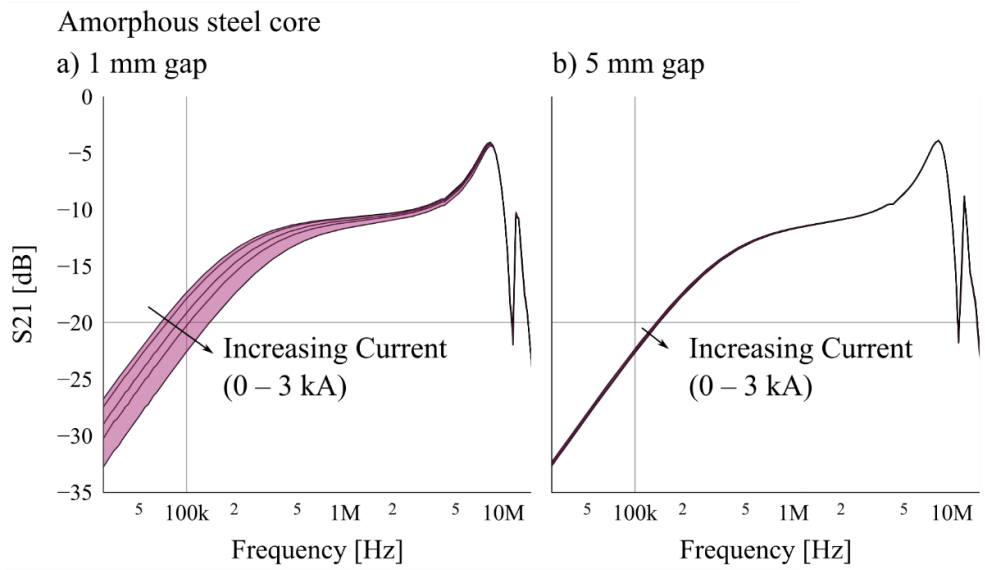

Fig. 4–58 The transfer function decrease with the power current increase.
In subsequent graphs, lines are not plotted and only the area of the curve-family distribution is filled with colour.

Fig. 4–59 shows the measurement results for both materials and several gap values. Already here it is evident that the materials behave differently. Silicon steel initially has a very broad spread, but then already at 2 – 3 mm, it converges into a line, while for amorphous steel, this process is more uniform. The reason for this is the differing main magnetization curves, or more precisely, the difference in how smoothly the transition from the linear part to saturation occurs. For amorphous steel, the optimal air gap value lies around 2 – 3mm, as for a larger (5mm) gap, the curve simply lies lower, and for a smaller (1 mm) gap, it experiences a greater decline under load. Now let's compare these two materials with each other, as shown in Fig. 4–60. Despite the fact that silicon steel has a higher saturation induction according to the datasheet, and hence can be used with smaller gaps, additional losses on it result in the transfer functions for this material still being lower than for amorphous steel. In other words, a higher saturation induction loses to higher losses independent of the superposition current.

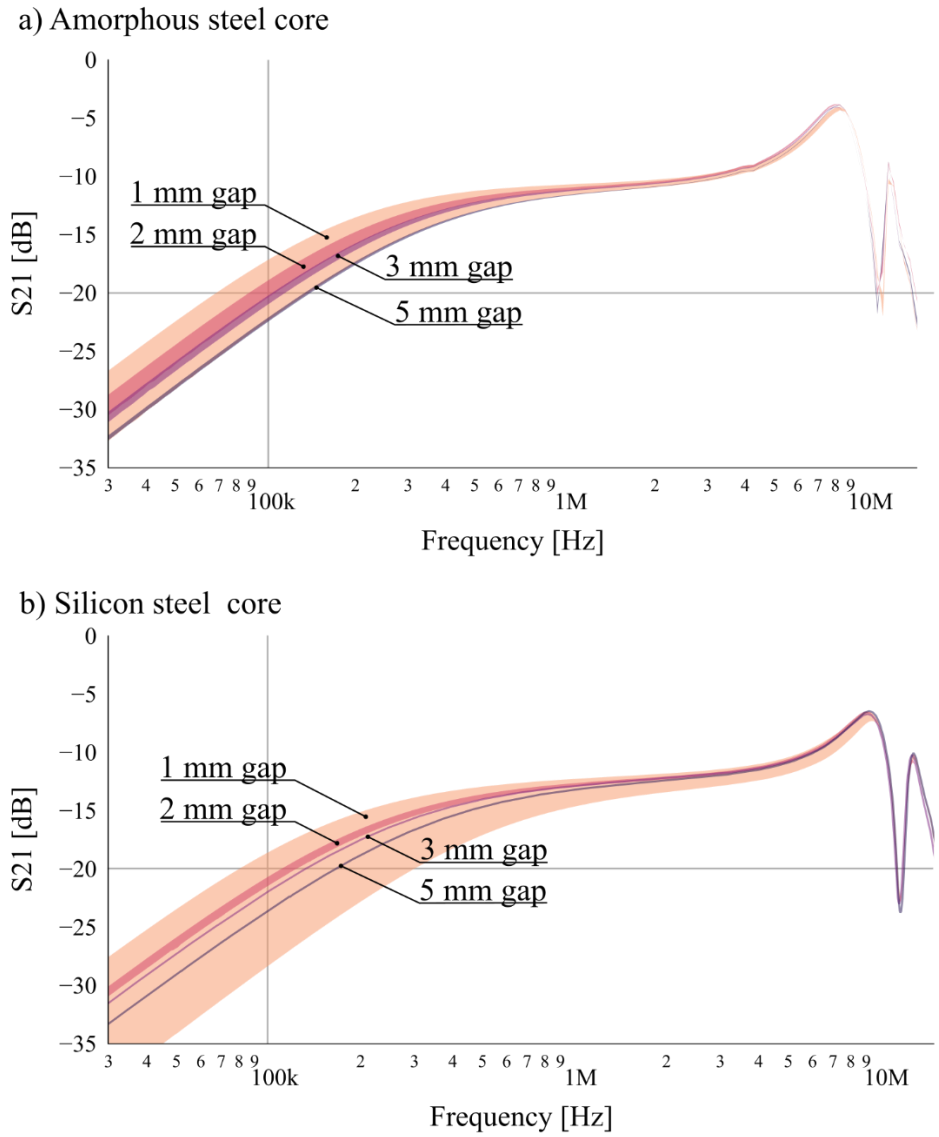

Fig. 4–59 The transfer function decrease with the power current increase.
The color fill indicates the distribution of a family of curves corresponding to one gap value.

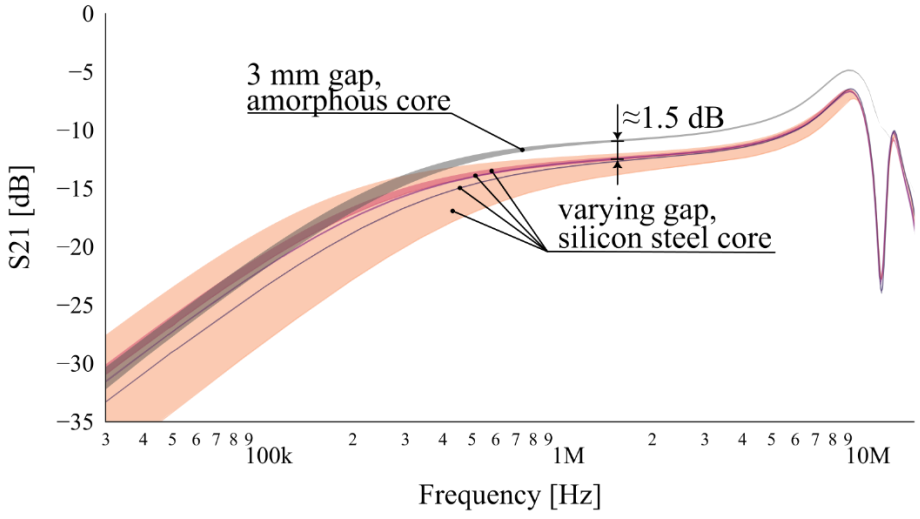

Fig. 4–60 Comparison of materials: the transfer function decrease with the power current increase.

As in the DC power current superposition experiments have shown that the amorphous steel performed better than the silicon steel, it was chosen as the preferred material. The plots for amorphous core shown above recommend a 2 – 3 mm gap, however, to cross-validate this value the same experiments were performed with the AC power current. The setup for the AC tests is shown on the Fig. 4–61.

Fig. 4–61 Measurement of HFCT transfer function with superimposed AC power current

This experiment has led to the same result as before for the DC setup: the amorphous steel cores were more beneficial, and the 2 – 3 mm gap was leading to the highest small-signal transfer function while being subjected to the 3 kA of power current. The figure below shows the spread of the transfer functions for the final selected gap of 3 mm between two halves of the HFCT (reason for preferring the higher value will be explained further).

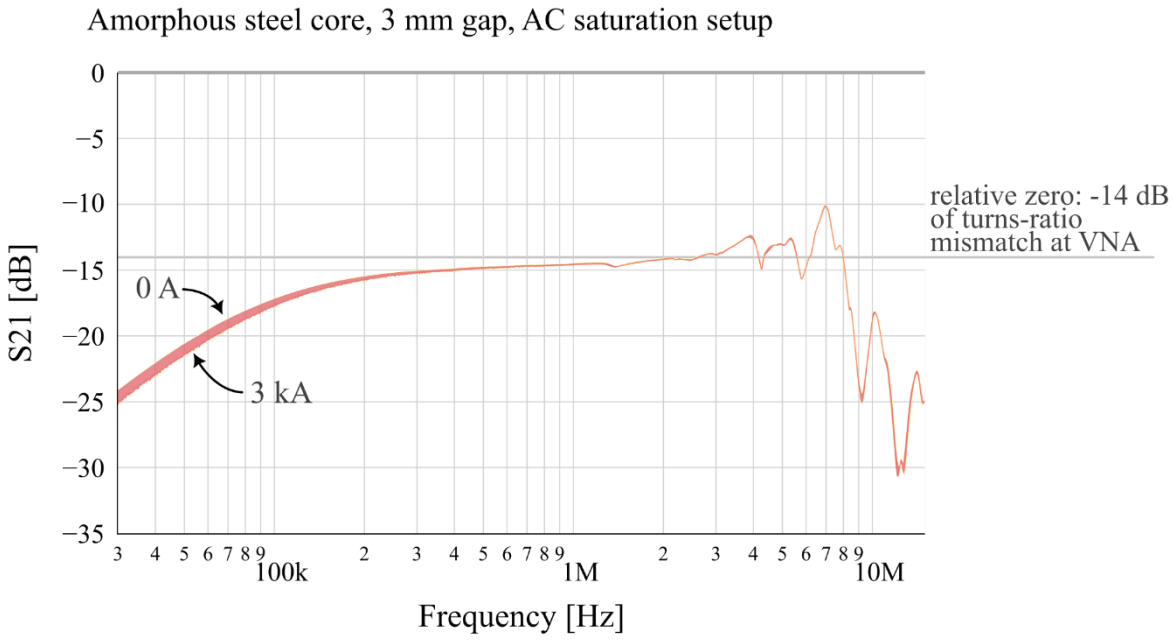

Fig. 4–62 Spread of the HFCT transfer functions with the increase of the power current for the selected gap value.

However, extended tests were needed to ensure that under AC current, with this gap being selected, the HFCT behaves stably: which means that no overheating or vibrations.

Regarding overheating, the testing process was straightforward: the HFCT prototype was subjected to the AC power current for an extended period of time, and the temperature of the casing was measured using thermal couples or a heat camera. At the end of these long-term test, the split designed HFCT was opened and the temperature at the core cross-section was measured to ensure that it does not significantly differ from the temperature of the outer casing. During the development process, I conducted these tests usually within 3 to 5 hours which was not enough to reach the steady state but were enough to predict the final temperature. Later a third-party company conducted the same long-term heat (more than a day) with a current of 3 kA on a single bar going through the aperture of the HFCT, showing that the settled temperature is 55.4 °C.

The next issue is vibrations and acoustic noise. As the air gap is relatively small, a significant magnetic flux flows through the magnetic core. In the previous, ferrite-based prototype, the gap was distributed, and this was distributing forces along the length of the magnetic core. However, for the U-shaped cores and a concentrated gap, and the resulting forces lead to a certain vibration of the two halves unless they are secured properly. From a mechanical standpoint, this issue was addressed by using additional profiles that securely bind the two halves together. Additionally, Fig. 4–65 shows the coils used for quicker installation on prototypes and convenient for identifying the source of noise.

During the vibration analysis, it became evident that vibrations and acoustic noise intensify significantly when the transformer transitions from the linear part of the magnetization curve to its hysteresis part. This is expectable since a non-sinusoidal magnetic flux leads to the emergence of higher harmonics in the acting forces. Consequently, the air gap was fixed to the value that would ensure a certain margin before the onset of pronounced saturation effects. In order to proof at what part of the main magnetization curve the HFCT operates, the hysteresis loops were recorded and used to construct the main magnetization curve, which is shown in Fig. 4–63.

Here, we can see that the magnetization curve for amorphous steel has a very smooth departure from linearity - saturation begins to manifest very gradually. The graph also indicates the point corresponding to the maximum cable current for which the transformer is designed, allowing us to assess the non-linearity of the curve, the resulting flux value and the proximity to saturation.

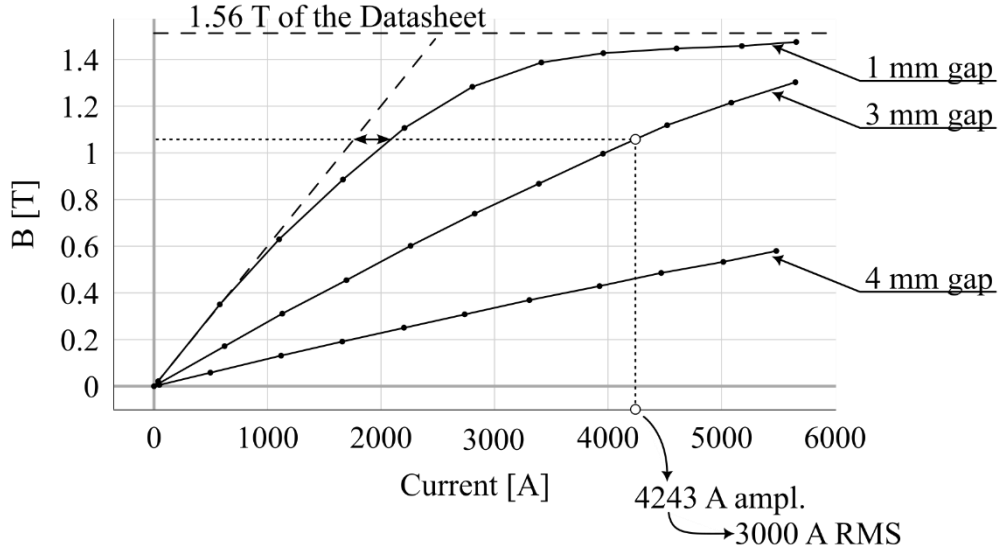

Fig. 4–63 Main magnetization curve of the amorphous steel core.

Also very representative are the graphs shown in Fig. 4–64. Here, we can assess how much the voltage on the transformer deviates from a sinusoid. The upper left part of this figure shows the curves measured on a core featuring 1 mm gap. Even at low currents, the presence of higher harmonics is visible. The voltage curve corresponding to the power current of 3200 A is also constructed in the frequency domain below on the left side of the same figure (part "c") - here a clear peak at 150 Hz can be seen. On the right side of the same figure, curves for a 3 mm gap are plotted, and appear very close to a pure sinusoid, which is evident in the frequency domain as well (part "d" of the same figure).

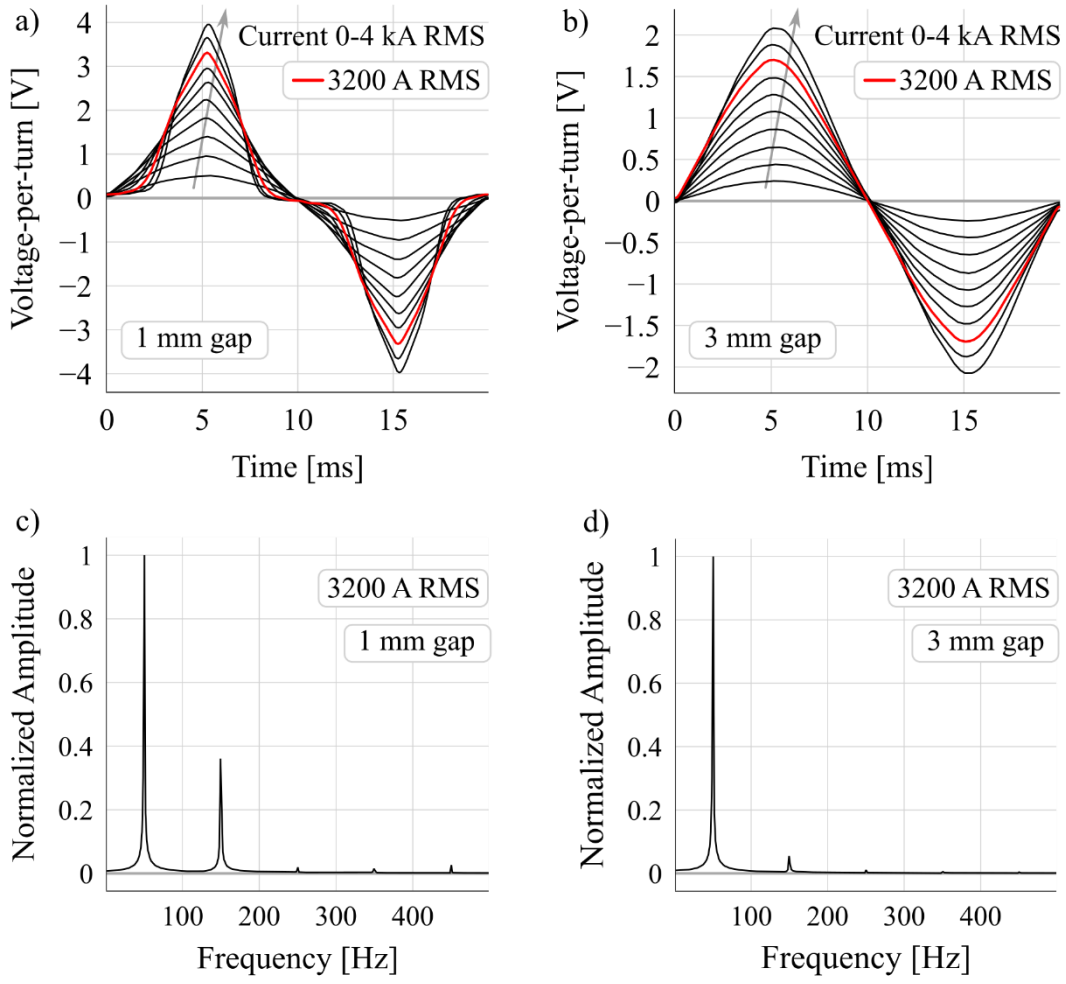

Fig. 4–64 Voltage measured on the winding of HFCT prototypes featuring varying gaps in the process of vibration & noise assessment

In this context, it should be noted that since the displayed voltage curves were reflected on an oscilloscope, it was convenient to compare the emergence of vibrations and changes in acoustic noise, with the deviation of the curve from the sinusoidal shape. As was already noted, a gap of three millimeters was chosen as optimal, both in terms of the transfer function and in terms of the current reserve before the appearance of saturation effects.

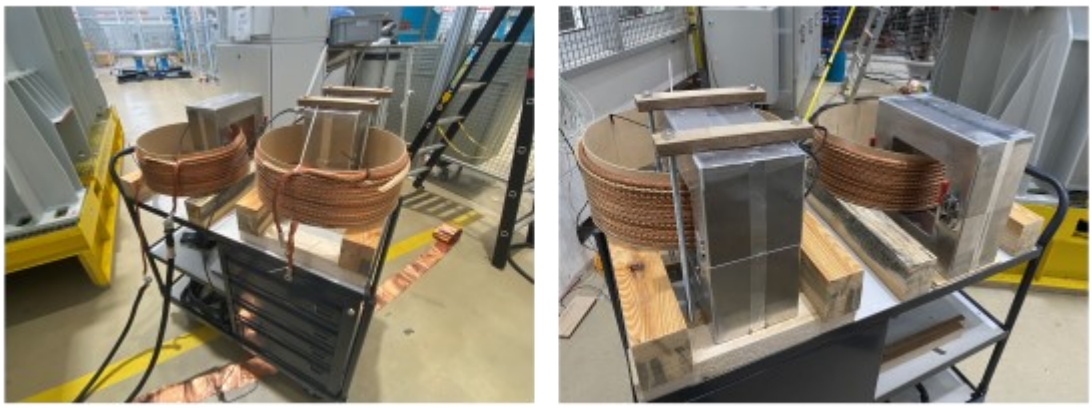

Fig. 4–65 Power current carrying coils

With the gap being fixed, the number of turns was chosen as a compromise between the desired lower cutoff frequency and transfer impedance, as described in the section 4.2 of this chapter.

Another feature that was implemented is the “symmetrical” or “balanced” design of HFCT, that was explained in the section 4.6 of this chapter. The main reason if its use is the advanced noise reduction. Long signal cables, extra-broadband frequency range and low power of measurement signals contribute to hard noise conditions which can be improved by the balancing of the system. In this regard, since a twin-axial cable with a characteristic impedance of 100 Ohms is used, the amplifier's input impedance (measuring resistance) is also set to be equal to 100 Ohms.

The example of the transfer function measured for the final device in the metallic housing (shown on Fig. 4–68) is depicted in Fig. 4–66. The transfer impedance in the passband is approximately 10 V/A.

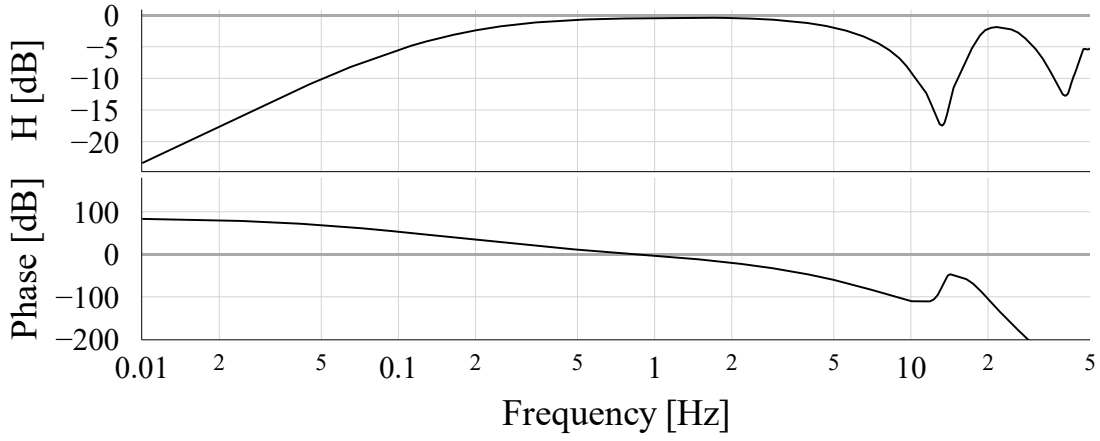

Fig. 4–66 HFCT transfer function (turns-ratio mismatch compensated)

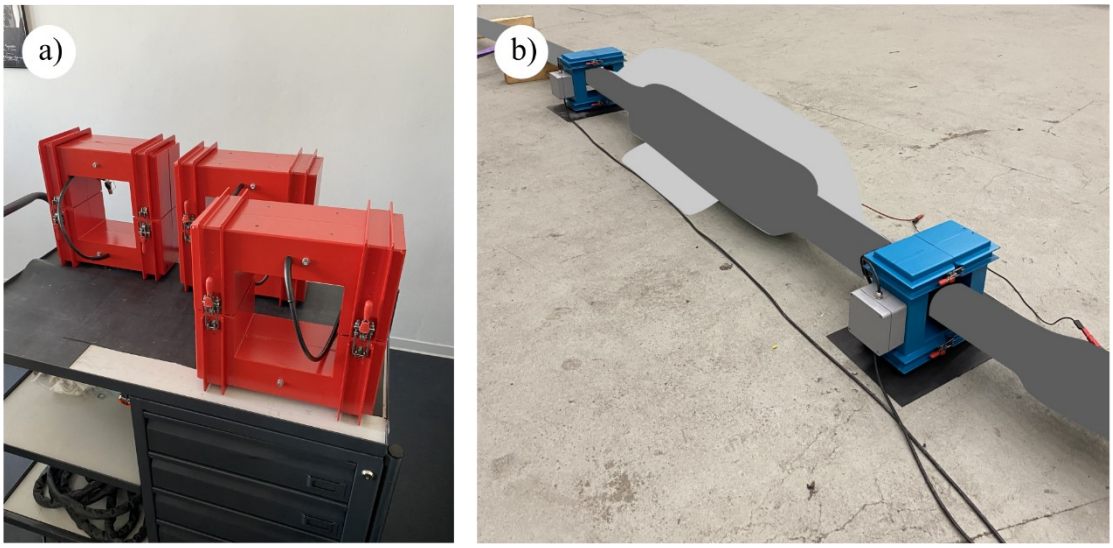

Fig. 4–67 Left: final appearance of HFCT (colour may vary),
right: installation of sensors on a joint during cable PQ testing.
Due to confidentiality reasons, the joint itself is not shown.

In conclusion of this chapter, a few words can be said about quality control. First of all, the obtained transfer function is monitored for all produced HFCTs. Additionally, the frequency-dependent inductance and equivalent resistance of the incoming magnetic cores is measured using an impedance analyzer integrated into a VNA and a special coil-fixture shown in the right part of the Fig. 4–68. This fixture can be conveniently placed on the magnetic core, ensuring consistency in the test winding used. Furthermore, to validate the measurements and ensure that no changes have been made to the VNA settings, an additional calibration is performed using a reference inductance of an air-core toroid.

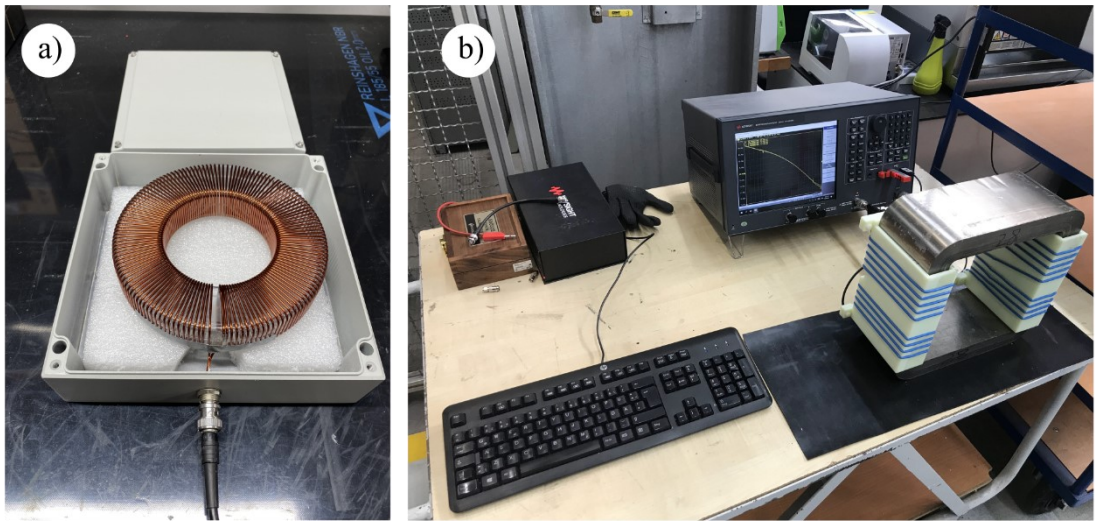

Fig. 4–68 Quality control

5. Chapter:

Signal Separation

5.1 Signal Separation

5.1.1 Objectives and Related Issues

In typical use cases, the PD signals are present only during a rather small portion of time. The aim of the signal separation algorithm is to convert the continuously registered data stream into signal-containing frames and noise-only frames in between. This is necessary, first of all, because each PD will be analyzed separately in the following stages, and secondly, in this way, we can immediately discard the noise frames and therefore significantly reduce the amount of processed data. The realization of the algorithm as part of monitoring system imposes some requirements and issues:

- Algorithm should run in real-time,
- The performed processing should be computationally light enough to be performed at local acquisition hardware with the use of FPGAs (e.g., of hardware in Fig. 7–2),
- The separation should be adaptive to the variations of the noise and adjust automatically. The variation of the noise is not only the alternation of the basic noise level, usually seen on the PRPD pattern. In the context of our problem, it is necessary to look deeper and consider noise as a complex phenomenon, grounded in both stochastic and deterministic processes.
- The maximization of the sensitivity is the objective. At best, even signals that are "buried" in the noise or overlapped with harmonics should be detected. The more accurately and sensitively this cutting is performed, the higher the sensitivity of the system is.
- Both the beginning and the end of the signal should be detected.

The presence of such requirements implies setting aside the amplitude thresholding. For better clarity let us consider the example recordings shown on Fig. 5–1 performed on 110kV HVAC cable with the use of an HFCT. Each recorded signal stream has a valuable PD signal, but also it shows how complex the noise can be. We see both high-frequency noise and relatively low-frequency harmonics, and those that lie close to the frequency range of the signal. The graphs are shown in order of increasing difficulty of distinguishing the signal: In the first plot, the signal differs significantly in frequency from the overall noise stream, while in the third the signal is extremely low in amplitude, and the frequencies contained in it are comparable with the frequency of the continuous interference. All these signals are below the baseline noise level, which means that they will not be separated by

energy or amplitude thresholds and therefore will not be visible on the PRPD plot. On the other hand, it is not too difficult to distinguish these signals by eye. And if so, then there must be ways to extract such signals automatically, the challenge is only in choosing the right approach and the need to keep the calculations easy enough for the hardware.

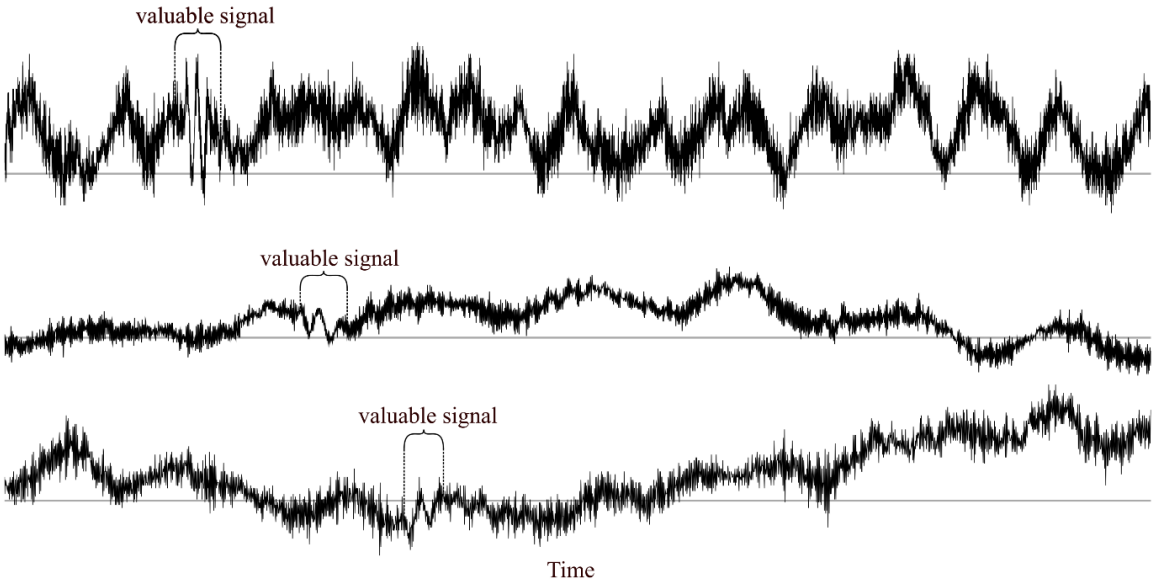

Fig. 5–1 PD signals hidden in the noise.

In contrast to the energy or amplitude threshold, the approach proposed by the co-authors in [Pub. 5] contains two major steps:

- description of the noise profile,
- extraction of the events that fall out of the description, in other words, which cannot be predicted.

A closely related problem is the denoising of the PD recordings is extensively studied by various authors and digital signal processing offers a long row of techniques for performing this task. Even though the addressed topic is alike, most publications' final goal is usually different from ours: they often deal with single records and aim at precise subtraction of the noise component, and most often operation in real-time is not their objective. The detailed comparison of the denoising techniques, or even listing them cannot be part of this paper, because, as it will be shown shortly, the amount of possible signal processing approaches to this problem is very high, and, moreover, each approach has many subspecies. However, it would be useful to study some of them in order to at least get an overview of how the problem is generally approached, what common issues exist, how they are addressed, etc., and to review the signal separation algorithm with this knowledge in the background.

5.1.2 Approaches to Noise Suppression in PD recordings

The description of noise reduction should start with filtering methods, which range from simple Infinite Impulse Response (IIR) lowpass filters to rather sophisticated adaptive solutions. From the very beginning, when choosing a filtration method, it makes sense to deviate from the general case and consider:

- the purpose of the measurement: e.g., conventional measurements of the apparent charge, time-of-arrival localization, shape recognition, etc.
- the environmental conditions: e.g., completely shielded room, low-frequency interferences, high-frequency EMC coupling, etc.
- properties of the equipment used for coupling and recording: analog bandwidth of sensor and recording hardware, sampling frequency, protection from interferences that may couple through the power supply, etc.

The simplest and probably the most commonly used ones are low-pass and band-pass analog and digital filters. In general, IIR filters require much lower order than Finite Impulse Response (FIR) to result in the same performance. Historically, for real-time operation, digital IIR filters were therefore easier to apply due to the smaller number of taps, although currently, the state-of-art FPGAs allow for the application of FIR filters as well. It can be useful if the waveform of the recorded PD should be preserved: FIR filters may be designed to have exactly linear phase, an advantage that IIR filters do not have, except for the digital version of the Bessel analog filter. On the other hand, for post-processing of single recordings, the IIR filters can be more beneficial: when the entire data sequence is available before filtering, it is possible to compensate for the phase shift caused by the IIR filter and have the zero-shift overall.

Let’s consider an example: PDs are registered on a cable line and the task is to detect signals coming from some remote location along the cable and to locate their source via TDR. In this case, signals reaching the sensor will no longer have a high-frequency component, and it makes sense to at least include a low-pass filter to suppress the radio interference, white or bit noise. If the task is performed offline (after data recording), a moving average filter, Savitzky-Golay filter, or IIR low-pass linear filters such as the Chebyshev filter of the second type (with bandstop ripple) or Butterworth filter, are well suited for this. Such filtering is often used in practice because it simplifies the visual perception of data and is very easy to implement [101], [102]. On the other hand, if we are interested in the shape of the PD signal, for example, to determine the type of defect in the equipment located in the

immediate vicinity, such filtering should be approached with caution: PD at the point of origin has a very broad frequency content that can enter the GHz range ([103], [104], [105]) therefore low-pass filtering even with the cut-off of the tens of MHz would alter and to some extent equalize the waveforms.

When the measurement is performed in accordance with IEC60270 for registration of the apparent charge, the bandpass filter has to be applied to meet the recommendations, which are specified as follows:

For wide-band measurements:

- low cut-off frequency: from 30 to 100 kHz,
- high cut-off frequency: less than 1 MHz,
- bandpass: from 100 to 900 kHz,

For narrowband measurements:

- centre frequency: from 50 kHz to 1 MHz,
- bandwidth: from 9 kHz to 30 kHz,

The actual type of the filter is not specified within the standard, it is only mentioned that for wide-band measurements the "adequate attenuation" should be provided outside the bandpass, and for narrowband measurements the attenuation of -20 dB from the bandpass peak value is recommended for the frequencies equal to ±bandwidth with respect to central frequency. Practically this is usually performed with the IIR linear bandpass filters, such as the Chebyshev of the second type, or Butterworth filters [106]. A good case showing the effect of IEC-conventional wide/narrowband filtering of an originally high-frequency PD pulse can be found in [107].

If the measurement is not performed in a shielded room, there is a high chance that apart from white noise the narrow-band interferences will be present in the recording. Radio is a good example of this issue. The row of its frequencies is spread around 100 MHz, which is far above the frequency range of IEC60270-compliant PD measurements. It is also far above the bandpass of the common HFCTs, though this does not necessarily mean that the interference will not be visible in the unfiltered recording – the resonant nature of the device may let these frequencies pass through. The low-frequency harmonics from power electronics (units and tens of kilohertz) and harmonics of the power transformers can be also considered narrow-band interferences. Here again, it is necessary to conclude, whether the interference lies within the frequency range of interest, and if not, then the bandpass filtering can be the easiest solution. Contrarily, if for some reason interference lies within

the frequency range exploited for the measurement of actual signal, and the interference's frequency is known and constant, it can be suppressed by IIR notch filters (or a cascade of them in the case of multiple interferences), or even its adaptive version if the frequencies deviate [108]. Of course, the according frequency components will be suppressed in the signal as well, but sometimes this is acceptable.

These are, of course, the simplest and most convenient filtering methods. However, noise is often a complex issue (e.g., colored noise) and at least partially overlaps with the frequency band of the signal. In this case, filtering can become more sophisticated and adaptive. The possibility to record the noise solely, without the presence of PD signals, enables the use of adaptive filters (Least Mean Squares (LMS) filter), Wiener filters, or spectral subtraction. Usually, PD signals are present only for a small part of the overall recording, during the rest, and the majority of the time only noise is present. Strictly speaking, the task appears to be a vicious circle: to apply an adaptive filter, one must first find and separate the signal from the noisy recording, for example with the amplitude trigger, which cannot be done for the low SNR recording unless the signal is filtered first. In practice, of course, there are ways to break out of this loop, as the task is to separate noise and signal only roughly: one can assign as "noise only" those sections of the recording where no signal is present with a high degree of probability, and the wide zone of uncertainty can be simply ignored. Moreover, if the time when the signal present in the recording is by far lower than the cumulative time the noise-only frames, even when being trained on complete data it is likely that the filter would adapt only to the noisy part of it, and PD signal will remain as a prediction error. Some examples of applying adaptive filtering can be found in [109], [110], [111]. In the design of an adaptive filter, different adaptation algorithms can be used: LMS, Recursive Least Squares (RLS), Least Mean Fourth Algorithm, etc. Different algorithms will have different efficiencies for different disturbances, and the article [113] compares them and offers one that is effective for both Gaussian noise and impulsive interferences.

A good example of implementing Power Spectral Subtraction (PSS) can be found in [112]. Here the PSS first estimates the noise Power Spectral Density (PSD) from the noisy signal during periods of silence, where only noise is present. The estimated noise PSD is then subtracted from the PSD of the noisy signal to obtain an estimate of the PSD of the clean signal and then transform back to the time domain. The main difficulty of the method is in estimating the noise power spectrum accurately, which can be challenging, particularly when the noise is non-stationary or varies over time.

Strictly speaking, an adaptive filter can be constructed based on the knowledge of the shape of the desired signal as well. In other words, if there is a recording of a single PD instance, and it correlates with subsequent instances, then this extracted signal can be used to filter the entire recording, and the parameters of the noise and its variability become less important, as long as it is not correlated with the signal.

If fact there is a dedicated solution for the case when knowledge about the shape of a useful signal (PD) is available, which is matched filter banks [114], [115], [116], [117]. The principle of their operation is simple: the noisy signal is cross-correlated with a time-reversed mock-up of the useful signal. The possibility of practical application depends on whether it is possible to obtain an example of a clean, noise-free signal. It can be a measured signal that was manually selected and denoised, it can result from a mathematical model, or it can be even an arbitrary waveform. The waveform of the PD is subjected to attenuation and dispersion which result from the properties of the signal propagation path from its origin to the measurement location, which can be estimated in some cases. For instance, if there is a mathematical model of a PD-producing equipment, it is possible to draw conclusions about the possible forms of PD. From a practical point of view, creating such a model is difficult in most practical cases. Cable lines may be the simplest subject in terms of mathematical description, compared to, for example, transformers or other electric machines. When there are multiple PD sources at different locations, the pulses themselves will differ from each other due to different propagation paths. The question is only how large the range of possible signal shapes is. In practice, instead of using a single matched filter, a finite set of them is usually implemented, which is called a filter bank. The matched filters within the filter bank are selected to represent the possible variations in the signal. If the matched filters are designed to have equal energy, the filter that best matches the input signal gives maximum output amplitude and can be considered optimal for denoising. In addition, this filter can be made adaptive over time: initially, some ready-made templates are used for filtering to measure and extract PD pulses, and while the system runs the extracted pulses are used to create new improved templates. This approach can be rather beneficial for some applications, such as Time-of-Arrival localization [115], [116].

More robust denoising can be achieved by using decomposition-based methods. A decomposition is essentially breaking down a complex signal into its constituent parts. After decomposition, the newly obtained components are analyzed to get a new insight into features inherent to the data. Clearly there are unlimited ways of separating signal into the

modes, which results in numerous developed denoising approaches. A decomposition usually includes a coordinate transformation, meaning that the data is “projected” onto a new basis system. There are data-independent basis systems where this basis is predefined and the data-dependent (or empirical) there resulting modes are “tailored” to the signal.

The most common data-independent decomposition is the Fourier transform. Though the Wavelet transform offers the possibility to choose the mother wavelet, at the first approximation this method can be considered as data independent. Denoising based on these techniques includes retrieving the series of frequency or wavelet coefficients, thresholding them, and recreation of the denoised signal by the inverse transform [118], [119]. As the actual noise suppression result depends on the thresholding of the coefficients (e.g., hard, soft, adaptive thresholding), the way this is performed plays a major role in the effectiveness of the method. Therefore, a great variety of sub-methods are based on finding the optimal way of setting the thresholding function [118], [120], [121], a good summary of them can be found in [119]. For sure already here a lot of the methods are useful only under the premise that the noise is random, even though this remark is usually not noted explicitly. For example, [119] proposes a wavelet threshold determination method for signal denoising, which considers the interscale correlation between wavelet coefficients and uses it for threshold adjustment. As shown, this concept works perfectly for various signals superimposed with the white Gaussian noise. Nonetheless, any interference that is deterministic, whether it is repetitive or singular, will remain intact.

The use of the classical Discrete Wavelet Transform (DWT) is concerned with a few problems, namely: oscillations, shift variance, aliasing, and lack of directionality. A rather thorough illustration of those can be found in [123]. Therefore, the extensions of the Wavelet transforms are often used. The shift variance, for example, can be addressed by the Undecimated Discrete Wavelet Transform (UDWT). The shift-variance means that a small shift of the signal greatly perturbs the wavelet coefficients and leads to a complicated relationship between the wavelet coefficients of the original signal and its shifted instance. From a practical point of view, it means that denoising performance can be affected by the shift in the starting position of the signal. The UDWT is a type of wavelet transform that does not implement downsampling after each filtering stage. This technique has a long history and was independently published by various author groups under different names. Therefore, in literature, it could be also referred to as the algorithme à trous [124], [125], the Overcomplete DWT (ODWT) [127], the shift-invariant DWT (SIDWT) [128], and

discrete wavelet frames (DWFs) [129]. The article [122] shows variances in the realization of this same idea. In the field of PD denoising, this technique is used quite often, for example in [130], [131] in comparison with other denoising techniques for the cases of gaussian, harmonic, and impulsive distortions.

As was mentioned the actual denoising effect is usually achieved by threshold, filtering, or, generally speaking, modifying the wavelet coefficients. In this case, the aliasing effect will take place. The way how the transformation is performed (iterated downsampling operations, filter banks) results in a delicate balance between the forward and inverse transforms, which is corrupted once the coefficients are modified. The result of the aliasing is the artifacts in the reconstructed signals. A further step in resolving this and the other aforementioned DWT issues can be made using complex wavelets, via the method named Complex Wavelet Transform. The actual implementation of the forward and inverse transforms for complex wavelets can be done with the Dual-Tree framework [132], [133], [134]. The idea behind it is rather simple: it utilizes two real DWTs to obtain the real and imaginary parts of the transform, allowing for the use of real filters without complex arithmetic in its implementation. The inversion of Dual-Tree Complex Wavelet Transform (DT-CWT) is straightforward and is done via the inverse of each of the two real DWTs, which leads to two real signals combined through averaging to produce the final output. Another step in this direction is to select wavelets in a way that they form a Hilbert transform pair [135]. Application of this method in the field of PD denoising can be found in [136] for the case of white noise.

Data-dependent decompositions split the signal into its constituent components based on the signal's properties. The decomposition process is driven by the data and does not rely on prior knowledge of the signal's underlying structure or frequency content. The most common examples of data-dependent decompositions are Empirical Mode Decomposition (EMD) and Singular Value Decomposition (SVD), which result in subsequent denoising techniques. In the simplest case of EMD-based approach, the original signal is decomposed until some stop criteria are fulfilled, which is followed by the reconstruction based on a limited number of selected components. The SVD-based denoising is alike but has the additional step of forming the Hankel-Matrix, and therefore in contrast to EMD, the decomposition is performed not on the original signal, but on its Hankel-Matrix representation instead. The way how decomposition is performed and how the components for reconstruction are selected determine whether PD signal or noise is the actual result of

this reconstruction. For example, in the EMD decomposition the first modes are responsible for the high-frequency content of the signal [137]. Therefore, if the recording contains high-frequency narrow-band noise and lower-frequency PD, the result of the reconstruction based on the first components will indeed be the interference. Contrarily, the SVD does not have this pronounced frequency-related effect [138], [139]. At the same time, different relations between signal and noise should be taken into account: both noise and signal can be lower, higher, or equal in frequency and in magnitude compared to each other [119]. Therefore, denoising in the general case, when SNR and frequency content of the noise are voluntary, can be a task that is hard to automate with the use of the pure EMD or SVD, or even more sophisticated algorithms based on them. Surely the straightforward denoising through reconstruction is indeed a simple case of denoising. Examples of more sophisticated approaches can be found in the following publications:

- The article [140] proposes the use of the Complementary Ensemble Empirical Mode Decomposition (CEEMD) with the use of the thresholding inherent from the Wavelet-based denoising.

- The EMD decomposition is sometimes extended to the Hilbert-Huang transform: once the signal is decomposed into Intrinsic Mode Functions (IMFs), the Hilbert transform is applied to each IMF to generate its associated analytic signal. Then the Hilbert spectrum can be obtained, which will represent the distribution of energy in the signal as a function of time and frequency, however, this is used rather for signal analyses and source recognition than for denoising purposes [141], [142], [143].

- One of the latest developed methods introduced in 2014 by [144] is the Variational Mode Decomposition has the benefit of being more robust to the mode mixing [146]. The constraint that drives this method is that each resulting IMF corresponds to a certain distinct frequency band. Implementation of this method for SNR enhancement of PD recording can be found in [145]. From one point of view, mode mixing is a global problem of the EMD, and addressing it is highly desirable, however, it's possible to foresee certain drawbacks, for example, an unattenuated PD with broadband frequency content would therefore be separated into different IMFs and mixed there with noise.

The SVD itself can be used as an add-on method on the already pre-processed signal. The examples shown below are listed not chronologically, but rather in the increasing complexity of pre-processing.

- In the articles [149] consider using a sliding window and constructing Hankel-Matrix and performing SVD within it for each shift – by analogy to the short-time Fourier transform (STFT), this method is called a "short-time SVD". The Minimum Description Length (MDL) criterium is used for the automatic selection of the singular values used for reconstruction. Even though the paper aims at white noise suppression only, the concept of short-time SVD with MDL is rather interesting for a more general case. The related approach is found in [147], where the windows for SVD are generated at random positions and with random widths so that the particle swarm algorithm can optimize these values.

- The article [148] goes further and proposes, in a nutshell, to first pre-process the signal by STFT and apply the SVD on the result. Like in the [149] the MDL criterium is used for the automatic rule for the selection of the optimal number of components for reconstruction.

- In [150] the SVD is used together with S-transform. The S-transform is a more general version of the Short-Time Fourier Transform (STFT). In contrast to STFT, which computes a series of Fourier transforms for overlapping windows with defined length, the S-transform uses a variable window size, which makes it more suitable for analysing non-stationary signals with time-varying frequency content – an actual benefit for our application. The procedure described in the publication implies the use of S-transform to derive a two-dimensional time-frequency matrix of a noisy signal, which is subjected to the common SVD with the order selected by the additionally proposed algorithm and reconstructed back to the time domain as the denoised signal.

- In [151] the mixture method of DT-CWT, Hankel matrix, and SVD is proposed. Firstly, the DT-CWT is used to decompose the signal into a set of sublayers. For each of them, the Hankel Matrix is built from the magnitudes of the complex wavelet coefficients, and then the SVD is applied to it. The article shows the evaluation for multiple recordings and shows that the resulting singular values for some of the decomposition levels are rather stable, and therefore can efficiently distinguish PDs.

- From a computational effectiveness perspective, there exists a faster version of the SVD technique, namely a fast-Hankel singular value decomposition (H-FSVD) [152], [153]. In the essence, the Hankel matrix is first tridiagonalized by the Lanczos method after which the SVD is computed for the tridiagnolized matrices using the twisted factorization method.

At the same time, in contrast to adding the pre-processing steps to SVD shown above, one can shift the aim to analysing the result of the SVD:

- In [139] a common Hankel matrix is subjected to singular value decomposition (SVD). The interesting point is that subsequently the K-means algorithm is used to extract the singular values that correspond to the narrowband interference in an adaptive manner.

- In [154] SVD is used for dimensionality reduction before subsequent clustering.

Linear Predictive Coding (LPC) is not typically referred to as a "decomposition technique" but can be used to decompose a signal into set of features. It is a widely used technique, mainly used for speech and audio signal processing. It is known since the 1950th but became extensively developed and used since the late 1960th for telecommunications [155]. In this regard, it was used for speech compression, as the growth of the telecommunication industry and introduction of the commercial cellular networks required the reduction of the bit rate of transmission while preserving the quality of the speech. Nowadays LPC is commonly used for speech coding and compression in various applications, including voice over IP (VoIP), digital voice recording, speech synthesis, speech recognition.

Linear prediction is a mathematical method for analysing time series data, which estimates future values of a signal as a linear combination of past values. The coefficients of the linear combination are calculated using an analysis window of a fixed length. The number of previous samples (or coefficients) used in the prediction is called the order of the prediction. In voice transmission application, for instance, coefficients can represent the spectral envelope of the speech signal, which can be used to reconstruct the original speech signal at the receiver end.

Even though the initial field of implementation of LPC was far from High-Voltage technology, it may serve as an additional mathematical toolbox for working with the PD recordings and is implemented in a row of publications, which we will discuss further.

Before we begin, it is worth noting the analogy between working with PD recordings and speech processing. In both cases, the goal is to provide a compact and accurate description of certain events (letters/PDs). There is one more rather important similarity: speech transmission was developed as a real-time application, just like the separation of the PDs should be, only the sampling rate in our case is about 30 thousand higher (8kHz – for speech/250 MHz – for PDs).

It is possible to denote at least several applications in which LPC is used with respect to PD signals. First of all, it is possible to use LPC for noise filtering and extracting the clearer pulse shape:

- In [156] the LPC is used deliberately within the task of PD location on power cables. The LPC itself is used for noise suppression: here the main idea behind is in taking the advantage of the certain correlation between the signal values to trace its waveform. The authors draw the conclusion that is important in our task:

  "**[**LPC**]** technique provides a very good way of tracing a signal when it is difficult to determine where such a signal started or terminated. **[]** This process can be considered as an adaptive filtration for the recovery of a signal. The greatest advantage of this prediction over the existing adaptive filtrations is that it does not require a simulated discharge for calculation of its coefficients, since the coefficients of this system are calculated from the signal alone."

Secondly, the LPC can be used for the detection of the signal start in TDR and TDR-related applications:

- In the [157] the task of source location is concerned, but this time in a transformer and with the use of acoustic signals. Alike as in the case of the cable lines, within the use of the TDR or Time-of-Arrival methods the detection of the signal start can be used, and the more precise this detection is, the more accurate is the result. Here the LPC is implemented for fulfilling exactly the task of start-of-the-signal detection. The mechanism here is remarkably simple: The LPC prediction of the future samples is running permanently, and when the signal starts its emergence cannot be foreseen based on the previous samples, therefore it yields an error between the predicted sample and the actual one. This error is called a residual within the publication. After the first few samples, the signal starts to appear in the past samples, which means that the next samples again can be predicted, and the residual decreases.

In contrast to the two previous more narrow applications LPC can be used for the general encoding of the PD waveform, or, in other words, describing the PD pulse by a feature vector. Usually, this is followed by further dimensionality reduction with Principal Component Analysis (PCA) and applying clustering on the resulting low-dimensional dataset. In this way, for example, the multi-source separation task is solved, so that PD clusters of different origins can be separated from the noise and from each other:

- [158] presents the study on the separation of artificial PDs sources inside the GIS and 35kV Transformer. Here instead of the common linear prediction coefficients the Linear Prediction Cepstrum Coefficients (LPCC) are used for 12th-order feature vector derivation, which is followed by PCA to reduce dimensionality to the 2-D space and the Isolation Forest Algorithm for further clustering.

- In [159] LPC is used for separating the signal and noise-only frames – a task that is closely related to the PD signal separation that we want to achieve – however in this case it is implemented at a rather late stage. The procedure explained includes the derivation of essential features of the signal shape, reducing the dimensionality via the PCA, clustering the resulting data set, and only then the separation of the noise frames from the signal-containing ones. A criterion for separation is the asymmetry of the LPC residual: while the residual distribution is symmetric for the pure noise, the appearance of a PD signal disrupts this equilibrium and introduces skewness.

It is easy to see the parallels between the LPC feature vectors, the components of SVD, and intrinsic modes of the EMD. Moreover, for example, signal reconstruction from PCA-processed LPC feature vector and from the first components of SVD would refer to the most significant modes of the signal. The intention of this comparison is to show that the LPC approach for PD signal processing is neither contradictory to the decomposition approaches that we considered before nor completely different from them. On the contrary, it can be considered a computationally effective, or, in other words, real-time applicable way of describing a signal with the low-dimensional vector.

5.1.3 Signal Separation Algorithm

The signal separation algorithm designed within the framework of LPC was designed and described by the co-authors in [Pub. 5] and is also denoted in [Pat. 4]. Here, I would like to take the opportunity to review it again with a bit more detail and slightly different focus. The main algorithm can be outlined as follows:

The raw samples coming from the digitizer are grouped into overlapping frames. The frame width may vary, e.g., we can specify 128 samples for a sampling rate of 4 ns; the overlap constitutes half of this window. A vector of two predictor coefficients $\vec{\alpha} = (\alpha_1, \alpha_2)^T$ is calculated for each frame. The calculation of them is done in the following way: the estimate of the future sample $\hat{x}(n)$ of a signal is based on a weighted sum of previous samples and yields a certain residual *e(n)*:

$$e(n) = x(n) - \hat{x}(n) = x(n) - \sum_{k=1}^{p} \alpha_k \cdot x(n-k) \tag{5.1}$$

The weights in the summation α_k are the predictor coefficients. The finding of the best predictor coefficients which give the most accurate prediction is done by minimizing the squared error E defined by Eq. (5.2) by setting partial derivatives of it to zero and solving the resulting system of p equations and p unknowns.

$$E = \sum_{n=1}^{N} e^2(n) = \sum_{n=1}^{N} \left[x(n) - \sum_{k=1}^{p} \alpha_k \cdot x(n-k) \right]^2 \tag{5.2}$$

The solution of the such system can be found with direct and iterative methods, well described in [160], but probably the most popular is the Levinson-Durbin recursion.

Let us make an intermediate summary: we obtain for each time frame two predictor coefficients (one feature vector) that describe its content. For now, we do not know which frames contain signals and which ones have noise-only content. Here we have to make a premise that is likely to be valid in most real cases: the frames with the lowest energies contain only noise. Indeed, even in the case of mixed noise sources, superposition with the uncorrelated signal is likely to result in an increase in the frame energy. Therefore, a minor percentage (e.g., 5%) of the accumulated frames with the lowest energies are assigned to the noise-only dataset. The predictor coefficients of these frames form a bivariate distribution with mean $\vec{\mu}$ and covariance matrix $\sum$. This would be the first description of the actual measurement noise. The predictor coefficients of the next upcoming frames are compared with this description. This comparison is performed by Mahalanobis distance *c*:

$$c = \sqrt{(\vec{\alpha} - \vec{\mu})\Sigma^{-1}(\vec{\alpha} - \vec{\mu})^{\mathbf{T}}} \tag{5.3}$$

Mahalanobis distance is a statistical measure that quantifies the distance between a point and a distribution, which can be used, for example, measure the similarity between an observation and a reference dataset. In simple terms, the Mahalanobis distance measures how many standard deviations away an observation is from the mean of a distribution, in a

direction that takes into account the correlations between the variables. It is useful for identifying outliers or anomalous observations in multivariate datasets, which is literally our task.

Now we can set an arbitrary threshold for Mahalanobis distance equal to a selected number of standard deviations σ, e.g., $\sigma = 5$. Therefore, the frames that result in the points at the greater distances are selected as signal-containing and saved for further post-processing. The ones that are below the threshold are rejected.

With the principle of the separation algorithm being explained, I want to show several examples of its work with different recordings. Following the usual approach in such cases, in the **first** example we will start with a signal overlapped with white noise (Fig. 5–2). For simplicity, we will take a decaying sine wave with a frequency of 1 MHz (Fig. 5–2, bottom graph) and add white noise to it (standard normal distribution, with zero mean and a standard deviation of one). The sampling frequency is 250 MHz. Although the SNR of the first half-period reaches two in this example, it is quite difficult to distinguish the signal with an eye without zooming and navigating along the recording, and the use of an amplitude trigger is impossible, at least without prior filtering.

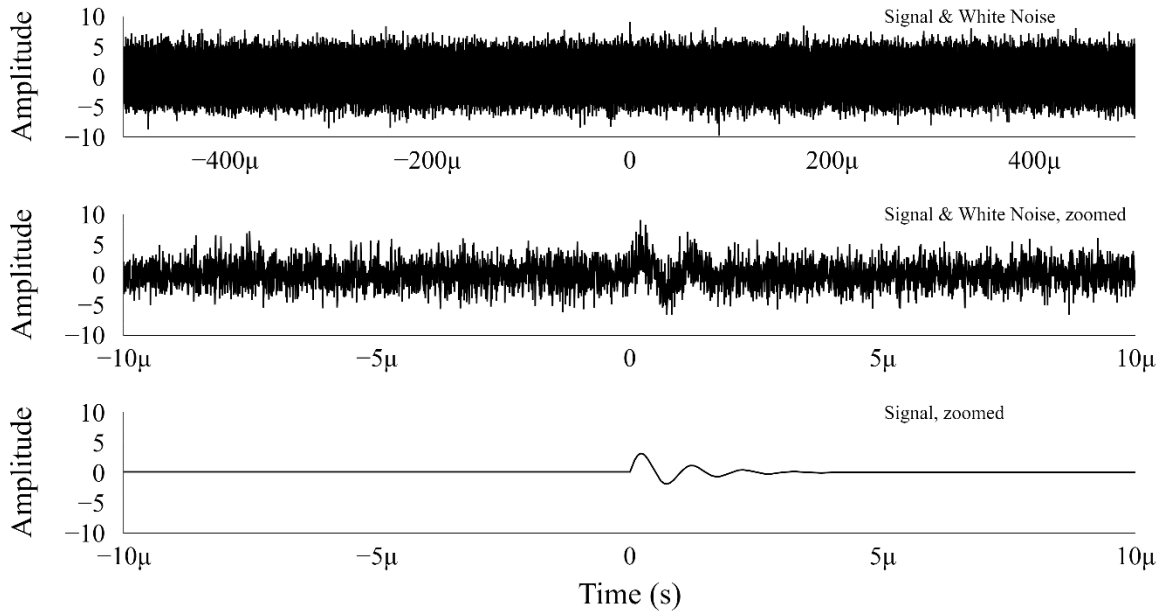

Fig. 5–2 Example 1, decaying sine wave hidden in the white noise.

The lower part of the Fig. 5–3 reveals a few plots essential for the algorithm: separated event highlighted in red on the uppermost plot, then both predictor coefficients α_1 and α_2, squared Mahalanobis distance at the lower one. It can be observed that the Mahalanobis distance exhibits a clear peak upon the occurrence of a signal, and in addition, the threshold value

can be specified as a number of standard deviations. The resulting distribution of the predictor coefficients is depicted in Fig. 5–4, where it can be seen that the obtained coefficients for the frames containing the event lie beyond 5 standard deviations.

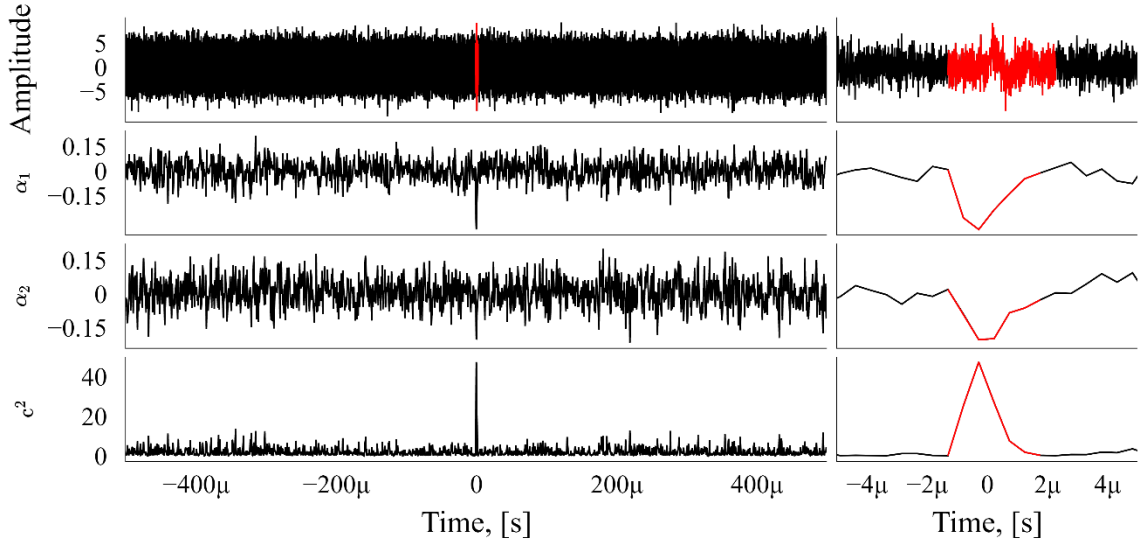

Fig. 5–3 Example 1; from top to bottom: original noisy recording, two predictor coefficients, squared Mahalanobis distance. Separated signal is marked in red.

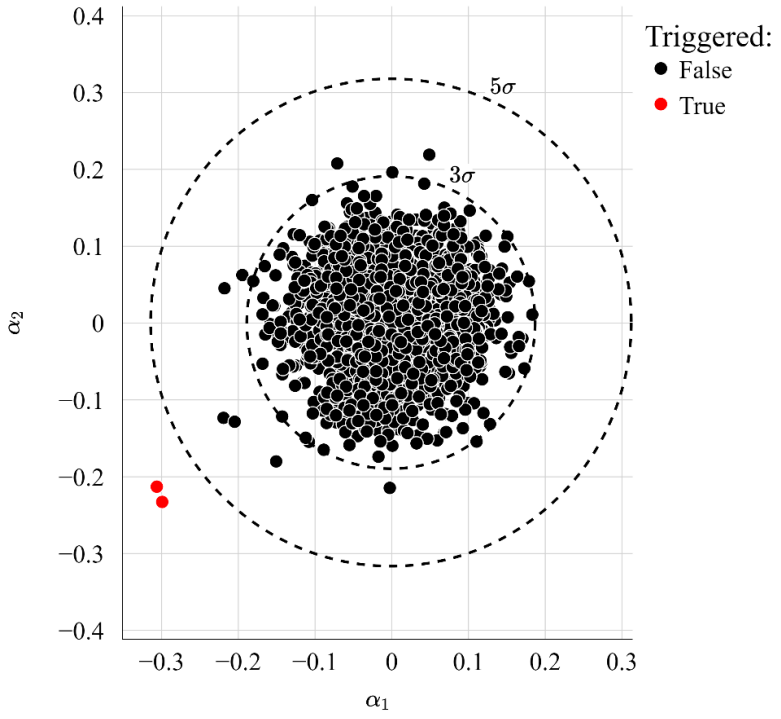

Fig. 5–4 Example 1; Distribution of the predictor coefficients

In the **second** example, I am using a signal that more closely resembles a real PD. Initially, a rectangular pulse is filtered by a low-frequency band-pass filter (10 kHz – 1 MHz), shown below in the Fig. 5–5, which “transforms” the original pulse into a pulse that has “traveled along the cable line and is measured by AC-coupled equipment ” – therefore no DC content

is left. As in the previous example, white noise is superimposed on the recording, as shown in Fig. 5–6. Additionally, prior to applying the algorithm, the signal undergoes downsampling by a factor of four, since the initial sampling frequency of 250 MHz is excessively high compared to the low-frequency signal. Without this step, the predictor coefficients of the noise and signal frames will be closer.

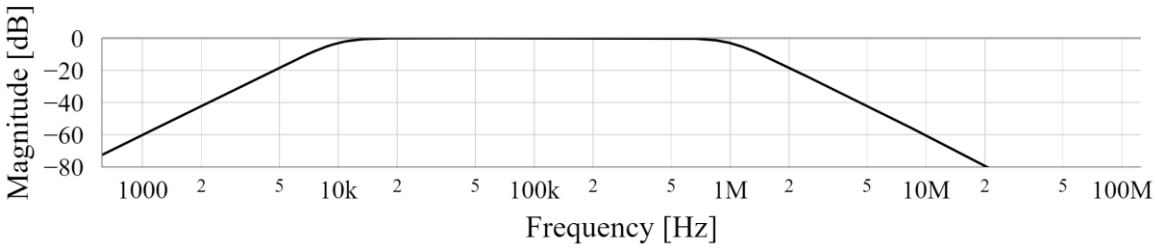

Fig. 5–5 Example 2; Frequency response of the used band-pass filter

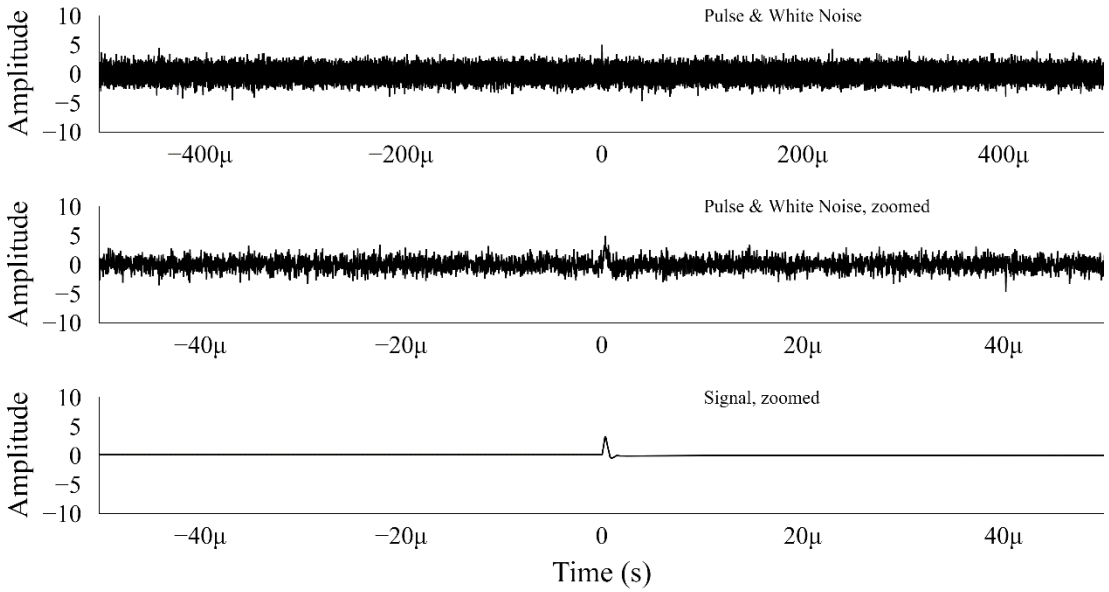

Fig. 5–6 Example 2; PD-shaped pulse hidden in the white noise.

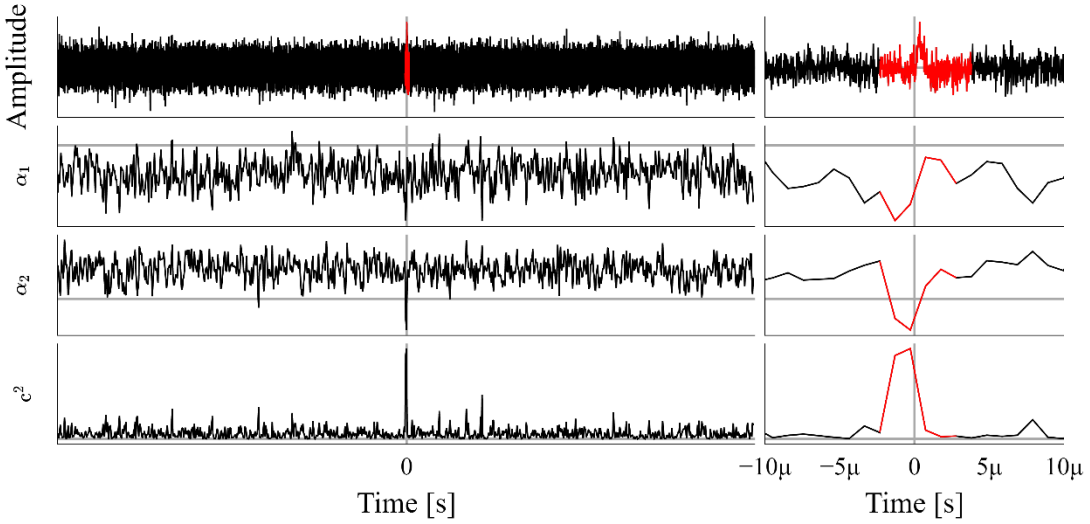

Fig. 5–7 Example 2; from top to bottom: original noisy recording, two predictor coefficients, squared Mahalanobis distance. Separated signal is marked in red.

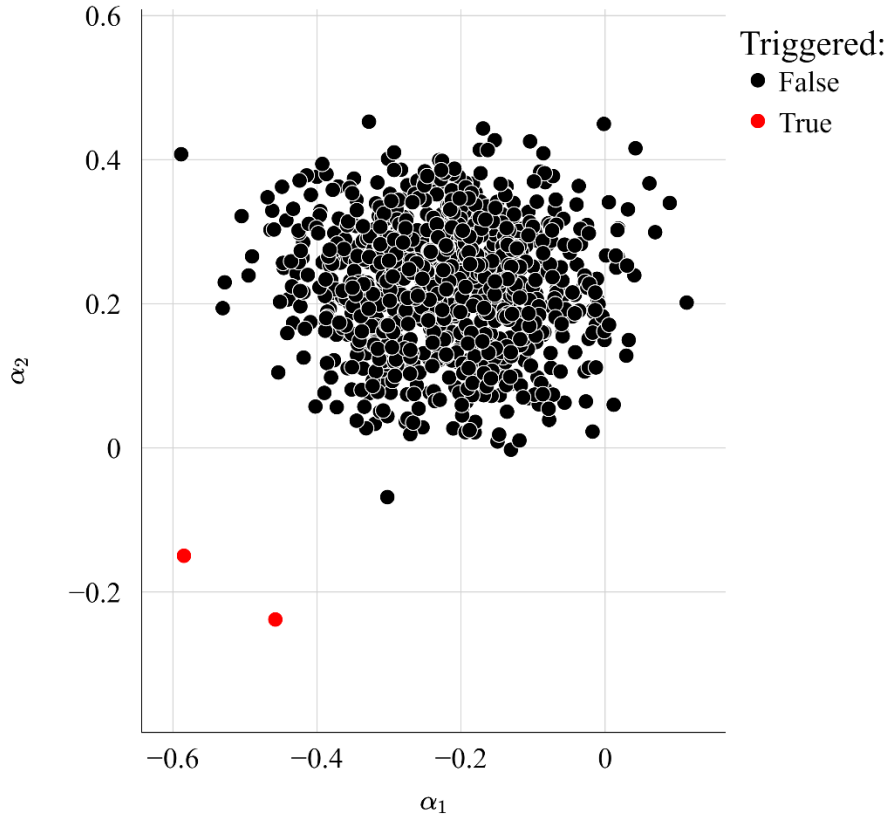

In the **third** example, I use a signal that have further limited bandwidth, both on the high frequencies – representing a longer propagation path through the transmission cable – and on the low frequencies, reflecting inductive sensor coupling. In addition to this, the recording is overlaid with a mixture of several narrow-band interferences, which are both above and below the signal frequency band. This situation is more complex, and it should be noted that in the application of LPC pipeline, it was necessary to include a warping factor (equal to 0.8 in this example), since without it, the resolution of low frequencies is not sufficient for effective signal separation.

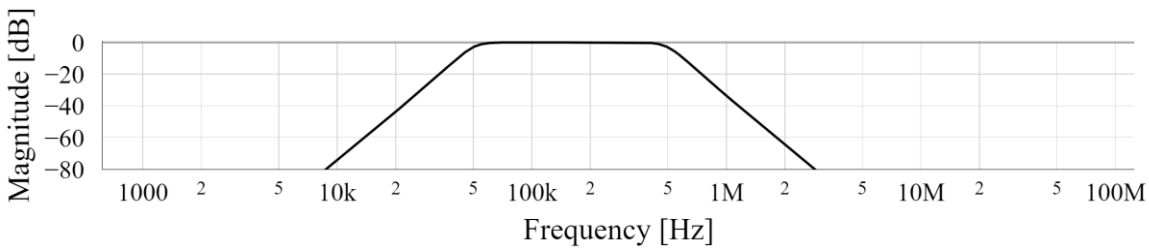

Fig. 5–8 Example 3; Distribution of the predictor coefficients.

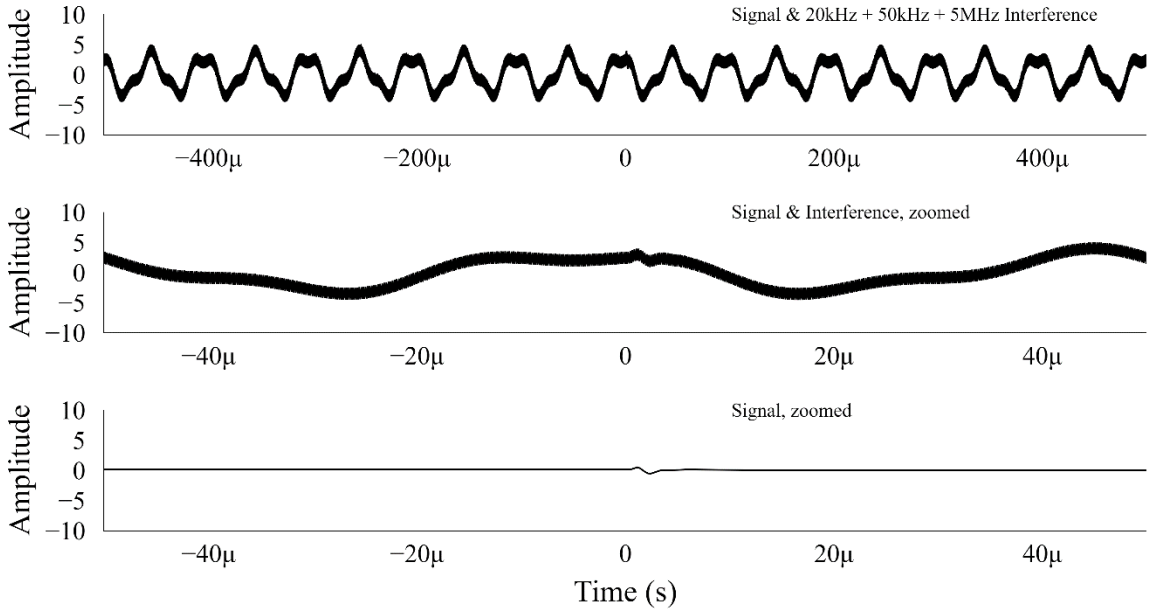

Fig. 5–9 Example 3; PD-shaped pulse hidden in the mixture of narrow-band interferences.

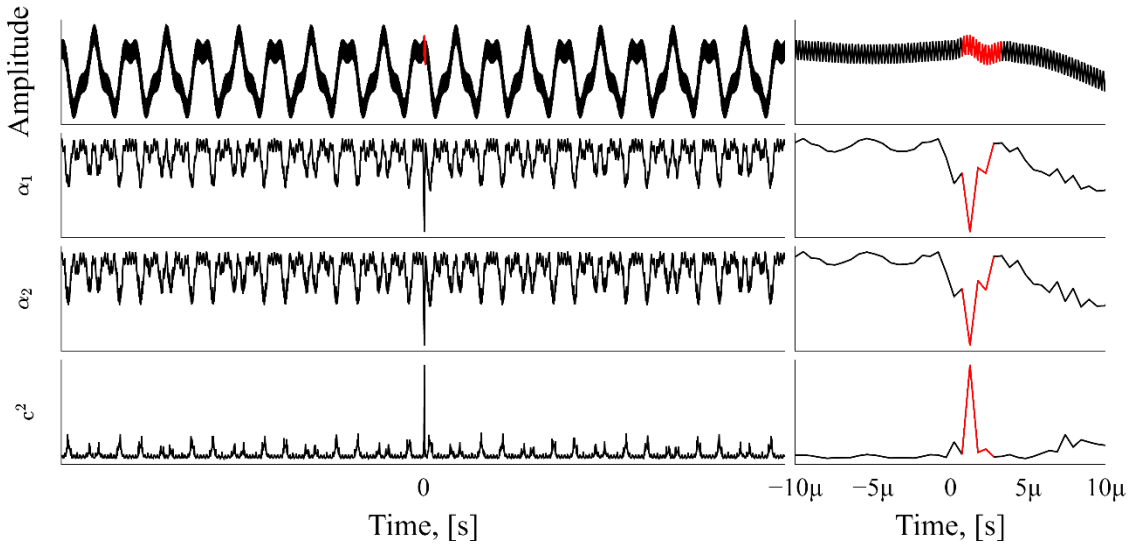

Fig. 5–10 Example 3; from top to bottom: original noisy recording, two predictor coefficients, squared Mahalanobis distance. Separated signal is marked in red.

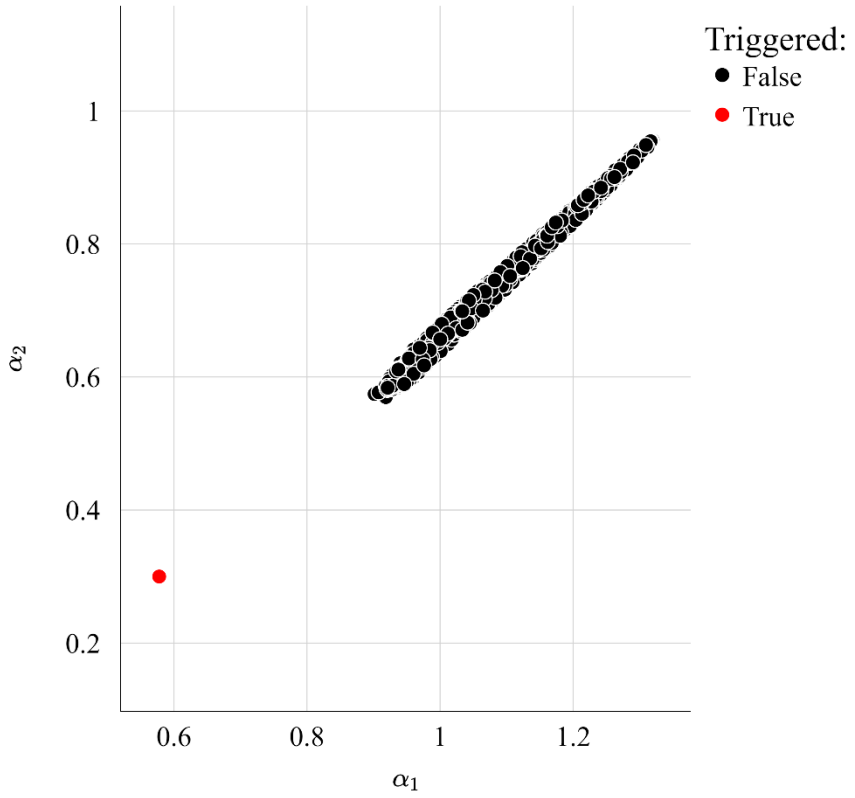

Fig. 5–11 Example 3; Distribution of the predictor coefficients.

In the last, **fourth**, example, I will demonstrate a recording actually made on an underground 110 kV cable line using a HFCT to couple the signal. This line and the equipment installed on it are detailed further in Chapter 8: On-site tests. The recording, made at the line terminations, contains signals with relatively high-magnitude (possibly PDs) apparently occurring near the terminations somewhere at the substation; they then propagate along the cable, are reflected at the joints of the first cross-bonding group propagate backwards and are registered again as much smaller signals. Therefore, the recording additionally contains a series of small-magnitude "reflection" signals which got attenuated while travelling through the cable. This recording is interesting due to its combination of large high-frequency signals and small low-frequency signals. These signals being separated by the algorithm are shown in Fig. 5–13: here we can observe the original signals (b), (e), (f) and the reflected signals (c), (d). Additionally, there are signals that are falsely identified. This example is quite complex for the current version of the signal separation algorithm, and the separation of coefficients on the diagram is less unequivocal than in previous examples, hence the threshold value had to be set carefully – nonetheless, the price of identifying reflections was the registration of some false signals.

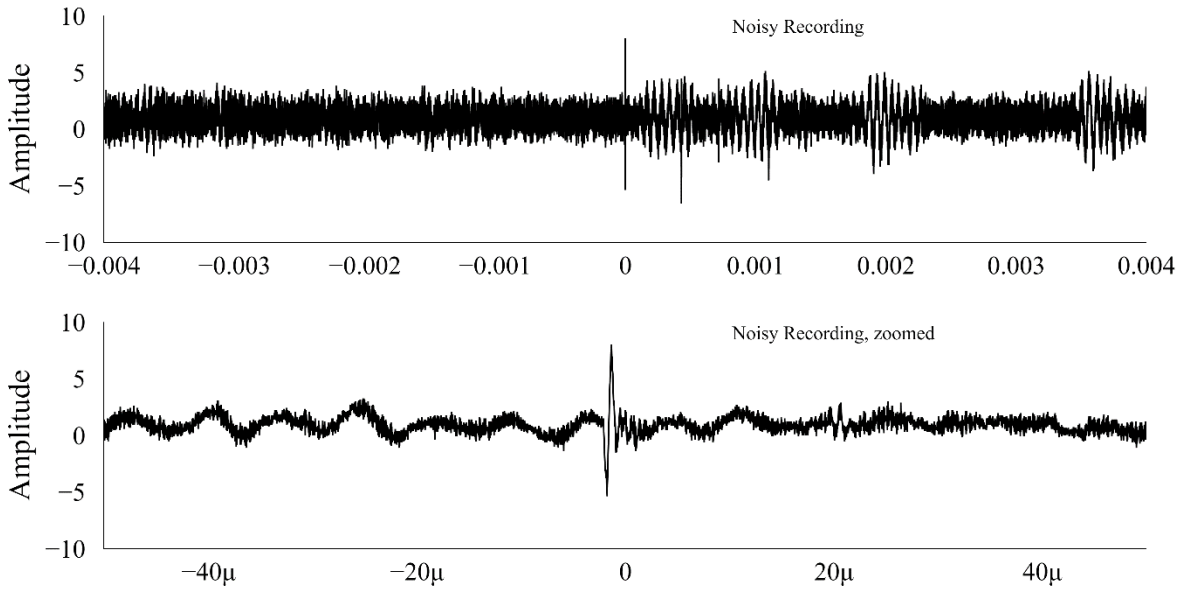

Fig. 5–12 Example 4; Recording from the 110 kV AC line

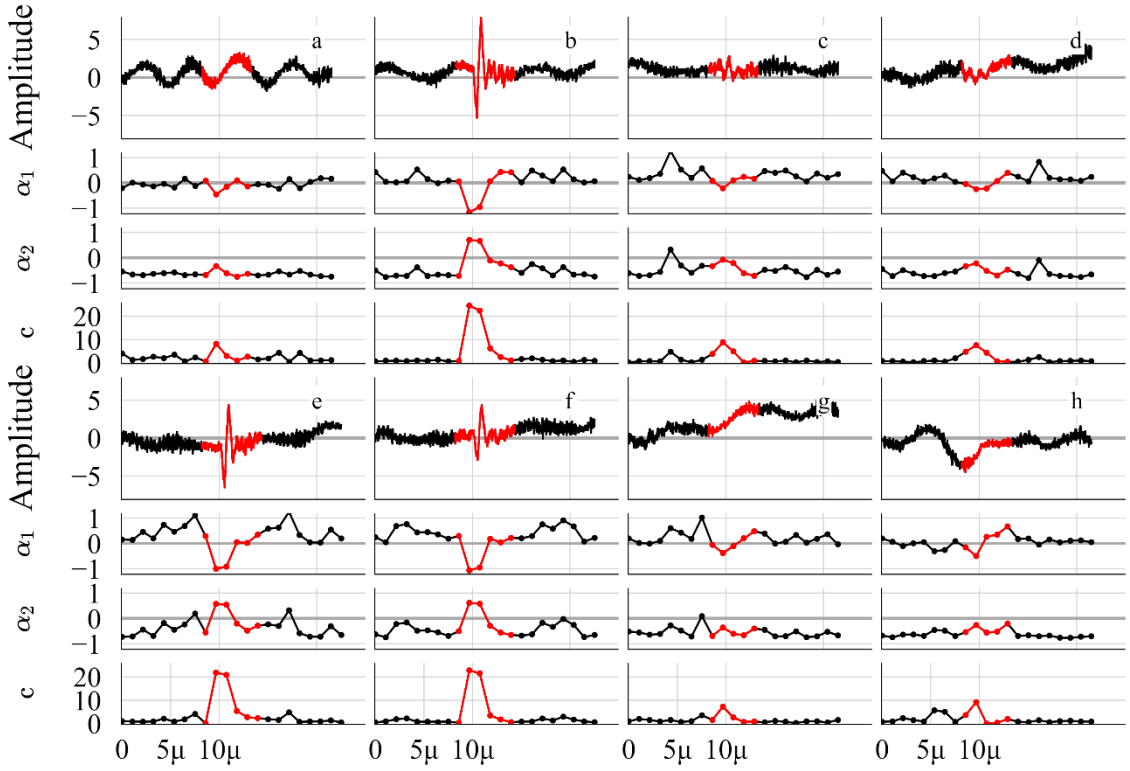

Fig. 5–13 Example 4; Separated frames with signals, two predictor coefficients, squared Mahalanobis distance. Separated signal is marked in red.

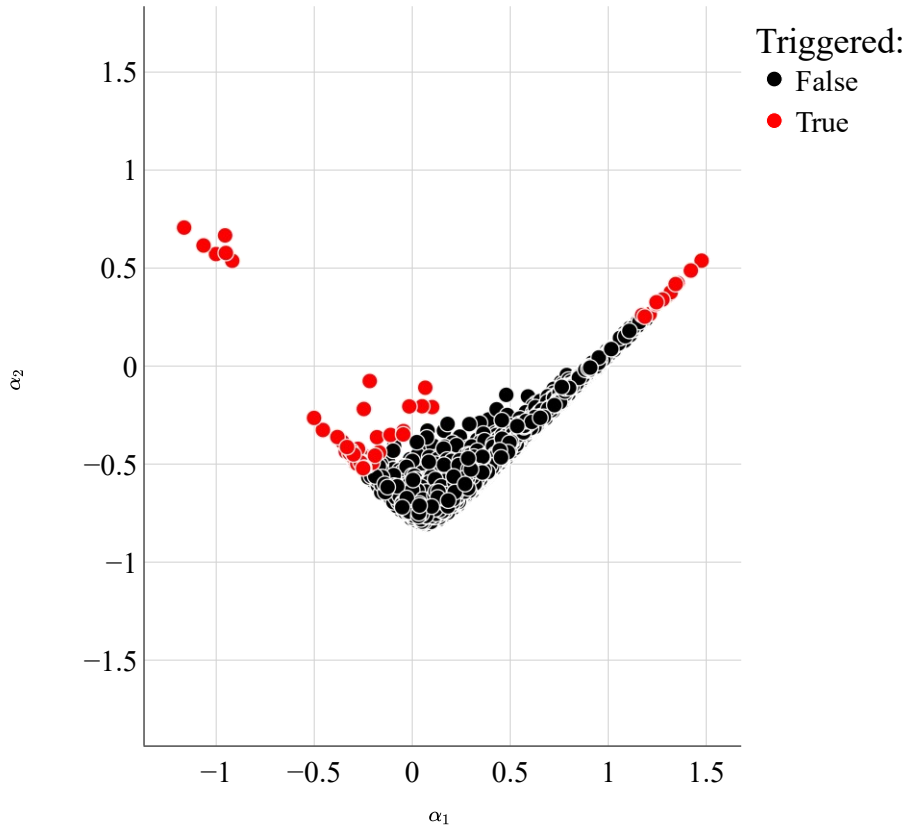

Fig. 5–14 Example 4; Distribution of the predictor coefficients.

6. Chapter:

Localization

6.1 Attenuation

Before we start discussing localization, it's important to say a few words about attenuation and dispersion of signals in a cable. Simply put, a power cable acts like a low-pass filter. As will be described in more detail in the "Laboratory Tests" chapter (Section 7.4, Line attenuation estimation), there are several loss mechanisms that contribute to attenuation, which "kick in" gradually along with frequency increase [169]. At low frequencies, the main contribution to the overall loss budget is given by the skin effect losses. The dielectric losses start to become pronounced as we approach the megahertz range. At a frequency of several megahertz, losses in the semiconductive screens come into play, leading to a sharp increase in signal attenuation in the cable. Moreover, since the properties of these layers are not provided in datasheets and vary from cable to cable, it's difficult to predict in advance at which frequency their influence will become predominant. Along with the increase in cable attenuation, reflection from joints, even straight ones, also increases.

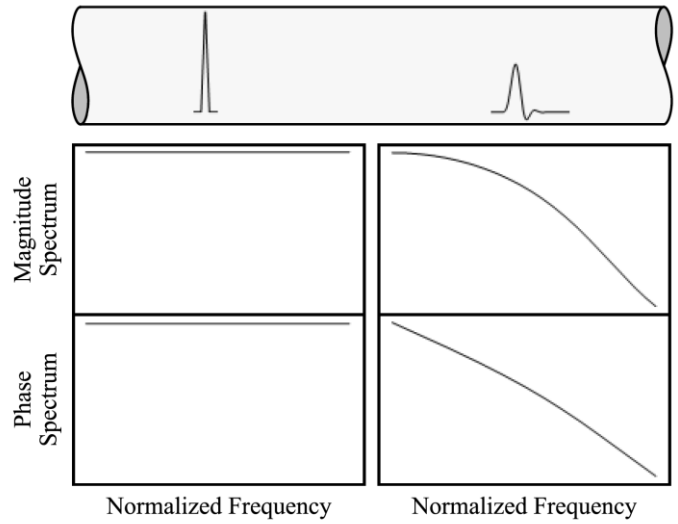

Fig. 6–1 Qualitative time-domain signals (top), magnitude and phase spectra of a propagating pulse (bottom), reused from [Pub. 1].

Fig. 6–1 shows the qualitative timedomain signals as well as magnitude and phase spectra of a PD at its origin and after travelling through the power cable. In the left part of Fig. 6–1 a pulse at the point-of-origin is shown, which features broad (almost flat) magnitude spectra and a constant phase. After travelling a certain length through the coaxial cable, the pulse is damped and the frequency components are shifted. Along with attenuation the signal undergoes dispersion: since higher frequencies propagate slower than lower frequencies, the signal becomes wider as it propagates through the cable. The magnitude spectrum shows

the typical low pass characteristics and the phase spectrum results from the difference in propagation speeds (Fig. 6–1, right plots).

6.2 Basic Idea

The task of PD localization can be addressed with reflectometry, e.g., as in [161] and [162]. However, this approach may lead to the low sensitivity: the original PD signal must be sufficiently large so that both the direct and reflected pulses will be registered. There are also methods based on synchronous measurements [163], [164], [165], which, obviously, require synchronizing equipment and thus complicate the practical implementation of the system. Therefore, this study uses a potentially more economical approach that is based on analyzing the frequency content of the acquired pulses.

The main principle of frequency-based signal localization is illustrated in Fig. 6–2. Here, a defect (shown as the red lightning symbol) along the monitored cable section generates a PD signal that splits into two not necessarily equal currents, one of which travels towards the measurement location A at one section end and the other travels towards B at the other end. As each of these currents travels through the cable, it is affected by attenuation and dispersion (in this simple example we are not yet considering impedance mismatches at the cable accessories).

The two outer weights on each side of the scale in Fig. 6–2 represent the measured spectra at locations A and B. These spectra are both scaled with transfer function "weights" that are related to one another by distances to the defect from each side: L^* and $L - L^*$, where L is the total distance of the monitored cable segment. An optimization algorithm then finds the best estimate of L^* that optimally balances the scale, i.e., that minimizes the spectral distance between the two scaled spectra A and B.

As mentioned before, the cornerstone of this approach is the knowledge of the cable transfer function. To measure it, a signal needs to be injected into the cable and measured at one or several points along its length: this is shown in the lower part of the Fig. 6–3. In practice, the same inductive sensor (HFCT) is used for injection and recording of the signal. As described in the chapter 4 devoted to the sensor, they are installed in pairs on terminations and joints with a screen separation. This allows injecting the signal through one sensor of the pair and measuring the current that has entered the cable with the second. In the case of an HVDC cable line, for example, the transfer function between sensors located at grounding points separated by the distance 6 – 12 km can be measured in this way.

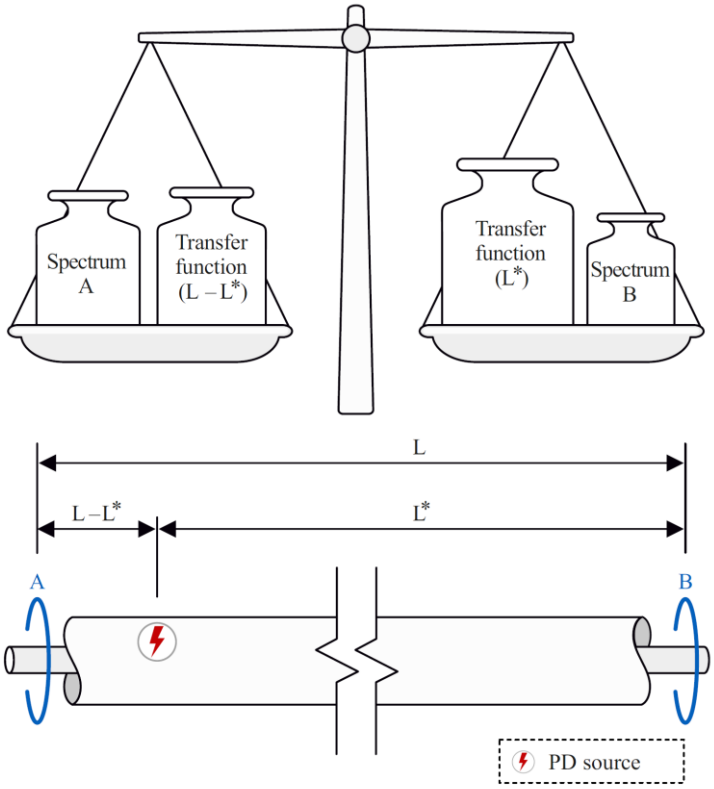

Fig. 6–2 Scaling of the signals measured at two measuring points A and B, reused from [Pub. 1].

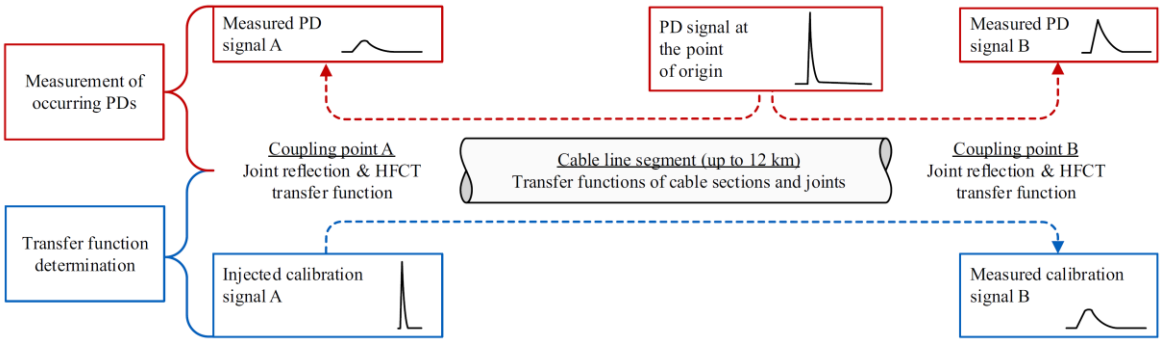

Fig. 6–3 Process of transfer function determination (blue) and registration of occurring PDs (red), modified from [Pub. 1].

As the transfer function should always correspond to reality, its measurement should be updated periodically. Thus, the system's cycle of operation is divided into two parts: continuous acquisition of signals (PDs or other events) coming from the line: upper part of Fig. 6–3, and periodical transfer function measurement: lower part of Fig. 6–3

To maintain contribution transparency, a disclaimer should be made here, that this basic idea of localisation was first introduced to the author of this thesis by the inventor of the patents [Pat. 2], [Pat. 3], is concerned by these patents and was later found in [166].

6.3 Detailed Approach

In the previous paragraph, we described the general idea of localization through spectral content analysis, and in this one, we will delve into some of the implementation specifics. To a certain extent this topic was opened in the papers [Pub. 1], [Pub. 4], [Pub. 6] published together with co-authors of TU Dresden, who deliberately worked on mathematical aspect of localization. Additional reference should be made to the work [166], that starts with alike methodology, but uses significant simplifications, e.g., reflection coefficients of the joints are excluded, phase information is not used. Here I would like to take opportunity to re-examine and consolidate this material, using the examples, that would additionally demonstrate how the task of localization becomes more complex when approaching a real-life scenario.

6.3.1 One-sided approach, amplitude/phase/complex-spectra based localization.

The simplest case is the representation of the cable as a homogeneous line as in the Fig. 6–4. The length-dependent transfer function of such cable can be expressed as:

$$H_{\text{cable}}(\omega, l) = \mathrm{e}^{\gamma(\omega) l}, \tag{6.1}$$

where $\gamma(\omega)$ – is the frequency-dependent attenuation constant, and l – is the signal propagation distance. If the transfer function of the cable segment between the two sensors with length L is known:

$$H_{\text{cable}}(\omega, L) = \mathrm{e}^{\gamma(\omega) L}, \tag{6.2}$$

it can be used to express the transfer function of the arbitrary length of this segment:

$$H_{\text{cable}}(\omega, l) = \mathrm{e}^{\gamma(\omega) L \cdot \frac{l}{L}} = \left(\mathrm{e}^{\gamma(\omega) L}\right)^{\frac{l}{L}} = (H_{\text{cable}}(\omega, L))^{\frac{l}{L}}, \tag{6.3}$$

to simplify further expressions, we will further address the transfer function of the whole cable segment between two sensors $H_{\text{cable}}(\omega, L)$ as H_{cable} without showing the arguments explicitly. Therefore, the transfer function over the arbitrary length l is expressed as:

$$H_{\text{cable}}(\omega, l) = (H_{\text{cable}}(\omega, L))^{\frac{l}{L}} = {H_{\text{cable}}}^{\frac{l}{L}}, \tag{6.4}$$

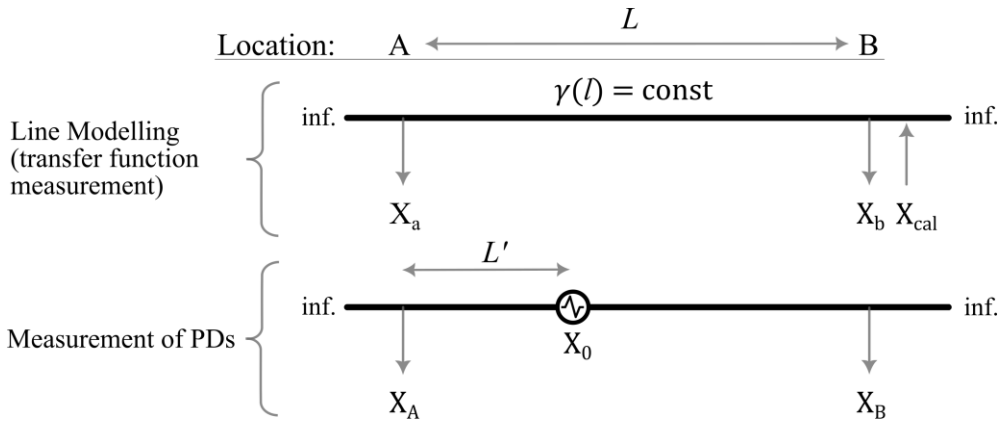

Fig. 6–4 Localization in a simplest case. Lowercase indices a and b refer to the calibration signals and uppercase indices A and B refer to the measured PD signals.

For this first simple example let us assume that the line ends with a matched characteristic impedance (absorbing or infinitely distant boundaries) on both sides of the monitored segment. In this case to measure transfer function of the cable segment, it is sufficient to inject a calibration signal $x_{cal}(t)$ at one side of the segment and measure the responses $x_a(t) \xrightarrow{\mathcal{F}} X_a = f_1(\omega)$ at the "far" end, and $x_b(t) \xrightarrow{\mathcal{F}} X_b = f_2(\omega)$ at the "near" end:

$$H_{\text{cable}} = \frac{X_a}{X_b}, \tag{6.5}$$

When a discharge signal with the spectrum X_0 appears at some point at a distance L' from the sensor installed at the location A, when it reaches the sensor, it will be altered in the following way:

$$X_A = X_0 \cdot H_{\text{cable}}{}^{\frac{L'}{L}}, \tag{6.6}$$

Certainly, in Eq. (6.6) and further on, signals X and transfer functions H are complex-valued functions of angular frequency ω, however, to visually simplify equations I avoid the form $X(\omega)$, $H(\omega)$, etc.

If the initial spectrum X_0 is defined, Eq. (6.6) can be used to determine the distance to the defect. Strictly speaking, a spectrum at the discharge point is an unknown quantity. However, the partial discharge itself has a very steep rise time, therefore its waveform resembles a Dirac impulse in a sense that it has a broad frequency spectrum and a phase close to zero for all frequencies, therefore this simplification is not far from the truth. With this assumption, we can assume that $X_0 = f(\omega) = const$, and make an estimate of the distance-to-fault $L'_{est.}$ by minimizing the spectral distance:

$$L'_{est.} = \underset{l}{\operatorname{argmin}}\, D_c\left(X_{\text{A}},\, H_{\text{cable}}{}^{l/L}\right), \tag{6.7}$$

where $D_c(\cdot\,,\,\cdot)$ – is the cosine distance measure. The cosine distance assess the similarity between two vectors in terms of their orientation, rather than their magnitude. For example, two vectors of different length pointing in the same direction will have a cosine distance of zero. Therefore, the use of cosine distance excludes the unknown amplitude of the initial signal X_0. Therefore (6.7) uses only the frequency-dependent part of the cable attenuation.

However, because formula (6.7) operates with complex spectra, it requires the measurement of the transfer function to be performed with the synchronized receivers at both ends of the line – otherwise, the phase transformation between the measured spectra X_a and X_b will include a desynchronization delay. Furthermore, the moment of recording the PD signal also changes the complex spectra X_A. As non-synchronization of the measurement points is an important aspect of the monitoring system, formula (6.7) is of little use in its raw form. The simplest way is to disregard dispersion and use the signal attenuation only. This will lead us to the so-called amplitude-based approach. By taking the absolute values in Eq. (6.7), we get the distance-to-fault estimate that is not affected by desynchronization:

$$L'_{est.} = \underset{l}{\operatorname{argmin}}\, D_c\left(|X_{\mathrm{c}}|, |H_{\mathrm{cable}}|^{l/L}\right). \tag{6.8}$$

There is still a way to use phase information for localization, without resorting to measurement synchronization. In an ideal lossless transmission line, the velocity of propagation is the same for all frequencies. However, as previously mentioned, a high-voltage cable inherently possesses a set of attenuation mechanisms. The phase velocity v_p and the phase constant β of a lossy transmission line can be expressed as:

$$v_p = \frac{\omega}{\beta}, \quad \beta = \mathrm{Im}\left[\sqrt{(R_d + j\omega L_d)(G_d + j\omega C_d)}\right], \tag{6.9), (6.10}$$

where R_d, L_d, G_d, and C_d are the distributed primary parameters (resistance, inductance capacitance conductance) of the transmission line model.
Therefore, attenuation ramping up with frequency is accompanied by the change of phase velocities and the severe dispersion of the transmitted signal.

As can be derived from (6.6), for perfectly synchronized measurements the phase spectrum $\varphi_{\mathrm{A}} = f(\omega)$ of the measured signal is determined by the phase response of the cable transfer function $\varphi_{\mathrm{cable}} = f(\omega)$ scaled by the propagation path L'/L:

$$\varphi_A - \varphi_0 = \frac{L'}{L} \cdot \varphi_{\mathrm{cable}}, \tag{6.11}$$

where initial phase $\varphi_0(\omega)$ can be assumed to be zero.
However, in non-synchronous measurements we have to consider two additional time shifts, which are: firstly, the unknown time Δt_1 that had passed between the emergence of the PD

and the moment of measurement, and, secondly, the desynchronization delay Δt_2 between two recording units that have measured the transfer function of the cable line. Each of these time delays introduce a linear phase shift $-\omega \cdot \Delta t_n$ in the frequency domain, which is the time-shifting property of the Fourier transform:

$$x(t - \Delta t_n) \overset{\mathcal{F}}{\leftrightarrow} e^{-j\omega \Delta t_n} \cdot X(\omega)\,. \tag{6.12}$$

Therefore, the Eq. (6.11) has to be modified accordingly:

$$\varphi_{\mathrm{A}} - \varphi_0 - \omega \cdot \Delta t_1 = \frac{L'}{L} \cdot (\varphi_{\text{cable}} - \omega \cdot \Delta t_2)\,, \tag{6.13}$$

$$\varphi_{\mathrm{A}} - \varphi_0 = \frac{L'}{L} \cdot \varphi_{\text{cable}} - \omega \left(\frac{L'}{L} \cdot \Delta t_2 - \Delta t_1 \right), \tag{6.14}$$

Summing up all the unknown time shifts to a certain unknown cumulative time shift Δt would lead us to:

$$\varphi_{\mathrm{A}} = \frac{L'}{L} \cdot \varphi_{\text{cable}} - \omega \cdot \Delta t\,. \tag{6.15}$$

Thus before finding the optimal estimate of L' by matching measured phase spectra φ_{A} with phase response of cable transfer function "weighted" by l/L, an additional task would be to eliminate linear slope introduced by $-\omega \cdot \Delta t$:

$$\begin{pmatrix} L'_{est.} \\ \Delta t_{est.} \end{pmatrix} = \underset{l,\ \Delta t}{\operatorname{argmin}}\, d\left(\varphi_{\mathrm{A}},\ \frac{l}{L} \cdot \varphi_{\text{cable}} - \omega \cdot \Delta t \right). \tag{6.16}$$

where $d(\cdot\,,\cdot)$ is a spectral distance measure.

One possible approach is to use covariance minimization, as was shown by the co-authors in [Pub. 4]. However, the key point here is that the linear decline brought into the frequency domain by the lack of synchronization does not hinder possibility of utilizing phase information in solving localization task, as the signal dispersion is significantly nonlinear due to the multitude of cable loss mechanisms.

Furthermore, it is possible to avoid separating the localization into amplitude-based and phase-based approaches and work with complex spectra. Certainly, the need to compensate for measurement desynchronization still exists. For this, a correction term $e^{j\omega \Delta t}$ is introduced into the Eq. (6.7), leading to:

$$\begin{pmatrix} L'_{est.} \\ \Delta t_{est.} \end{pmatrix} = \underset{l,\ \Delta t}{\operatorname{argmin}}\, D_c\left(X_{\mathrm{A}},\ X_0 \cdot {H_{\text{cable}}}^{l/L} \cdot e^{-j\omega \Delta t} \right). \tag{6.17}$$

6.3.2 Two-sided approach

In contrast to the "one-sided" approach that was reviewed until now, there is an alternative in comparing not the original and measured PD signals, but two signals received by sensors

at both ends of the line. From here on, I will refer to this as the “two-sided” approach. The core idea of it, is that both signals measured at the boundaries of the segment are generated by a single wave-source with an arbitrary spectrum. The main benefit of this approach is that there is no need to make assumptions about the shape of the spectrum of the signal at the point of origin X_0, as was done earlier by approximating it to a certain constant.

Referring again to the same line topology of the Fig. 6–4, let us assume that a signal with initial spectra X_0 that appeared at some point along the line was registered at left (A) and right (B) ends of the cable segment as signals with spectra X_A and X_B:

$$X_\mathrm{A} = X_0 \cdot {H_\mathrm{cable}}^{\frac{L'}{L}}, \tag{6.18}$$

$$X_\mathrm{B} = X_0 \cdot {H_\mathrm{cable}}^{\frac{L-L'}{L}}, \tag{6.19}$$

where L' is the distance from point A to the point of signal origin.

Then the estimate distance to the defect $L'_{est.}$ and appropriate time shift $\Delta t_{est.}$ are the arguments of the minimization function:

$$\begin{pmatrix} L'_{est.} \\ \Delta t_{est.} \end{pmatrix} = \underset{l,\ \Delta t}{\operatorname{argmin}}\, d\left(X_\mathrm{A} \cdot {H_\mathrm{cable}}^{-\frac{l}{L}},\ X_\mathrm{B} \cdot {H_\mathrm{cable}}^{\frac{l-L}{L}} \cdot e^{j\omega\Delta t}\right). \tag{6.20}$$

During optimization it is easier not to recalculate both spectra searching for their coincidence at corresponding distances $L - L'$ and L' from the defect to each of its ends, but to modify the formula to recalculate one spectrum keeping the other constant.

$$X_\mathrm{B} = X_\mathrm{A} \cdot \frac{{H_\mathrm{cable}}^{\frac{L-L'}{L}}}{{H_\mathrm{cable}}^{\frac{L'}{L}}} = X_\mathrm{A} \cdot {H_\mathrm{cable}}^{\frac{L-2L'}{L}}, \tag{6.21}$$

$$\begin{pmatrix} L'_{est.} \\ \Delta t_{est.} \end{pmatrix} = \underset{l,\ \Delta t}{\operatorname{argmin}}\, d\left(X_\mathrm{B},\ X_\mathrm{A} \cdot {H_\mathrm{cable}}^{\frac{L-2l}{L}} \cdot e^{j\omega\Delta t}\right). \tag{6.22}$$

6.3.3 Incorporating Sensor Transfer Functions

Until now we have considered the simplest case of line topology. In practice, it is necessary to take into account that the cable line is not homogeneous: each joint represents an impedance jump yielding a frequency-dependent reflection coefficient. Moreover, the cable never ends with the matched impedance, on the contrary, it can feature a couple hundred meters long substation busbar and equipment connected to it: other cables of the same voltage class, a transformer, low-voltage cables, overhead lines, etc.

These features do not contradict the approaches described above, but they lead to the fact that all these factors need to be taken into account as corresponding transfer functions and furthermore, we have to estimate constrains or even actual values for some of them.

The example described above we can extend by assuming that coupling of the signals includes some unknown transfer functions $H_{A,out}$ и $H_{B,out}$, as shown on Fig. 6–5.

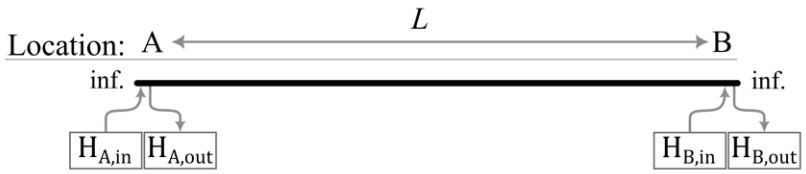

Fig. 6–5 Localization with the in- and out-coupling transfer functions included.

Content Omission Placeholder

Publication note: In order to protect intellectual property, the mathematical derivations of subchapter 6.3.3 of the original document have been shortened in the publication. Nevertheless, for completeness, the essence of the omitted part is shortly presented below.

Omitted content summary: The example in Fig. 6–5 illustrates that the ratio of the coupling-out transfer functions is influences the distance to the defect estimation. However, if we have the capability to inject a calibration signal from both ends of the line, then for this relatively simple line configuration it is possible to isolate the cable's transfer function in the resulting system of equations. Additionally, the ratio of the coupling-out transfer functions for extracting signals from the cable can be determined as well. By modifying Eq. (6.22) to account for these additional transfer functions, an estimate of the distance to the defect can be derived. On the other hand, the line discussed still represents an overly simplified example that doesn't account for reflections, as discussed in the next subchapter.

This content was omitted from the publication.

This content was omitted from the publication.

End of the Content Omission Placeholder

6.3.4 Incorporating Reflection Coefficients

In reality, however, line neither extend to infinity nor is terminated with the matched load, but has some impedance discontinuities at the ends, such as joints or cable end terminations, which can be expressed with the current reflection coefficients r_A and r_B. This is the case shown on Fig. 6–6. Additionally, along the line two impedance discontinuities are placed (e.g., joints) which introduce the according current reflection coefficients r_{j1} and r_{j2}.

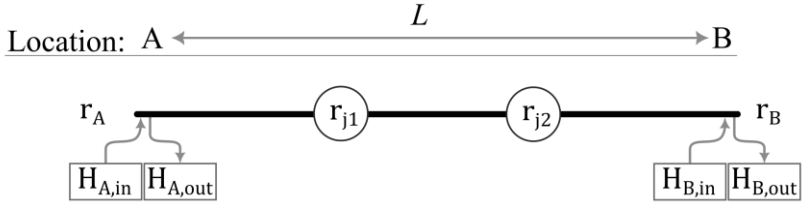

Fig. 6–6 Localization with reflections included.

Content Omission Placeholder

Publication note: In order to protect intellectual property, the mathematical derivations of subchapter 6.3.4 of the original document have been shortened in the publication. For completeness, the essence of the omitted part is summarized below. The last concluding paragraph of the subchapter also remain.

Omitted content summary: Since the examined line is finite at both ends, waves will bounce and propagate along it, reflecting at the ends and splitting at every mismatch into transmitted and reflected parts. For example, Fig. 6–7 shows the propagation paths of the waves caused by injection the signal at the left end of the line (location A). Using this line example and formulating propagation equations for each of the reflected/transmitted waves, a solution for the registered signals can be derived. However, the solving the resulting system of equations becomes increasingly challenging.

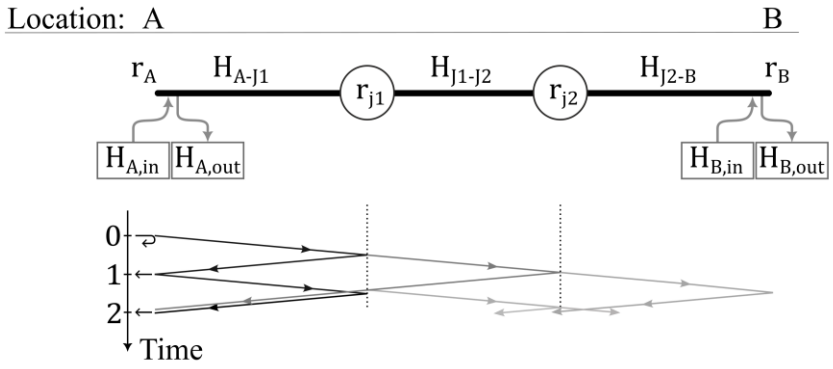

Fig. 6–7 Bouncing waves

The conclusions of this subsection remain and can be found below after the following blank placeholder.

This content was omitted from the publication.

End of the Content Omission Placeholder

Each impedance discontinuity introduces into the system of equations a reflection coefficient – a new frequency-dependent variable. In practice to find a solution to the resulting system, one can introduce some additional constraints: for example, that the reflection coefficients are the same for all joints of one type, that all sections of the cable have the same per-meter transfer function, that attenuation in the cable should have increasing trend with frequency, etc. Apart from constraints, some of the parameters can be estimated, the simplest example, if the termination is properly short-circuited the current reflection coefficient can be assumed as equal to one. When considering real termination with connected busbars and various power equipment, the calculation of the reflection

coefficient can be rather challenging. However, in the case of a joint with the known geometry it is relatively simple to estimate the reflection coefficient it yields. In this context, it is sufficient to consider the joint as inductance connected in series, since its length is much smaller than the wavelengths of the frequencies that can propagate in the power cable.

Localization studies that were carried out with the group of co-authors and published in [Pub. 1] used the estimates for the impedances introduced by the cable accessories which I have estimated rather coarsely based on the geometry of accessories. These experiments were carried out on a test cable line - which is described at the beginning of Chapter 7, "Laboratory Tests". This line was rather similar in topology to the example of the Fig. 6–7 – it featured three cable segments of 800, 600, and 800 meters, with two joints between them. With these inputs, despite the roughness of estimation it was possible to achieve a relatively low localization error of several percent.

Nonetheless, strictly speaking, the final localization module should not require precalculated parameters of cable accessories. Therefore, the purpose of the line modeling step is to determine the transfer functions of cable segments and reflection coefficients of accessories. In the examples given above, modeling was first limited to measuring the cable's transfer function (section 6.3.1 and 6.3.2), and further to additionally determining the ratio of coupling out transfer functions (section 6.3.3). These examples however did not consider cable accessories. As shown in the last example by equations (6.38) – (6.40), frequency responses contain information about the impedance jumps present in the line, and therefore can be used to derive reflection coefficients along with cable transfer function and therefore obtain a line model. To avoid considering all propagation paths separately, one could, for instance, approach the problem with Helmholtz equation and boundary conditions. Once the model is obtained, the localisation itself has to be performed – that is getting the estimate of the distance-to-the-fault with the use of the measured PD signals. For the simple cases this was done through minimization of the spectral distance, e.g., Eq. (6.22), (6.25). However, using the same approach for the more complex line featuring joints can be inconvenient, as the combination of paths that bouncing waves propagate through before arrival at the sensor depends on the starting point of the partial discharge.

6.3.5 Simulation-based approach

To overcome this issue, a more intuitive solution, so-called adaptive model, was proposed, developed, and further published by the main author of [Pub. 6]. From my point of view, the adaptive model is more akin to a one-dimensional numerical simulation in which

reflection coefficients serve as optimization parameters. The graphical user interface of the adaptive model is shown in Fig. 6–8.

The calculation domain, as mentioned before, is a one-dimensional space consisting of segments with non-zero lengths corresponding to cable sections and points with complex reflection coefficients corresponding to local impedance discontinuities (Fig. 6–8, left part). Both transfer functions and reflection coefficients depend on frequency, and in the simplest case, they are approximated by linear interpolation through two points (Fig. 6–8, right part).

The operation of this model, like the operation of the entire monitoring system, is divided into two parts: modelling (characterization) of the line and localization of the received signal.

During the modelling, calibration pulses are introduced into the cable line model – alike they are injected in the real cable, they pass through the cable, reflect on the accessories, and are detected by sensors. As the wave object is moved along the cable it is recalculated with the according transfer function, as soon as it gets to the reflection point, it yields the appropriately calculated transmitted and reflected waves, which propagate respectively in the forward and backward directions, get compensated by transfer function and so on. The signal recorded on virtual sensors is compared with the real responses measured by corresponding sensors on the cable line, and the resulting error corresponding to the initial set of parameters is calculated. On the next step, the optimization algorithm changes the parameters, and the simulation is repeated until the global minimum is found. The set of parameter values corresponding to this minimum is considered the most accurate reproduction of the cable line and is used for signal localization.

The localization can be carried out either iteratively, by shifting the location of the signal and comparing the resulting response with the measured PD signals, or by direct calculation, since all unknown transfer functions have already been determined.

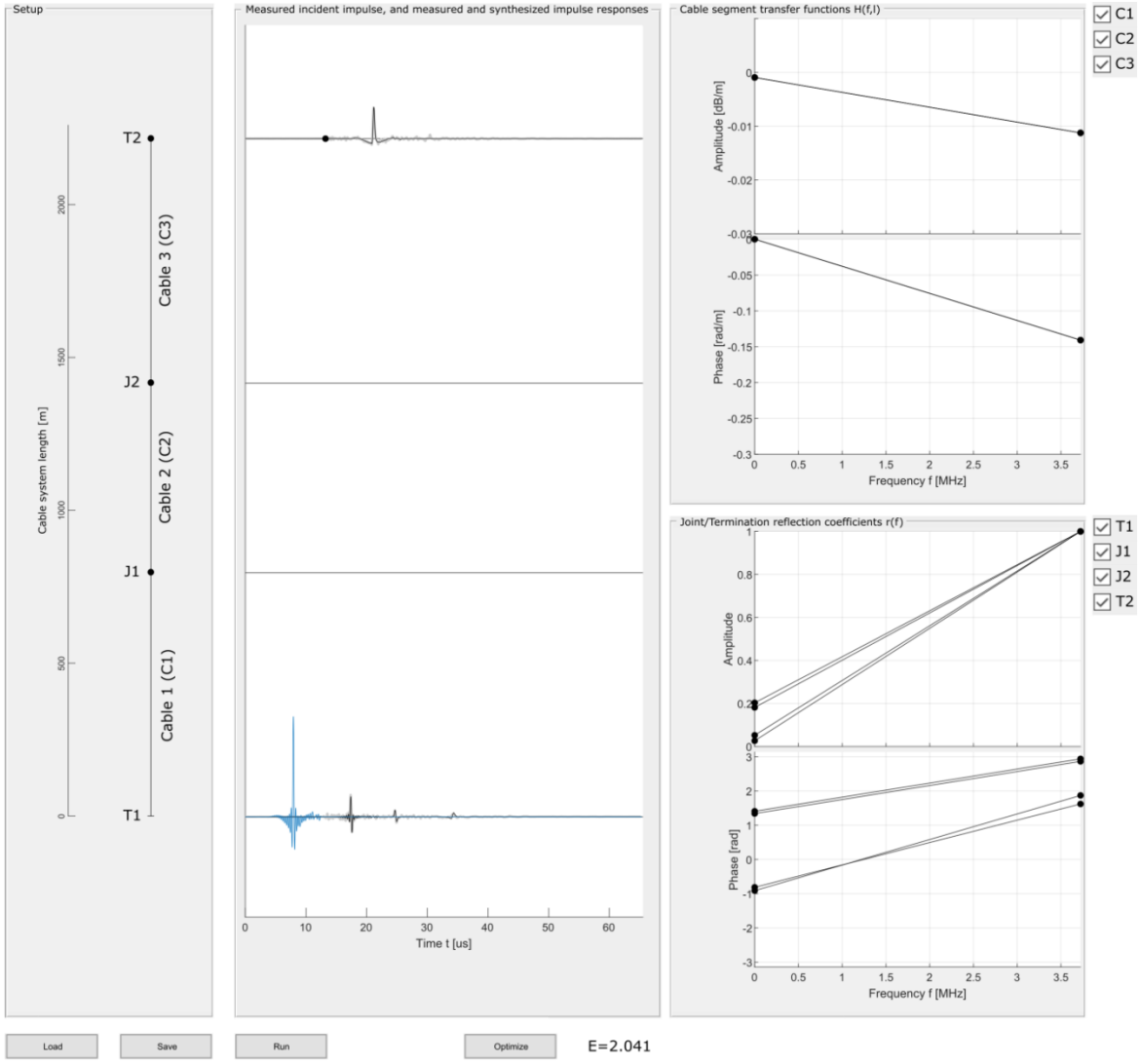

Fig. 6–8 Interface of the adaptive model

6.3.6 Signal Injection and the Generator Influence

Up to this point, the topic of how an incident wave appears in a cable has been pushed into the background through the use of an appropriate coupling-in transfer function. Let us now concider signal injection into the line and the role the generator`s impedance places in it.

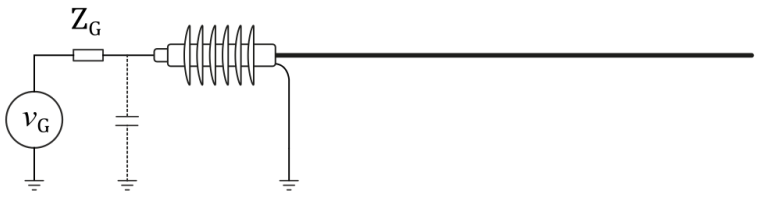

Fig. 6–9 Signal injection on termination

In Fig. 6–9 a generator with an internal impedance R_G is connected to the termination at the end of the electrically infinite line. The incident wave that will be injected into the cable is

determined through a divider formed by the generator's impedance and the characteristic impedance of the line.

$$v^+ = \frac{v_G}{R_G + Z_{cable}} Z_{cable}\,, \quad i^+ = \frac{v_G}{R_G + Z_{cable}} \qquad (6.42), (6.43)$$

After the injected wave reflects at the accessories of the line and returns to the generator, the reflection coefficient of the termination comes into play:

$$r_{T_v} = \frac{R_T - Z_o}{R_T + Z_o} = -r_{T_i} \qquad (6.44)$$

The state of the generator at the moment of the return wave's arrival plays a crucial role – and it differs for different devices. For instance, if we use a regular PD calibrator to galvanically inject a pulse into the line, its impedance after injection, as well as in the off state, consists of a capacitance of 100 pF and a parallel resistance of about 50 Ohms. Accordingly, the reflection coefficient apparent for the returning signal will also depend on this device. Even when the signal is injected and measured by an inductive sensor, the reflection coefficient will still depend on the input impedance of the downstream electronics.

6.3.7 Incident Wave Splitting

Another interesting case is when a discharge occurs in a joint, for instance, of a straight type, near one of its sides. In this case, although from the monitoring system's point of view it is not so important where exactly within the joint body the discharge occurs – it is enough to simply know that this exact joint is defective – within the localization problem solution, this cannot be completely neglected. In this scenario, as shown in Fig. 6–10, to the left of the discharge is the cable waveguide, and to the right is the joint inductance, followed again by the cable impedance. Waves propagating in both directions from the defective joint will not be identical, as the joint inductance will reflect the signal, and the higher the frequency, the more this reflection will be. Of course, we can consider this situation as two tandem lines: joint as a transmission line connected to the "cable" transmission line on both of its sides. But since the length of the joint should not exceed ten meters, from the transmission line model we can leave only the lumped inductance. Then the currents and voltages going to the left and right from the failure point will be related as:

$$\frac{i_{right}}{i_{left}} = \frac{v_{right}}{v_{left}} = \frac{Z_{cable}}{j\omega L_{joint} + Z_{cable}} \qquad (6.45)$$

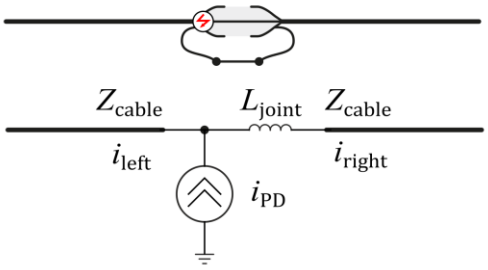

Fig. 6–10 Failure spot on the left side of the joint and resulting equivalent circuit

The correctness of representing the joint as a lumped inductance can be confirmed by conducting a simple simulation in COMSOL Multiphysics. In Fig. 6–11, we can see the geometry of the model – two segments of a cable line, ending with an absorbing boundary condition. Each of the segments is defined as a lossless line with distributed capacitance and inductance, chosen in this example to match a medium voltage cable. Between them is a joint whose length can be varied. Two simulations are conducted: with distributed and lumped joint model. In the first, the joint is modelled as a 2-meter lossless line with calculated per-meter inductance and capacitance. For the second simulation, since the COMSOL "Transmission Lines Module" only deals with transmission lines and does not have lumped passive elements, to reproduce the lumped case we reduce the length of the line to some small value, for example 10 cm, and leave only the inductance among all line parameters, with a value equivalent to a two-meter joint. The resulting graphs for both cases are presented in Fig. 6–12. The current distribution for both simulations almost coincide, and the ratio of currents is indeed described by equation (6.45). Furthermore, it is worth to note, that the ratio of currents introduced in the left and right directions is quite high, e.g., 1.5 times at 1 MHz, 4 times at 4 MHz. Despite the fact that a rather small-sized joint was used, it led to a strong imbalance of currents already at the beginning of the megahertz range.

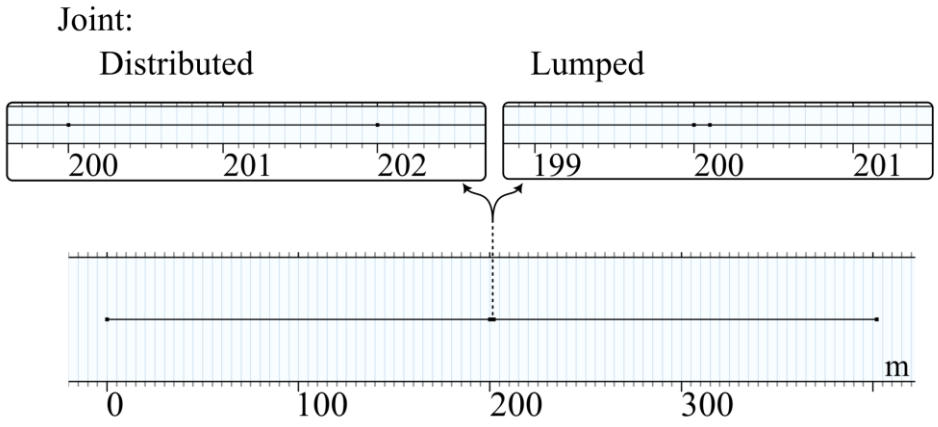

Fig. 6–11 Model geometry with lumped and distributed joint models

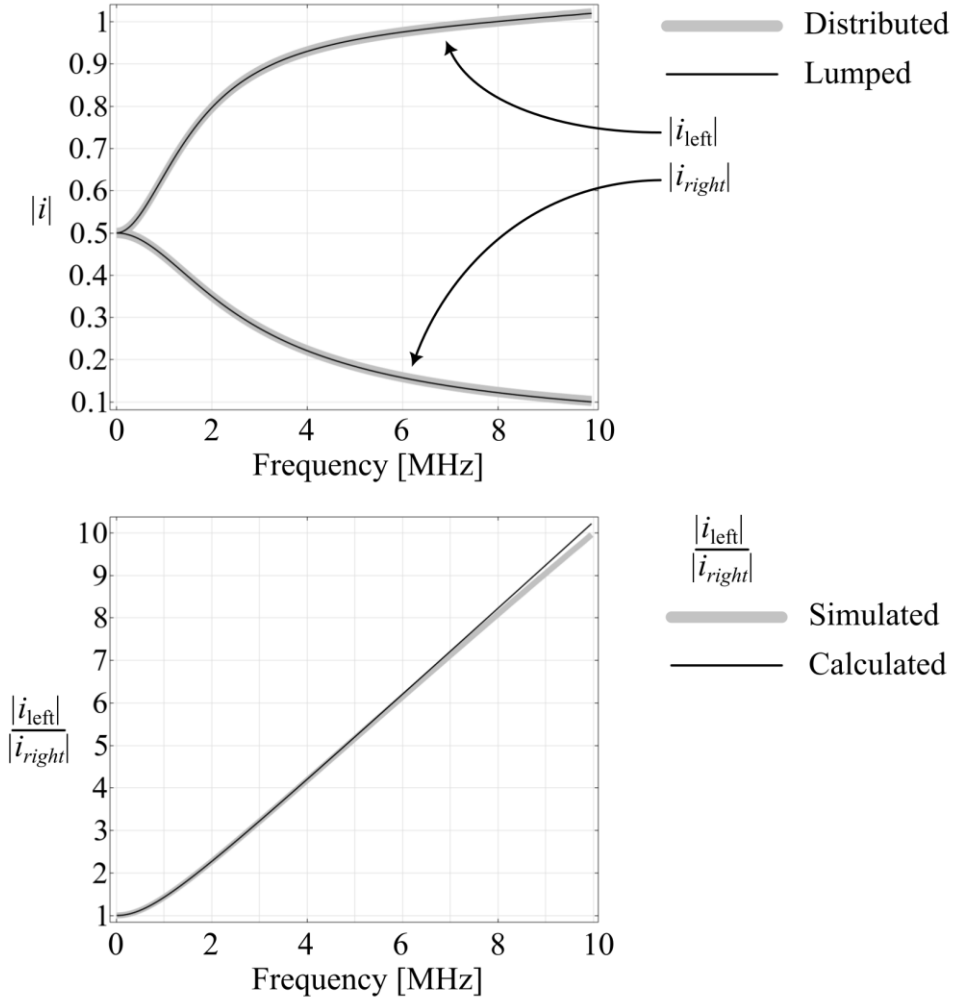

Fig. 6–12 Distribution of the injection currents in the vicinity of the joint

7. Chapter:

Laboratory Tests

7.1 Hardware

The term "Hardware" in the context of this chapter refers to electronic equipment that receives and digitizes signals coming from sensors. It should be noted that different equipment was used in different situations as the project developed. For example, equipment that is convenient in laboratory conditions may be impractical in the field and vice versa. Therefore, in this subsection, we will describe several devices used both in laboratory measurements and in pilot projects.

In laboratory conditions, the transient recorder HiRES by HighVolt Prüftechnik was used as recording equipment (Fig. 7–1). Its main advantage is a set of separate active probes that are connected to the central unit through optical fiber cables, allowing different channels to be located in different places along the test cable line and thus minimizing the length of the electrical signal cables. This is very advantageous when one wants to eliminate or investigate the influence of the length/capacitance of those.

Fig. 7–1 HiRES active probe (left), HiRES central unit (right)

The central unit is controlled by an embedded industrial PC running Windows and the HiRES GUI software package, which allows for recording, evaluating, and saving measurement data, and automated recording of multiple frames on trigger.

Thus, compared to a regular oscilloscope, this solution is more convenient in the following ways:

- Main unit has 8 channels, sampling rate of 250MS/s and allows for very long recordings (120 megasamples per channel → 480 ms with 4 ns sampling time), which can be rather convenient at certain occasions. Furthermore, its GUI on

windows machine provides more convenient navigation withing long recordings comparing to that of an oscilloscope.

- Each channel uses floating active probes, so they can be located in remote places and are not connected together over grounding.
- Vertical resolution of 14 bits and a dynamic range selector with a minimum of 50mV. Thus, the least significant bit (LSB) is $50\ mV/2^{13} \approx 6$ uV. This is important when compared to common 8-bit oscilloscopes, especially when searching for small signals.

Another device that is applicable in both laboratory and field conditions is the device produced under RedPitaya label: the SIGNALlab 250-12 (Fig. 7–2). It is a small-sized device that includes a set of electronic components and interfaces that enable it to perform signal processing and measurement tasks. Some of the key features and components of this device include:

- Two input channels and two output channels. This allows the device to not only perform measurements but also inject signals into the cable. And since there are two channels for both input and output, differential measurements can also be performed in addition to single-ended ones,
- A triggering input which can be used for time synchronization of measurements between multiple devices.
- Analog bandwidth from DC to 60 MHz, which is more than sufficient considering that frequencies above five megahertz are practically absent in the cable lines,
- 250 MSPS (Mega Samples Per Second) ADCs,
- 12-bit resolution ADCs, with a minimal range of 1V, and LSB of approximately 0.4 mV, which is a sufficient,
- 14-bit resolution DACs,
- High-quality front-end circuitry, including amplifiers and filters,
- On-board FPGA for real-time processing,
- Processor running Linux,
- Ethernet, USB and microSD interfaces for data transfer and communication,
- FPGA expansion connector for adding custom interfaces and functionality,

Here, it is very important that on the one hand, this device has good measurement parameters (vertical resolution, bandwidth, and LSB value), but at the same time, it has small dimensions and is therefore convenient to handle.

Furthermore, this device provides extensive possibilities for remote control. On the one hand, it can be controlled via Standard Commands for Programmable Instruments (SCPI) commands through a launched SCPI server. Thus, if the measurements are performed manually at the location of the test-setup, one or several of these devices can be connected directly to a laptop via the Local Area Network (LAN) port or USB-adaptor. Resultingly, devices appear in the local network, and can be accessed by IP addresses using, for example, a Python script that performs both the measurement procedure and the first steps of post-processing. Therefore, this units have shown themselves to be rather suitable for measurements requiring automation.

Fig. 7–2 SIGNALlab 250-12

Often it was necessary to perform remote measurements, for example, for connection from the office to the equipment installed at the substation. In this case, the remote side can be configured in two ways:

- connect all devices to one router and access each one directly through a VPN-connection to the router's local network,
- include an Industrial Personal Computer (IPC) on the remote side, connect all units to it and communicate with each unit through network-accessible industrial PC.

This provides the opportunity to select an optimal location for executing the main program cycle. Usually, this cycle involves sending various command sequences to different devices, collecting measurement buffers, saving them to files, conducting parametric sweeps,

performing post-processing, and so on. For example, if measurements need to be performed constantly, or at regular intervals without operator's control, this cycle can be carried out entirely on the remote machine. Of course, remote debugging and monitoring are still possible if there is access to the remote machine, for example, through Team Viewer.

On the other hand, sometimes the measurement script requires manual launching each time, for example, to analyze the results immediately after each measurement, for manual post-processing, etc. In this case, it is easier to run the script directly on the user-side computer since its computational performance is likely to exceed that of the remote machine. However, it should be noted that this requires sufficient internet speed since in this case both commands and collected data will be transmitted from remote devices to the local machine, while when script runs on a remote machine, all this traffic remains on the remote side. Moreover, using these same devices, instead of using SCIPI-commands we can switch to operation through Linux and FPGA, which enable sophisticated real-time signal processing methods.

Fig. 7–3 Custom acquisition unit

More possibilities are offered by custom-produced electronics. For these purposes, a device was established by HighVolt which combines the necessary functionality, somewhat similar to what was described above, but much more expanded and tailored to the tasks (Fig. 7–3). Since usually two HFCTs are installed at one location on the cable line, it has two differential inputs/outputs: one for each sensor. Each of them is intended, firstly, for signal injection into the cable by means of the HFCT, and, secondly, for registering signals coming from it. When measuring the transfer function of the cable, the accuracy of the measured transfer function is higher the higher the amplitude of the injected calibration signal is. Therefore, during development one of the goals was to maximize the latter as much as possible from a practical point of view. At the same time, the possible output value is limited both by the resulting power of the amplifier and by the features of working on same physical

channel with the measuring channel. These criteria determine the selected range of 80V peak to peak signal, sampled with 14-bit resolution.

Regarding the measurement path, the design was chosen to suit the task of detecting small signals. There are two fully differential inputs, each of which has an analog low-pass and high-pass filters, programmable gain amplifiers, a 14-bit ADC with a 250MHz sampling frequency, and an FPGA for implementing real-time algorithms. At the same time feedback is sent to the amplifier to adjust the gain so that the input signal optimally utilizes the ADC resolution. The System-on-a-chip technology plays an important role in the device's operation, allowing for the optimization of the FPGA's operation in conjunction with the processor. It is worth noting that both channels are separately adjustable and are even divided into separate boards to minimize crosstalk.

It should be noted separately that the device also includes protective blocks against input overvoltages. Since high-frequency surges, such as switching impulses, and cable breakdown impulses can come through the sensors on the inputs of the device, the equipment must be protected accordingly.

In its current implementation, the released device has a nineteen-inch form factor and is designed to operate in a temperature range from -40 to +55 °C. Fig. 7–4 shows its installation in one of the pilot projects.

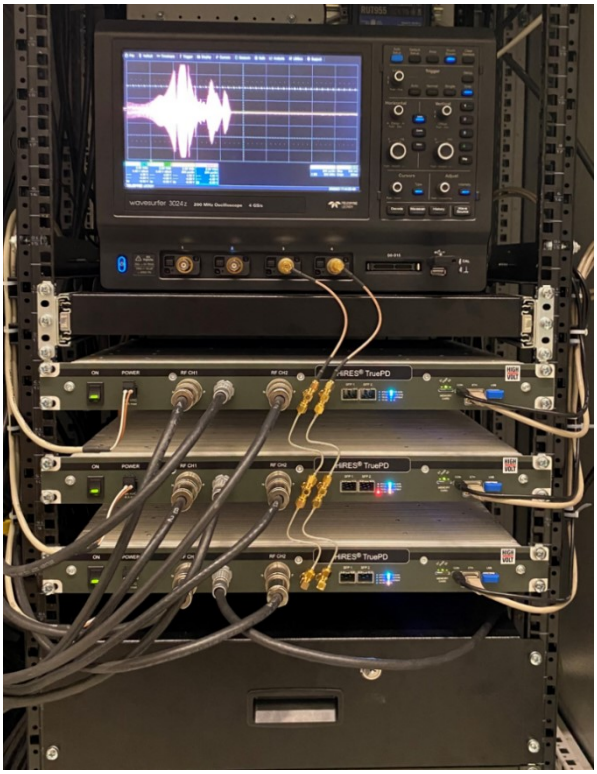

Fig. 7–4 Acquisition hardware in 19-inch rack

7.2 Cable Test Line

During the course of the project, it became apparent that the development and testing of the system would require a cable line on which experiments could be conducted and which would be permanently available. In some studies, similar investigations are performed on common coaxial signal cables. While this approach is convenient, it introduces challenges due to their properties being different from real-world cable lines. One of the main aspects is the mechanism of attenuation of higher frequencies, which is associated with the presence of semiconducting layers between the cable conductors and its main insulation in power cables, which is not present in signal cables. Even at lower frequencies, when the role of the semiconductive layers is limited, the significantly smaller cross-sectional dimensions of signal cables make them bad representatives for the attenuation of the power cables. Furthermore, it would be advantageous to energize the cable line and obtain real discharges of various types. For this purpose, a voltage of at least 4 – 5 kV would be required. On the other hand, a laboratory setup with a real high-voltage cable would be costly, large in size, and difficult to install. A good compromise was a medium-voltage cable, as such a cable has semiconducting layers and attenuation comparable to high-voltage cables. Based on such cable, to be more precise, a 30 kV XLPE cable, a line was created for laboratory testing, which is referred to as the “cable test line” in further in this work. In its initial design, the cable line consisted of three cable drums and two joints between them, and terminations on the ends, as shown in Fig. 7–5. High-voltage joints with screen separation were used as joints, allowing for inductive sensors to be installed on each joint and both end terminations.

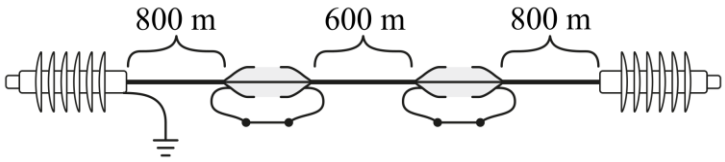

Fig. 7–5 Cable test line

Since laying a cable line in the ground is a complex undertaking, the cable was left on the drums (Fig. 7–6), which introduces some discrepancies with reality. The main problem here is the lack of earth around the cable, which could play the role of a third conductor. In addition, the cable ends and joints are located in the same geometric location, so all conductors that are grounded, whether it grounding leads of terminations or joints, will be interconnected at one spatial point. On the other hand, if the line is grounded at only one

point, the signal injected between the screen and the cable propagates in the same way as it does in a real cable line, which makes the test line appropriate for our studies.

The total length of the first setup was 2.2 km. With a wave propagation speed of about 6 ns/m, the total travel time from one end of the line to another was about 13 us, and the distance from the termination to the first joint and back was just under 10 us. Thus, if the length of the injected signal is, e.g., 5 us, the resulting reflections are well visible and distinguishable from each other in the time domain without additional processing. In other words, to understand and study step-by-step localization methods, such long cable segment lengths were rather convenient.

Fig. 7–6 Foreground: Joints with mounted HFCT prototypes and connected transient recorders. Background: MV cable drums. Published before in [Pub. 1].

7.3 Line characterization

The first experiment presented here shows the characterization of the cable line, in other words, the determination of its structure. In the context of monitoring a cable line, its topology, such as the lengths of cable segments, locations of joints, etc., is usually known in advance. However, in cases where the line structure is unknown or should be validated, a process called line characterization can be carried out, which involves determining the locations of accessories and their distances. This can be done, for example, using TDR, if

the parsing signal is electrically short, or via correlation of recorded response with the original signal, if the long sweeps are used, as is done, for example, in [Pub. 6].

By utilizing the presented high-frequency current transformers as bidirectional coupling devices, it is possible to inject known signals into the cable line. Each joint, even a straight one, acts as an impedance step and causes the partial reflection of the propagating pulse. The wave-reflection capabilities of cable accessories can be used to analyze the section structure in the following way: The wave is injected via the coupling unit at some point of the line and the response is measured at the same location. The recorded signal will contain a number of reflections from joints and terminations. While reflections from joints are relatively equal, the termination produces a higher response. Therefore, the heights' ratios in the reflection sequence give insight into distinguishing whether a particular reflection represents a joint of a certain type or a termination. If the location of the cable end can be determined within the recorded reflection sequence, or actually a reflection from any known location at a known distance, the locations of all accessories can be rescaled from time-scale to meters. Otherwise, these distances can be calculated from the wave propagation speed, where the least can be estimated from the cable geometry and material properties.

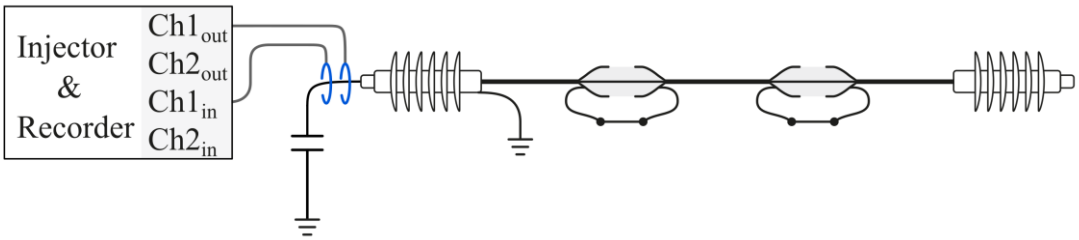

Fig. 7–7 Setup for line characterization on a cable test line

The structure determination was studied at the cable test line, with the setup presented in Fig. 7–7. Here, the signal, namely mono-frequency windowed burst, is injected via HFCT at termination. As it propagates along the line, parts of the pulse reflect at joints and run back to the injection point. The second HFCT installed at the same termination where the injection was performed, receives forward pulse, reflections from the joints, and the reflection from the termination at the far end. The received signal is shown in Fig. 7–8 and Fig. 7–9 for 500 kHz and 1 MHz burst waves respectively. At first sight it is evident that the reflected waves include the phase shift, and therefore, determining the exact arrival time of the reflected wave with simple cross-correlation is not optimal.

The first method used to obtain the signal amplitude at the desired frequency involved applying the Discrete Fourier Transform (DFT) with a second-order Goertzel algorithm in

a moving window that shifts over the signal. The Goertzel algorithm evaluates the amplitude for a single specified frequency, which in our case is set equal to the frequency of the injected signal. The window width is equal to the duration of the injected pulse. The maximums of the resulting function correspond to the windows that overlap with either incident pulse or upcoming reflections. With this method and the setup used the maximal error is below 4% (estimated 825 meters compared to 800 meters of real length)., furthermore, if a row of different frequencies is injected and analyzed, the accuracy can be refined further.

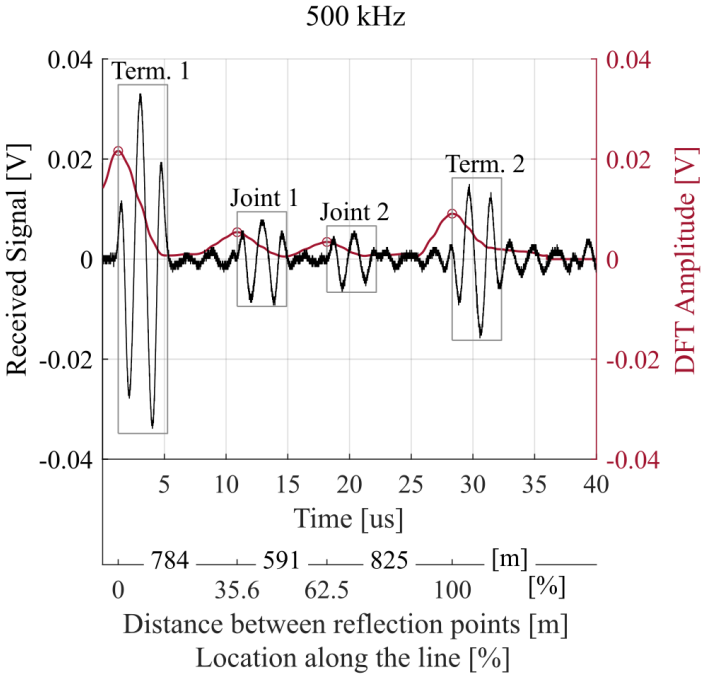

Fig. 7–8 Line characterization with Goertzel algorithm (500 kHz burst)

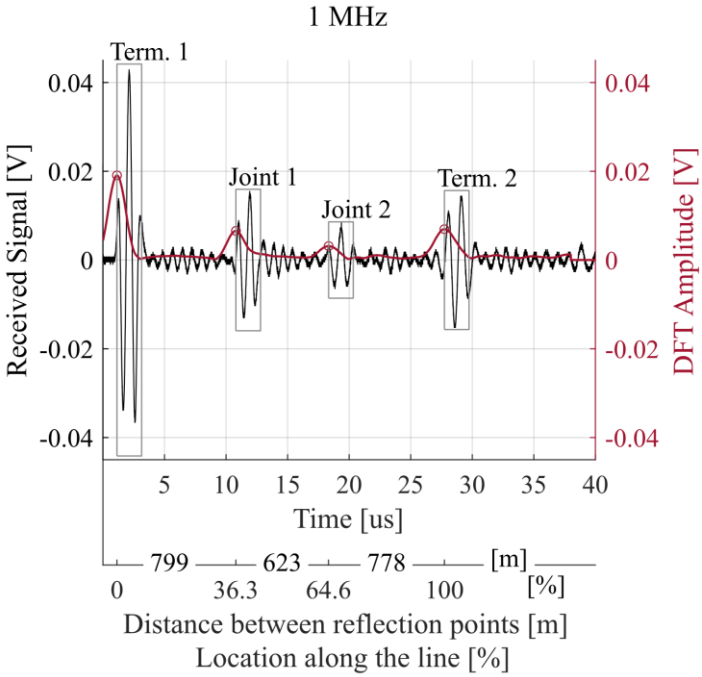

Fig. 7–9 Line characterization with Goertzel algorithm (1 MHz burst)

Alternative way is to use the filter-Hilbert method to obtain the signal amplitude. In this case, the signal processing chain will include three stages:

- first, filter the signal with some narrow band-pass filter,
- then apply the Hilbert transform, which allows us to retrieve the analytic signal of a real-valued signal,
- take the absolute value of the obtained analytic signal.

Additionally, it is important for the original burst to be windowed, so that its amplitude would have a single maximum.

As a result, the curve shown in Fig. 7–10 is obtained. In this case, the localization accuracy largely depends on the filter settings – and here, of course, one has to compromise between the filter's resolution in the time and frequency domains, which is a fundamental problem in the field of digital signal processing: if the filter has higher resolution in the frequency domain, it loses resolution in the time domain. In our case, finding a compromise is difficult: we need both time-domain resolutions to avoid mixing reflections and good filtering with a narrow passband to obtain an accurate analytic signal. The resulting output shows a higher level of accuracy then the previous method: the maximal error is below 0.5% (estimated 598 meters compared to 600 meters of real length).

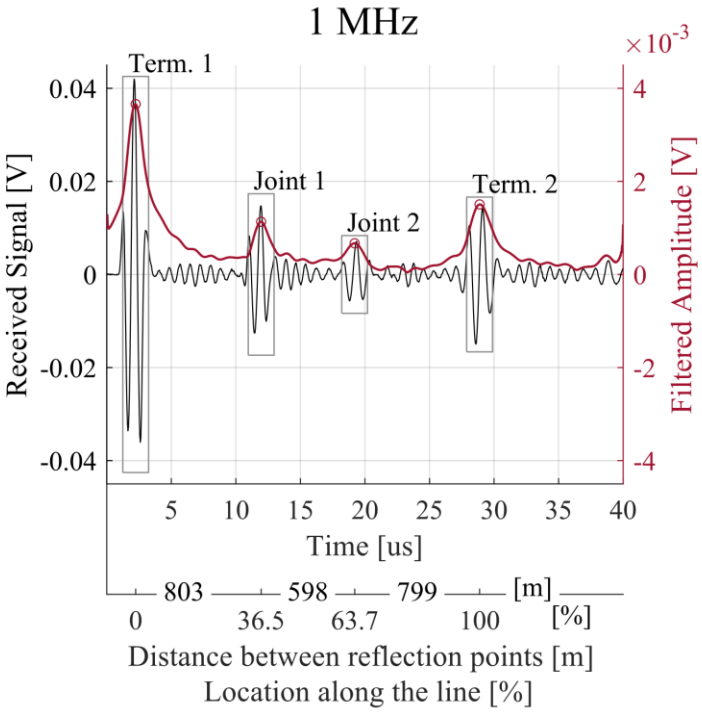

Fig. 7–10 Line characterization with filter-Hilbert method

7.4 Line attenuation estimation

When studying the localization of PD, the necessity to at least roughly estimate the cable attenuation arises, for example, for cross-validation of the results. However, the use of a common pi-section model will lead to an extraordinarily low attenuation for frequencies above several megahertz. An article describing the high-frequency behavior of HV power cables was introduced by Stone and Boggs in 1982 [167]. The high attenuation rate was explained by the presence of semi-conductive layers, that introduce an additional resistive impedance, which causes fast damping of high-frequency signals. In further studies, it was shown, that the semiconductive losses depend not only on absolute values of relative permittivity and electrical conductivity of the semiconductive layers but rather on their ratio [168], which makes the attenuation calculation accuracy less stable. Furthermore, semiconducting screen properties are not included in the common datasheets, and that complicates the calculation from the practical point of view. To summarize, the mathematical model for attenuation is simple and straightforward, however, variables are either unknown or unreliable. However, semiconductive losses begin to dominate only in after several megahertz, while at low frequencies the main mechanism of losses is associated with the developing skin-effect in conductors [167], [169]. The latter, of course, can be estimated from the geometry and conductors' properties. However, different loss mechanisms (skin effect, dielectric losses, losses in semiconducting layers) can contribute to a different amount to the total loss budget for different cables, and there are no standardized data available in this regard.

In practice, if it is necessary to determine the attenuation of a specific cable, it is easier to resort to measurements. If it is possible to inject a signal into a cable that is homogeneous in length and measure the signal at two locations at a distance L: $x(t, l = 0)$, $x(t, l = L)$, then the attenuation constant α can be related to the amplitude difference by the following formula:

$$\frac{|X(\omega, l = L)|}{|X(\omega, l = 0)|} = e^{-\alpha(\omega)\cdot L}, \tag{7.1}$$

This can be both pulses and sweep signals, in any case, they will enter the formula as a result of Fourier transform, unless the measurement is taken at discrete points. The problem here is that cable lines in general, and in particular the test cable line used for our studies, are not homogeneous in length, and the measured signals are affected by reflections.

In contrast to manual injection and recording of arbitrary signals, a common approach would be to calculate attenuation from one of the cable's S-parameters, such as S11 or S21, measured using a vector network analyzer (VNA), e.g., [170]. This approach is optimal in terms of the setup and post-processing minimization: indeed, no signal generator with an arbitrary sweep or multiple measurement points are needed here. This approach is often used for high frequencies and coaxial cables, where it is generally easier to work with S-parameters. Again, based on the field of application, this measurement is most often performed for coaxial signal cables whose characteristic impedance at least approximately matches the output impedance the VNA, so the resulting reflection is negligible. In the case when it is necessary to measure a cable with an impedance different from the VNA impedance, a correction for the output reflection must be introduced into the calculation. A good example of this is described in [171], where the Eq. (7.2) for the case of no reflection is extended to the Eq. (7.3), in which the reflection it is taken into account through a coefficient Γ_0:

$$\alpha = \frac{ln\big(\Re(S_{11})\big)}{-2z}, \tag{7.2}$$

$$\alpha = \frac{ln\left(\frac{\Re(S_{11})}{(1-\Gamma_0^2)}\right)}{-2z}, \tag{7.3}$$

where z is the length of the measured cable.

A more complete description of this case is given in [172], where not just attenuation, but the propagation constant is derived from S11 and S21. The connections to VNA are performed on both sides of the cable, therefore the mathematical model should take in account reflections on both sides. The approach is further complicated by the fact that S-parameters cannot be cascaded, so a transition to T-parameters is needed, etc.

In our case, in addition to the input and output mismatches, the joints in the line represent impedance jumps, as well as high-voltage cable terminations, the large sizes of which add their impedances to the mismatch between the VNA output and the cable. In general, the analytical approach described in [172] could be extended to our case, but I will perform a more straightforward solution: to use auxiliary 1D simulation of transmission lines to estimate attenuation quickly, roughly, yet reliably, without extensive mathematical calculations. In this work, the calculation was performed in “Transmission Lines” module of COMSOL, but it can also be done in any other program that works with transmission lines and S-parameters.

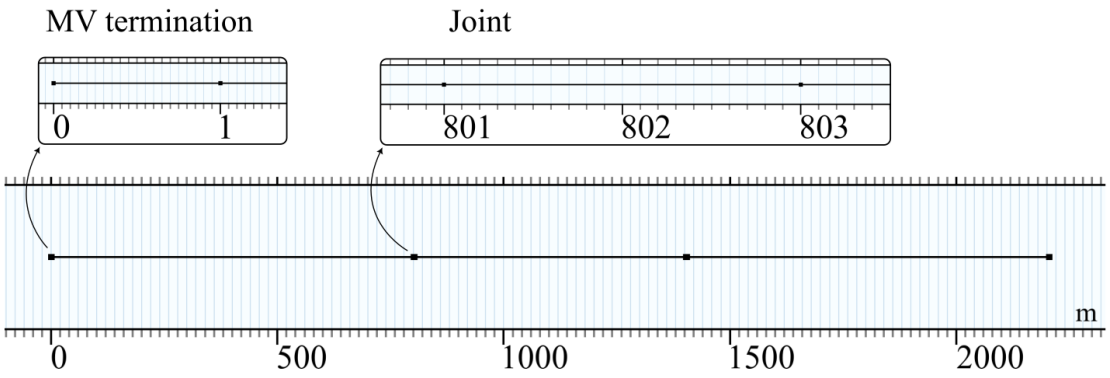

Fig. 7–11 Attenuation model geometry

The main idea is to model the reactive part of cables, joints, and terminations based on available geometry data, introduce a basic loss model, and then adjust it according to measurements. Fig. 7–11 shows the geometry of the model. Each of the line constituents: cable pieces, joints, and terminations, is modelled using a Pi-model of a transmission line, which includes a series inductance L, resistance R, and parallel conductance G and capacitance C. These parameters are estimated manually for each of the segments, joints, and terminations. The calculations here are minimal, but it is fortunate that the reactive parameters can be accurately calculated from the geometry. R and G, which represent the reactive losses of interest, are only specified for the cable segments, since for the other elements they are relatively small. According to the article [169], at low frequencies (up to several hundred kilohertz), skin effect losses dominate by a large margin, and as the frequency gets close and enters the megahertz range, losses in the dielectric begin to contribute as well. In the same article, it is mentioned that skin effect losses increase as roughly the square root of frequency, while the increase of the dielectric losses is approximately proportional to frequency. As we are interested in attenuation specifically in this frequency range (kHz to MHz range), we will use these two loss mechanisms to model attenuation. Approximate values for R and G are calculated as initial guess, and while calculating losses due to skin effect is simple and reliable, for estimation of the dielectric losses the problem of finding reliable data on the imaginary part of the dielectric permittivity/conductivity/loss tangent arises again. Nevertheless, the knowledge that these losses increase proportionally to frequency and that they should not have an impact at low frequencies helps us.

The result of the simulation will be a plot of the selected S-parameter, for example, S11. This same parameter can be measured using a VNA by directly connecting it to the termination as shown in the Fig. 7–12.

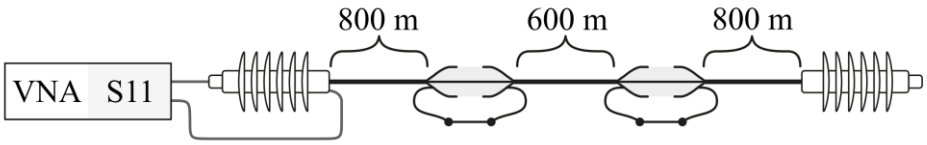

Fig. 7–12 Setup for attenuation estimation via S11-parameter

The results of the measurement and simulation are compared in Fig. 7–14 (a). It can be seen that although the model accurately describes the frequency dependence of S11, the applied loss model yields underestimated attenuation values. Therefore, we can add a correction coefficient to the R-parameter of transmission line (the one that accounts for the screen losses), which will change the slope of the S11 curve and lead to a more accurate description of the attenuation, which is shown in Fig. 7–14 (b). It can be observed that now the low-frequency loss has a rather accurate fit, but is still underestimated for higher frequencies. To further compensate for it, we will increase the correction coefficient for the G-parameter, until the curves are nearly overlapping as shown on Fig. 7–14 (c).

For cross-validation the same procedure can be performed for the S21 parameter. Here the measurement can be performed with the connection to both terminations, as shown in Fig. 7–13. The sequence of adapting the coefficients, shown in Fig. 7–15, was the same, as for S11, it is, and the most accurate fitting was achieved with the same values of correction coefficients as for S11.

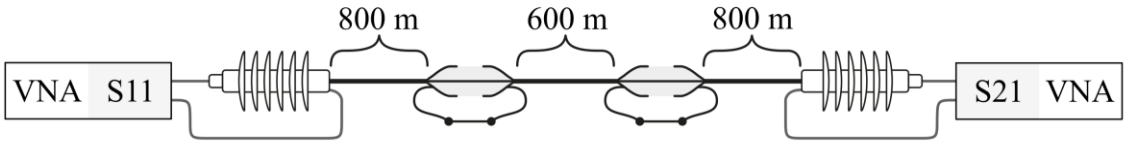

Fig. 7–13 Setup for attenuation estimation via S11-parameter

Once the optimal correction coefficients are obtained, the attenuation of the cable can be calculated and additionally verified by simulation. The calculation of the attenuation constant can be performed from the obtained values of the series impedance Z and shunt admittance Y of the transmission line model:

$$\alpha = \Re(\gamma(\omega)) = \Re\left(\sqrt{Z(\omega)Y(\omega)}\right), \tag{7.4}$$

At the same time, we want to obtain not the attenuation constant itself, but rather the attenuation per kilometer in decibels:

$$H_{calc} = 1000 \cdot 20 \cdot \log_{10}\left(-\Re\left(\sqrt{Z(\omega)Y(\omega)}\right)\right) \ [dB/km] \tag{7.5}$$

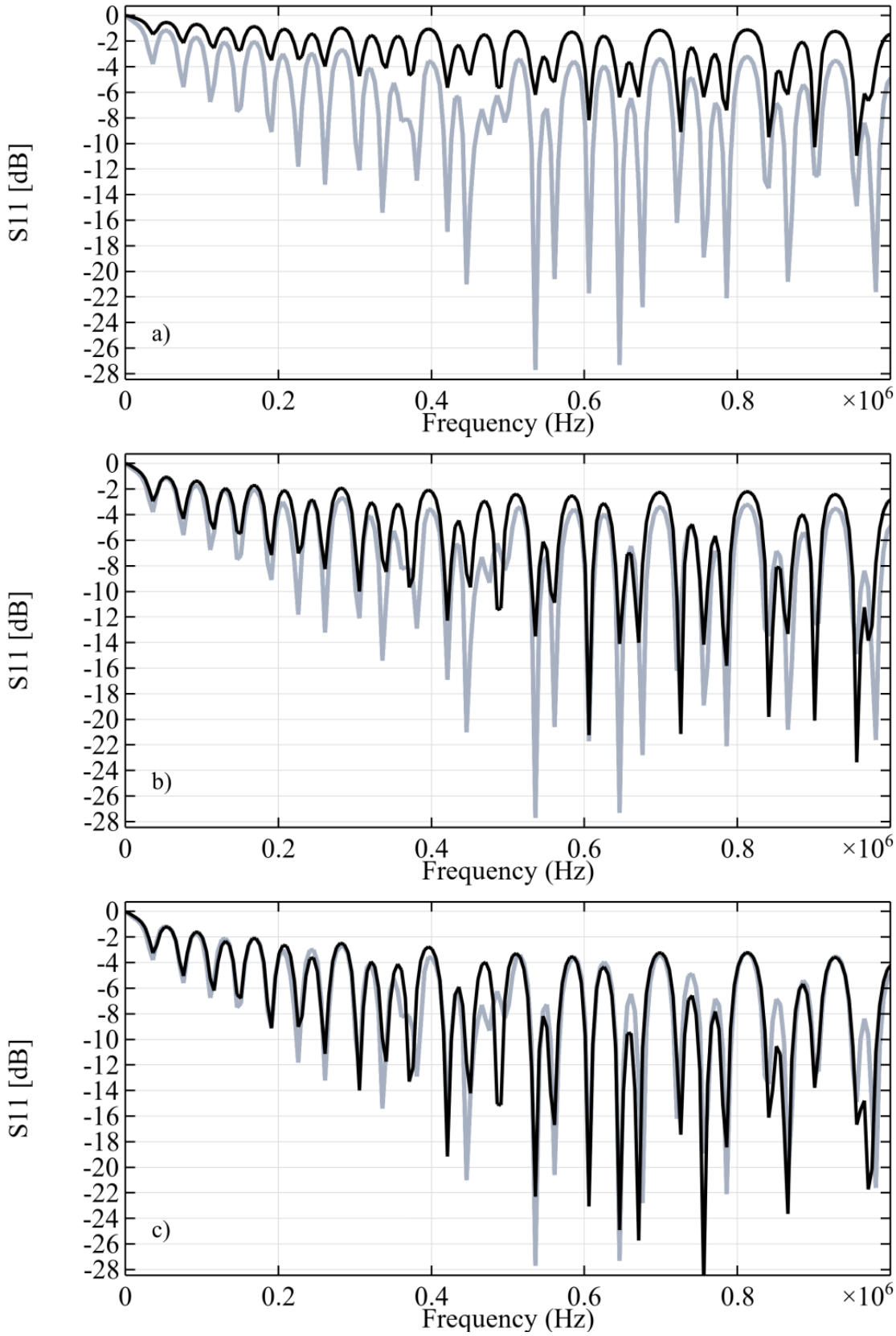

Fig. 7–14 Comparison between measured (grey curve) and simulated (black curve) S11-parameter.

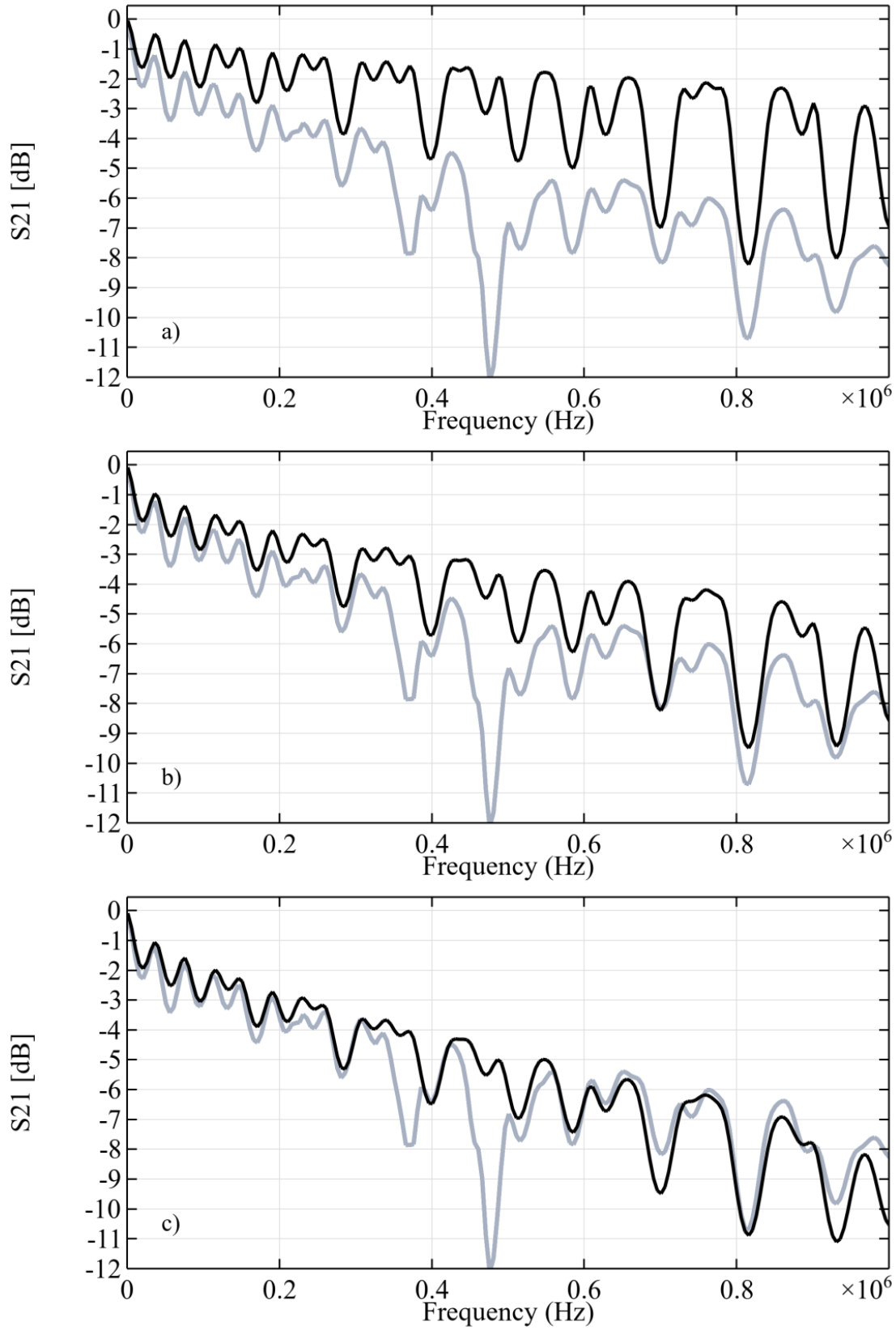

Fig. 7–15 Comparison between measured and simulated S21-parameter.

Simulation verification involves excluding everything from the calculation domain except for the cable segment of arbitrary length l, applying a wave condition at its one end and an absorption condition at the other. By measuring the difference in amplitude at the ends of the selected segment, the attenuation curve can be obtained:

$$H_{sim} = \frac{1000}{l} \cdot 20 \cdot \log_{10}\left(\frac{|V(\omega, l)|}{|V(\omega, 0)|}\right) \tag{7.6}$$

Fig. 7–16 shows it as a grey curve, which is overlaid by a dashed curve of calculated decay:

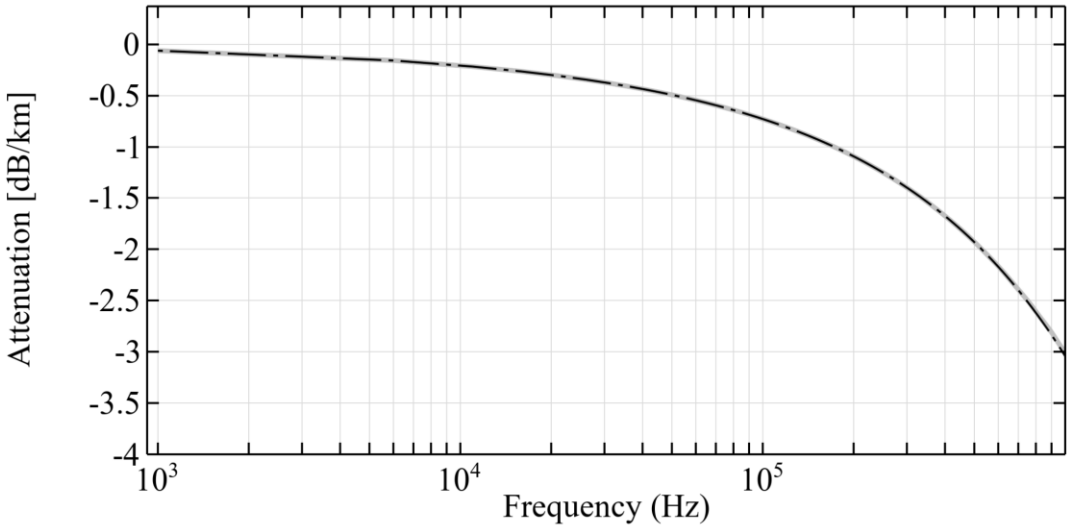

Fig. 7–16 Attenuation of the cable used in the test cable line. Grey curve – calculated through transmission line parameters according to Eq. (7.5), black curve – derived from (7.6).

7.5 Sensitivity Estimation

During the development of the monitoring system, one of the first tests conducted was to determine the achievable sensitivity, which refers to the ability to detect even small changes when monitoring a cable of a specific length. It is important to consider that sensitivity is affected by a variety of factors, including the attenuation of the cable, the performance of the sensors and amplifiers, and the presence of interferences on the line.

The conducted test involved injecting a charge of 20 pC galvanically using a standard calibrator at one („near“) end of the cable line (Fig. 7–17). A sensor was placed at the other („far“) end of the line. The injected signal passed through the line, reached the far end, reflected, propagated in the opposite direction, reflected from the near end of the cable, and so on.

At the same time, the sensor installed at the far end registered both the first impulse and subsequent reflected ones. Consequently, it was possible to estimate at what propagation distance the impulse becomes lost in the noise and ceases to be detectable. A discharge of 20 pC was chosen arbitrarily based on the experience that this value usually indicates a small insulation defect.

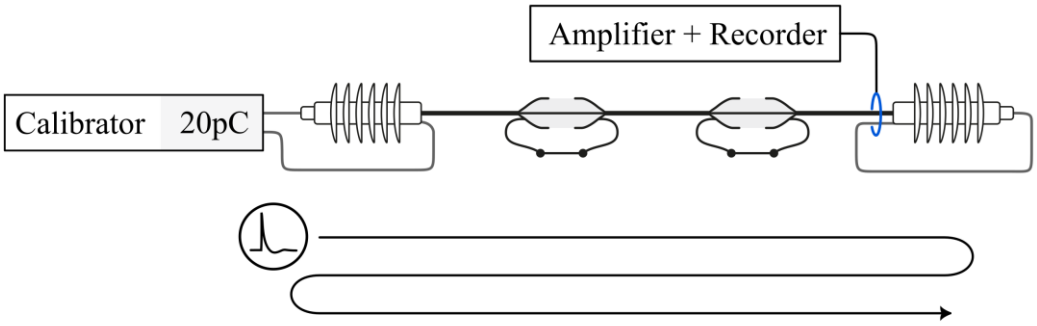

Fig. 7–17 Setup for sensitivity estimation

Regarding attenuation, our use of medium voltage cable leads to higher signal attenuation compared to HV cables: thinner dielectric insulation and smaller conductors result in greater losses in the dielectric and skin effect, which was discussed in more detail in [Pub. 4].

Therefore, this measurement can be considered the worst-case scenario in terms of attenuation. As for interference on the line, the setup is located in the vicinity of a high-voltage hall, so the measurements were not taken during times when the operation of other equipment caused strong colored noise interference.

Noise during quiet periods is certainly present – this includes white noise, radio interference, and narrow-band interferences whose source is difficult to identify. Noise on a real cable line can vary greatly from case to case – if we are considering groups of joints of a long underground line, the noise will be minimal due to the low-pass properties of the cable and attenuation properties of the soil, which would dampen external EM interference. On the other hand, if sensors are installed at a working substation, any noise level can be expected. Therefore, the experiment in this regard is conducted under existing conditions and can be compared with certain cases of real measurements, but not with some generic case.

Since the experiment was conducted at the beginning of the project work, not the custom recording hardware described at the end of the section 7.1 was used, but rather the equipment that was available at the time. At the same time, it was desired to neglect the influence of noise and lower limit of dynamic range of the recording device. Therefore, the device named Libera produced by Instrumentation Technologies was used, which had very

low intrinsic noise and a suitable dynamic range. In addition, I have installed a board with a fully differential amplifier (DC961B-ND by Analog Devices Inc.) between Libera and the passive sensor, as shown on Fig. 7–18. Several available amplifier models were tested: LMH6553SDEVAL/NOPB (Texas Instruments), DC800A-C (Analog Devices Inc.), LMH6401EVM (Texas Instruments), and THS7530EVM (Texas Instruments). Some of these models improved the SNR, while others did not. Although datasheet values of all tested models met the requirements, the final choice was based on the resulting SNR gain. However, this matter is not further analyzed, as it falls within the field of electronics.

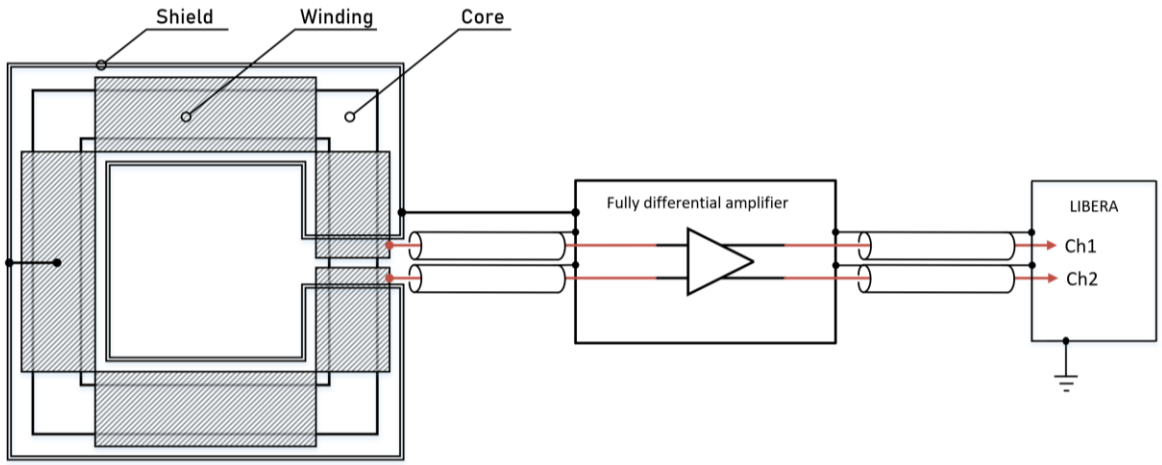

Fig. 7–18 Signal acquisition path used in sensitivity estimation setup.

The recorded sequence of pulses is shown in Fig. 7–19. The displayed signal was only filtered using a low-pass filter with a cut-off frequency of 1 MHz. Here we clearly see at least three separate pulses. The first pulse passed through a distance of 2200 m, followed by the second pulse which was reflected back from the near end and traveled in sum 6600 m. The third pulse passed through the line five times in total, covering a distance of 11,000 m.

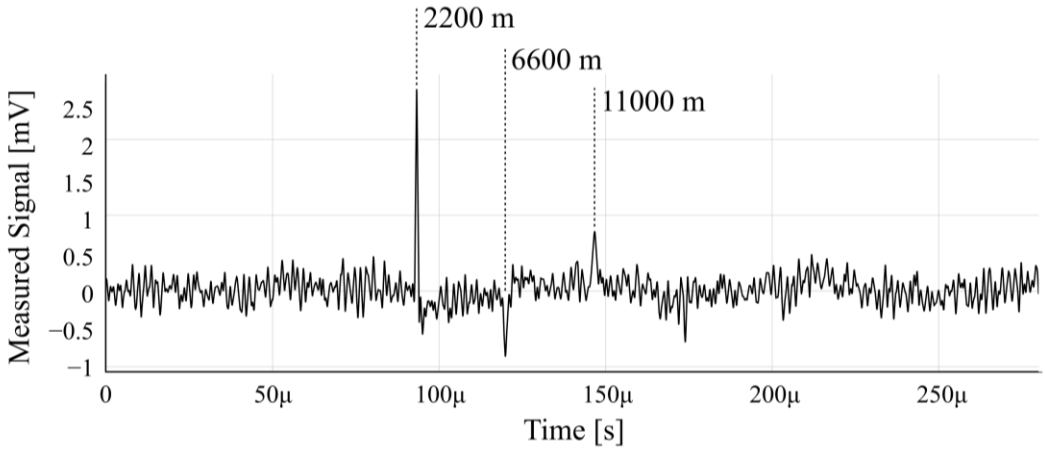

Fig. 7–19 Recorded sequence of pulses propagated over different distances.

Here, I am using only simple low-pass filtering to show that this result is achievable even without advanced signal processing. A more careful extraction of this signal from the noise was done by a co-author with the use of the Wiener filter in the article [Pub. 4].

7.6 Artificial PD source and Line Energization

Experiments on the localization of partial discharges (PD) could be carried out by injecting the discharge either through a calibrator or by energizing the line to obtain real PD on artificially created defects. Certainly, the most optimal approach is to start with the calibrator and then move on to a real PD. Energization of the line can be performed either with DC or AC voltage. Since a medium voltage cable was used, the possible limits of the applied voltages were rather limited. Obtaining a stable and continuous discharge at a constant current was quite difficult in this case, since those microscopic structures such as defects/bubbles and cavities, the recharge of which would lead to the emergence and development of PD, are absent. To obtain a stable and reproducible discharge, I developed an additional setup, which is presented in the publication [Pub. 1] and duplicated below in Fig. 7–20.

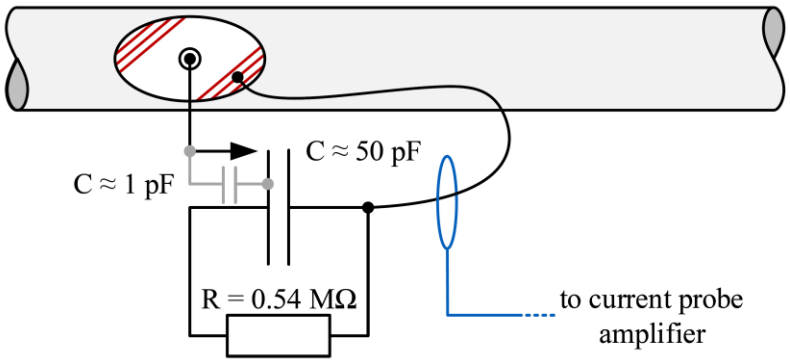

Fig. 7–20 Artificial generation of PD on DC, modified from [Pub. 1]

Generating PD on AC voltage is a much simpler task. A corona discharge occurs on a pointed conductor at a voltage of 3-5 kV, with the amplitude of the discharge increasing as the voltage increases. However, due to the large capacitance of the cable, it was necessary to compensate for reactive power – a small-sized power supply of a minor high-voltage test field could not maintain the required current. The methods of compensation are well known and well described, including in the new Cigre brochure [20], and a common schematic is placed below in Fig. 7–21.

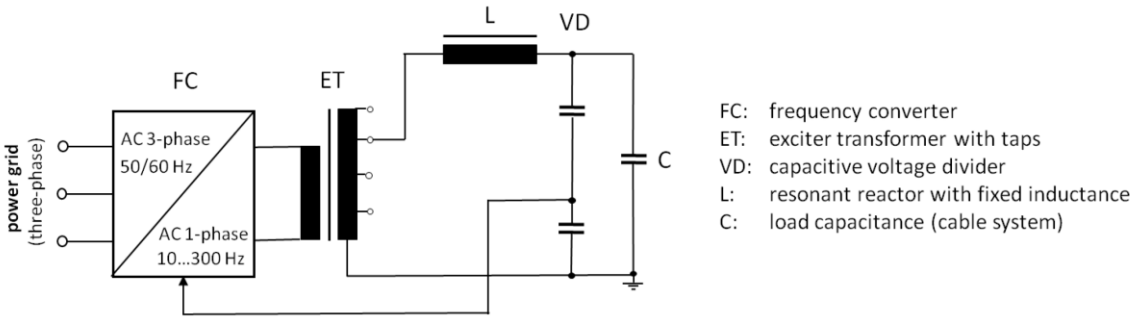

Fig. 7–21 Compensation as in [20].

However, here it is worth making a remark that in our case, firstly, it was not possible to change the power supply frequency, and secondly, the cable capacitance, although too large for supply without compensation, would require a very high inductance to resonate at 50 Hz if connected directly to the cable. Therefore, it was more practical to move it to the primary side of the step-up transformer, where the required inductance is reduced according to the square of the turns ratio. The resulting setup obtained for energizing is shown in Fig. 7–22, and as photos on Fig. 7–23.

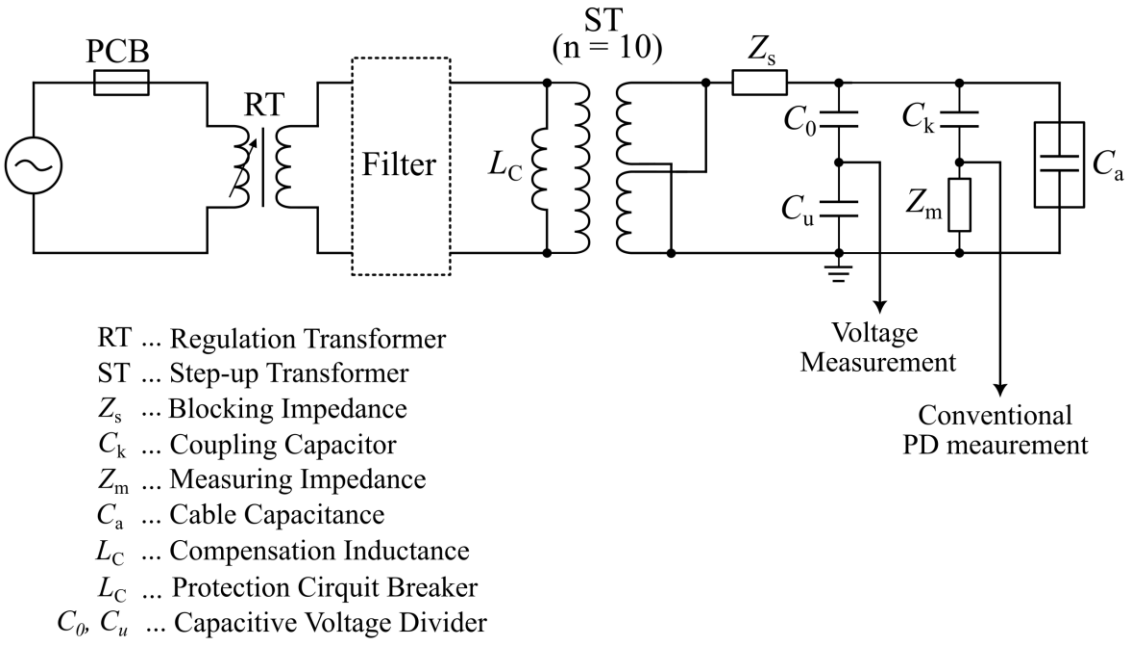

Fig. 7–22 Schematic of AC energizing setup with parallel compensation on the primary side

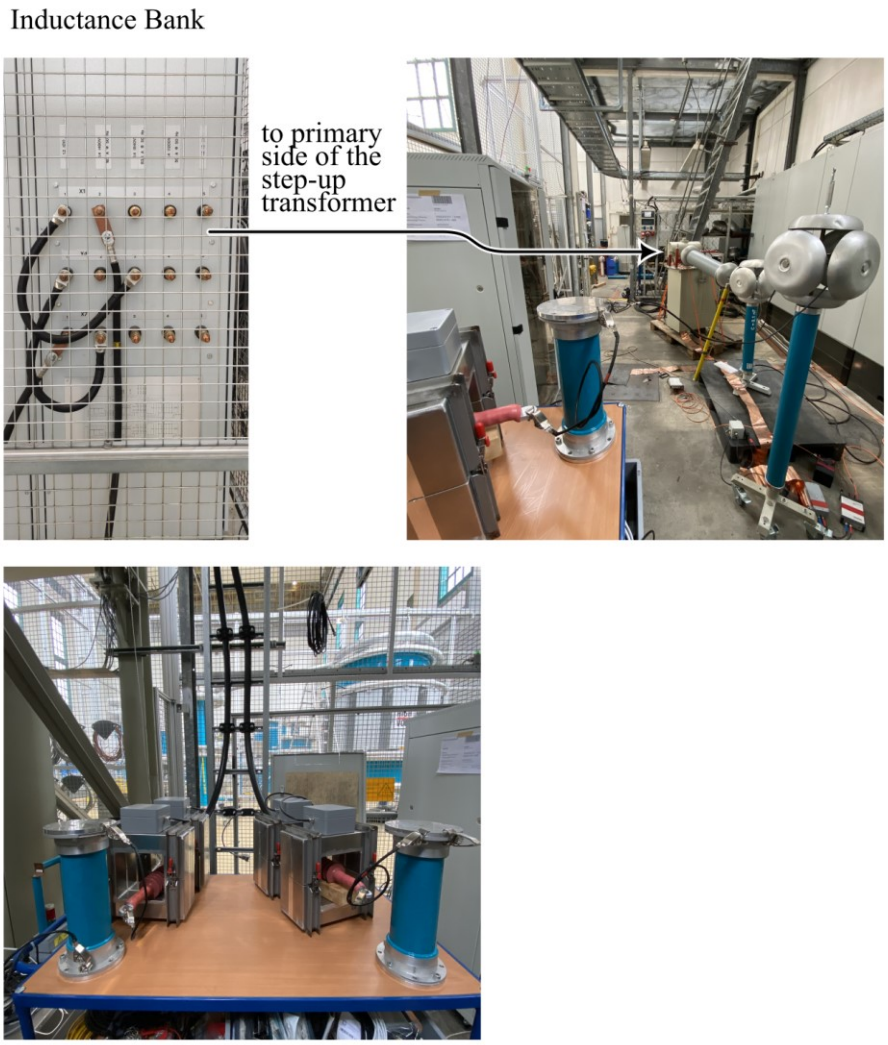

Fig. 7–23 AC energizing setup with parallel compensation on the primary side

7.7 Localization & Reflection Coefficients

The experiments on the localization of PD were primarily aimed at testing various mathematical approaches. An important initial requirement was to obtain data close to how it would be produced in a real case, thus verifying the realism of the approach. Some of these experiments were described in articles [Pub. 1], [Pub. 2], [Pub. 4], [Pub. 6]. The main contribution to the development of the mathematical model of localization was made by colleagues from the Acoustics Department of the Technical University of Dresden. To a certain extent, the author of this work also contributed to this development, especially with regard to the adaptation of models to real working conditions. Apart from that, experimental setups, data collection, and preliminary analysis of results were my responsibility. Although descriptions of the experiments and localization results have already been published in the

aforementioned articles, it would be interesting to provide a more extensive commentary on one of the topics related more to the experimental technique than to the direct mathematics of localization.

The adaptive model presented in the publication [Pub. 6] simulates line accessories such as joints and terminations as frequency-dependent complex reflection coefficients. In the simplest case, their spectra are approximated through linear interpolation between two points in the frequency domain, as shown in Fig. 6–8. Naturally, this raises the question of how accurate such an approximation is. Consequently, it is desirable to measure these reflection coefficients and compare them with the optimization result. Certainly, one could inject a wave into the line and measure the reflected signal; however, conducting this experiment "cleanly" is challenging, meaning excluding the influence transfer function of the cable, of the sensor, and so on. Instead, the author proposed an alternative approach.

The VNA proves to be useful in this context as well. The upper part of Fig. 7–24 depicts one of the setups for training PD localization when the line is energized with AC to get a real discharge. At the ends of the line, 10 nF capacitors are installed to close the signal propagation path, along with inductive sensors that also contribute to the reflection coefficient – those are also visible in Fig. 7–23. Additionally, to one of the terminations the AC-supply setup is connected.

To measure the reflection coefficient, the cable termination was replaced with a VNA. The positions of all connecting cables and elements remained unchanged. Though usually VNA is used to measure S-parameters, it also has a built-in function for converting them into reflection coefficients, with the source impedance taken into account. In this case, the source impedance was specified as equal to the cable's characteristic impedance, which was calculated approximately and, within this approximation, did not depend on frequency. The obtained reflection coefficients are shown in Fig. 7–25. They were directly incorporated into the adaptive model, resulting in a more accurate signal synthesis. Moreover, it is possible to assess the influence of various setup elements on the reflection coefficient. For example, from Fig. 7–25, it can be seen that connecting the setup for AC voltage generation only led to a small local minimum in the low-frequency region.

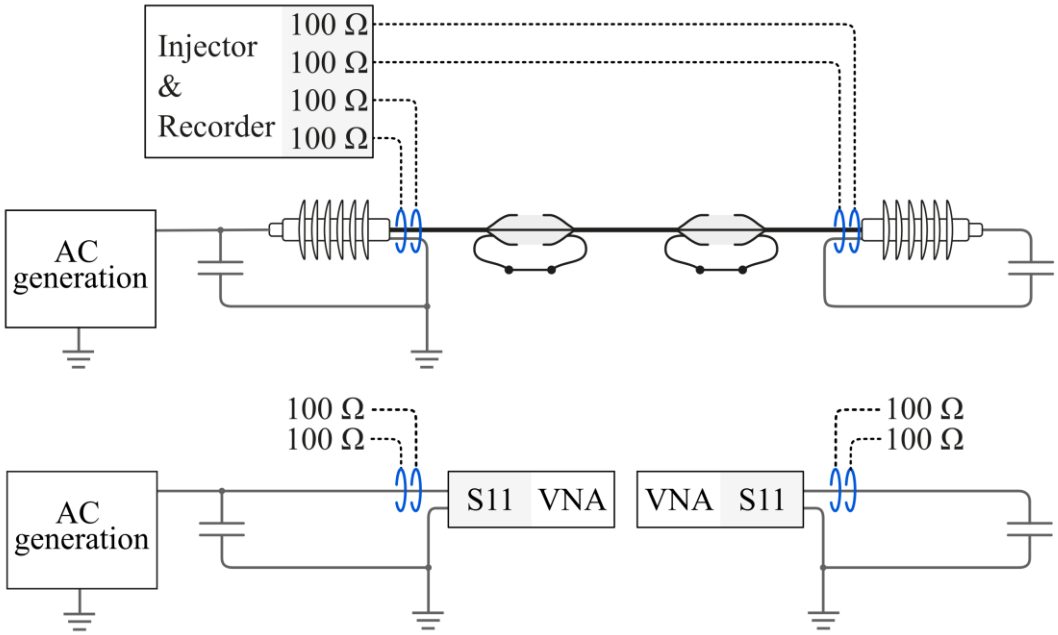

Fig. 7–24 Setups for localization (upper part)
and measurement of the reflection coefficients (lower part)

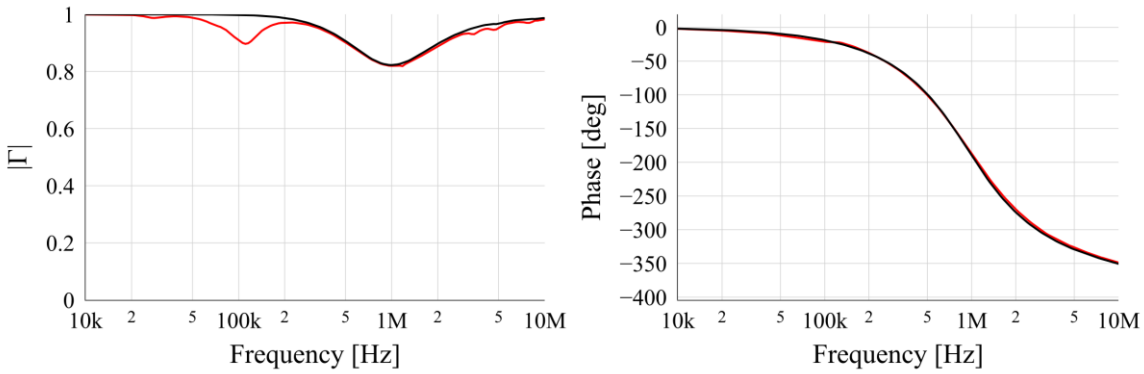

Fig. 7–25 Magnitude and phase of the reflection coefficient measured with VNA

8. Chapter:

On-site Test

8.1 HVAC Cable Line

A 110 kV HVAC cable line was used as the object of investigation. This line connects a feeder overhead line on the outskirts with a distribution substation located close to the city center, however both substations feature other upcoming cable- and overhead lines which can be connected with the cable line selected for monitoring. The total length of this line is just over ten kilometers. The average length of the single cable segment in this case ranges from 500 to 700 meters, which leads to a large number of joints. The topology of the line is shown in Fig. 8–2. The line is constructed using a sectionalized cross-bonding scheme: it has two major sections and a joint with screen grounding between them. Each major section has cross-bonding joints and number of straight ones, which alters from section to section. The sensors were installed only at the cable terminations at both ends of this line and can be seen on Fig. 8–1.

Fig. 8–1 HFCTs installed on the cable end terminations of 110 kV AC line.

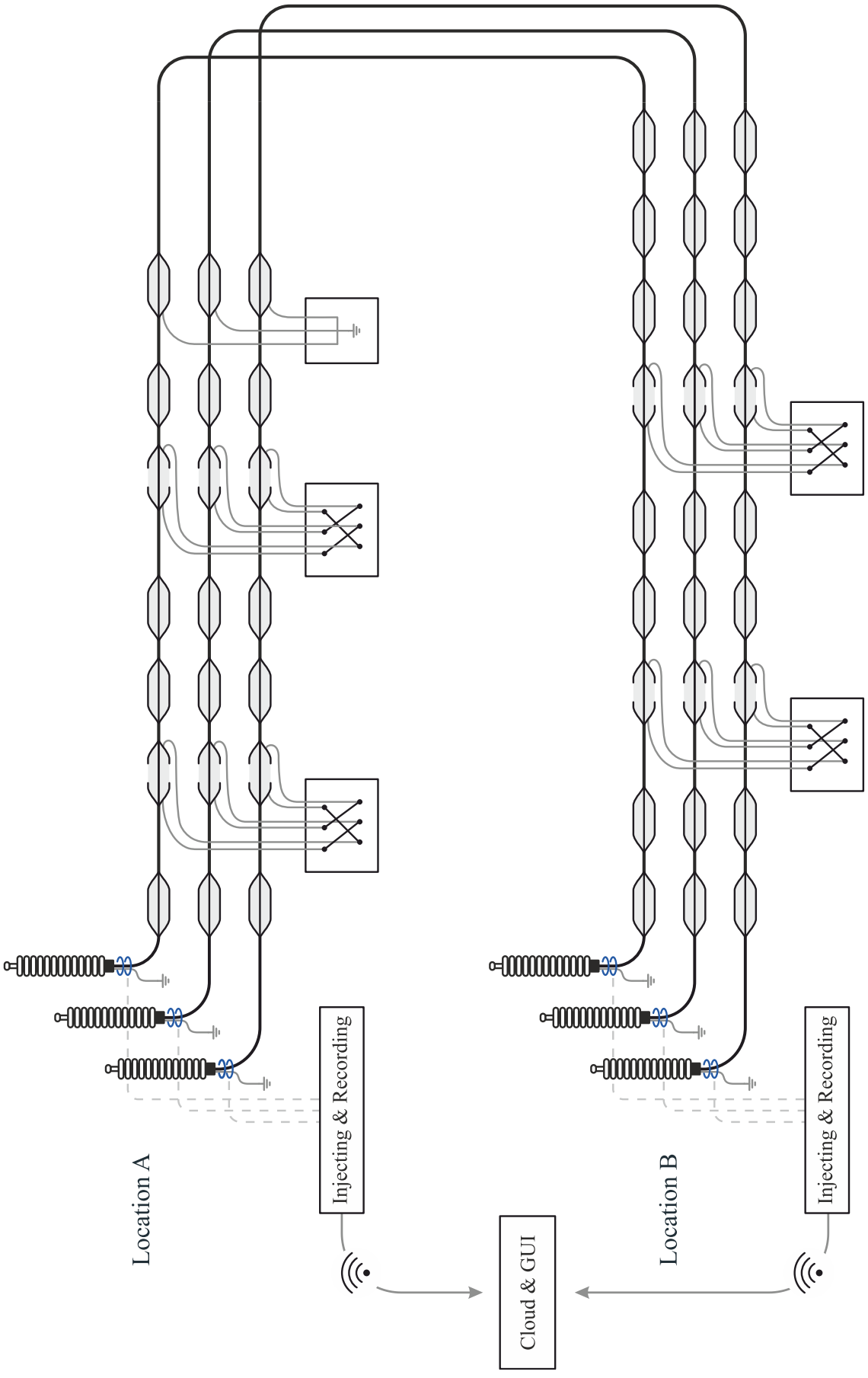

Fig. 8–2 Topology of the 110 kV HVAC line used in study

In order to model the line, a calibration signal is injected by sensor on each of its ends. At the time of launching this pilot project, custom recording & injecting hardware had not yet been manufactured. Therefore, to inject and measure signals on three phases and two sides of the line, I utilized RedPitaya devices described at the beginning of the chapter 7.1 in the "Hardware" section, controlling them with SCPI commands.

One of the consequent issues was the limited buffer of the injected signal. Therefore, in the measurements a pair of sweep signals were used – one covering a lower frequency range (approx. 100 kHz – 2 MHz), and another for a higher frequency range (approx. 250 kHz – 3.5 MHz). Both are shown below in the Fig. 8–3 and Fig. 8–4.

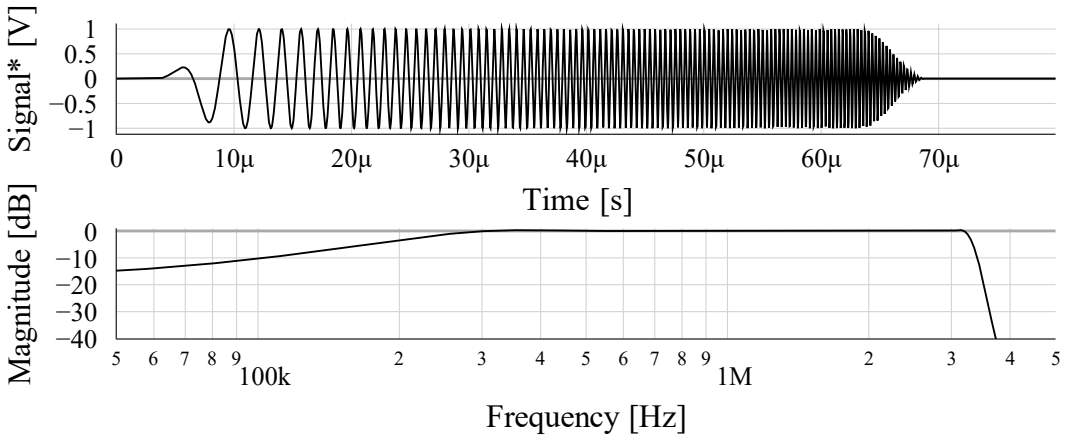

Fig. 8–3 Higher frequency sweep.
*Signal amplitude at the output of the amplifier and input of the HFCT was roughly 60 V peak-to-peak, that resulted in the injected current in the cable below 1 A.

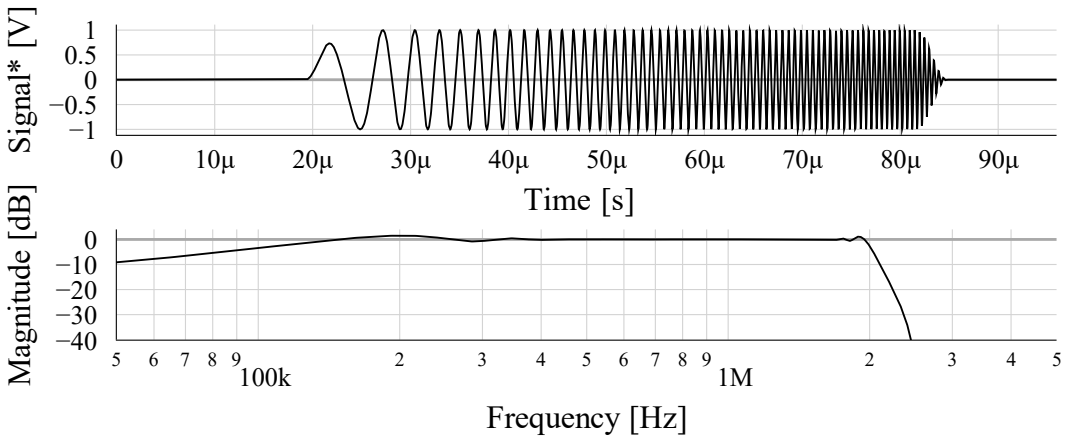

Fig. 8–4 Lower frequency sweep.
*Signal amplitude at the output of the amplifier and input of the HFCT was roughly 60 V peak-to-peak, that resulted in the injected current in the cable below 1 A.

Certainly, the wave actually injected into the cable differs significantly from the ideal digital sweeps shown on figures above. As mentioned at the end of the chapter 6 (Localization), the impedance of the substation equipment connected to the line, as “seen” from the line's side, plays a major role. Calculating its value would be a rather complicated endeavour – while the transmission line parameters of the busbars can be estimated from the geometry, assessing the frequency dependant impedances of other substation facilities is hard to perform. In addition, the transfer function of the HFCTs should not be overlooked.

Let us denote two measurement locations on both sides of the line with letters A and B, as also shown on Fig. 8–2. The higher-frequency sweep injected at location A and measured at the “near” and “far” ends of the line – naturally, the “near end” is the one where the signal injection occurs is shown on Fig. 8–5. The Fig. 8–6 shows the same sweep injected at location B, therefore at the plot “near” and “far” ends changed accordingly. It is evident that the near and far end recordings from Point A differ from those at Point B. This differences and similarities are even easier to assess in the frequency domain, as shown in the graphs in Fig. 8–7 and Fig. 8–8.

As can be seen, in both cases, the coupling into the cable increases with frequency and reaches its maximum at roughly 1 MHz. This behavior can be explained in several ways - as the influence of the current transformer and as the effect of the termination impedance. Concerning the first explanation, it is necessary to refer to the equivalent circuit of the transformer and note with regard to the signal injection, that the wave impedance of the cable greatly exceeds the single-turn impedance of the used HFCT. For instance, if the single-turn inductance (referred to from the cable side) is 1 μH, then at a frequency of 100 kHz the impedance of the magnetizing branch is about 0.6 Ohms, while the characteristic impedance of the cable will most likely fall within the range 20 – 50 Ohms. This leads to weak coupling at lower frequencies and its increase with higher frequencies.

As for the second explanation, the following example can be given: For a frequency of 1 MHz, the wave quarter-wavelength in a free space is only about 75 meters, therefore, even if at the substation only a long busbar is connected to the termination, this will be sufficient on its own to ensure signal coupling. Below the first resonance point, the higher the frequency the higher such coupling would be. Furthermore, if considering power equipment that could be connected to the busbars, it is highly likely that at certain frequencies, some form of resonant mode will occur, facilitating signal transmission into the line.

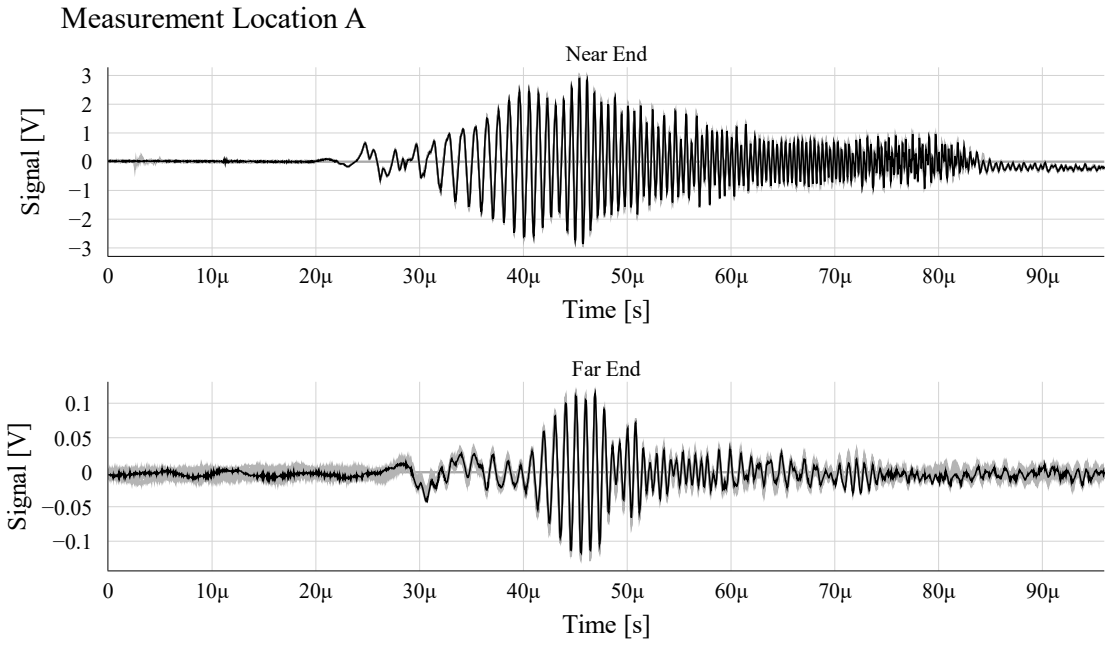

Fig. 8–5 Higher-frequency sweep injected at location A and measured at the “near” (A) and “far” (B) ends of the line.

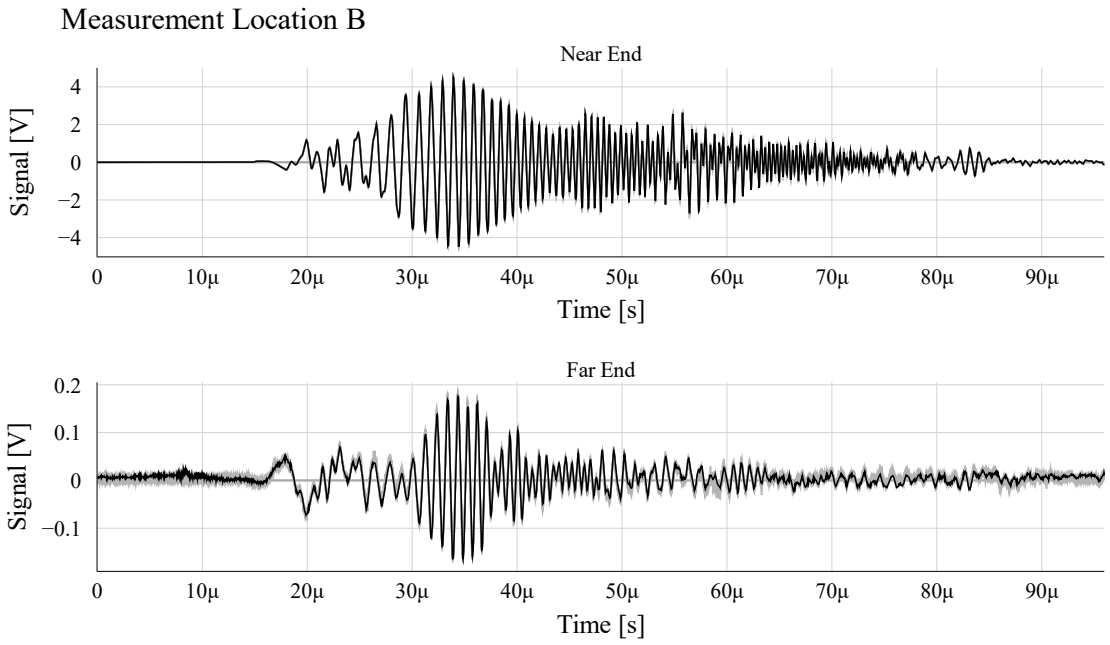

Fig. 8–6 Higher-frequency sweep injected at location B and measured at the “near” (B) and “far” (A) ends of the line.

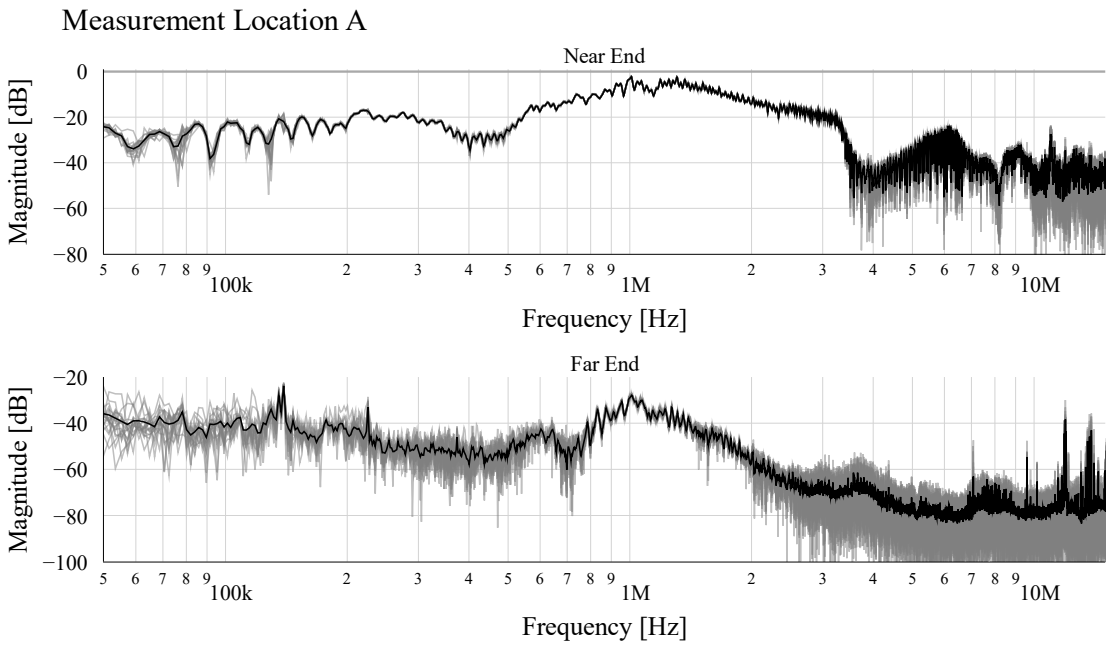

Fig. 8–7 FFT-derived magnitude spectra of higher-frequency sweeps injected at location A and measured at the “near” (A) and “far” (B) ends of the line.

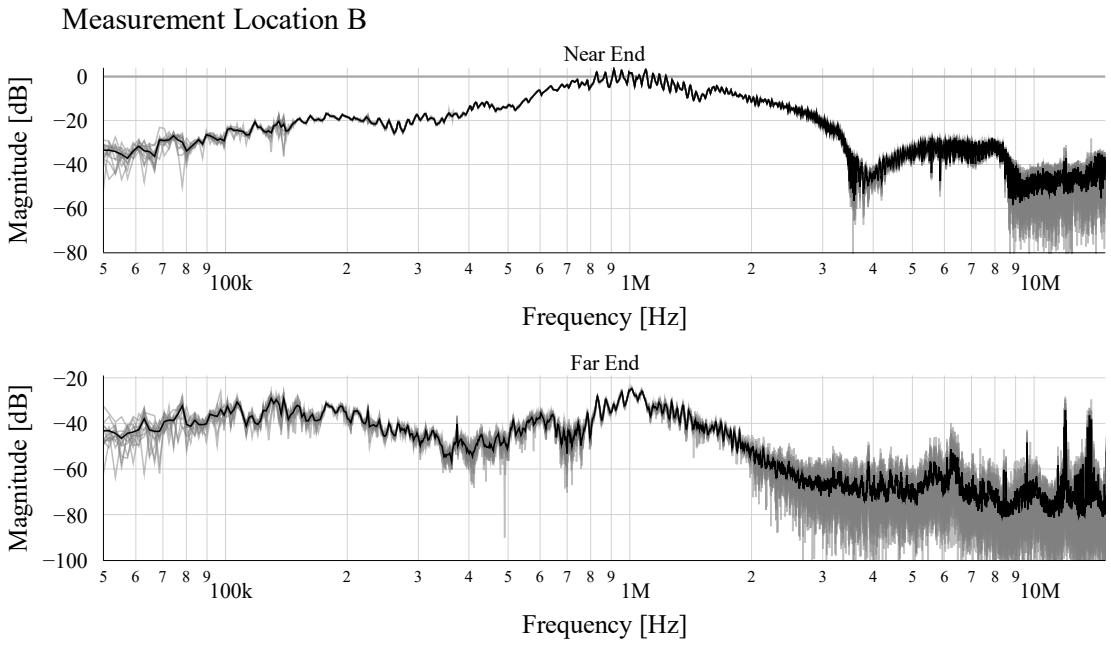

Fig. 8–8 FFT-derived magnitude spectra of sigher-frequency sweeps injected at location B and measured at the “near” (B) and “far” (A) ends of the line.

Now let's consider the transfer function between the measurement locations A and B: since the signal could be sent from either side, we obtain two transfer functions displayed in Fig. 8–9 and Fig. 8–10. Both graphs are composed of two parts, resulting from two sweep signals with different frequencies, which accurately overlap in the middle of the frequency range.

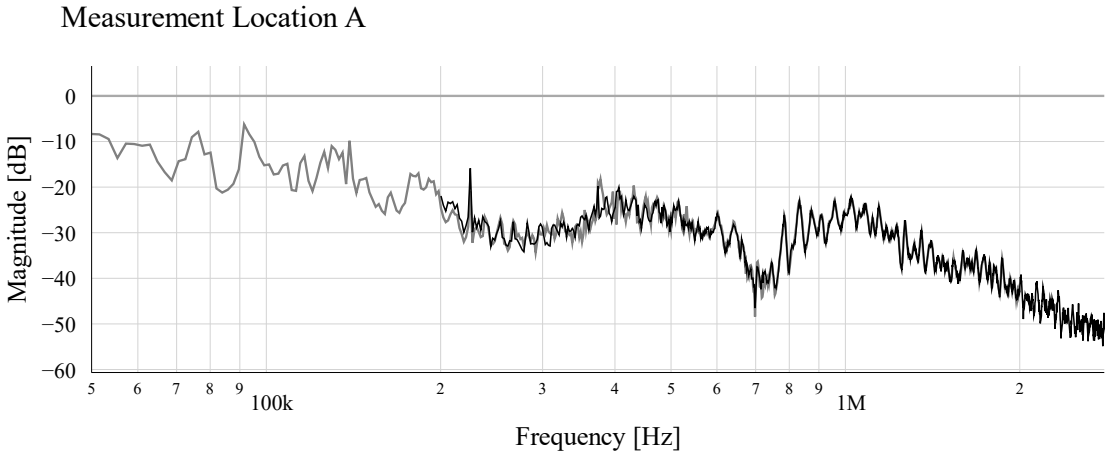

Fig. 8–9 Transfer function measured from location A to location B

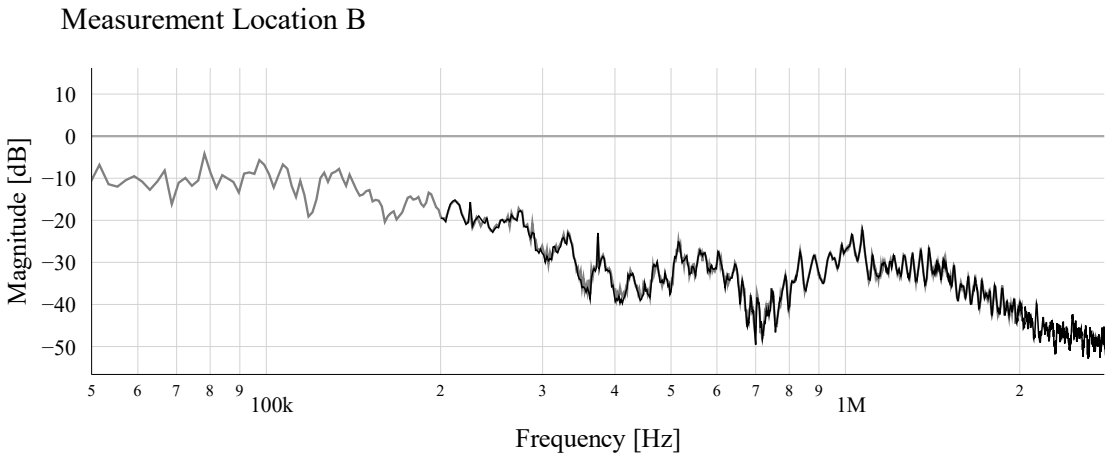

Fig. 8–10 Transfer function measured from location B to location A

The transfer functions from locations A and B generally have alike overall shapes, yet there are certain differences. Furthermore, the shape of the obtained characteristic itself is interesting by itself. Before delving into its analysis, it is important to note that we are examining the transfer function between two distant measuring locations, which should not be mistaken for cable attenuation, or a transfer function of single cable piece on its own. Attenuation certainly plays its role, but in addition to it, the impedance jumps, the input impedance of the line and elements connected at the injection point, and reflection coefficients at the receiving ends contribute to the overall effect. The combination of these factors leads to a better transmission of some frequencies and damp the others. This is also the reason why the transfer function from A to B is not equal to the one from B to A.

As to be expected, the transfer functions indeed show lower attenuation at lower frequencies, with only around $10 - 15$ dB for a line longer than 10 km with multiple cross-bonding sections. This is followed by a decline and an uneven plateau from roughly 250 kHz to a bit over 1 MHz: for example, the curve on the upper graph crosses the -30 dB mark multiple times within the range of 220 kHz to 1.2 MHz. At the same time, within this plateau, exists a distinct minimum (around 700 kHz), where the transfer function drops to -40 dB. This is interesting, because in practical applications like "power-line communication" between units signals of this frequency are unlikely to pass through and be received. Going further to the high-frequency range above one megahertz, we see a gradual decrease in the transfer function – as mentioned in the previous chapter, various cable attenuation mechanisms come into play here effectively. The graph ends when the measured signals in the frequency domain approach the noise level.

It can be concluded that for such a complex case, the obtained graphs showing a decrease in the transfer function from approx. -10 to -35 dB (100 kHz – 1.3 Mhz) provide an optimistic forecast of the global-sensitivity approach in cable monitoring. Even within the framework of this complex line topology, PD pulses originating from one accessory of this line are likely to be registered at its ends. Put simply, if this experiment had shown that the complete transfer function lies below -40 dB, the forecast would have been negative.

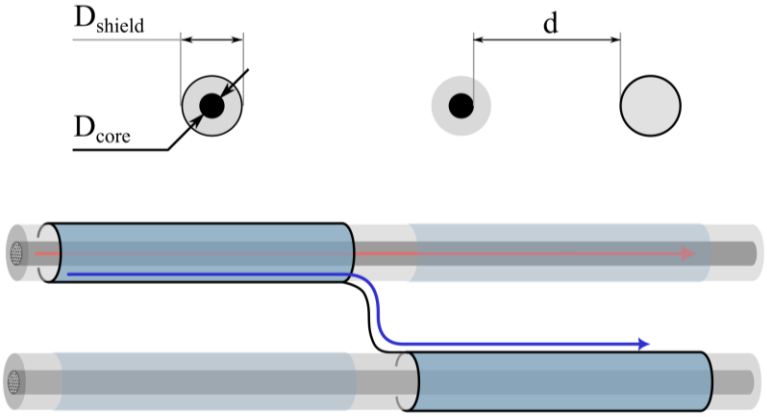

Fig. 8–11 Shield transposition at the cross-bonding group leading to the impedance mismatch

The Fig. 8–11 highlights a primary obstacle in signal propagation in AC lines, namely, cross-bonding of the cable shield. As was explained in chapter 2.4 and also visible on Fig. 8–2 the cross-bonding features connecting the shield of one phase to the one of another phase. Consequently, the propagating PD signal has to follow this route. This is a case with two tandem transmission lines, the impedances of which can significantly differ, leading to

substantial signal reflection and, consequently, a decrease in the transfer function between measurement points at the line ends.

The reflection coefficient can be derived from the line impedances before and after the screen separation occurred. We will not perform a numerical calculation, but the geometry already indicates that if the cables are laid in the air (for example, in a concrete duct), the impedance of the “parallel conductors” waveguide after the split (Fig. 8–11, top right) will be much higher than that of a coaxial line (Fig. 8–11, top left). Accordingly, the reflection coefficient will go high as well.

On the other hand, if the line is buried in soil, which is most often the case with AC lines, the dielectric permittivity of the earth (sand, or other material into which the line is buried) will play a significant role. Its real part can be quite high; for many soils at frequencies around one megahertz, it can be by several orders higher than vacuum permittivity [174], [175], [176]. Soil, as a high-permittivity material, between two conductors of the waveguide will decrease the characteristic impedance and the reflection coefficient as well. However, the imaginary part of the dielectric permeability should not be ignored within this calculation as it can be quite high accounting for damping of the soil, while on the other hand, it will be compensated to some extent by the cable's main insulation. For such relatively complex geometry, one could perform a fairly simple impedance calculation through FEA, which could result in a rather accurate estimate of the reflection coefficient – after all, the frequency-dependent values of complex dielectric permittivity are published in many sources and for different types of soils. However, this will remain outside the scope of this work.

9. Chapter:

Conclusion and Outlook

9.1 Summary and contributions

This thesis starts with collecting and analysing issues related to the PD monitoring of underground power cables, first within the framework of existing AC lines, for which well-known solutions exist, and afterwards shifts the focus to the long HVDC projects, for which a universally recognized solution is yet to be developed. Special attention is given to line topologies of HVAC and HVDC cases, particularly in terms of sensor installation. The framework of the thesis is given by the description of a PD monitoring system capable of addressing the shortcomings of existing solutions, which was to some extent outlined in previous co-authored publications, e.g., [Pub. 1], [Pub. 2]. Based on this description, selected components that constitute this system are examined in the subsequent chapters.

Significant attention has been devoted to the high-frequency current transformer (HFCT). Detailed examination of design aspects of the device has been carried out, particularly from a practical perspective. Formulas that are most relevant for the HFCT design have been provided. The estimation of leakage inductance has been explored using the FEA method. The calculation methodologies demonstrated can be applied not only to HFCTs but also to a wide range of other magnetic devices. The balanced design of HFCT aiming at improving SNR in noisy environment was proposed. The occurrence of various resonance modes in the magnetic core have been demonstrated, along with exploration on the proper construction of a simulation models. It has been shown that models with simplified winding may hinder the appearance of longitudinal resonance mode. The aspects of HFCT prototyping, material selection, performance assessment methodology, quality control and the description of the device that was placed in the series production have been presented. One of the core differences of the developed HFCT from the ones available on the market, is the ability to operate in the presence of up to 3 kA of superimposed power current AC or DC. Therefore, development description pays attention to this via FEA-based approach and a row of experiments.

In the chapter dedicated to signal separation, the algorithm for PD signal extraction from noisy recordings used in the current version of the monitoring system and based on LPC coefficients is re-described with the reference to the initial contribution of the co-authors in proceeding [Pub. 5] and patent [Pat. 4]. This thesis shows that there are alternatives to the applied algorithm and gives a literature review of contemporary methods for PD signal extraction from noise. Several examples of the separation algorithm's performance are

provided, including the extraction of different signals (decaying sinusoid, PD-shaped pulse) from various types of noise (white noise, narrowband interference, colored noise). A field-data example of signal extraction from a real recording obtained from a 110 kV cable line is presented.

One of the chapters was dedicated to the theoretical aspects of the localization algorithm. The high-voltage power cable for PD signals behaves as a low-pass filter, leading to differing dispersion and attenuation of signals that have propagated over different paths. This opens up the possibility of localization based on the frequency content of the signals and the transfer function of the cable, which is discussed in articles [Pub. 1], [Pub. 4], [Pub. 6], and patents [Pat. 1 – Pat. 4], and further supplemented by this work. Examples are provided with increasing complexity, demonstrating the challenges of this approach, particularly due to the cable's non-uniformity: impedance mismatches at cable accessories.

The chapter dedicated to laboratory tests complements the research presented in the articles [Pub. 1 – Pub. 6] in which the author made his contribution in working on experiments and issues related to PD signal propagation and localization problems. The content of these articles is mostly excluded from this thesis, so the reader who is willing to follow the line of monitoring system development is encouraged to explore them additionally. On the other hand, this chapter can be considered separately and may be useful for other studies. Firstly, it discusses the recording devices used in the tests mentioned in the aforementioned articles, highlighting their strengths and weaknesses, especially in the regard of obtaining multi-channel PD measurements and signal injections. Secondly, a description of the test cable line that was established for PD localization tests is provided. This description was followed by the characterization of its topology using TDR-based methods, the estimation of the cable attenuation via COMSOL simulation combined with S-parameters measured with the vector network analyzer. Further application of this device is found in the determination of cable accessories reflection coefficients. System sensitivity tests through small signal detection were presented. The process of energizing the line using a compensating reactor is demonstrated, along with the peculiarities of obtaining PD signals under the DC stress.

The final chapter describes the installation of the system on a 110 kV AC cable line. The topology of the line, the installation of the developed HFCTs, injected signals, the transfer function between the installed sensors, and the peculiarities of reflections on cross-bonding groups are presented.

9.2 Outlook

Since this work only focuses on certain aspects of the monitoring system, there are numerous directions in which further research can be conducted. The sensor, which has already been released into serial production, is perhaps one of the most complete component of the overall system, as it has the required performance. Though this work had covered most significant aspects of the HFCT design, it would be interesting to explore the influence of magnetic core material, compound, shielding, and other factors on its resonance behavior.

In regard to signal separation, the algorithm can be infinitely refined. Signal processing offers a wide range of methods suitable for partitioning a signal into mode components or coefficients, and most of those can be employed in extracting PD signals from noise. The application of these techniques to real-time scenarios, facilitating the separation of signals, presents an area of compelling interest. Furthermore, even within the framework of the LPC approach, a considerable amount of optimization space exists. This includes the use of warped LPC coefficients, determining the number of coefficients applied, enhancing resilience to interference and modulated noise, among other elements.

Additionally, this study does not mention methods based on neural networks, e.g., utilization of an autoencoder for the generation of feature vectors.

The localization module is one of those blocks that require the most extensive further research. The achievable accuracy in the articles [Pub. 1] and [Pub. 4] show that the selected approach is generally viable and particularly well-suited for the case of HVDC cables due to the simplicity of their structure. Contrary to the cable test line used in this study, a real long line would consist of numerous monitored segments, and the monitoring system must encompass all of them. At this juncture, it is crucial to remember that each measurement point on the joint will capture signals from two line segments that it bounds. Moreover, signals from other distant segments may also reach it. Therefore, the architecture of the system must be designed with this in mind. From a technical standpoint, this scaling challenge should not be an impediment; rather, it is a task that needs to be addressed and accomplished. A more complex challenge lies in applying the localization algorithm to different line topologies, such as cross-bonded AC lines, offshore lines connecting wind generators and substations, and drawing conclusions on achievable sensitivity in each scenario.

Within the mathematical model of localization, still remains a several issues to consider, one such being the incorporation of sensor transfer functions into localization algorithms. Generally, the transfer function of every sensor produced is measured in a laboratory as part of quality assessment. However, when dealing with analog device as HFCT is, we cannot account for it by simply multiplying the transformer's transfer function, measured in the lab, with the signal recorded by the sensor installed on the cable. This issue also relates to the challenge of calculating reflection parameters of terminations from the received frequency response measured at the point of signal injection, as it results from the interaction of the HFCT, terminations with connected equipment, and outgoing cable.

Moreover, there are still functional blocks mentioned in the description of the monitoring system that had not received further attention in this work, such as:

- clustering - to group the extracted signals into sets (clusters), and in this way differentiate between multiple PD sources
- pairing of the events - as the result of the signal separation or clustering module, we acquire separate signals or signal clusters from both ends of the monitored segment. Before we proceed with the localization, it is necessary to identify pairs of signals (or clusters) from both ends that will be further utilized in the localization algorithm.
- calculation of the PD charge at the point of origin by compensating measured signal with appropriate transfer function of the propagation path.

In addition to monitoring, such system can also be used for other applications, such as aging diagnostics for cable or other electrical devices, line-damage monitoring, fault location.

Publications

[Pub. 1] E. Winkelmann, I. Shevchenko, C. Steiner, C. Kleiner, U. Kaltenborn, P. Birkholz, H. Schwarz, and T. Steiner, "**Monitoring of Partial Discharges in HVDC Power Cables**," in **IEEE Electrical Insulation Magazine**, vol. 38, no. 1, pp. 7-18, January/February 2022, doi: 10.1109/MEI.2022.9648269.

[Pub. 2] E. Winkelmann, I. Shevchenko, C. Steiner, P. Steiner, C. Kleiner, U. Kaltenborn, P. Birkholz, F. Böhme, A. Küchler, M. H. Zink, S. Kornhuber, H. Schwarz, T. Steiner, and S. Markalous, "**Advanced Analysis of Partial Discharges and Breakdowns on HVDC Power Cables**," in Proceedings of **Cigre**, Study Committee B1 (Insulated Cables), PS1 (Preferential Subject), 1073. Presenter**: I. Shevchenko**

[Pub. 3] I. Shevchenko, E. Winkelmann, C. Steiner, U. Kaltenborn, H. Schwarz, and T. Steiner, "**Grid Compatibility of a High-Frequency Current Transformer Designed for Coupling to the Cable Central Conductor**," in Proceedings of the 2021 IEEE Conference on Electrical Insulation and Dielectric Phenomena (**CEIDP**), Vancouver, BC, Canada, December 2021, pp. 315-323, doi: 10.1109/CEIDP50766.2021.9705455. Presenter**: I. Shevchenko**

[Pub. 4] E. Winkelmann, C. Kleiner, I. Shevchenko, C. Steiner, S. Stone, P. Birkholz, and T. Steiner, **"A Novel Approach for a Highly Sensitive Localization of Dielectric Defects in Cable Systems Based on an Adaptive Model**," in Proceedings of the 2021 International **ETG** Congress, May 2021, pp. 554-560.

[Pub. 5] E. Winkelmann, C. Steiner, I. Shevchenko, P. Steiner, P. Birkholz, and U. Kaltenborn, "**Machine Learning Based Evaluation of Dynamic Events in Medium Voltage Grid Components**," in Proceedings of the 26th International Conference and Exhibition on Electricity Distribution (**CIRED** 2021), Online Conference, 2021, pp. 46-50, doi: 10.1049/icp.2021.1859.

[Pub. 6] C. Kleiner, C. Steiner, I. Shevchenko, T. Steiner, and P. Birkholz, "**Analysis of Cable Systems by Modelling their Transfer Functions**," in Proceedings of the **HIGHVOLT KOLLOQUIUM** '23, Dresden, Germany, May 4-5, 2023.

Relevant Patents

[Pat. 1] I. Shevchenko and E. Winkelmann, "Messvorrichtung für einen Stromwandler," [Non-official translation: Measurement device for a current transformer"], Patent application WO2022214307A1.

[Pat. 2] E. Winkelmann, "Zustandsanalyse eines elektrischen Betriebsmittels," [Non-official translation: "Condition Analysis of an Electrical Device."], German Patent DE102018126743B3, Jan. 9, 2020.

[Pat. 3] E. Winkelmann, T. Steiner, and P. Birkholz, "System für eine Kabelstrecke, Übertragungssystem zum Übertragen von elektrischer Energie und Verfahren zum Betrieb des Systems," German Patent DE102020108382A1, Sep. 30, 2021.

[Pat. 4] E. Winkelmann and C. Steiner, "Vorrichtung, System und Verfahren zur Bestimmung von Fehlersignalfenstern in einem Messsignal," German Patent DE102020122792A1.

Bibliography

[1] Gesetz zur Einführung von Ausschreibungen für Strom aus erneuerbaren Energien und zu weiteren Änderungen des Rechts der erneuerbaren Energien Vom 13. Oktober 2016. [Online]. Available: https://www.erneuerbare-energien.de/EE/Redaktion/DE/Dossier/eeg.html?cms_docId=132292

[2] European Commission, "Commission staff working document 'Impact assessment' accompanying the document 'Communication from the commission to the European Parliament, the council, the European economic and social Committee and the committee of the regions,'" Brussels, 17.9.2020, SWD(2020) 176 final.

[3] Bundesministerium des Justiz, "Atomgesetz in der Fassung der Bekanntmachung vom 15. Juli 1985 (BGBl. I S. 1565), das zuletzt durch Artikel 1 des Gesetzes vom 10. August 2021 (BGBl. I S. 3530) geändert worden ist," Gesetze im Internet. [Online]. Available: http://www.gesetze-im-internet.de/atg/index.html [Accessed: Aug. 11, 2022].

[4] Das Bundesamt für die Sicherheit der nuklearen Entsorgung, "Der Atomausstieg in Deutschland," Bundesamt für die Sicherheit der nuklearen Entsorgung. [Online]. Available: https://www.base.bund.de/DE/themen/kt/ausstieg-atomkraft/ausstieg_node.html [Accessed: Sep. 02, 2022].

[5] The European Environment Agency (EEA), "Recorded hydropower plants in Europe," European Environment Agency (EEA). [Online]. Available: https://www.eea.europa.eu/data-and-maps/figures/recorded-hydropower-plants-in-europe. [Accessed: Sep. 02, 2022].

[6] "NGOs call on the EU to end support for new hydropower," WWF Europe. [Online]. Available: https://www.wwf.eu/?1007466/NGOs-call-on-the-EU-to-end-support-for-new-hydropower [Accessed: Aug. 09, 2022].

[7] Saman Amanpour, Thesis, A Cellular Approach To Optimize The Integration Of Renewable Generation Into Distribution Networks, Brandenburgischen Technischen Universität Cottbus-Senftenberg, 2022, DOI: https://doi.org/10.26127/BTUOpen-5900

[8] ENTSO-E, "Ten-Year Network Development Plan 2020," 2021. [Online]. Available: https://www.entsoe.eu/publications/ten-year-network-development-plan-2020/.

[9] 50Hertz Transmission GmbH, Amprion GmbH, TenneT TSO GmbH, TransnetBW GmbH. (2019). Netzentwicklungsplan Strom 2030.

[10] CIGRE, "Experience of reconstruction and expansion of Vyborg back-to-back HVDC link," SESSION MATERIALS, Reference: 14-103_2002 [Online]. Available: https://e-cigre.org/publication/14-103_2002-experience-of-reconstruction-and-expansion-of-vyborg-back-to-back-hvdc-link. [Accessed: Sep. 02, 2022].

[11] CIGRE, Study Committee B1, Working Group B1.07, "Statistics of AC Underground Cables in Power Networks," CIGRE Technical Brochure, no. 338, pp. 1-139, 2008. ISBN: 978-2-85873-026-1.

[12] CIGRE, Study Committee B1, Working Group B1.50, "Sheath Bonding Systems of AC Transmission Cables - Design, Testing, and Maintenance," Technical Brochures, no. 797, pp. 1-116, 2020. ISBN: 978-2-85873-502-0.

[13] General Cable, "High & Extra-High Voltage Underground Solutions," 2013, Brochure.

[14] Nexans, "60-500 kV High Voltage Underground Power Cables XLPE insulated cables," Brochure.

[15] M. Saltzer, M. Nguyen-Tuan, A. Crippa, S. Wenig, M. Goertz and H. Saad “Surge and extended overvoltage testing of HVDC cable systems”, Int. Conf. Insulated Power Cables, Dunkerque, France, Nov. 2017, JICABLEHVDC 17, S3.3.

[16] CIGRE, Study Committee B1, Working Group B1.07, "Statistics of AC underground cables in power networks," Technical Brochure, no. 338, December 2007. ISBN: 978-2-85873-026-1.

[17] Y. Zhou, B. Dang, H. Wang, J. Liu, Q. Li, J. Hu, and J. He, "Polypropylene-based ternary nanocomposites for recyclable high-voltage direct-current cable insulation," Composites Science and Technology, vol. 165, pp. 168-174, 2018. [Online]. Available: https://doi.org/10.1016/j.compscitech.2018.06.022

[18] I. L. Hosier, L. Cozzarini, A. S. Vaughan, and S. G. Swingler, "Propylene based systems for high voltage cable insulation applications," in Journal of Physics: Conference Series, vol. 183, no. 1, Art. no. 012015, Aug. 2009. [Online]. Available: https://dx.doi.org/10.1088/1742-6596/183/1/012015

[19] CIGRE, Study Committee B1, Working Group B1.22, "Cable Accessory Workmanship on Extruded High Voltage Cables," Technical Brochure, no. 476, October 2011. ISBN: 978-2-85873-167-1.

[20] CIGRE, Study Committee B1, Working Group B1.38, "After laying tests on AC and DC cable systems with new technologies," Technical Brochure, no. 841, September 2021. ISBN: 978-2-85873-546-4.

[21] CIGRE, Study Committee B1, Working Group B1.57, "Update of service experience of HV underground and submarine cable systems," Technical Brochure, no. 815, September 2020. ISBN: 978-2-85873-520-4.

[22] CIGRE, Study Committee B1, Working Group B1.10, "Update of Service Experience of HV Underground and Submarine Cable Systems," Technical Brochure, no. 379, April 2009. ISBN: 978-2-85873-520-4.

[23] International Electrotechnical Commission, "IEC 60270: High-voltage test techniques – Partial discharge measurements," 3rd ed., 2015.

[24] International Electrotechnical Commission, "IEC 62067: Power cables with extruded insulation and their accessories for rated voltages above 150 kV (U_m = 170 kV) up to 500 kV (U_m = 550 kV) – Test methods and requirements," Edition 3.0, 2022.

[25] International Electrotechnical Commission, "IEC 60060-3: High-voltage test techniques – Part 3: Definitions and requirements for on-site testing," 2006.

[26] International Electrotechnical Commission, "IEC 60060-1: High-voltage test techniques – Part 1: General definitions and test requirements," 2010.

[27] International Electrotechnical Commission, "IEC 60885-3: Electrical test methods for electric cables – Part 3: Test methods for partial discharge measurements on lengths of extruded power cables," Edition 2.0, 2003.

[28] IEEE Power Engineering Society, "IEEE Guide for Partial Discharge Testing of Shielded Power Cable Systems in a Field Environment," in IEEE Std 400.3-2006 , vol., no., pp.1-44, 5 Feb. 2007, doi: 10.1109/IEEESTD.2007.305045.

[29] CIGRE, Study Committee B1, Working Group B1.28, "On-site Partial Discharge Assessment of HV and EHV Cable Systems," Technical Brochure, no. 728, May 2018. ISBN: 978-2-85873-430-6.

[30] CIGRE, Study Committee B4, Working Group B4.68, "DC Side Harmonics and Filtering in HVDC Transmission Systems," Technical Brochure, no. 811, September 2020. ISBN: 978-2-85873-516-7.

[31] CIGRE, Working Group 21.16, "Partial Discharge Detection in Installed HV Extruded Cable Systems," Technical Report, no. 182, 2001.

[32] IEEE Power and Energy Society "IEEE Guide for Bonding Shields and Sheaths of Single-Conductor Power Cables Rated 5 kV through 500 kV," in IEEE Std 575-2014 (Revision of IEEE Std 575-1988), vol., no., pp.1-83, 18 Sept. 2014, doi: 10.1109/IEEESTD.2014.6905681.

[33] CIGRE, Study Committee B1, Working Group B1.50, "Sheath Bonding Systems of AC Transmission Cables - Design, Testing, and Maintenance," Technical Brochure, no. 797, March 2020. ISBN: 978-2-85873-502-0.

[34] CIGRE, Study Committee B1, "Proposal for the Creation of a New Working Group WG No. B1.83," November 23, 2021.

[35] M. Asif, H. Lee, K. Park and B. Lee, "Accurate Evaluation of Steady-State Sheath Voltage and Current in HVDC Cable Using Electromagnetic Transient Simulation," Energies, vol. 12, no. 21, 4161, October 2019. [Online]. Available: https://doi.org/10.3390/en12214161

[36] M. Goertz, S. Wenig, S. Gorges, M. Kahl, S. Beckler, J. Christian, M. Suriyah, and T. Leibfried, "Lightning Overvoltages in a HVDC Transmission System Comprising Mixed Overhead-Cable Lines," in Proceedings of the International Conference on Power Systems Transients (IPST), Seoul, South Korea, June 2017.

[37] CIGRE, Study Committee B2, "Overhead Lines". CIGRE Green Books. ISBN: 978-3-319-31746-5, ISBN: 978-3-319-31747-2 (eBook), ISBN: 978-3-319-31748-9 (print and electronic bundle). DOI: 10.1007/978-3-319-31747-2.

[38] CIGRE, Study Committee B1, "Accessories for HV and EHV Extruded Cables: Volume 1: Components". CIGRE Green Books. ISBN: 978-3-030-39465-3, ISBN: 978-3-030-39466-0 (eBook), ISBN: 978-3-030-39467-7 (print and electronic bundle). DOI: 10.1007/978-3-030-39466-0.

[39] A. Troeger, U. Riechert, S. Burow, and S. Tenbohlen, "Sensitivity Evaluation of Different Types of PD Sensors for UHF-PD-Measurements," in Proceedings of the Conference on Condition Monitoring and Diagnosis, 2010, pp. 2-5.

[40] A. Itose, Y. Tai, M. Kozako, and M. Hikita, "Partial Discharge Detection by TEV Sensors and Signal Propagation Analysis in Transformer Model," Proceedings of the 19th International Symposium on High Voltage Engineering, Pilsen, Czech Republic, pp. 23-28, August 2015. Kyushu Institute of Technology, Kitakyushu, Japan.

[41] J. A. Ardila-Rey, E. Montero, and N. Medina Poblete, "Application of Meta-Heuristic Approaches in the Spectral Power Clustering Technique (SPCT) to Improve the Separation of Partial Discharge and Electrical Noise Sources," in IEEE Access, vol. 7, pp. 110580-110593, 2019. [Online]. Available: https://doi.org/10.1109/ACCESS.2019.2934388.

[42] K. Firuzi, M. Vakilian, V. P. Darabad, B. T. Phung and T. R. Blackburn, "A novel method for differentiating and clustering multiple partial discharge sources using S

transform and bag of words feature," in IEEE Transactions on Dielectrics and Electrical Insulation, vol. 24, no. 6, pp. 3694-3702, Dec. 2017, doi: 10.1109/TDEI.2017.006758.

[43] P. Donoso, R. Schurch, J. Ardila-Rey and J. Montana, "Stationarity in Partial Discharge Time Series of Electrical Trees," 2022 IEEE Conference on Electrical Insulation and Dielectric Phenomena (CEIDP), Denver, CO, USA, 2022, pp. 360-363, doi: 10.1109/CEIDP55452.2022.9985359.

[44] R. Ghosh, P. Seri, and G.C. Montanari, "Partial discharge measurements and life estimation in DC electrical insulation during voltage transients and steady state," Electric Power Systems Research, vol. 194, 107117, 2021. [Online]. Available: https://doi.org/10.1016/j.epsr.2021.107117.

[45] R. Ghosh, P. Seri and G. C. Montanari, "A Track Towards Unsupervised Partial Discharge Inference in Electrical Insulation Systems," 2020 IEEE Electrical Insulation Conference (EIC), Knoxville, TN, USA, 2020, pp. 190-193, doi: 10.1109/EIC47619.2020.9158742.

[46] R. Ghosh, P. Seri, and G.C. Montanari, "Partial discharge measurements and life estimation in DC electrical insulation during voltage transients and steady state," Electric Power Systems Research, vol. 194, 107117, 2021. [Online]. Available: https://doi.org/10.1016/j.epsr.2021.107117.

[47] S. Govindarajan, M. Natarajan, J. A. Ardila-Rey and S. Venkatraman, "Partial Discharge Location Identification Using Permutation Entropy Based Instantaneous Energy Features," in IEEE Transactions on Instrumentation and Measurement, vol. 70, pp. 1-12, 2021, Art no. 6011412, doi: 10.1109/TIM.2021.3121477.[47]

[48] A. Contin, A. Cavallini, G. C. Montanari, G. Pasini and F. Puletti, "Artificial intelligence methodology for separation and classification of partial discharge signals," 2000 Annual Report Conference on Electrical Insulation and Dielectric Phenomena (Cat. No.00CH37132), Victoria, BC, Canada, 2000, pp. 522-526 vol.2, doi: 10.1109/CEIDP.2000.884013.

[49] A. Cavallini, A. Contin, G. C. Montanari and F. Puletti, "Advanced PD inference in on-field measurements. I. Noise rejection," in IEEE Transactions on Dielectrics and Electrical Insulation, vol. 10, no. 2, pp. 216-224, April 2003, doi: 10.1109/TDEI.2003.1194102.

[50] L. Wang, A. Cavallini, G. C. Montanari and L. Testa, "Evolution of pd patterns in polyethylene insulation cavities under AC voltage," in IEEE Transactions on

Dielectrics and Electrical Insulation, vol. 19, no. 2, pp. 533-542, April 2012, doi: 10.1109/TDEI.2012.6180247.

[51] J. A. Ardila-Rey, E. Montero and N. Medina Poblete, "Application of Meta-Heuristic Approaches in the Spectral Power Clustering Technique (SPCT) to Improve the Separation of Partial Discharge and Electrical Noise Sources," in IEEE Access, vol. 7, pp. 110580-110593, 2019, doi: 10.1109/ACCESS.2019.2934388.

[52] J. A. Ardila-Rey, R. Schurch, N. M. Poblete, S. Govindarajan, O. Muñoz and B. A. de Castro, "Separation of Partial Discharges Sources and Noise Based on the Temporal and Spectral Response of the Signals," in IEEE Transactions on Instrumentation and Measurement, vol. 70, pp. 1-13, 2021, Art no. 3526013, doi: 10.1109/TIM.2021.3121488.

[53] J. A. Ardila-Rey, M. P. Cerda-Luna, R. A. Rozas-Valderrama, B. A. de Castro, A. L. Andreoli and F. Muhammad-Sukki, "Separation Techniques of Partial Discharges and Electrical Noise Sources: A Review of Recent Progress," in IEEE Access, vol. 8, pp. 199449-199461, 2020, doi: 10.1109/ACCESS.2020.3035249.

[54] J. K. Raymond, H. A. Illias, and A. H. Abu Bakar, "Classification of Partial Discharge Measured under Different Levels of Noise Contamination," in PLOS ONE, vol. 12, no. 1, e0170111, 2017. [Online]. Available: https://doi.org/10.1371/journal.pone.0170111.

[55] M. Chen, K. Urano, Z. Zhou, and T. Chen, “Application study of variable pd sensors for pd measurement of power cable circuit in operation,” in 2016 International Conference on Condition Monitoring and Diagnosis (CMD), 2016, pp. 118–122, doi: 10.1109/CMD.2016.7757771.

[56] F. A´ lvarez, F. Garnacho, J. Ortego, and M. A´ ngel Sa´nchez-Ura´n, “Application of HFCT and UHF Sensors in On-Line Partial Discharge Measurements for Insulation Diagnosis of High Voltage Equipment,” Sensors, vol. 15, no. 4, pp. 7360–7387, 2015, doi: 10.3390/s150407360.

[57] P. C. V. D. Wielen, J. Veen, P. A. Wouters, and E. F. Steennis, “On-line partial discharche detection of mv cables with defect localisation (pdol) based on two time synchronised sensors,” in CIRED 18th International Conference on Electricity Distribution, Paper, 2005, pp. 1–5, doi: 10.1049/cp:20050973.

[58] L. A. Renforth, R. Giussani, M. T. Mendiola, and L. Dodd, “Online Partial Discharge Insulation Condition Monitoring of Complete High- Voltage Networks,” IEEE Transactions on Industry Applications, vol. 55, no. 1, pp. 1021–1029, Jan.-Feb. 2019, doi: 10.1109/TIA.2018.2866983.

[59] Lauri Kütt, "Analysis and Development of Inductive Current Sensor for Power Line On-Line Measurements of Fast Transients," Tallin University of Technology, Department of Fundamentals of Electrical Engineering and Electrical Machines, 2012. ISSN 1406-474X. ISBN 978-9949-23-301-4 (publication), ISBN 978-9949-23-302-1 (PDF).

[60] Y. Ye, D. Liang, J. Du, M. Tang and X. Liu, "Design and optimization of high frequency current transformer," *2014 17th International Conference on Electrical Machines and Systems (ICEMS)*, Hangzhou, China, 2014, pp. 963-966, doi: 10.1109/ICEMS.2014.7013616.

[61] C. Zachariades, R. Shuttleworth, R. Giussani and R. MacKinlay, "Optimization of a High-Frequency Current Transformer Sensor for Partial Discharge Detection Using Finite-Element Analysis," in IEEE Sensors Journal, vol. 16, no. 20, pp. 7526-7533, Oct.15, 2016, doi: 10.1109/JSEN.2016.2600272.

[62] B. M. Amna and U. Khayam, "Design and simulation of high frequency current transformer as partial discharge detector," 2016 3rd Conference on Power Engineering and Renewable Energy (ICPERE), Yogyakarta, Indonesia, 2016, pp. 135-139, doi: 10.1109/ICPERE.2016.7904854.

[63] B. A. Siddiqui, P. Pakonen and P. Verho, "Novel inductive sensor solutions for on-line partial discharge and power quality monitoring," in IEEE Transactions on Dielectrics and Electrical Insulation, vol. 24, no. 1, pp. 209-216, Feb. 2017, doi: 10.1109/TDEI.2016.005908.

[64] X. Hu, W. H. Siew, M. D. Judd and X. Peng, "Transfer function characterization for HFCTs used in partial discharge detection," in IEEE Transactions on Dielectrics and Electrical Insulation, vol. 24, no. 2, pp. 1088-1096, April 2017, doi: 10.1109/TDEI.2017.006115.

[65] G. Bao, X. Gao, R. Jiang, and K. Huang, "A Novel Differential High-Frequency Current Transformer Sensor for Series Arc Fault Detection," Sensors, vol. 19, no. 17, pp. 3649, 2019. doi: 10.3390/s19173649.

[66] J. V. Klüss, A. -P. Elg and C. Wingqvist, "High-Frequency Current Transformer Design and Implementation Considerations for Wideband Partial Discharge Applications," in *IEEE Transactions on Instrumentation and Measurement*, vol. 70, pp. 1-9, 2021, Art no. 6003809, doi: 10.1109/TIM.2021.3052002.

[67] L. Guowei, L. Nianbai, D. Jiayi, G. Guowei, L. Shaohui and B. Chun, "A high sensitivity high-frequency current sensor design," 2022 IEEE 4th International

Conference on Power, Intelligent Computing and Systems (ICPICS), Shenyang, China, 2022, pp. 620-626, doi: 10.1109/ICPICS55264.2022.9873581.

[68] M. Fritsch and M. Wolter, "High-Frequency Current Transformer Design and Construction Guide," in IEEE Transactions on Instrumentation and Measurement, vol. 71, pp. 1-9, 2022, Art no. 9004309, doi: 10.1109/TIM.2022.3177189.

[69] M. Miljanovic, M. Kearns and B. G. Stewart, "Simulation of HFCT PD Detection in MV Bus Bar Chamber," 2022 IEEE Electrical Insulation Conference (EIC), Knoxville, TN, USA, 2022, pp. 162-165, doi: 10.1109/EIC51169.2022.9833179.

[70] D. Passow et al., "Validation of a PD Monitoring System for Power Cables by Evaluating Joints with Defined Assembly Defects," VDE High Voltage Technology; 4. ETG-Symposium, Berlin, Germany, 2022, pp. 1-6.

[71] D. A. Polyakov, "Research of Partial Discharge Registration Effectiveness Using HFCT Sensor," 2022 Dynamics of Systems, Mechanisms and Machines (Dynamics), Omsk, Russian Federation, 2022, pp. 1-5, doi: 10.1109/Dynamics56256.2022.10014796.

[72] Y. Xu, X. Gu, B. Liu, B. Hui, Z. Ren and S. Meng, "Special requirements of high frequency current transformers in the on-line detection of partial discharges in power cables," in IEEE Electrical Insulation Magazine, vol. 32, no. 6, pp. 8-19, November-December 2016, doi: 10.1109/MEI.2016.7656806.

[73] J. P. Uwiringiyimana, U. Khayam, Suwarno and G. C. Montanari, "Comparative Analysis of Partial Discharge Detection Features Using a UHF Antenna and Conventional HFCT Sensor," in IEEE Access, vol. 10, pp. 107214-107226, 2022, doi: 10.1109/ACCESS.2022.3212746.

[74] A. Subramaniam, S. J. Raman and S. K. Panda, "Comparison of Partial Discharge signal in a Three phase Transformer by UHF, TEV and HFCT sensors," 2021 1st International Conference on Power Electronics and Energy (ICPEE), Bhubaneswar, India, 2021, pp. 1-4, doi: 10.1109/ICPEE50452.2021.9358502.

[75] N. P. Ardiansyah, U. Khayam and R. Nurdiansyah, "Measurement of Partial Discharge on PCB using RC Detector, HFCT, and Loop Antenna," 2020 FORTEI-International Conference on Electrical Engineering (FORTEI-ICEE), Bandung, Indonesia, 2020, pp. 64-68, doi: 10.1109/FORTEI-ICEE50915.2020.9249908.

[76] P. Wenger, S. A. Madhar and M. Beltle, "Simultaneous Electrical, UHF, Current and Optical PD Measurements on Floating Potential under DC Stress," 2019 IEEE Conference on Electrical Insulation and Dielectric Phenomena (CEIDP), Richland, WA, USA, 2019, pp. 287-290, doi: 10.1109/CEIDP47102.2019.9010548.

[77] COMSOL, COMSOL Multiphysics©, 2023. [Online]. Available: https://www.comsol.com/.

[78] J. Schliewe, S. Schefler, and S. Weber, "Simulating saturation behavior of inductive components," in PCIM Europe 2014; International Exhibition and Conference for Power Electronics, Intelligent Motion, Renewable Energy and Energy Management, January 2014, pp. 1–8.

[79] W. G. Hurley and W. H. Wölfle, Transformers and Inductors for Power Electronics: Theory, Design and Applications. John Wiley & Sons Ltd, April 2013, pp. 370.

[80] J. Schliewe, S. Schefler, M. Koeppen et al., "Inductance versus DC Current Measurements on the Anhysteresis of Magnetic Material," in PCIM Europe 2017; International Exhibition and Conference for Power Electronics, Intelligent Motion, Renewable Energy and Energy Management, May 2017, pp. 1–6.

[81] W. Sima, B. Zou, M. Yang, and F. de León, "New method to measure deep-saturated magnetizing inductances for dual reversible models of single-phase two-winding transformers," IEEE Transactions on Power Delivery, vol. 36, no. 1, pp. 488–491, 2021, doi: 10.1109/TEC.2020.3023596.

[82] S. Pokharel and A. Dimitrovski, "Modeling of an enhanced three-phase continuously variable reactor," in 2020 IEEE Power Energy Society General Meeting (PESGM), 2020, pp. 1–5, doi: 10.1109/PESGM41954.2020.9282074.

[83] G. Grandi, M. K. Kazimierczuk, A. Massarini and U. Reggiani, "Stray capacitances of single-layer solenoid air-core inductors," in IEEE Transactions on Industry Applications, vol. 35, no. 5, pp. 1162-1168, Sept.-Oct. 1999, doi: 10.1109/28.793378.

[84] A. Rodrigo-Mor, F. A. Muñoz and L. C. Castro-Heredia, "Principles of Charge Estimation Methods Using High-Frequency Current Transformer Sensors in Partial Discharge Measurements," in Sensors, vol. 20, no. 9, pp. 2520, 2020, doi: 10.3390/s20092520.

[85] Q. Yu and T. W. Holmes, "Stray capacitance modeling of inductors by using the finite element method," 1999 IEEE International Symposium on Electromagnetic Compatability. Symposium Record (Cat. No.99CH36261), Seattle, WA, USA, 1999, pp. 305-310 vol.1, doi: 10.1109/ISEMC.1999.812918.

[86] M. Kovacic, Z. Hanic, S. Stipetic, S. Krishnamurthy and D. Zarko, "Analytical Wideband Model of a Common-Mode Choke," in IEEE Transactions on Power Electronics, vol. 27, no. 7, pp. 3173-3185, July 2012, doi: 10.1109/TPEL.2011.2182060.

[87] D. W. Knight, "The self-resonance and self-capacitance of solenoid coils: applicable theory, models and calculation methods," Tech. Rep., 2016, doi: 10.13140/RG.2.1.1472.0887.

[88] C. M. de Miranda and S. F. Pichorim, "Self-resonant frequencies of air-core single-layer solenoid coils calculated by a simple method," Electrical Engineering, vol. 97, pp. 57-64, 2015, doi: 10.1007/s00202-014-0312-3.

[89] Н. А. Семенов, "Техническая электродинамика", Moscow, Russia: Svyaz, 1973, p. 318. [Translated: N. A. Semenov, Technical Electrodynamics]

[90] A. Kandoian and W. Sichak, "Wide-frequency-range tuned helical antennas and circuits," in IRE International Convention Record, New York, NY, USA, 1953, pp. 42-47, doi: 10.1109/IRECON.1953.1148696.

[91] F. Ollendorff, "Die Grundlagen der Hochfrequenztechnik". Berlin, Germany: Springer, 1926, pp. 79-87. [Translated: Foundations of high-frequency technology, "Dynamic field of multi-turn coils"].

[92] S. Sensiper, "Electromagnetic wave propagation on helical conductors," Tech. Rep. 194, Massachusetts Institute of Technology, Research Laboratory of Electronics, Cambridge, MA, USA, May 16, 1951.

[93] D. Konig and K. Kress, "Study of power coil resonance phenomena based on traveling wave theory," in IEEE Transactions on Electrical Insulation, vol. 26, no. 3, pp. 349-357, June 1991. doi: 10.1109/14.85103.

[94] R. G. Medhurst, "HF Resistance and Self-Capacitance of Single-Layer Solenoids," Wireless Engineer, vol. 24, no. 267, pp. 35-43, Feb. 1947, and vol. 24, no. 268, pp. 80-92, Mar. 1947.

[95] G. R. Skutt, "High-Frequency Dimensional Effects in Ferrite-Core Magnetic Devices," Ph.D. dissertation, Virginia Polytechnic Institute and State University, Blacksburg, VA, USA, October 4, 1996.

[96] M. Kącki, M. S. Ryłko, J. G. Hayes and C. R. Sullivan, "Analysis and Experimental Investigation of High-Frequency Magnetic Flux Distribution in Mn-Zn Ferrite Cores," in IEEE Transactions on Power Electronics, vol. 38, no. 1, pp. 703-716, Jan. 2023, doi: 10.1109/TPEL.2022.3200954.

[97] T. P. Todorova, A. Van den Bossche, and V. C. Valchev, "A Procedure for the Extraction of Intrinsic AC Conductivity and Dielectric Constant of N87 Mn–Zn Ferrite Samples Based on Impedance Measurements and Equivalent Electrical Circuit Modeling," in IEEE Transactions on Power Electronics, vol. 33, no. 12, pp. 10723-10735, Dec. 2018. doi: 10.1109/TPEL.2018.2802787.

[98] B. Parvatheeswara Rao and K. H. Rao, "Dimensional Effects Resulting from High Dielectric Constants in NiZnSc-Ferrites," Journal of The Magnetics Society of Japan, vol. 22, supplement, no. S1, pp. 305-307, 1998.

[99] Ferroxcube. "Ferrite Materials Survey" September 1, 2008. [Online]. Available: https://ferroxcube.home.pl/prod/assets/sfmatgra_frnt.pdf. Accessed: May 19, 2023.

[100] Ferroxcube. "Ferroxcube 4F1 Material Specification," September 1, 2008. [Online]. Available: https://ferroxcube.home.pl/prod/assets/4f1.pdf. Accessed: May 19, 2023.

[101] S. Sriram, S. Nitin, K. M. M. Prabhu and M. J. Bastiaans, "Signal denoising techniques for partial discharge measurements," in IEEE Transactions on Dielectrics and Electrical Insulation, vol. 12, no. 6, pp. 1182-1191, Dec. 2005, doi: 10.1109/TDEI.2005.1561798.

[102] L. Damião, J. Guimarães, G. M. F. Ferraz, E. Bortoni, R. Rossi, R. Capelini, R. Salustiano, and E. Tavares, "Online Monitoring of Partial Discharges in Power Transformers Using Capacitive Coupling in the Tap of Condenser Bushings," Energies, vol. 13, no. 17, p. 4351, 2020. doi: 10.3390/en13174351.

[103] B. Sheng, C. Zhou, D. M. Hepburn, X. Dong, G. Peers, W. Zhou, and Z. Tang, "A novel on-line cable PD localization method based on cable transfer function and detected PD pulse rise-time," in IEEE Transactions on Dielectrics and Electrical Insulation, vol. 22, no. 4, pp. 2087-2096, August 2015. doi: 10.1109/TDEI.2015.004398.

[104] E. H. R. Gaxiola and J. M. Wetzer, "Partial discharge modelling and measurements on micrometer voids in solid dielectrics," Seventh International Conference on Dielectric Materials, Measurements and Applications (Conf. Publ. No. 430), Bath, UK, 1996, pp. 322-325, doi: 10.1049/cp:19961050.

[105] S. A. Boggs and G. C. Stone, "Fundamental Limitations in the Measurement of Corona and Partial Discharge," in IEEE Transactions on Electrical Insulation, vol. EI-17, no. 2, pp. 143-150, April 1982, doi: 10.1109/TEI.1982.298548.

[106] P. Treyer, P. Mraz, U. Hammer, and S. Gonzalez, "Breaking the Limit of Power Capacitor Resonance Frequency with Help of PD Pulse Spectrum to Check and Setup PD Measurement," in The 19th International Symposium on High Voltage Engineering, Pilsen, Czech Republic, August 23-28, 2015.

[107] K. Backhaus, L. Elspaß, and K. Pasche, "Detection Technique of Partial Discharges at Impulse Voltage with Appropriate Filter Settings for Signal Separation," Energies, vol. 12, no. 23, 2019. DOI: 10.3390/en12234480.

[108] Zhifang Du and M. S. Mashikian, "Self-learning digital filter for the field location of partial discharge in cables," Proceedings of 1994 IEEE International Symposium on Electrical Insulation, Pittsburgh, PA, USA, 1994, pp. 245-248, doi: 10.1109/ELINSL.1994.401520.

[109] L. Lu, G. Zhu, X. Yang, K. Zhou, Z. Liu and W. Wu, "Affine Projection Algorithm-Based High-Order Error Power for Partial Discharge Denoising in Power Cables," in IEEE Transactions on Instrumentation and Measurement, vol. 69, no. 4, pp. 1821-1832, April 2020, doi: 10.1109/TIM.2019.2914710.

[110] A. Mohammadirad, A. A. Shayegani Akmal, and R. Vakili, "Localization of Partial Discharge in a Transformer Winding Using Frequency Response Assurance Criterion and LMS Adaptive Filter," Electric Power Systems Research, vol. 163, part A, pp. 461-469, 2018. ISSN: 0378-7796. doi: 10.1016/j.epsr.2018.07.020.

[111] Q. Su, "An Adaptive Filtering Method for Noise Suppression in Partial Discharge Measurements," Proceedings of IEEE Conference on Electrical Insulation and Dielectric Phenomena - (CEIDP '93), Pocono Manor, PA, USA, 1993, pp. 481-486, doi: 10.1109/CEIDP.1993.378926.

[112] L. C. Yong, K. R. Wong Jee and K. T. Mei, "Evaluation of Partial Discharge Denoising using Power Spectral Subtraction," 2020 IEEE Student Conference on Research and Development (SCOReD), Batu Pahat, Malaysia, 2020, pp. 86-89, doi: 10.1109/SCOReD50371.2020.9250942.

[113] L. Lu, K. Zhou, G. Zhu, B. Chen and X. Yana, "Partial Discharge Signal Denoising with Recursive Continuous S-Shaped Algorithm in Cables," in IEEE Transactions on Dielectrics and Electrical Insulation, vol. 28, no. 5, pp. 1802-1809, October 2021, doi: 10.1109/TDEI.2021.009662.

[114] J. Veen and P. C. J. M. van der Wiellen, "The application of matched filters to PD detection and localization," in IEEE Electrical Insulation Magazine, vol. 19, no. 5, pp. 20-26, Sept.-Oct. 2003, doi: 10.1109/MEI.2003.1238714.

[115] P. Wagenaars, P. A. A. F. Wouters, P. C. J. M. van der Wielen and E. F. Steennis, "Adaptive matched filter bank for noise reduction in online partial discharge monitoring," 2009 IEEE Conference on Electrical Insulation and Dielectric Phenomena, Virginia Beach, VA, USA, 2009, pp. 356-359, doi: 10.1109/CEIDP.2009.5377880.

[116] P. Wagenaars, P. A. A. F. Wouters, P. C. J. M. Van Der Wielen and E. F. Steennis, "Adaptive templates for matched filter bank for continuous online partial discharge

monitoring," in IEEE Transactions on Dielectrics and Electrical Insulation, vol. 18, no. 5, pp. 1693-1701, October 2011, doi: 10.1109/TDEI.2011.6032841.

[117] Ren Lijia Ren, Pei Lei and Gu Chunyuan, "Ultrasonic partial discharge detection using negentropy-based matched filter," CICED 2010 Proceedings, Nanjing, China, 2010, pp. 1-4.

[118] D. L. Donoho and I. M. Johnstone, "Ideal Spatial Adaptation by Wavelet Shrinkage," Biometrika, vol. 81, no. 3, pp. 425-455, 1994. doi: 10.2307/2337118.

[119] C. He, J. Xing, J. Li, Q. Yang, and R. Wang, "A New Wavelet Threshold Determination Method Considering Interscale Correlation in Signal Denoising," Mathematical Problems in Engineering, vol. 2015, Article ID 280251, 9 pages, 2015. doi: 10.1155/2015/280251.

[120] T. Cai and H. Zhou, "A Data-Driven Block Thresholding Approach to Wavelet Estimation," The Annals of Statistics, vol. 37, no. 2, pp. 569-595, 2009. doi: 10.1214/07-AOS538. © Institute of Mathematical Statistics, 2009.

[121] Z. Tao, H.-M. Zhao, X.-J. Zhang, and D. Wu, "Speech Enhancement Based on the Multi-Scales and Multi-Thresholds of the Auditory Perception Wavelet Transform," Archives of Acoustics, vol. 36, no. 3, pp. 519-532, 2011. DOI: 10.2478/v10168-011-0037-5.

[122] J. Fowler, "The Redundant Discrete Wavelet Transform and Additive Noise," IEEE Signal Processing Letters, vol. 12, pp. 629-632, 2005. doi: 10.1109/LSP.2005.853048.

[123] I. W. Selesnick, R. G. Baraniuk, and N. C. Kingsbury, "The Dual-Tree Complex Wavelet Transform," IEEE Signal Processing Magazine, vol. 22, pp. 123-151, 2005. doi: 10.1109/MSP.2005.1550194.

[124] M. Holschneider, R. Kronland-Martinet, J. Morlet, and P. Tchamitchian, “A real-time algorithm for signal analysis with the help of the wavelet transform,” in Wavelets: Time-Frequency Methods and Phase Space, J.-M. Combes, A. Grossman, and P. Tchamitchian, Eds. Berlin, Germany: Springer-Verlag, 1989, pp. 286–297.

[125] P. Dutilleux, “An implementation of the algorithme à trous to compute the wavelet transform,” in Wavelets: Time-Frequency Methods and Phase Space, J.-M. Combes, A. Grossman, and P. Tchamitchian, Eds. Berlin, Germany: Springer-Verlag, 1989, pp. 298–304.

[126] M. Lang, H. Guo, J. E. Odegard, C. S. Burrus, and R. O. Wells Jr, “Noise reduction using an undecimated discrete wavelet transform,” IEEE Signal Process. Lett., vol. 3, no. 1, pp. 10–12, Jan. 1996.

[127] R. Zaciu, C. Lamba, C. Burlacu, and G. Nicula, “Image compression using an RE,” IEEE Trans. Consum. Electron., vol. 42, no. 3, pp. 800–807, Aug. 1996.

[128] M. Lang, H. Guo, J. E. Odegard, C. S. Burrus, and R. O. Wells, "Nonlinear processing of a shift invariant DWT for noise reduction," in Proceedings of SPIE, Mathematical Imaging: Wavelet Applications for Dual Use, SPIE Symposium on OE/Aerospace Sensing and Dual Use Photonics, 17-21 April 1995, Orlando, FL.

[129] M. Unser, “Texture classification and segmentation using wavelet frames,” IEEE Trans. Image Process., vol. 4, no. 11, pp. 1549–1560, Nov. 1995.

[130] P. K. Shetty and T. S. Ramu, "An Undecimated Wavelet Transform Based Enhancement, Statistical Feature Extraction and Detection-Classification of PD Signals," in 2004 IEEE International Conference on Acoustics, Speech, and Signal Processing, Montreal, QC, Canada, 2004, pp. V-401. doi: 10.1109/ICASSP.2004.1327132.

[131] G. de O. Andrade, A. S. O. Avelar and H. de O. Mota, "Comparative Analysis of Partial Discharge Denoising Techniques," 2021 IEEE Electrical Insulation Conference (EIC), Denver, CO, USA, 2021, pp. 678-681, doi: 10.1109/EIC49891.2021.9612387.

[132] N.G. Kingsbury, "The Dual-Tree Complex Wavelet Transform: A New Technique for Shift Invariance and Directional Filters," in Proc. 8th IEEE DSP Workshop, Utah, Aug. 9–12, 1998, Paper No. 86.

[133] N.G. Kingsbury, "Image Processing with Complex Wavelets," Philos. Trans. R. Soc. London A, Math. Phys. Sci., vol. 357, no. 1760, pp. 2543–2560, Sept. 1999.

[134] N.G. Kingsbury, "Complex Wavelets for Shift Invariant Analysis and Filtering of Signals," Appl. Comput. Harmon. Anal., vol. 10, no. 3, pp. 234–253, May 2001.

[135] I. W. Selesnick, "The Design of Approximate Hilbert Transform Pairs of Wavelet Bases" in IEEE Transactions on Signal Processing, vol. 50, no. 5, pp. 1144-1152, May 2002. doi: 10.1109/78.995070.

[136] X. Yang, Y. Cai, J. Zhang, L. Cheng, and F. Wang, "Denoising of Partial Discharge Signal by Common Factor Method and Wavelet Thresholding," in 2020 IEEE 4th Conference on Energy Internet and Energy System Integration (EI2), Wuhan, China, 2020, pp. 2252-2255, doi: 10.1109/EI250167.2020.9346639.

[137] C. Herold, S. Wenig, and T. Leibfried, "Advanced de-noising of power cable Partial Discharge signals by Empirical Mode Decomposition," in 2010 20th

Australasian Universities Power Engineering Conference, Christchurch, New Zealand, 2010, pp. 1-5.

[138] X. Zhao and B. Ye, "Separation of Single Frequency Component Using Singular Value Decomposition," Circuits, Systems, and Signal Processing, vol. 38, 2019. doi: 10.1007/s00034-018-0852-2.

[139] H. Ran, Y. Xu, J. Jiang, K. Tang, Z. He, T. Zhang, and X. Tang, "Application of Singular Value Reconstruction in Suppressing Narrowband Interference of Partial Discharge," in 2019 4th International Conference on Power and Renewable Energy (ICPRE), Chengdu, China, 2019, pp. 239-243, doi: 10.1109/ICPRE48497.2019.9034709.

[140] Q. Zhang and L. Lou, "Research on partial discharge signal denoising of transformer based on improved CEEMD and adaptive wavelet threshold," 2021 3rd International Academic Exchange Conference on Science and Technology Innovation (IAECST), Guangzhou, China, 2021, pp. 1708-1712, doi: 10.1109/IAECST54258.2021.9695898.

[141] H.-C. Chang, F.-C. Gu, and C.-C. Kuo, "Applying Hilbert-Huang Transform on Partial Discharge Pattern Recognition of a Gas Insulated Switchgear," in 2012 IEEE International Power Modulator and High Voltage Conference (IPMHVC), San Diego, CA, USA, 2012, pp. 165-168. doi: 10.1109/IPMHVC.2012.6518705.

[142] Y.-W. Tang, C.-C. Tai, C.-C. Su, C.-Y. Chen, J.-C. Hsieh, and J.-F. Chen, "Partial Discharge Signal Analysis Using HHT for Cast-Resin Dry-Type Transformer," in 2008 International Conference on Condition Monitoring and Diagnosis, Beijing, China, 2008, pp. 521-524. doi: 10.1109/CMD.2008.4580340.

[143] Y. Wang, H.-d. Chiang, and N. Dong, "Power-Line Partial Discharge Recognition with Hilbert–Huang Transform Features," Energies, vol. 15, no. 18, article 6521, 2022. doi: 10.3390/en15186521.

[144] K. Dragomiretskiy and D. Zosso, "Variational Mode Decomposition," in IEEE Transactions on Signal Processing, vol. 62, no. 3, pp. 531-544, Feb.1, 2014, doi: 10.1109/TSP.2013.2288675.

[145] S. Jiao, W. Shi and Q. Liu, "Self-adaptive partial discharge denoising based on variational mode decomposition and wavelet packet transform," 2017 Chinese Automation Congress (CAC), Jinan, China, 2017, pp. 7301-7306, doi: 10.1109/CAC.2017.8244097.

[146] M. F. Isham, M. Leong, M. Lim, and Z. A. Ahmad, "Variational mode decomposition: Mode determination method for rotating machinery diagnosis," Journal of Vibroengineering, vol. 20, 2018. doi: 10.21595/jve.2018.19479.

[147] B. Zhang, H. Mu, Y. Zheng, J. Zhan, S. Xianjun, C. Li, C. Zhang, and G. Zhang, "Adaptive Window Singular Value Decomposition Method Based on Particle Swarm Optimization for Partial Discharge Denoising," in 2021 Power System and Green Energy Conference (PSGEC), Shanghai, China, 2021, pp. 702-707, doi: 10.1109/PSGEC51302.2021.9541900.

[148] Y. Yan, R. Trinchero, I. S. Stievano, H. Li and Y. -Z. Xie, "An Automatic Tool for Partial Discharge De-Noising via Short-Time Fourier Transform and Matrix Factorization," in IEEE Transactions on Instrumentation and Measurement, vol. 71, pp. 1-12, 2022, Art no. 3528512, doi: 10.1109/TIM.2022.3216583.

[149] K. Zhou, M. Li, Y. Li, M. Xie, and Y. Huang, "An Improved Denoising Method for Partial Discharge Signals Contaminated by White Noise Based on Adaptive Short-Time Singular Value Decomposition," Energies, vol. 12, no. 18, article 3465, 2019. doi: 10.3390/en12183465.

[150] Y. Xu, J. Jiang, T. Zhang, K. Tang, J. Fu and W. Zhang, "A Noise Suppression Method for Partial Discharge Based on Two-dimensional SVD," 2019 IEEE Sustainable Power and Energy Conference (iSPEC), Beijing, China, 2019, pp. 667-671, doi: 10.1109/iSPEC48194.2019.8975013.

[151] J. Zhong, X. Bi, Q. Shu, M. Chen, D. Zhou and D. Zhang, "Partial Discharge Signal Denoising Based on Singular Value Decomposition and Empirical Wavelet Transform," in IEEE Transactions on Instrumentation and Measurement, vol. 69, no. 11, pp. 8866-8873, Nov. 2020, doi: 10.1109/TIM.2020.2996717.

[152] S. Govindarajan, J. Subbaiah, A. Cavallini, K. Krithivasan and J. Jayakumar, "Partial Discharge Random Noise Removal Using Hankel Matrix-Based Fast Singular Value Decomposition," in IEEE Transactions on Instrumentation and Measurement, vol. 69, no. 7, pp. 4093-4102, July 2020, doi: 10.1109/TIM.2019.2945826.

[153] W. Xu and S. Qiao, "A Fast Symmetric SVD Algorithm for Square Hankel Matrices," Linear Algebra and Its Applications, vol. 428, pp. 550-563, 2008. doi: 10.1016/j.laa.2007.05.027.

[154] R. Liao, Y. Fernandess, K. Tavernier, G. A. Taylor and M. R. Irving, "Recognition of partial discharge patterns," 2012 IEEE Power and Energy Society General Meeting, San Diego, CA, USA, 2012, pp. 1-8, doi: 10.1109/PESGM.2012.6344929.

[155] B. S. Atal, "The History of Linear Prediction," in IEEE Signal Processing Magazine, vol. 23, no. 2, pp. 154-161, March 2006, doi: 10.1109/MSP.2006.1598091.

[156] H. N. Bidhendi and Q. Su, "Partial Discharge Location on Power Cables Using Linear Prediction," in Proceedings of 5th International Conference on Properties and Applications of Dielectric Materials, Seoul, Korea (South), 1997, pp. 406-409 vol.1, doi: 10.1109/ICPADM.1997.617622.

[157] R. Ghosh, B. Chatterjee, and S. Dalai, "A Method for the Localization of Partial Discharge Sources Using Partial Discharge Pulse Information from Acoustic Emissions," in IEEE Transactions on Dielectrics and Electrical Insulation, vol. 24, no. 1, pp. 237-245, Feb. 2017. doi: 10.1109/TDEI.2016.006080.

[158] Y. -B. Wang, D. -G. Chang, S. -R. Qin, Y. -H. Fan, H. -B. Mu and G. -J. Zhang, "Separating Multi-Source Partial Discharge Signals Using Linear Prediction Analysis and Isolation Forest Algorithm," in IEEE Transactions on Instrumentation and Measurement, vol. 69, no. 6, pp. 2734-2742, June 2020, doi: 10.1109/TIM.2019.2926688.

[159] G. Montanari and R. Ghosh, "An Innovative Approach to Partial Discharge Measurement and Analysis in DC Insulation Systems during Voltage Transient and in Steady State," High Voltage, vol. 6, pp. 565-575, 2021. doi: 10.1049/hve2.12131.

[160] J. Makhoul, "Linear Prediction: A Tutorial Review," in Proceedings of the IEEE, vol. 63, no. 4, pp. 561-580, April 1975, doi: 10.1109/PROC.1975.9792.

[161] Q. Shi, U. Troeltzsch, and O. Kanoun, “Detection and localization of cable faults by time and frequency domain measurements,” in Proc. 7th Int. Multi- Conf. Syst., Signals Devices, 2010.

[162] R. Mardiana and C. Q. Su, “Partial discharge location in power cables using a phase difference method,” IEEE Trans. Dielect. Elect. Insul., vol. 17, no. 6, pp. 1738–1746, 2010.

[163] F. P. Mohamed, W. H. Siew, J. J. Soraghan, S. M. Strachan, and J. McWilliam, “Partial discharge location in power cables using a double ended method based on time triggering with GPS,” IEEE Trans. Dielect. Elect. Insul., vol. 20, no. 6, pp. 2212–2221, 2013.

[164] K. Yamashita, S. Watanuki, T. Miyake, T. Sakoda, and W. Kawano, “Development of on-line partial discharge locator for electric power cable,” in Proc. 2018 IEEE Elect. Insul. Conf., 2018, pp. 216–219.

[165] P. Wagenaars, P. Wouters, P. Van Der Wielen, and E. Steennis, “Accurate estimation of the time-of-arrival of partial discharge pulses in cable systems in service,” IEEE Trans. Dielect. Elect. Insul., vol. 15, no. 4, pp. 1190–1199, 2008.

[166] M. Mahdipour, A. Akbari, P. Werle and H. Borsi, "Partial Discharge Localization on Power Cables Using On-Line Transfer Function," in *IEEE Transactions on Power Delivery*, vol. 34, no. 4, pp. 1490-1498, Aug. 2019, doi: 10.1109/TPWRD.2019.2908124.

[167] G. C. Stone and S. A. Boggs, "Propagation of Partial Discharge Pulses in Shielded Power Cable," in Conference on Electrical Insulation & Dielectric Phenomena - Annual Report 1982, Amherst, MA, USA, 1982, pp. 275-280, doi: 10.1109/CEIDP.1982.7726545.

[168] C. Xu and S. A. Boggs, "High Frequency Properties of Shielded Power Cable. 3. Loss from Neutral Wire-Shield Interaction," in IEEE Electrical Insulation Magazine, vol. 23, no. 2, pp. 12-16, March-April 2007. doi: 10.1109/MEI.2007.357807.

[169] C. Xu, L. Zhou, J. Y. Zhou, and S. Boggs, "High Frequency Properties of Shielded Power Cable - Part 1: Overview of Mechanisms," in IEEE Electrical Insulation Magazine, vol. 21, no. 6, pp. 24-28, Nov.-Dec. 2005, doi: 10.1109/MEI.2005.1541486.

[170] K. Futatsukawa, Z. Fang, Y. Fukui, T. Kobayashi, and S. Michizono, KEK, Ibaraki, Japan, F. Sato and S. Shinozaki, JAEA, Ibaraki, Japan, "Investigation of the Approaches to Measure the RF Cable Attenuation," in Proceedings of IPAC2012, New Orleans, Louisiana, USA, THPPC009, ISBN 978-3-95450-115-1.

[171] A. Ferrero, L. Ducimetière, T. Kramer, and L. Sermeus, "Measurement and Characterization of Cable Losses for High Voltage Coaxial Cables Used in Kicker Systems," in Proceedings of IPAC2017, Copenhagen, Denmark, ISBN 978-3-95450-182.

[172] R. Papazyan, P. Pettersson, H. Edin, R. Eriksson, and U. Gafvert, "Extraction of High-Frequency Power Cable Characteristics from S-Parameter Measurements," in IEEE Transactions on Dielectrics and Electrical Insulation, vol. 11, no. 3, pp. 461-470, June 2004. doi: 10.1109/TDEI.2004.1306724

[173] H. W. Ott, "Noise Reduction Techniques in Electronic Systems," 2nd ed., J. Wiley, 1989, pp. 426

[174] D. Cavka, N. Mora and F. Rachidi, "A Comparison of Frequency-Dependent Soil Models: Application to the Analysis of Grounding Systems," in IEEE Transactions

on Electromagnetic Compatibility, vol. 56, no. 1, pp. 177-187, Feb. 2014, doi: 10.1109/TEMC.2013.2271913.

[175] N. Wagner, K. Emmerich, F. Bonitz and K. Kupfer, "Experimental Investigations on the Frequency- and Temperature-Dependent Dielectric Material Properties of Soil," in IEEE Transactions on Geoscience and Remote Sensing, vol. 49, no. 7, pp. 2518-2530, July 2011, doi: 10.1109/TGRS.2011.2108303.

[176] R. Alipio and S. Visacro, "Modeling the Frequency Dependence of Electrical Parameters of Soil," in IEEE Transactions on Electromagnetic Compatibility, vol. 56, no. 5, pp. 1163-1171, Oct. 2014, doi: 10.1109/TEMC.2014.2313977.